Universitat de les
Illes Balears

Programa Oficial de Postgrau
de
Ciències Experimentals i Tecnologies (Física)

Doctor per la Universitat de les Illes Balears

# Two satellite-based rainfall algorithms, calibration methods and post-processing corrections applied to Mediterranean flood cases.

Tesis doctoral

Angel Luis De Luque Söllheim

Director: Prof. Sergio Alonso Oroza

Departament de Física

Grup de Meteorologia

# Two satellite-based rainfall algorithms, calibration methods and post-processing corrections applied to Mediterranean flood cases.

Tesis doctoral presentada por

**Angel Luis de Luque Söllheim**

para la obtención del grado de Doctor por la Universidad de les Illes Balears

**Director de Tesis**

Prof. Sergio Alonso Oroza

Palma de Mallorca, Marzo de 2008

# Acknowledgements

*A special thank in first place to my director, Prof. Sergio Alonso Oroza, for revising patiently this thesis and his important comments that helped notably to improve the work. Our colleagues from the Meteorology Group of the Balearic Islands University (UIB) are acknowledged for their collaboration in many important topics for the development of this research: Lluis Fita Borrell for his help in computer programming and for providing access to ECMWF analyses used in section 5 and NCEP analyses in section 8. Dr. Romualdo Romero March for the detailed revision of sections 5, 6 and 7 of this thesis. Dr. Victor Homar Santander for his valuable help in the synoptic description of the case study in section 5 and particularly, to Alberto Martin for the two numerical simulations performed for the two studied flood cases.*

*The Meteorological Centre at Balearic Islands belonging to the Spanish Weather Service (INM) is acknowledged, especially: Dr. J. A. Guijarro, Dr. A. Jansá, M. Pons and M. Gayá for the resources, the Meteosat-7 satellite, radar and lightning data facilitated.*

*The content of chapter 4 (CRR) would not be possible without the valuable help of the INM staff members of the SAF (Satellite Application Facility) project; I. Gómez, P. Fernández, Dr. M. A. Martínez and M. Manso.*

*The rain gauge datasets used in section 5 were supplied by the Hydrometeorological Institute of Albania (HMIA). Many thanks to Tanja Porja from the HMIA for the digitalization of the rain rates from the hydrographs and the close collaboration with the author in the work described in chapter 5.*

*Ramón Pascual from the Meteorological Centre at Catalonia (INM) is acknowledged for the fruitful support regarding local radar developments and important documentation for section 7.*

*The Swedish Meteorological and Hydrological Institute (SMHI) has supplied kindly the radar data for the study concerning the CRR matrices. Rain gauge data of the internal basins of Catalonia were provided by the Agencia Catalana del Agua (ACA). NCAR/Scientific Computer Division (sponsored by the National Science Foundation) is acknowledged for providing access to NCEP analyses used in section 6.*

*The research described from chapter 5 to 8 was developed under the objectives and financial support of the Interreg IIIB-Medocc European project AMPHORE (2003-03-4.3-I-079) and the Spanish project PRECIOSO MEC (CGL2005-03918/CLI).*

*Many thanks to the EUMETSAT organization for providing free and direct access to the Meteosat archived data.*

## Resumen

Este trabajo de tesis se introduce con un breve repaso de los distintos métodos de estimación de precipitación con datos de satélite. A continuación, en el mismo capitulo inicial, se explica porqué de todas las alternativas posibles el método del Auto-Estimator es un buen comienzo y la importancia a la hora de aplicarlo sobre regiones del Mediterráneo. En el segundo capítulo se describe de forma breve el procedimiento por el cual la radiación terrestre es detectada por el sensor MVIRI (Meteosat Visible and Infrared Radiation Imager), a bordo del la plataforma geoestacionaria Meteosat-7, y como dicha radiación es transformada en temperatura de brillo para los dos canales infrarrojos.

En el tercer capítulo se explica el algoritmo del Auto-Estimator y las diferentes correcciones aplicables a posteriori sobre los campos de precipitación. Algunas de estas correcciones deben ser alimentadas con datos procedentes de modelos numéricos como por ejemplo, el MM5. Dicho modelo se ha considerado el mejor candidato para esta tarea tal y como se justifica al final de este tercer capítulo. El método experimental llamado CRR (Convective Rainfall Rate) se describe en detalle en el cuarto capítulo y se aplica y se evalúa en el capitulo siguiente junto con el Auto-Estimator y las distintas correcciones en un caso de inundaciones ocurrido el 21, 22 y 23 de septiembre de 2002 en Albania. Se destaca en este quinto capítulo los métodos de calibración de la curva del Auto-Estimator puesto en práctica con medidas in situ de precipitación obtenidas por estaciones meteorológicas.

El siguiente estudio se realizó en Cataluña motivado por otro caso de inundaciones severas centradas en la montaña de Montserrat entre el 9 y el 10 de Junio de 2000. En el capítulo 6 se analiza de forma breve este caso utilizando una simulación del MM5. Sin embargo a diferencia del caso anterior los datos disponibles del radar de Barcelona son previamente calibrados utilizando observaciones pluviométricas (capítulo 7) con el fin de obtener la mejor estimación posible de la precipitación desde el radar. Desde el punto de vista del Meteosat-7 la precipitación se calcula utilizando las dos técnicas, además de las correspondientes correcciones (capítulo 8). Finalmente, éstas fueron evaluadas con respecto a la precipitación radar y medidas in situ de estaciones. Es importante destacar que en este segundo caso se vuelve a aplicar los métodos de calibración con datos de estaciones pluviométricas y por otro lado, se utilizaron datos de descargas eléctricas para determinar las células convectivas más destacables del sistema

nuboso. Como consecuencia, las estimaciones de precipitación desde el satélite han sido mejoradas tal y como se describe en la sección 8.3 y 8.4.

Finalmente, en el capítulo 9, se incluyen las conclusiones más importantes con respecto a los dos casos de estudio y se comenta las futuras líneas de investigación.

**Contents**

## 1. Introduction

### *a) Abstract*

This thesis work shows, in the first chapters, a brief overview of the different satellite rainfall estimation methods. Next, it explains why from many alternatives, an empirical method such as the Auto-Estimator is a basis to begin study, and why application to Mediterranean countries is important. Chapter 2 it is describes briefly how earth radiances are captured by MVIRI (Meteosat Visible and Infrared Radiation Imager) sensors on board the geostationary satellite Meteosat-7 and later transformed into physical units like brightness temperatures for the two infrared bands.

In chapter 3 the Auto-Estimator algorithm and the different post-processing rainfall corrections are explained. Some of these corrections have to be fed by meteorological outputs from a numerical model, such as the MM5, which was considered as the optimum for this task as clarified in section 3.6. Next, the Convective Rainfall Rate (CRR) experimental estimation method is fully described in chapter 4 and applied, later, within the Auto-Estimator and correction factors in a flood case which occurred from September 21st to September 23rd, 2002 over Albania (section 5). In section 5.5, a method developed by us to calibrate satellite brightness temperatures with in situ rain rate ground observations is explained.

The next study was completed in Spain over the Catalonian region, provoked by another severe flood centred in the Montserrat Mountain region on June 10th, 2000. Chapter 6 briefly analyses this case from a synoptic point of view using a MM5 simulation. However, the available data from the Barcelona radar were first checked and calibrated using rain gauges (section 7) in order to estimate the best possible radar-based rainfall. From the satellite; rain rate estimates from Auto-Estimator, CRR and correction factors were performed and verified in the last case study (section 8). Calibration experiments using radar and rain gauges are applied and verified. It is important to mention that electrical discharges from ground detector networks were used here to detect the most convective cells of the cloud system and, as a consequence, precipitation estimates were improved as described in section 8.3 and 8.4.

Finally, chapter 9 contains the most important conclusions derived from the two studies and opens future research lines.

*b) A brief overview of satellite rainfall methods.*

It is difficult to look at satellite precipitation estimates from a unified perspective encompassing all possible applications. A very complete overview of the early work and physical premises of visible (VIS) and thermal infrared (IR) (10.5 – 12.5 µm) techniques is provided by Barrett and Martin (1981). Following their classification the rainfall estimation methods can be divided into the following simple categories: 1) cloud-indexing, 2) bi-spectral, 3) life history, and 4) cloud model-based. Each of the categories exploits a particular aspect of the sensing of cloud physics properties using satellite imagery (Levizzani *et al*. 2002).

1) Cloud indexing techniques assign a rain rate level to each cloud type identified in the satellite imagery. The simplest and perhaps most widely used is the one developed by Arkin (1979) during the GARP (Global Atmosphere Research Programme) on the basis of a high correlation between radar-estimated precipitation and the fraction of the area colder than 235 K in the IR. The scheme, named GOES Precipitation Index (GPI) (Arkin and Meisner, 1987), assigns these areas a constant rain rate(1) of 3 mm $h^{-1}$, which is appropriate for tropical precipitation over 2.5° by 2.5° areas. The GPI is a standard for long term rainfall analysis (Arkin and Janowiak, 1991) and is regularly applied and archived for climatologically.

2) Bi-spectral methods are based on the very simple, although not always true, relationship between cold and bright clouds and the high probability of precipitation, which is characteristic of cumulonimbus. Lower probabilities are associated to cold but dull clouds (thin cirrus) or bright but warm (stratus). The Rainsat technique (Lovejoy and Austin, 1979; Bellon *et al*. 1980) obscures cold but not highly reflective clouds or those that are highly reflective but have a relatively warm top. The number of false alarms is reduced over the pure IR techniques. The algorithm is based on a supervised classification trained by radar to recognize precipitation from both VIS brightness and IR brightness temperature $T_B$. Rainsat was applied to Meteosat and optimized over the UK by Cheng *et al.* (1993) and Cheng and Brown (1995).

3) Life-history methods belong to a family of techniques that specifically require geostationary satellite imagery because they rely upon a detailed analysis of the cloud life cycle, which is particularly relevant for convective clouds. An example is the technique described by Griffith *et al*. (1978). A greater problem arises in the presence of

---

[1] Units assigned to rain rates in most of the references used for the elaboration of this thesis report. The equivalence to S. I. units is: 1 mm $h^{-1}$ = 2.778 $10^{-4}$ kg $m^{-2}$ $s^{-1}$

cirrus anvils from the neighbouring clouds: they often obscure the cloud life cycle underneath leading to possible under-estimates early in the day and over-estimates toward the evening. Negri *et al.* (1984) have simplified the Griffith-Woodley technique eliminating cloud tracking and producing a precipitation scheme that treats each cloud as if existing only in one image. The resulting Negri-Adler-Wetzel (NAW) scheme has been proved to perform at the same level as Griffith-Woodley for tropical environments. The NAW technique was calibrated by the authors for convective rainfall over Florida. It assigns rain rates to cloudy pixels colder than an isotherm threshold of 253 K. All adjacent pixels colder than this threshold temperature constitute a cluster, which then can be defined as a cloud in this method. For every cloud, the simplified version of the NAW scheme defines three areas with different rain rates. It assigns 8 mm $h^{-1}$ to the coldest 10 percent of the pixels in the cloud, 2 mm $h^{-1}$ to the next warmest 40 percent of the pixels and no rain is assigned to the remaining 50 percent.

4) Cloud model techniques aim at introducing the cloud physics into the retrieval process for quantitative improvement derived from the overall better physical description of the rain development phases. Gruber (1973) first introduced a cumulus convection parameterization to relate fractional cloud cover to rain rate. Wylie (1979) used a cloud model to adjust calibration coefficients. A one-dimensional cloud model relates cloud top temperature to rain rate and rain area in the Convective Stratiform Technique (CST) (Adler and Negri, 1988; Anagnostou *et al.* 1999). Reudenbach *et al.* (2001) have modified the CST using numerical model data (1D cloud model and mesoscale model) and their Enhanced CST (ECST) is better adjusted to meteorological conditions in Western Europe, not as before, relying on vertical profiles from the tropics. Once the locations of the convective cells have been identified, the rain parameters are assigned based on a 1-D cloud model (e.g. Adler and Mack, 1984) that calculates maximum rain rates and maximum volume rain rates from a sequence of models as a function of maximum cloud height (or minimum cloud model temperature, *Tc*). The convective rain area (*Ar*) is assumed to be five times the model updraft area (on the basis of observations). Therefore

$$A_r = 5\pi r^2 \tag{1.1}$$

The average rain rate ($R_{mean}$) over the raining area of the cell is

$$R_{mean} = VRR / Ar \qquad (1.2)$$

where $VRR$ is the instantaneous volume rainfall rate calculated from the cloud model results. A linear fit of $Tc$ and $R_{mean}$ for the Florida Area Cumulus Experiment (FACE) yields

$$R_{mean} = 74.89 - 0.266 \cdot Tc \qquad (1.3)$$

While a similar log-linear fit of $Tc$ and $Ar$ yields

$$Ar = \exp(15.27\text{-}0.0465 \cdot Tc) \qquad (1.4)$$

To every other element colder than the stratiform threshold a fixed rain rate of 2 mm $h^{-1}$ is assigned.

### *c) A brief introduction*

Heavy rainfalls are an important climatic feature of the Mediterranean region (Romero *et al*. 1999). They usually take place at the end of the Summer (Homar *et al*. 2003) and during Autumn (Doswell III *et al*. 1998, Homar *et al*. 1999) although can happen in other seasons as well. The Mediterranean hydrographical configuration is characterized by numerous small and steep river basins and by highly populated and industrialized areas. Crucial aspects of heavy rainfalls are the high intensity they attain and their fatal consequences. They contribute generally to the seasonal torrent and river overflowing; causing severe flooding that has a great impact on the society the economy and landscape.

Real time rainfall estimation using geosynchronous satellite data has several applications in meteorology and hydrology. Although the estimates are indirect, the high frequency and high spatial resolution of the measurements, as well as the broad area that they cover, make them uniquely complementary to rain gauge and radar measurements (Vicente *et al*. 1998). Conventional rain gauges, when they exist, have a mostly sparse distribution and data is not usually available in real time. However, meteorological radars have limited spatial coverage and are often affected by attenuation problems, beam overshoot or ground and mountain echoes.

The Auto-Estimator technique proposed by Vicente *et al*. (1998) follows another concept and can not be easily included in any of the Barrett and Martin (1981) four categories. This technique makes use of IR 11 µm GOES satellite and radar data from the US network with applications to flash flood forecasting, numerical modelling, and operational hydrology. The rainfall retrieval is performed through statistical analysis between surface radar-derived instantaneous rainfall estimates and satellite-derived IR cloud top temperatures collocated in space and time. A power law regression curve is computed between IR cloud top temperature and radar-derived rainfall estimates on the ground. Rain rates from the power law were corrected taking into account clouds textures and clouds grow. Rainfall estimates are also adjusted for different moisture regimes using precipitable water and relative humidity fields from the NCEP Eta Model and SSM/I measurements. This approach reverses traditional methodology with respect to physical initialization of numerical models. Therefore, it is a new concept that has caught our attention in order to apply and verify it within the CRR algorithm in the two proposed flood cases.

The CRR (Convective Rainfall Rate) algorithm was developed by the SAFNWC (Satellite Application Facility on support to Nowcasting) project to detect intense mesoscale convective systems and to screen the most probable precipitation associated. It estimates rain rates using the three bands of the Meteosat-7 and matrices calibrated with earth-based radars. Matrices were performed following an accurate version of the Rainsat techniques but combining the infrared bands (IR and WV) as first suggested by Kurino (1997a) to detect convective clouds. The CRR method could be classified into the second Barrett and Martin (1981) category, Bi-spectral, but also uses the Meteosat-7 water vapour band (WV). This experimental algorithm is applied and verified in the two flood cases.

Our study focuses heavily on the application and evaluation of rainfall correction factors on Mediterranean areas. These were delineated to modify satellite rain rate estimates under certain special conditions. The moisture correction factor, cloud growth rate, cloud top temperature gradient, parallax and orography were proposed by Vicente in various research articles (Vicente *et al*. 1998, 2002) and they are described in Chapter 3.

The aim of this work is not only an assessment or verification of different satellite methodologies and rainfall corrections. New options to improve results are proposed and applied in a practical way. These are focused on new calibration methods or to study the effect over the algorithms after a recalibration in such severe events. For example, in section 5.4 a way to adjust satellite measures directly with rain gauges caused by the lack of radar data over the Albanian region, is investigated. The other research line explored here is the modification of standard correction factors to improve them and the generation of new ones. One example of this is the new lightning correction factor developed in section 8.4.

## 2. An overview of the Meteosat-7. Radiances calibration

### *a) Meteosat-7*

Meteosat-7, the last satellite in the series, was launched in 1997. It is part of the Meteosat Transition Programme (MTP) which will manage the handover between first and second generation satellites. Meteosat Second Generation (MSG) is an upgraded series of satellites employing state of the art technology, which continues the fine tradition of the first series, but with improved data gathering capabilities. Meteosat produces images of the full Earth disc as viewed from its geostationary orbit at around 36000 km above the sea level. At the time the two flood cases occurred (Jun-2000 and Sep-2002) the sub-satellite point was located at 0º latitude and 0º longitude, in the gulf of Guinea,. Its spatial image coverage was extended from approximately 60 degrees west to 60 degrees east. In the present time the Meteosat-7 satellite is located at 57.5º longitude east over the Indian Ocean. This sensor provides a set of three images, one in each spectral band, produced every 30 minutes. The communications package aboard a Meteosat-7 consisted of a transponder and its antenna subsystem. This communications package transmits data every half hour to the ground facilities located at the European Satellite Operations Centre (ESOC) in Darmstadt, Germany. The communications package also receives processed images from the ESOC which are then relayed to user stations in over 16 countries. The primary instrument aboard the Meteosat-7 satellite was the three-channel visible, infrared spin imaging radiometer at 100 rpm called MVIRI (Meteosat Visible and Infrared Radiation Imager). The visible spectrum (VIS) band is scanned between 0.4 - 1.1 μm, the infrared window region (IR) between 10.5 – 12.5 μm, and in the water vapour (WV) absorption band between 5.7 – 7.1 μm. The radiometer scans the Earth point by point and line by line from south to north, which takes about 25 minutes to create a complete IR and WV image of the earth with 2500 lines by 2500 elements and double sized for the VIS image. Then the sensor takes 5 minutes to retrace to its initial scanning position and to transmit the image data to the ground station. Spatial resolution of the WV and IR images is about 5 km and 2.5 km of the VIS images in the sub-satellite point. This spatial resolution decreases when the scan point is farther from the sub-satellite point, for example a WV or IR pixel size over Albania[2] is around 7 km in latitude and 7 km in longitude. The UTC time is assigned to

---

[2] One of the studies is performed in this small country located at the southwest of Italy on the other side of the Adriatic Sea.

each Meteosat image at the end of the radiometer scans meaning that the real UTC time over the Mediterranean area is around 10 min before the image time. This factor is important when comparing Meteosat-7 measurements with other sources.

### *b) Radiances calibration*

The Meteosat measurements were traditionally, but not absolutely, calibrated on earth due to a lack of an on-board blackbody calibration system for preoperational satellites (Meteosat-1, Meteosat-2, and Meteosat-3). A malfunction in the blackbody mirror of Meteosat-4 prevented the use of an on-board blackbody calibration system. It was not used with the following instruments on board Meteosat-5 and Meteosat-6. Instead different vicarious calibration schemes were implemented over the first 30 years to perform the operational calibration of the instruments. Detailed descriptions of these procedures are given by Gube *et al.* (1996) for the IR and by Schmetz (1989) and Van de Berg *et al.* (1995) for the WV, respectively. In summary, vicarious methods are based on selected in situ measurements of temperature and humidity from the earth's surface and atmosphere. These measurements are used to simulate, by transfer models, the radiances observed by the three channels of the Meteosat image radiometer. Since May 2000, the on-board blackbody viewing system of the spacecraft Meteosat-7 has been working properly. Early comparisons with the previously used vicarious calibration procedure indicate that the major difference to be found concerns a strong improvement of the high-frequency stability of the WV calibration coefficients (Tjemkes *et al.* 2001). The absolute values of the calibration coefficients, nevertheless, do not exhibit a large departure from the vicarious scheme (less than 0.8%).

This thesis work is focused on the two flood cases that occurred on the 9th and 10th of June 2000 (Montserrat, Spain) and the 21st to the 23rd of September 2002 (Albania) studied with the MVIRI sensor on board Meteosat-7. Therefore, more details about the black body calibration system between May 2000 and December 2003 are provided by the EUMETSAT technical reports and summarized in the following paragraphs.

The black body calibration mechanism consists of two black bodies with know temperatures, which can be viewed sequentially. The observed counts (IR and WV) can then be related to the known radiance in the two channels, resulting in two black body calibration coefficients. However, as the front optics are not part of the optical path during a black body observation, and as the viewing geometry is different when performing a black body observation with respect to nominal Earth observation, a correction model has been designed allowing for these effects. Hence, the corrected black body calibration is used for operational calibration. The black body observations are performed at least once a day. The mechanism uses two black bodies: one having the ambient spacecraft temperature and one heated to about 50 K above it. First the black body at ambient spacecraft temperature is viewed, and forms the reference signal. Then the heated black body is viewed, and the temperature difference between both black bodies is used to obtain the response of the detectors. The obtained response is converted into counts and transmitted to earth. For both channels (IR and WV) the observed black body counts ($C_{bb}$) and the known radiances ($R_{bb}$) are related to each other via a linear relationship of which the angle gives the black body calibration coefficient ($\alpha_{bb}$):

$$R_{bb} = \alpha_{bb} \cdot ( C_{bb} - C_{sc}) \tag{2.1}$$

Where $C_{sc}$ is the space count assigned to the lowest detected radiation. The viewing of the black bodies is performed by moving a mirror into the nominal optical path of the radiometer, between the optical block and the front optics. Therefore, the front optics of the radiometer is not included into the optical path of the black body calibration mechanism. In addition, the viewing geometry is not similar for black body and Earth view. Hence, the pure black body calibration coefficients cannot be used directly for calibration of the infrared channels. A correction model has been designed allowing for the following factors:

- Correcting for the impact of the response functions of the mirrors of the front optics not viewed during a black body observation.
- Correcting for the viewing geometry. For a black body observation the viewing geometry is limited by the pupil of the optical block. For an Earth scan the viewing geometry is defined by the geometry of the first mirror, which is partially obscured by the second mirror.

The correction model for the black body calibration coefficients ($\alpha_{bb}$) is described as:

$$\alpha = \alpha_{bb} / ((\cos A_1 - \cos A_2) / ( K (1 - \cos A_3))) \tag{2.2}$$

in which the following parameters are used:

$\alpha$ : The absolute calibration coefficient (IR or WV)

$\alpha_{bb}$ :  The black body calibration coefficients (IR or WV)

$A_1$ : The maximum angle at which the detector can see the 1st mirror.

$A_2$ : The maximum angle at which the detector can see the 2nd mirror.

$A_3$ : The maximum angle at which the detector can see the black body, which is determined by the pupil of the optical block.

$K$ : A constant factor used to remove the response function of the front mirrors that are not viewed during a black body scan.

The absolute calibration coefficient "$\alpha$" and the space count "$C_{sc}$" are computed by the black body operationally for every day and every infrared band (IR and WV) and also provided by the EUMETSAT calibration reports via internet. These parameters make it possible to calculate the relationship between radiation and satellite counts by applying equation 2.1.

*c) Radiances to brightness temperatures*

In the Annexes of EUMETSAT, calibration reports are given for the radiance to temperature relation based on the Planck function and the instrument's spectral response function. To facilitate the use of these tables, designed to highlight radiances given by the blackbody to brightness temperature for the IR and WV channels, an accurate exponential fit of the above mentioned tables is expressed as follows:

$$R(T) = \exp( A + B/T) \tag{2.3}$$

where R: is the radiance (in W $m^{-2}$ $sr^{-1}$)

T: the temperature (in K)

A: regression coefficient (is dimensionless)

B: regression coefficient (in K)

The equation fits the relationship with a root mean square error less than 0.2 K in the range between 200 K and 330 K. Therefore, the following table provides the regression coefficients for the infrared channels of Meteosat-7.

Table 3.1 Meteosat-7 infrared bands radiation to temperature conversion coefficients

| | |
|---|---|
| IR: A | 6.9618 |
| IR: B | -1255.5465 |
| WV: A | 9.2477 |
| WV: B | -2233.4882 |

A different procedure is used for the visible channel. Measurements of reflected solar radiation for this channel were performed during dedicated campaigns by an airborne radiometer, at the same time and under the same observation geometry as the satellite. This allowed to direct assignment of the measured radiance to the digital count delivered by the satellite, after supplementary transfer calculations of radiation absorbed by the atmosphere between aircraft and satellite. Such campaigns are expensive and have been performed only once for every satellite except for Meteosat-3. This has been considered sufficient for Meteosat VIS channels as they have been found to be quite stable with a steady degradation of response of the order of between 1-2% per year and closely followed in the EUMETSAT calibration reports. Various studies have been done to transform VIS counts to radiances units (Govaerts *et al.* 1998, 1999), however this thesis will not go through this feature because the CRR matrices use corrected VIS counts without any further calibration to radiance units.

Correct calibration of satellite images has been ensured using the McIDAS open software (http://www.unidata.ucar.edu/software/mcidas/). An updated version of this programme detects the satellite platform, sensor and band of every image and it applies the correspondent calibration module to transform digital counts to physical units such as radiances in W $m^{-2}$ $sr^{-1}$ or brightness temperatures in K. The correct performance of the McIDAS calibration modules in each flood case have been checked selecting a few points from the satellite images in order to test count quality and the conversion to radiances and temperatures (WV and IR). These were compared with ones offered by the EUMETSAT reports. Technical reports for the Meteosat-7 are available at the time of writing this work in:
http://www.eumetsat.int/Home/Main/Access_to_Data/Meteosat_Meteorological_Products/Calibration/SP_1119512203627

## 3. Auto-Estimator, rainfall correction factors and the numerical model

The operational GOES infrared rainfall technique (Vicente *et al*. 1998) called Auto-Estimator (A-E), computes rainfall rates based on a fixed non-linear, power-law regression relationship between the infrared cloud top brightness temperatures and collocated radar rainfall. After extensive analysis looking for clearly convective cores in the Great Plains of the central USA and areas adjacent to the Gulf of Mexico, the calibration dataset finally consisted of 16 radar satellite pairs of 4 by 4 km resolution images. These were collected from different convective systems over several days during the months of March to June 1995. The mean radar rainfall was calculated for each 1 K temperature interval from 195 to 260 K as illustrated in figure 3.1 by the red dots and the solid curve which represents the regression fit given by:

$$R = 1.1183\ 10^{11} \exp(-3.6382\ 10^{-2}\ T_{IR}^{1.2}) \qquad (3.1)$$

where $R$ is the rainfall rate in mm h$^{-1}$ and $T_{IR}$ is the cloud top temperature in Kelvin. Both rain and no rain pixels are considered in the computation of the regression fit.

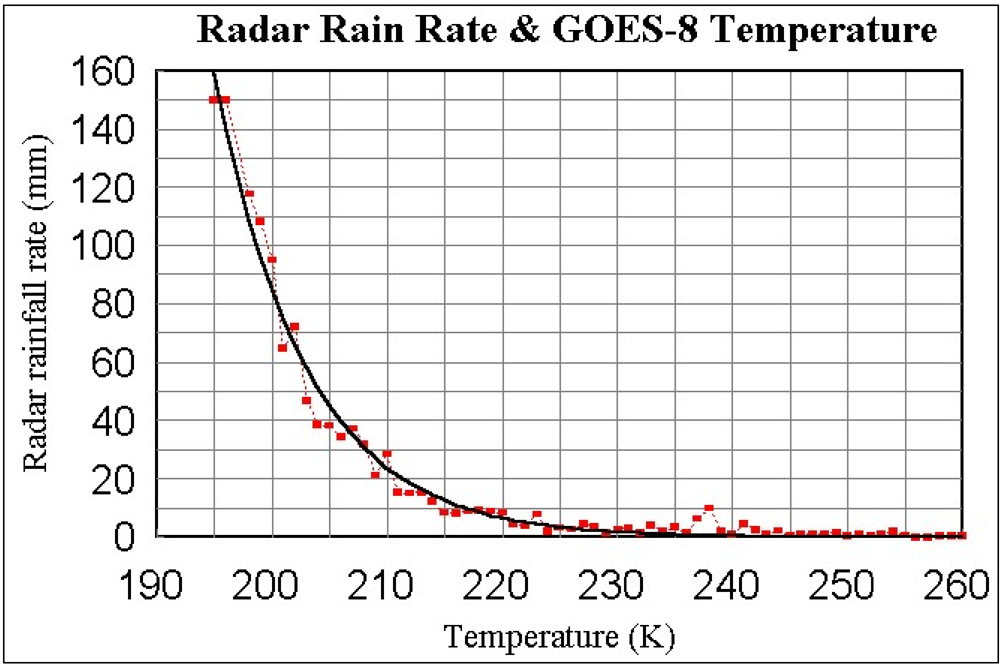

Figure 3.1. Mean rainfall rate for each temperature from 195.0 to 260.0 K computed from collocated pairs of radar derived from rainfall rate and IR cloud top temperature (dotted curve).

The radar reflectivity to rainfall rate conversion was based on the Miami Z-R relation used during the Experimental Meteorology Laboratory (EML) experiments (Woodley, 1970) and shown in equation 3.2 where $Z$ is the reflectivity in $\mathrm{mm}^6\ \mathrm{m}^{-3}$ and $R$ is the rainfall rate in $\mathrm{mm\ h}^{-1}$.

$$Z = 300\ R^{1.4} \tag{3.2}$$

In the case studies shown in this thesis, the A-E curve is applied but, the derived rain rates should be considered with caution for two important factors. The first one is that the A-E curve was initially developed in the south of the US, very far from the Mediterranean area and the second reason is that A-E is applied to two flood cases with their uniquely special circumstances. Our study focuses on correction factors of satellite rain fields proposed by Vicente in different papers (Vicente *et al.* 1998, 2002). These corrections are important because a single regression curve for rainfall rate retrieval is very limited due to the variety of physical processes associated with rain generation. The relationship between cloud top temperature and surface rainfall rate varies with storm type, season, location, low level environment and many other factors that make it impossible to be accurate with a single regression curve. Estimated rainfall from a generic curve should be adjusted to a specific case condition after being modified by the moisture correction factor, cloud growth rate, cloud top temperature gradient, parallax and orographic corrections. The moisture and orographic correction factors need data from numerical model outputs. The MM5 numerical flood case settings are described in sections 5.2 and 6.1 respectively. The model chosen is the optimal for this task as commented in section 3.6.

The advantage and new aspect in correction factors when compared to other methods is that they can be applied one by one or combined in a second phase after satellite rainfall estimates of any kind from a standard method are available. Therefore a sensitivity test of the mentioned correction factors for CRR estimates is also planned.

A new version of the A-E called Hydro-estimator (Scofield and Kuligowski, 2003) has been recently developed. The main difference in A-E is that raining pixels are defined as those with 10.7 µm brightness temperature below the average value for a predetermined region surrounding the pixel of interest. This approach has substantially reduced the size of the rain area that, in fact, used to be exaggerated by the A-E. Therefore, it is an interesting research line that should be explored by us in the near future. However, this new method has to be considered with caution because the same article (Scofield and Kuligowski, 2003) found that the performance of A-E in the operational context in the US is only marginally better, in general, to that of the Hydro-estimator.

### *3.1 Moisture correction factor (PWRH)*

A rainfall infrared curve or a CRR matrix is not enough to represent accurate rainfall estimates over anywhere at anytime. There is a tendency to over-estimate rain rates in dry environments and under-estimate them under high moisture conditions. This problem was discussed by Scofield (1987), who proposed the use of a moisture correction factor defined as Precipitable Water, PW, in the layer from the surface to 500 hPa and the mean Relative Humidity between the surface and the 500 hPa level. The PW fields in mm of water and RH in percentage in this study are derived from the MM5 numerical simulation, completed every 30 minutes. Following instructions given by Vicente *et al.* (1998), the PWRH factor is empirically scaled from 0.0 to 2.0, and the environment is considered dry if PWRH is significantly lower than 1.0 and quite moist if PWRH is greater than 1.0. Satellite rain rates are multiplied by the PWRH factor in all cases but taking into account the next restrictions for the A-E:

- If $T_{IR}$ is lower than 210 K and the PWRH factor is greater than 1.0, the estimated rain rate in equation 3.1 is quite high and environmental moisture would increase it much more. In this case the computed rainfall rate should not be multiplied by the PWRH correction factor.
- If $T_{IR}$ is lower than 200 K the rainfall rate should be limited to 72.0 mm $h^{-1}$, approximately the maximum rainfall rate found over the US for a 4 by 4 km grid.

For the CRR the only limitation recommended by the SAFNWC (Satellite Application Facility on support to Nowcasting) technical Report (INM 2002) is that, if the pixel latitude is greater than 55ºN, $T_{IR}$ is lower than 215 K and the PWRH factor is greater than 1.0, the computed rainfall should not be multiplied by the PWRH correction factor.

### *3.2 Cloud growth rate correction factor (GR1, GR2)*

The next important feature to focus on is the rain/no rain discrimination problem. A convective system is more active and produces the greatest rainfall rates when the tops are becoming colder and expanding (Woodley *et al*. 1975; Griffith *et al*. 1978; Scofield and Oliver, 1977). Thus, the detection of active or decaying portions of thunderstorms can be attempted by searching for collocated pixels in two consecutive infrared images that become colder, warmer or stay at the same temperature. Based on the assumption that decaying clouds or clouds with cold tops that are becoming warmer produce little or no rainfall (Woodley *et al*. 1972, Scofield, 1987), the rainfall rate computed via A-E and CRR are then modified according to the following:

- If the coldest infrared pixels in the analysed image are colder than those in the previous one, the convective system is intensifying and the pixels in the first image are associated with the heaviest precipitation rates. In this case the rainfall rate remains unchanged.
- If the coldest Infrared pixels in the analysed image are warmer than those in the previous one, the convective system is weakening and upward vertical motion has likely ceased. In this case, the rainfall rate is adjusted to zero for those pixels.
- If there has been no change in the cloud top temperature in the two consecutive images (no growth or decay in the half-hour interval), the rainfall rate stays the same.

The original growth rate correction for the GOES-8 called GR1 in this document was proposed by Vicente *et al*. (1998). This method presents some inconveniences which can be detected from qualitative observations. One of the most important is that clouds in mid-latitudes can move several kilometres in thirty minutes between infrared images and the correction factor would be applied over shifted pixels. Therefore, rain rates located in the front of a cloud system in movement do not experience any change throughout the process while rain rates in the back side are systematically eliminated. This has motivated the development of another growth rate correction factor called GR2 that takes in account displacements of clouds applying a cross correlation method. Virtual position of the cloudy point 30 minutes before was calculated using a grid of 15 by 15 pixels centred in a point. By moving the grid around the same point position in the previous infrared image, correlation coefficients are calculated. The translation to higher correlation is then selected and the grid central points in both images are associated to calculate the temperature variation with time. Finally, the rain rate of this central point is set to zero or not depending on its temperature change as explained in the beginning of this subsection.

### *3.3 Cloud-top temperature gradient correction (TGR)*

Much information can be extracted from the cloud-top structure on a single infrared image or the cloud top temperature gradient. The method of finite difference is used to locate the local temperature maxima and minima within grids of 3 by 3 or 5 by 5 pixels. The idea is to search for the pixels that are above the average cloud top surface height (local temperature minima), and assume that these pixels indicate active convection associated with precipitation beneath. Negri and Adler (1981) showed that in most cases, the GOES IR pixels that are colder than a local satellite IR temperature minimum coincide with individual radar echoes. As a result the procedure consists of searching for the highest (coldest) and lowest (warmest) cloud tops within a 3 x 3 pixel area centred on the point $P_o = (x_o, y_o)$. If the cloud-top surface is defined by $T = T(x,y)$, where $x$ and $y$ are the point coordinates, the maxima and minima can be determined by analysing the first and second derivative of $T$. The second derivatives of $T$ on the point or pixel $P_o = (x_o, y_o)$ are given using discrete summations by.

$$T_{xx}(x_0, y_0) = \left.\frac{\partial^2 T}{\partial x^2}\right|_{(x_0, y_0)} \approx \left.\frac{T_{i+1,j} - 2T_{i,j} + T_{i-1,j}}{(x_i - x_{i-1})^2}\right|_{(x_0, y_0)} \tag{3.3}$$

$$T_{yy}(x_0, y_0) = \left.\frac{\partial^2 T}{\partial y^2}\right|_{(x_0, y_0)} \approx \left.\frac{T_{i,j+1} - 2T_{i,j} + T_{i,j-1}}{(y_j - y_{j-1})^2}\right|_{(x_0, y_0)} \tag{3.4}$$

$$T_{xy}(x_0, y_0) = \left.\frac{\partial^2 T}{\partial x \partial y}\right|_{(x_0, y_0)} \approx \left.\frac{T_{i+1,j+1} + T_{i-1,j-1} - T_{i+1,j-1} - T_{i-1,j+1}}{4(x_i - x_{i-1})(y_j - y_{j-1})}\right|_{(x_0, y_0)} \tag{3.5}$$

where i and j are the image coordinates, x and y are the point positions in km. So the Hessian matrix H is defined as

$$H = \begin{pmatrix} T_{xx} & T_{xy} \\ T_{yx} & T_{yy} \end{pmatrix} \tag{3.6}$$

and $|H|$ is the Hessian matrix determinant and given by

$$|H| = T_{xx}\,T_{yy} - T_{xy}\;T_{yx} \tag{3.7}$$

Here $P_o$ is characterized in the following way:

- If $|H| > 0$ and $T_{xx} < 0$ the point $P_o$ is a maximum temperature.
- If $|H| > 0$ and $T_{xx} > 0$ the point $P_o$ is a minimum temperature.
- If $|H| < 0$ the point $P_o$ is not a maximum and not a minimum.
- If $|H| = 0$ the point $P_o$ cannot be defined.

Using this information, the rainfall rate for A-E and CRR is adjusted in the following way:

- If the pixel $P_o$ has a temperature maximum, indicating a relatively low cloud top with $P_o$ warmer than its surroundings, the previous rainfall rate is set to zero.
- If the pixel $P_o$ has a temperature minimum, which means that $P_o$ is colder than its surroundings indicating a high cloud top, the previous rainfall rate stays the same.
- If $P_o$ is neither a maximum nor a minimum, indicating $P_o$ is at the same height and temperature as its surroundings, the previous rainfall rate is set to zero.
- if $P_o$ temperature cannot be defined as a maximum or a minimum, the whole process is repeated using pixels within a 5 by 5 pixels grid.
- If $P_o$ temperature cannot be defined again using the 5 by 5 pixels grid, the previous rainfall rate is set to zero.

### *3.4 Parallax correction*

An important factor for accurately estimating precipitation from satellite imagery is the position of the cloud tops as viewed by the satellite. This problem has to do with the fact that the accurate location of precipitation requires the knowledge of the exact position of the cloud tops in relation to the ground below. This is not a problem when a cloud is located directly below the satellite; however, as one looks away from the sub-satellite point, the cloud top appears to be farther away from the satellite than the cloud base. This effect increases as one gets closer to the limb and as clouds get higher. The parallax problem is easier to view in a two dimensional analysis as illustrated in the next figure 3.2.

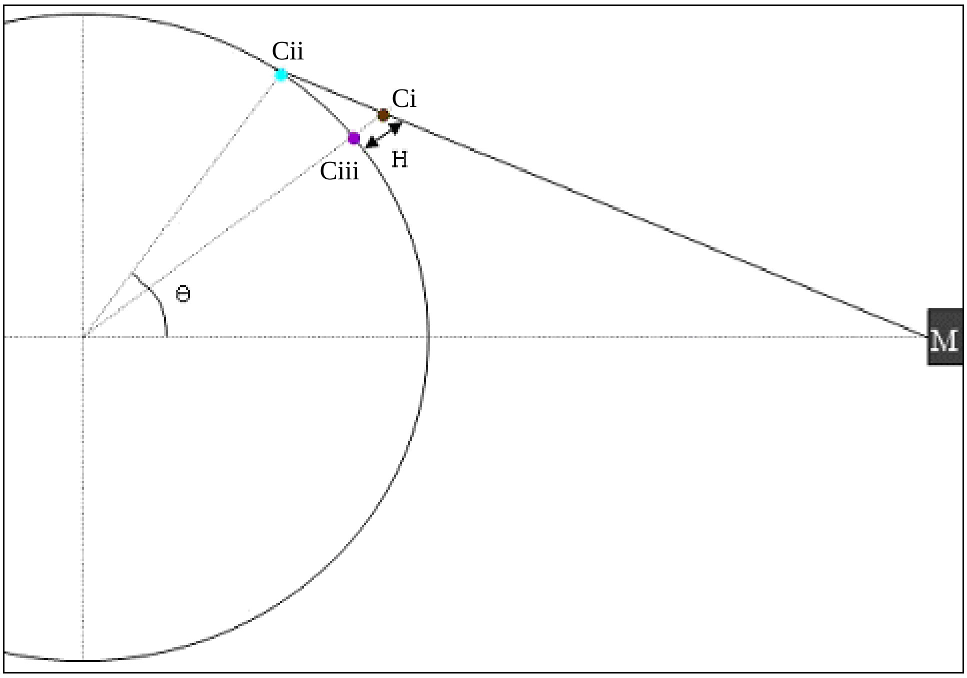

Figure 3.2. The earth and the Meteosat satellite (M) are viewed following the meridian plane. A cloud ‘Ci’ at a height of ‘H’ in relation to the earth’s surface in the northern hemisphere is observed in position ‘Cii’ by the satellite sensor. A correction of the parallax effect should move ‘Cii’ to the correct position ‘Ciii’ in the same vertical as ‘Ci’.

The Parallax correction in the three dimensions of space is a more complex mathematical problem. It is computed following instructions given by Vicente *et al.* (2002) where the cloud top height in every point was estimated from satellite cloud top temperature using US Standard Atmosphere.

The parallax correction depends on three things: the height of the cloud ($H_c$), the apparent position on the earth of that cloud (latitude $\theta_c$, longitude $\varphi_c$), and the position of the satellite (orbiting the Earth at a distance $R_s$ from the centre of the Earth, with a sub-orbital point at the latitude $\theta_c$ and longitude $\varphi_c$).

The parallax correction begins by converting these locations into Cartesian coordinates using the centre of the earth as the origin. The $Z$-axis runs through the intersection of the equator and prime meridian, the $Y$-axis through the poles, the $X$-axis through the equator at longitude 90 E. We consider the earth's surface as an ellipsoid with an equatorial radius $R_{equator}$= 6378.1 km and a polar radius $R_{pole}$= 6356.6 km. Using the ellipsoid equation as the earth surface,

$$(X^2+Z^2)/(R_{equator})^2 + Y^2/(R_{pole})^2 = 1 \tag{3.8}$$

We represent the Cartesian co-ordinates of the apparent position of the cloud ($X_c$, $Y_c$, $Z_c$) on the surface at a distance $R$ from the centre as

$$X_c = R_e \cos \theta_c \sin \varphi_c \tag{3.9}$$

$$Y_c = R_e \sin \theta_c \tag{3.10}$$

$$Z_c = R_e \cos \theta_c \cos \varphi_c \tag{3.11}$$

where $R_e$ is the equivalent of the earth's radius. This can be expressed by

$$R_e = R_{equator} / \sqrt{\cos^2 \theta_c + R_{ob}^2 sen^2 \theta_c} \tag{3.12}$$

where

$$R_{ob} = R_{equator} / R_{pole} = 1.0034 \tag{3.13}$$

The satellite Cartesian coordinates are given by

$$X_s = R_s \cos \theta_S \sin \varphi_S \tag{3.14}$$

$$Y_s = R_s \sin \theta_S \tag{3.15}$$

$$Z_s = R_s \cos \theta_S \cos \varphi_S \tag{3.16}$$

For a satellite in a geostationary orbit, $\theta_S = 0$ and hence $Y_s = 0$.

The relationship between the cloud and the satellite can be found by noting that the line connecting the apparent cloud location and the satellite position intersects the line from the centre of the Earth through the actual cloud location at a height of $H_c$ (estimated by the cloud top temperature and the model atmospheres of the US Standard) above the surface, at a radius $R_c = R_e + H_c$. This implies that

$$(X_a^2 + Z_a^2)/(R_{equator} + H_c)^2 + Y_a^2/(R_{pole} + H_c)^2 = 1 \qquad (3.17)$$

The actual rectangular coordinates of the cloud are given by:

$$X_a = X_c + A\,(X_s - X_c) \qquad (3.18)$$

$$Y_a = Y_c + A\,(X_s - Y_c) \qquad (3.19)$$

$$Z_a = Z_c + A\,(Z_s - Z_c) \qquad (3.20)$$

and $A$ is a parameter determined by the substitution of (3.18), (3.19) and (3.20) on (3.17). The resulting second degree equation on $A$ has a solution given by:

$$A = (-D + \sqrt{(D^2 - 4CE)}\ /2C \qquad (3.21)$$

where $C$, $D$ and $E$ are defined as:

$$C = (X_s - X_c)^2 + (Z_s - Z_c)^2 + B\,(Y_s - Y_c) \qquad (3.22)$$

$$D = 2\,[X_c\,(X_s - X_c) + Z_c\,(Z_s - Z_c) + B\,Y_c\,(Y_s - Y_c)] \qquad (3.23)$$

$$E = X_c^2 + Z_c^2 - (R_{equator} + H_c) + B \cdot Y_c^2 \qquad (3.24)$$

with

$$B = [(R_{equator} + H_c)/(R_{polar} + H_c)]^2 \qquad (3.25)$$

The actual Cartesian coordinates are converted back to final actual latitude at the cloud:

$$\theta_a = \tan^{-1}(Y_a / \sqrt{X_a^2 + Z_a^2}) \qquad (3.26)$$

The actual longitude at the cloud is:

$$\varphi_a = \tan^{-1}(X_a/Z_a) \qquad \text{if } Z_a>0\text{, northern hemisphere} \qquad (3.27)$$

$$\varphi_a = \tan^{-1}(X_a/Z_a)-180^\circ \qquad \text{if } Z_a>0\text{, southern hemisphere} \qquad (3.28)$$

The effect of the parallax correction over a complete Meteosat image is a small movement of clouds toward the sub satellite point (image centre) as illustrated in figure 3.3. The translation is more significant for those points with higher (colder) cloud tops and less noticeable for those located closer to the sub satellite point (SP).

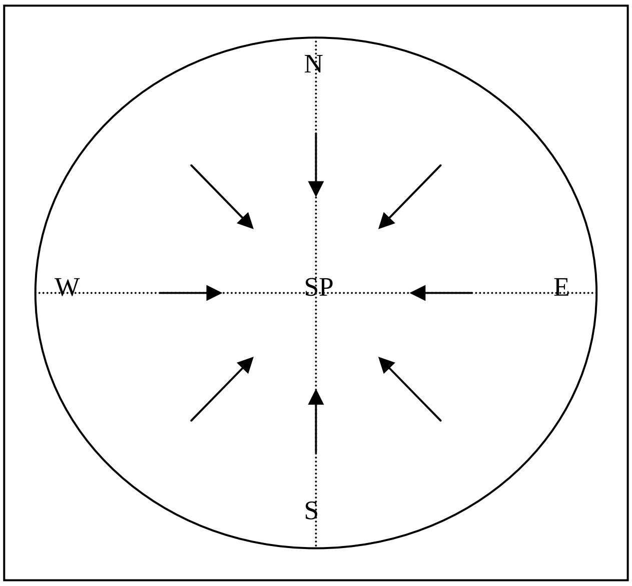

Figure 3.3. Graphic representation of the general movement of cloudy pixels in a geostationary satellite image after a parallax correction. SP, means sub satellite point.

### *3.5 Orographic correction factor*

The orographic problem has to do with the variations in rainfall distribution with elevation combined with wind speed and direction. Rainfall amounts are dependent on the atmospheric flow disturbances created by the mountains themselves. The orographic correction applied on the A-E and CRR uses the interaction between the wind vector $\vec{V}$ and the local terrain height gradient $\vec{\nabla} h$ in the direction of $\vec{V}$ to create a multiplier which enhances or diminishes the rainfall estimate, as appropriate (see figure 3.4). Winds are taken every 30 minutes from the 850 hPa level of the MM5 model and terrain heights are taken from the MM5 earth surface representation initially at a spatial resolution close to the original Meteosat-7 resolution in each case of study. The resultant correction factor varies from 0.2 and 3.5 and represents how much the rainfall rate should be increased or decreased on a pixel (Vicente *et al*. 2002). This correction factor map is later remapped to the exact satellite resolution at the given flood area and the satellite rain rate estimate in each point is multiplied by the correspondent correction factor.

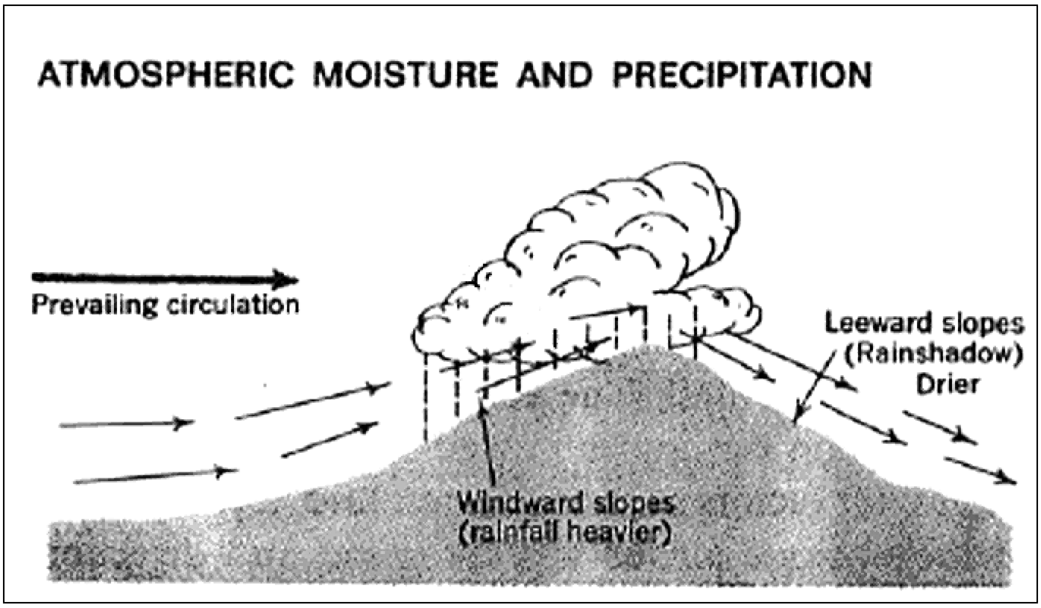

Figure 3.4. Atmospheric flow disturbance caused by mountain effect, wind speed and direction and its influence on rainfall enhancement and suppression.

In a one dimensional cross section of the terrain the width of the affected area by terrain effects before and after a mountain is first determined from the wind speed and direction and the elevation map. The wind path length $D$ is variable from 6 to 24 km depending upon the wind speed $U$ (in m $s^{-1}$) and the equivalent time scale $T_f$ determined by a 15 min fetch. The product of wind speed and time fetch has to be divided by the point spatial resolution in metres $R_s$ in order to get $D$ in pixel units as follows

$$D = (U\,T_f)/R_s \qquad (3.29)$$

The extracted terrain cross-section length extends $D$ pixels upwind and downwind from the reference site, giving a total length of $2D+1$ pixels. The height of the test location can be denoted as $Z_{D+1}$; the location farthest upwind is $Z_1$, the location farthest downwind is $Z_{2D+1}$. The slope between a point $A$ and a downwind point $B$ is be defined as

$$S_{AB} = (Z_B - Z_A)/(B - A) \qquad (3.30)$$

where all the variables of this equation are in m or km, therefore, $S_{AB}$ has no units. For each pixel, $A$, upwind of the site and the site itself (from 1 to $D$+1), the slope is calculated between it and each point $B$ within $D$ pixels downwind (from $A$+1 to $A$+$D$ as shown in figure 3.5). The maximum slope found for each point $A$ is retained as the slope $S_A$. The net slope, $S$, used for the correction is equal to the mean of the $S_A$ values:

$$S = \left( \sum_{A=1}^{D+1} S_A \right) / (D+1) \qquad (3.31)$$

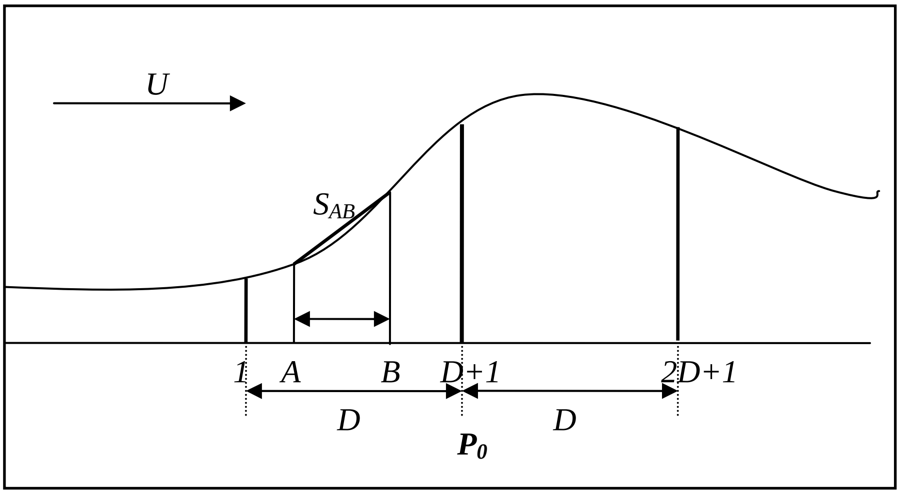

Figure 3.5. Graphical representation of the process applied to calculate the mean slope from a site $P_0$. At a distance of $D$ pixels in both wind directions from $P_0$, the maximum slope $S_A$ is calculated $D$ times in the downwind sense from $A+1$ to $A+D$. Then the mean slope $S$ for the point $P_0$ is obtained from equation 3.31. This process assures positive slopes on the tops of the mountains where precipitation should also be enhanced.

Finally we can define a rainfall rate enhancement parameter $M$, as the result of the vertical velocity induced by a wind with horizontal speed $U$ blowing over a surface with a slope of $S$. Since $M$ should have no effect on the rainfall amounts on a flat terrain, it can be written as:

$$M = 1 + SU \qquad (3.32)$$

where $M$ is defined as a non dimensional variable for $U$ in m s$^{-1}$. Although $M$ can assume negative values, it does not represent a meaningful physical value. Based on the studies of Urbanski (1982) relating terrain induced vertical velocities to differences between estimated and observed precipitation, $M$ is limited to be between 0.2 and 3.5.

### *3.6 MM5 Numerical Model*

The MM5 model is a widely used among the research and operational communities. It is the Fifth Generation of the *Mesoscale Limited-Area Model*, a collaborative project between the Pennsylvania State University (PSU) and the National Centre for Atmospheric Research (NCAR) of the United States. It started in the early 70´s and was later documented by Anthes and Warner (1978). Its non-hydrostatic dynamics core is derived from the primitive set of equations on a vertical terrain-following-sigma-coordinate ($\sigma$) and a horizontal projected grid. The equations are integrated over an Arakawa-C staggered grid and use a temporal finite differencing scheme. It is a versatile modular modelling system with four-dimensional data assimilation and multiple-nest capabilities.

In the vertical, 24 $\sigma$ levels are used, with higher density near the surface to better resolve near-ground processes. The standard version 3 of MM5 distribution incorporates a set of physical parameterizations for the sub grid processes of atmospheric radiation, microphysics, convection, turbulent fluxes of energy and moment, and near-surface processes. For the set of simulations presented here, the grid-resolved microphysics processes are represented by the Reisner *et al*. (1998) scheme, which considers graupel and ice number concentration. The coarser domain uses the Betts and Miller (1986) convective adjustment and the 18 km domain parameterizes convection with the modified Kain-Fritsch scheme (Kain and Fritsch, 1993). No cumulus parameterization is used for the 6 km domain. Planetary boundary layer (PBL) processes are parameterized with the MRF PBL or Hong-Pan (1996) scheme, adequate also for high-resolution domains. This is an efficient scheme based on Troen-Mahrt (1986) representation of the countergradient term and K profile in the well mixed PBL. The atmospheric radiation is parameterized using the Rapid Radiative Transfer Model (RRTM longwave scheme; see Mlawer *et al*. 1997), which represents the effects of the detailed absorption spectrum taking into account water vapor, carbon dioxide and ozone. A 5-layers diffusive soil model with a fixed substrate below is used. Additionally, moisture availability varies with time, particularly in response to rainfall and evaporation rates. Regarding the initial and boundary datasets, the NCEP (National Centres for Environmental Prediction) or the ECMWF (European Centre for Medium-Range Weather Forecasting) global analysis, depending on each study case, are reanalyzed to the coarser domain every 12 hours, incorporating surface and sounding observations to recuperate structures smoothed out in the global datasets. The initial fields for the inner domains are interpolated from the coarser mesh. Upper boundary conditions are represented by the top vertical motion that is calculated to sponge up reflections of energy, and hence reducing spurious noise, especially over prominent orography.

There are many reasons behind the choice to use the MM5 numerical model as opposed to other models in the two experiments proposed in this thesis work. Firstly, it is free software that is relatively easy to install and configure. It can be set up over an area of study for specific spatial and temporal resolution, comparable to Meteosat-7 images space-time scales (6 km and 30 minutes). Secondly, the Meteorology Group of the Balearic Island’s University (UIB) has considerable experience studying severe weather events using the MM5 over Mediterranean regions with complex terrain (Romero *et al*. 2000, 2001; Homar *et al*. 2002, 2003) such as the two proposed flood cases.

## 4. Convective Rainfall Rate (CRR)

The CRR (Convective Rainfall Rate) algorithm was developed by the SAFNWC project to detect intense mesoscale convective systems and to screen the most probable precipitation associated. It estimates rainfall intensity using the three bands of the Meteosat-7 and matrices[3] calibrated with earth-based radars. Calibration matrices are performed following an accurate version of the Rainsat techniques but combining the infrared bands to detect convective clouds. Diurnal and nocturnal matrices are configured for the North of Europe, over the Baltics, with radar images of the Baltex Project provided by the SMHI (Swedish Meteorological and Hydrological Institute) and for the South of Europe, over the Iberian Peninsula, with radar provided by the INM (Spanish Meteorological Institute). In the present research, the CRR calibration methodology is described and validated, an analysis of calibration matrices differences in both areas over Europe is detailed and CRR resulting images are verified in a qualitative manner using rainfall radar images as so-called “ground true”.

### *4.1 CRR introduction and data used in the matrices calibration*

#### *a) Introduction to CRR*

Bi-spectral calibration tables were introduced by Lovejoy and Austin as early as 1979 and applied by Bellon *et al*. (1980). They were developed to improve the rain rate estimations from those derived from infrared only methods. These tables are based on the premise that the higher and thicker are the observed clouds, the higher is the probability of occurrence and intensity of precipitation. Information about cloud top height and about cloud thickness can be obtained, respectively, from the infrared brightness temperature and from visible radiances (Scofield, 1987; Vicente and Scofield, 1996). The role of visible data in improving rainfall estimates was also examined by King *et al*. (1995). Their results show a higher correlation when compared to validation data using visible-infrared methods as opposed to the infrared alone for the case of warm, orographically induced, rainfall. For cold, bright clouds the correlations are similar. Additionally, the brightness temperature difference between the 11 µm and 6.7 µm channels was used in the calibration process because it is a useful parameter to detect highly developed convective cloudy cells (Kurino, 1997a). Infrared water vapour

---

[3] The term matrix or matrices are references to the new spectral calibration tables developed in this work. These tables, called arrays in some cases, do not have to satisfy mathematical conditions of the matrices.

band was found to be important in convective processes since stratospheric water above deep convective clouds has been identified from Meteosat observations in the infrared window and water vapour bands (Schmetz, *et al*. 1997). It was demonstrated that the equivalent brightness temperature in the water vapour can exceed that in the infrared window by several degrees because of stratospheric water vapour above cloud top.

The calibration of the matrices requires a set of precipitation data derived from radar images used as so-called “ground true” to compute the relationship between satellite measurements and rainfall rate. The radar data is used only for system configuration and not as a part of the CRR rain estimations.

The spatial correlation between radar and satellite, done as the first step in the calibration of matrices, is of crucial importance to the present research and two processes are applied. First, as the European continent is distributed over mid and high latitudes, the parallax effect observed from a geostationary orbit satellite is significant. Here a correction for this feature is put into practice as described in section 3.4 of this report. Often an error of a few minutes between satellite and radar images scan can produce substantial inaccuracies in the spatial sampling of both fields. This error factor is attempted to be minimized by application of a second correction based on of a spatial fit on grid zones between satellite and radar images.

The CRR basic estimation for each pixel is obtained from calibration matrices. These are different depending on whether pixels correspond to a diurnal or nocturnal image. To distinguish clearly between them the pixel solar zenith angle was used in which it was considered daytime for the points where sun zenith angles are smaller than 80º and night for the rest.

CRR output images are evaluated in a qualitative manner by comparing them with radar images over Spain in September and October 2002 and over the Baltic Sea in June and July 2000. At the end of this chapter, the most outstanding differences between calibration matrices are detailed and discussed.

### *b) Data used in the matrices calibration*

The matrices for the Iberian Peninsula are calibrated using images derived from C-band radars. These are composite images of the Iberian Peninsula computed from the Spanish radar network belonging to the INM. They are focused on 40ºN and 3ºW, with 512 by 512 pixel size and 4 km spatial resolution. Radar images are generated operationally every 10 minutes and were selected for the present research corresponding to convective rainfall episodes between 1999 and 2000, preferably during spring, summer and part of autumn.

Matrices of the Baltic area are calibrated using images derived from the same kind of C-band radars than the Spanish ones. These are composite images from a radar network over the Baltic area covering Denmark, the south of Norway, Sweden and part of the Baltic Sea. They are generated every 15 minutes for operational purposes under the Baltex project objectives and provided by the SMHI (Swedish Meteorological and Hydrological Institute). The radar images are centred on 57.3ºN and 18.4ºE, 550 by 900 pixels size and 2 km spatial resolution. They were pre-selected for this work during rainy days in June and July of 2000, as shown in table 4.1.

In both places, composite CAPPI (Constant Altitude Plan Position Indicator) images at 2.5 km altitudes, registered in decibel units (*dBZ)* and derived from reflectivity measurements[4] $Z$ (in mm$^6$ m$^{-3}$), are transformed into rain rates in mm h$^{-1}$ using the Marshall-Palmer Z-R relation ($Z$ = a $R^b$). The two coefficients of this relation (a and b) depend, in general, on the climatic area where the radar are employed. As an initial approximation and using a long set of data to perform the calibration of tables for general rain type over mid and high latitudes, it has been decided to use the ones proposed by Marshall and Palmer (1948), a = 200, b = 1.6. The following chapters demonstrate that these coefficients should be adjusted for short time or local studies. Echo-top images, used to measure cloud top heights in km were available for the Iberian Peninsula. They have the same geographical settings as the radar images described in the beginning of this subsection and they are used in this work to select the radar pixels with high cloud tops as commented in the following methodology section.

The Meteosat-7 data used in this work is: infrared band brightness temperature in Kelvin $T_{IR}$(K), infrared water vapour band in Kelvin $T_{WV}$(K) and the visible channel in brightness counts. Normalized visible counts (*Vc*) are obtained for all diurnal pixels by dividing each count with respect the cosine of the corresponding solar zenith angle (Binder, 1988).

---

[4] In this thesis work it is used the common magnitudes and units used in the radar meteorology field.

Table 4.1 Radar-satellite datasets used to develop the calibration matrices over the Baltic Sea. Days in June and July 2000 for the 2-D matrix and days only in July 2000 for the 3-D one.

| 2-D | |
|---|---|
| | 3-D |
| Days (Jun 2000) | Days (Jul 2000) |
| 5 | 1-5 |
| 7-8 | 7-13 |
| 10-11 | 15 |
| 16 | 17-19 |
| 19-28 | 22-25 |
| Nº of days: 15 | 20 |
| Total Nº of days: | 35 |

### 4.2 CRR calibration methodology

a) *Rainfall matrices calibration*

Before calibration it is important to explain that an echo-top image is employed over the Iberian Peninsula domain to locate radar pixels with and without rainfall linked to high clouds tops and, therefore, suspicious of being convective points. A radar point, shown as $R_{INT}$ in figure 4.1, associated with a parallel echo-top value greater than six kilometres above sea level ($H_{E\text{-}T} > 6$ km) is a presumable convective radar point ($R_{CINT}$). This simple criterion has been used by the INM with good results before new and accurate methods were developed. Qualitative observations not shown in this chapter confirm the efficiency of the method by comparing these convective radar echoes with electrical discharge images from the INM detector network at the same area and time. Over the Baltic area this correlation between convection and high altitude radar echoes was not observed and no convective threshold was applied for radar images.

The fundamental calibration algorithm consists basically of obtaining two frequency distributions by correlating spatially simultaneous radar and satellite images in order to discriminate between raining and non-raining clouds (Bellon *et al*. 1980). The next section *b)* describes in detail the spatial and temporal correlation method. One time radar pixels in rain rate units ($R_{CINT}$) are associated with their correspondent satellite measurements ($T_{IR}$, $T_{WV}$ and $Vc$), the next step is the development of three arrays as shown in figure 4.1. Two of them are frequency distributions (rain and no rain) and the third is an accumulation of rain rates (accumulated rain). Figure 4.1 shows each array with three axes in the function of satellite measurements ($Vc$, $T_{IR}$-$T_{WV}$ and $T_{IR}$) which will define the spectral domain of precipitation. The row axis ($T_{IR}$-$T_{WV}$) is the difference between $T_{IR}$ and $T_{WV}$ temperatures, shown as $\Delta T_{IR}$ in the following. The rain matrix counts radar-satellite points with a rainfall rate greater than 0 mm h$^{-1}$ ($R_{CINT} > 0$ mm h$^{-1}$). In the no rain matrix is the same but numbers points with no rainfall ($R_{CINT} = 0$ mm h$^{-1}$). The accumulated rain matrix is the same as the rain one but here each radar rain rate value in mm h$^{-1}$ is added. In such a way, elements of rain and no rain frequency arrays are $F_R(Vc,\Delta T_{IR},T_{IR})$ and $F_{NR}(Vc,\Delta T_{IR},T_{IR})$ respectively. Elements of the accumulated rain matrix are $SR_{CINT}(Vc, \Delta T_{IR},T_{IR})$. So the rainfall probability matrix ($P_R$) is calculated from the rain and no rain array elements expressed by the relation:

$$P_R(Vc,\Delta V_{IR},T_{IR}) = \frac{F_R(Vc,\Delta V_{IR},T_{IR})}{F_R(Vc,\Delta V_{IR},T_{IR}) + F_{NR}(Vc,\Delta V_{IR},T_{IR})} \tag{4.1}$$

where $F_R(Vc, \Delta T_{IR}, T_{IR}) + F_{NR}(Vc, \Delta T_{IR}, T_{IR})$ is the total number of rain and no-rain pixels associated with the satellite data.

The mean rainfall array is computed using the following criterion: array elements with a rainfall probability lower than a defined probability variable known as *EQ_PC* and described section *c)* , are set to zero ($\overline{R}_{CINT} = 0$). If they have a rainfall probability greater than the *EQ_PC* parameter, the mean rainfall intensity for each element is computed as shown below.

$$\overline{R}_{CIINT}(Vc,\Delta V_{IR},T_{IR}) = \frac{SR_{CINT}(Vc,\Delta V_{IR},T_{IR})}{F_R(Vc,\Delta V_{IR},T_{IR})} \tag{4.2}$$

In the nocturnal array or 2-D matrix, the process is similar but, obviously, without regard to visible channel counts. The results are arrays performed by using only the two Meteosat infrared bands, in which columns are ordered depending on $T_{IR}$ and rows on $\Delta T_{IR}$ as illustrated in Tables 4.3 and 4.4.

### *b) Temporal and Spatial correlation*

The time resolution in the calibration process is clearly defined by the dataset with the poorer time resolution, as occurred in this case by the Meteosat-7 with 30 minutes between satellite images. Therefore, the spatial correlation between radar and satellite datasets is completed each 30 minutes as indicated in figure 4.1 ($t$-$t_1$ = 30 min).

The calibration is thought to keep the quality and resolution of radar data throughout the whole process, it was decided to remap satellite images to radar projection, resolution and size. Remapped satellite coordinates are corrected spatially (Lat*, Lon*) with respect to radar pixels (Lat, Lon) after two steps: The first is the parallax correction, described in section 3.4 and applied here due to the effects on the angle of vision from a geostationary satellite produced by the high latitudes of the European regions. The second step tries to minimize errors in the spatial sampling between radar and satellite fields caused by slight differences in the time of the images. Another important reason to apply a spatial cross-correlation sampling is that areas of maximum radar rain rates would be fitted with areas of minimum infrared satellite temperatures. To do that, radar rain rates are compared with a satellite derived rainfall image. Over the Iberian Peninsula for daytime this previous satellite rainfall image was estimated using a bi-spectral IR/VIS matrix generated by the INM for operational purposes. In night time, due to the lack of data in the visible band, the rainfall image was estimated applying the A-E technique. Over the Baltic area an IR/VIS array is not known, the preceding rainfall image is also computed via A-E technique. The maximum spatial correlation is obtained by carrying out slight spatial displacements of the satellite rainfall image in 15x15 pixels grids around the significant radar pixels. Translations that provide the best correlation coefficients are then selected to modify each satellite pixel position (INM, 2000) and to continue with the matrices assembly as described in the beginning of this section.

### *c) Validation of the method*

The matrices calibration technique described in this work can be evaluated using statistical indices such as: *EQ_PC* (Probability of equal satellite-radar rain area), *POD* (Probability of Detection), *FAR* (False Alarm Ratio) and *CSI* (Critical Success Index). They are calculated using data stored in matrices.

The *EQ_PC* index is the probability level that matches the total number of radar rain points with satellite rain points. This factor establishes a so-called “stability criterion” and it is computed as proposed by Lovejoy and Austin (1979) and later applied also by Cheng *et al.* (1993). Here, it is important to identify radar rain points as those stored only in the rain matrix. Additionally, the total number of radar rain points is the sum of all the rain matrix elements and is called NºR (see equation 4.3 and the 2-D rain matrix in table 4.3a). Satellite rain points are identified as those stored in the rain and in the no rain matrices. This is based on the assumption that all the satellite points are suspicious of being rainy. But observations show that only a small number of them coincide with significant radar echoes and, fortunately, satellite rain points can be ordered depending on the probability of rain given by the probability matrix (equation 4.1). The assumption of satellite rain points is clear, obviously, for those places in matrices where the probability of rain is higher and thus, where the numbering of rain points should be started. For every probability value (*P*) the total number of satellite rain points (*TSAT*) is accumulated from higher to lower probability as shown in the expression (4.4).

$$N^oR = \Sigma F_R(Vc,\Delta V_{IR},T_{IR}) \qquad (4.3)$$

$$TSAT(P) = \sum_{100\%}^{P}\left[\Sigma F_R^{\,P}(Vc,\Delta V_{IR},T_{IR}) + \Sigma F_{NR}^{\,P}(Vc,\Delta V_{IR},T_{IR})\right] \qquad (4.4)$$

where $\Sigma = \sum_{Vc=148}^{240}\ \sum_{\Delta T_{IR}=-11^\circ}^{25^\circ}\ \sum_{T_{IR}=-66^\circ}^{2^\circ}$ is the sum of all the matrices elements.

*TSAT(P)* is compared to *NºR* from the highest probability (*P* = 100%), where *NºR* should be bigger than *TSAT(P),* to the lowest (*P* = 0 %), where *NºR* is smaller than *TSAT(P)*. The probability level is reached for the probability in which *TSAT(P)* is closer to *NºR* and, therefore, *EQ_PC* = *P*. At this moment of the process the total number of satellite rain points in matrices should be the same than the total number of radar rain points. Now the “stability criterion” is satisfied and the delineated rain area from satellite should be equal to that of the radar. However, a significant amount of data employed in the calibration process does not guarantee the stability in the number satellite rain points in a single CRR image.

To calculate *POD*, *FAR* and *CSI* a contingency table (Marzban, 1998) is performed for each matrix as follows:

$$C\text{-}table = \begin{pmatrix} A & B \\ C & D \end{pmatrix} = \begin{pmatrix} N^o\ of\ hits & N^o\ of\ misses \\ N^o\ of\ alse\ alarms & N^o\ of\ correct\ \ negative \end{pmatrix}$$

*A*, is the number of hits or number of radar rain points correctly detected by CRR. Taking into account the matrices, *A* is the number of rain points from the rain matrix with probability greater than the *EQ_PC*. *B*, is the number of misses or number of radar rain points not detected by CRR. In other words, it is the number of rain points from the rain array with probability smaller than the *EQ_PC*. *C* is the number of false alarms or number of radar no rain points estimated as rainy by CRR. Using the matrices, it is the number of no rain points from the no rain array with probability greater than the *EQ_PC* variable. *D* is the number of correct negative or total number of radar no rain points correctly estimated by the CRR as no rainy. *POD*, *FAR* and *CSI* are easily calculated as shown below:

$$POD = \frac{hits}{hits + misses} = \frac{A}{A+B} \tag{4.5}$$

$$FAR = \frac{false\ alarms}{hits + false\ alarms} = \frac{C}{A+C} \tag{4.6}$$

$$CSI = \frac{hits}{hits + misses + false\ alarms} = \frac{A}{A+B+C} \tag{4.7}$$

The Pearson correlation coefficients can be calculated for each matrix by using the calibration data after matrices are configured. They are performed for every set of radar (*R*) and CRR estimated from a (*S*) set of satellite images in mm h$^{-1}$ following equation 4.8 where 'n' is the total number of R and S pair of points considered in the calibration:

$$CORR = \frac{n \cdot \left(\sum R \cdot S\right) - \left(\sum R\right)\left(\sum S\right)}{\sqrt{\left(n \cdot \sum R^2 - \left(\sum R\right)^2\right) \cdot \left(n \cdot \sum S^2 - \left(\sum S\right)^2\right)}} \tag{4.8}$$

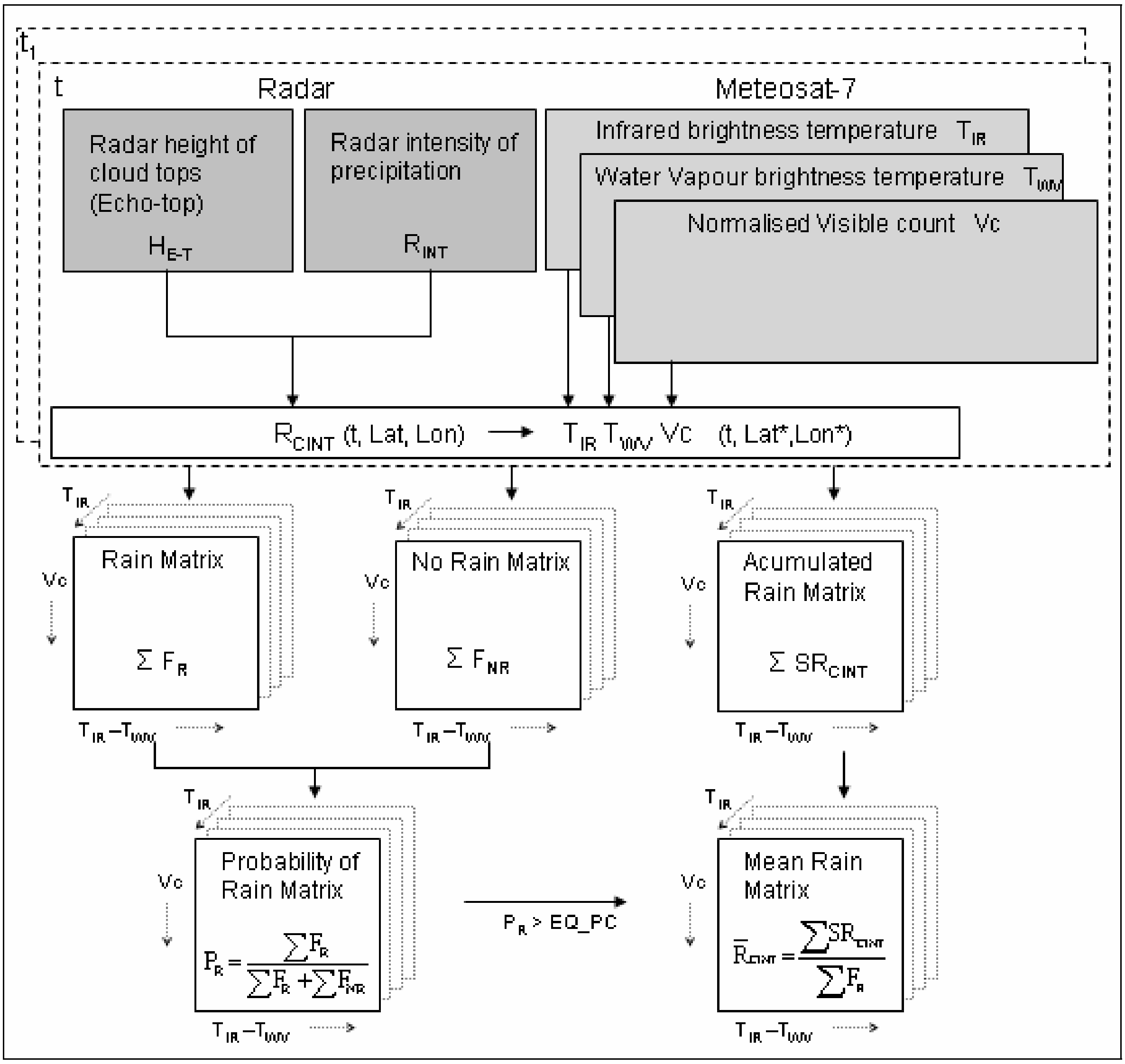

Figure 4.1. 3-D matrices generation scheme. As illustrated, firstly radar rain rates ($R_{CINT}$) are associated in time and space with the satellite measurements from the three bands ($T_{IR}$, $T_{WV}$, Vc). Rain, No Rain and Accumulated Rain Matrices are configured in second place. Finally a probability and Mean Rain Matrices with the help of the EQ_PC index are computed. Dotted boxes on the top of the figure denote that radar-satellite datasets are correlated each thirty minutes ($t-t_1= 30$ min.). Satellite point coordinates with an asterisk (Lat*, Lon*) indicate that the parallax correction and a spatial cross-correlation method is carried out around radar point coordinates (Lat, Lon).

### *4.3 CRR results*

*a) Rainfall matrices*

Two (2-D) and three dimensional (3-D) calibration matrices are developed for the Iberian Peninsula and for the Baltic Sea. The 2-D arrays are configured with data from the infrared bands as afore mentioned, thus, they are planned to be used only during night time and the 3-D matrices, with infrared and visible measurements, for daytime. Those points with sun zenith angles smaller than 80º are considered as daytime points. The 2-D arrays have two axes that correspond respectively to: $T_{IR}$ as column axis, from -66ºC to 2º C each 2 degrees and $T_{IR}$ - $T_{WV}$ as row axis, from -11ºC to 25ºC each 2 degrees (see tables 4.3d and 4.4). The 3-D arrays include a third axis, composed by Vc from 148 to 240, each 4 counts as shown in tables 4.5 and 4.6. In these the 3-D matrices are partially represented and for every $T_{IR}$ value, the Vc range is viewed along the column axis. Empty cells in matrices are spectral places with no data retrieved from radar and satellite.

Matrice elements are rain classes derived from rain rates in mm $h^{-1}$ according to table 4.2. Multiplying every rainfall class by 24, they are scaled to an 8-bit count range (0 – 255) used in the final CRR coloured images as shown in figures 4.3 and 4.5. The CRR images were generated from a simple class association extracted from matrices and satellite parameters.

Table 4.2. Relationship between rainfall intensities in mm $h^{-1}$, matrices classes and CRR 8-bit counts.

| Rainfall intensity (mm $h^{-1}$) | Rainfall matrices Classes | CRR 8-bit count (Classes x 24) |
|---|---|---|
| No data | | |
| 0 | 0 | 0 |
| 0. – 1 | 1 | 24 |
| 1. – 2 | 2 | 48 |
| 2. – 3 | 3 | 72 |
| 3. – 5 | 4 | 96 |
| 5. – 7 | 5 | 120 |
| 7. – 10 | 6 | 144 |
| 10. – 15 | 7 | 168 |
| 15. – 20 | 8 | 192 |
| 20. – 50 | 9 | 216 |
| >50 | 10 | 240 |

Table 4.3 illustrates the resulting 2D rain (a), no rain (b), probability (c) and mean rainfall (d) arrays performed over the Iberian Peninsula. The rain and no rain tables show the number of rain (*NºR*) and no rain (*NºNR*) points and thus, reveal the size of the samples used to develop the algorithm. The probability table highlights, in grey, colour cells with a probability higher than the *EQ_PC* parameter and therefore, CRR rainy points. As commented in the methodology section, mean rain classes are calculated in table 4.3(d) only for those rainy places indicated by the probability table. In this last table, significant mean rain classes are shaded in grey to facilitate visualization.

Table 4.3. 2-D matrices computed over the Iberian Peninsula. (a) Rain array with a total number of rain points around 19700. (b) No rain array with a total of 48587 no rain points. (b) Probability table, magnitudes greater than EQ_PC = 44% as in the rest of tables are shaded in grey to facilitate the identification of the highest values. (d) Mean Rain array in which elements are classes which are transformed into rainfall intensity or a CRR 8-bit count according to table 4.2. Statistical indices of the calibration process in percentages are shown in table 3(d). As described in the first paragraph of the result section, columns are $T_{IR}$ values from -66ºC to 2º C each two degrees and rows $\Delta T_{IR}$ from -11ºC to 25ºC each two degrees also.

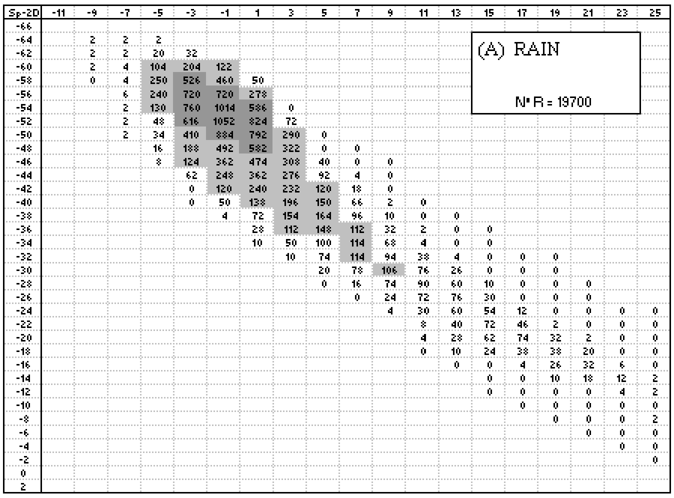

(A) RAIN

Nº R = 19700

| Sp-2D | -11 | -9 | -7 | -5 | -3 | -1 | 1 | 3 | 5 | 7 | 9 | 11 | 13 | 15 | 17 | 19 | 21 | 23 | 25 |
|---|---|---|---|---|---|---|---|---|---|---|---|---|---|---|---|---|---|---|---|
| -66 | | | | | | | | | | | | | | | | | | | |
| -64 | | 2 | 2 | 2 | | | | | | | | | | | | | | | |
| -62 | | 2 | 2 | 20 | 32 | | | | | | | | | | | | | | |
| -60 | | 2 | 4 | 104 | 204 | 122 | | | | | | | | | | | | | |
| -58 | | 0 | 4 | 250 | 526 | 460 | 50 | | | | | | | | | | | | |
| -56 | | | 6 | 240 | 720 | 720 | 278 | | | | | | | | | | | | |
| -54 | | | 2 | 130 | 760 | 1014 | 586 | 0 | | | | | | | | | | | |
| -52 | | | 2 | 48 | 616 | 1052 | 824 | 72 | | | | | | | | | | | |
| -50 | | | 2 | 34 | 410 | 884 | 792 | 290 | 0 | | | | | | | | | | |
| -48 | | | | 16 | 188 | 492 | 582 | 322 | 0 | 0 | | | | | | | | | |
| -46 | | | | 8 | 124 | 362 | 474 | 308 | 40 | 0 | 0 | | | | | | | | |
| -44 | | | | | 62 | 248 | 362 | 276 | 92 | 4 | 0 | | | | | | | | |
| -42 | | | | | 0 | 120 | 240 | 232 | 120 | 18 | 0 | | | | | | | | |
| -40 | | | | | 0 | 50 | 138 | 196 | 150 | 66 | 2 | 0 | | | | | | | |
| -38 | | | | | | 4 | 72 | 154 | 164 | 96 | 10 | 0 | 0 | | | | | | |
| -36 | | | | | | | 28 | 112 | 148 | 112 | 32 | 2 | 0 | 0 | | | | | |
| -34 | | | | | | | 10 | 50 | 100 | 114 | 68 | 4 | 0 | 0 | | | | | |
| -32 | | | | | | | | 10 | 74 | 114 | 94 | 38 | 4 | 0 | 0 | 0 | | | |
| -30 | | | | | | | | | 20 | 78 | 106 | 76 | 26 | 0 | 0 | 0 | | | |
| -28 | | | | | | | | | 0 | 16 | 74 | 90 | 60 | 10 | 0 | 0 | 0 | | |
| -26 | | | | | | | | | | 0 | 24 | 72 | 76 | 30 | 0 | 0 | 0 | | |
| -24 | | | | | | | | | | | 4 | 30 | 60 | 54 | 12 | 0 | 0 | 0 | 0 |
| -22 | | | | | | | | | | | | 8 | 40 | 72 | 46 | 2 | 0 | 0 | 0 |
| -20 | | | | | | | | | | | | 4 | 28 | 62 | 74 | 32 | 2 | 0 | 0 |
| -18 | | | | | | | | | | | | 0 | 10 | 24 | 38 | 38 | 20 | 0 | 0 |
| -16 | | | | | | | | | | | | | 0 | 0 | 4 | 26 | 32 | 6 | 0 |
| -14 | | | | | | | | | | | | | | 0 | 0 | 10 | 18 | 12 | 2 |
| -12 | | | | | | | | | | | | | | 0 | 0 | 0 | 0 | 4 | 2 |
| -10 | | | | | | | | | | | | | | | 0 | 0 | 0 | 0 | 0 |
| -8 | | | | | | | | | | | | | | | | 0 | 0 | 0 | 2 |
| -6 | | | | | | | | | | | | | | | | | 0 | 0 | 0 |
| -4 | | | | | | | | | | | | | | | | | | 0 | 0 |
| -2 | | | | | | | | | | | | | | | | | | | 0 |
| 0 | | | | | | | | | | | | | | | | | | | |
| 2 | | | | | | | | | | | | | | | | | | | |

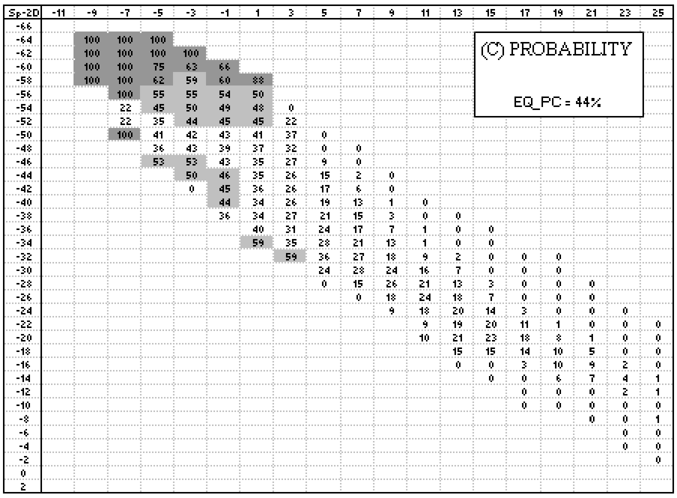

(C) PROBABILITY

EQ_PC = 44%

| Sp-2D | -11 | -9 | -7 | -5 | -3 | -1 | 1 | 3 | 5 | 7 | 9 | 11 | 13 | 15 | 17 | 19 | 21 | 23 | 25 |
|---|---|---|---|---|---|---|---|---|---|---|---|---|---|---|---|---|---|---|---|
| -66 | | | | | | | | | | | | | | | | | | | |
| -64 | | 100 | 100 | 100 | | | | | | | | | | | | | | | |
| -62 | | 100 | 100 | 100 | 100 | | | | | | | | | | | | | | |
| -60 | | 100 | 100 | 75 | 63 | 66 | | | | | | | | | | | | | |
| -58 | | 100 | 100 | 62 | 59 | 60 | 88 | | | | | | | | | | | | |
| -56 | | | 100 | 55 | 55 | 54 | 50 | | | | | | | | | | | | |
| -54 | | | 22 | 45 | 50 | 49 | 48 | 0 | | | | | | | | | | | |
| -52 | | | 22 | 35 | 44 | 45 | 45 | 22 | | | | | | | | | | | |
| -50 | | | 100 | 41 | 42 | 43 | 41 | 37 | 0 | | | | | | | | | | |
| -48 | | | | 36 | 43 | 39 | 37 | 32 | 0 | 0 | | | | | | | | | |
| -46 | | | | 53 | 53 | 43 | 35 | 27 | 9 | 0 | | | | | | | | | |
| -44 | | | | | 50 | 46 | 35 | 26 | 15 | 2 | 0 | | | | | | | | |
| -42 | | | | | 0 | 45 | 36 | 26 | 17 | 6 | 0 | | | | | | | | |
| -40 | | | | | | 44 | 34 | 26 | 19 | 13 | 1 | 0 | | | | | | | |
| -38 | | | | | | 36 | 34 | 27 | 21 | 15 | 3 | 0 | 0 | | | | | | |
| -36 | | | | | | | 40 | 31 | 24 | 17 | 7 | 1 | 0 | 0 | | | | | |
| -34 | | | | | | | 59 | 35 | 28 | 21 | 13 | 1 | 0 | 0 | | | | | |
| -32 | | | | | | | | 59 | 36 | 27 | 18 | 9 | 2 | 0 | 0 | 0 | | | |
| -30 | | | | | | | | | 24 | 28 | 24 | 16 | 7 | 0 | 0 | 0 | | | |
| -28 | | | | | | | | | 0 | 15 | 26 | 21 | 13 | 3 | 0 | 0 | 0 | | |
| -26 | | | | | | | | | | 0 | 18 | 24 | 18 | 7 | 0 | 0 | 0 | | |
| -24 | | | | | | | | | | | 9 | 18 | 20 | 14 | 3 | 0 | 0 | 0 | |
| -22 | | | | | | | | | | | | 9 | 19 | 20 | 11 | 1 | 0 | 0 | 0 |
| -20 | | | | | | | | | | | | 10 | 21 | 23 | 18 | 8 | 1 | 0 | 0 |
| -18 | | | | | | | | | | | | | 15 | 15 | 14 | 10 | 5 | 0 | 0 |
| -16 | | | | | | | | | | | | | 0 | 0 | 3 | 10 | 9 | 2 | 0 |
| -14 | | | | | | | | | | | | | | 0 | 0 | 6 | 7 | 4 | 1 |
| -12 | | | | | | | | | | | | | | | 0 | 0 | 0 | 2 | 1 |
| -10 | | | | | | | | | | | | | | | 0 | 0 | 0 | 0 | 0 |
| -8 | | | | | | | | | | | | | | | | | 0 | 0 | 1 |
| -6 | | | | | | | | | | | | | | | | | | 0 | 0 |
| -4 | | | | | | | | | | | | | | | | | | 0 | 0 |
| -2 | | | | | | | | | | | | | | | | | | | 0 |
| 0 | | | | | | | | | | | | | | | | | | | |
| 2 | | | | | | | | | | | | | | | | | | | |

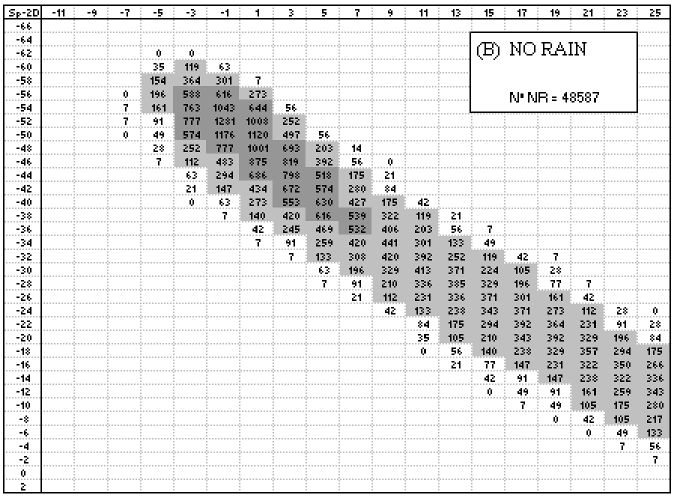

(B) NO RAIN

Nº NR = 48587

| Sp-2D | -11 | -9 | -7 | -5 | -3 | -1 | 1 | 3 | 5 | 7 | 9 | 11 | 13 | 15 | 17 | 19 | 21 | 23 | 25 |
|---|---|---|---|---|---|---|---|---|---|---|---|---|---|---|---|---|---|---|---|
| -66 | | | | | | | | | | | | | | | | | | | |
| -64 | | | | | | | | | | | | | | | | | | | |
| -62 | | | | 0 | 0 | | | | | | | | | | | | | | |
| -60 | | | | 35 | 119 | 63 | | | | | | | | | | | | | |
| -58 | | | | 154 | 364 | 301 | 7 | | | | | | | | | | | | |
| -56 | | | 0 | 196 | 588 | 616 | 273 | | | | | | | | | | | | |
| -54 | | | 7 | 161 | 763 | 1043 | 644 | 56 | | | | | | | | | | | |
| -52 | | | 7 | 91 | 777 | 1281 | 1008 | 252 | | | | | | | | | | | |
| -50 | | | 0 | 49 | 574 | 1176 | 1120 | 497 | 56 | | | | | | | | | | |
| -48 | | | | 28 | 252 | 777 | 1001 | 693 | 203 | 14 | | | | | | | | | |
| -46 | | | | 7 | 112 | 483 | 875 | 819 | 392 | 56 | 0 | | | | | | | | |
| -44 | | | | | 63 | 294 | 686 | 798 | 518 | 175 | 21 | | | | | | | | |
| -42 | | | | | 21 | 147 | 434 | 672 | 574 | 280 | 84 | | | | | | | | |
| -40 | | | | | 0 | 63 | 273 | 553 | 630 | 427 | 175 | 42 | | | | | | | |
| -38 | | | | | | 7 | 140 | 420 | 616 | 539 | 322 | 119 | 21 | | | | | | |
| -36 | | | | | | | 42 | 245 | 469 | 532 | 406 | 203 | 56 | 7 | | | | | |
| -34 | | | | | | | 7 | 91 | 259 | 420 | 441 | 301 | 133 | 49 | | | | | |
| -32 | | | | | | | | 7 | 133 | 308 | 420 | 392 | 252 | 119 | 42 | 7 | | | |
| -30 | | | | | | | | | 63 | 196 | 329 | 413 | 371 | 224 | 105 | 28 | | | |
| -28 | | | | | | | | | 7 | 91 | 210 | 336 | 385 | 329 | 196 | 77 | 7 | | |
| -26 | | | | | | | | | | 21 | 112 | 231 | 336 | 371 | 301 | 161 | 42 | | |
| -24 | | | | | | | | | | | 42 | 133 | 238 | 343 | 371 | 273 | 112 | 28 | 0 |
| -22 | | | | | | | | | | | | 84 | 175 | 294 | 392 | 364 | 231 | 91 | 28 |
| -20 | | | | | | | | | | | | 35 | 105 | 210 | 343 | 392 | 329 | 196 | 84 |
| -18 | | | | | | | | | | | | 0 | 56 | 140 | 238 | 329 | 357 | 294 | 175 |
| -16 | | | | | | | | | | | | | 21 | 77 | 147 | 231 | 322 | 350 | 266 |
| -14 | | | | | | | | | | | | | | 42 | 91 | 147 | 238 | 322 | 336 |
| -12 | | | | | | | | | | | | | | 0 | 49 | 91 | 161 | 259 | 343 |
| -10 | | | | | | | | | | | | | | | 7 | 49 | 105 | 175 | 280 |
| -8 | | | | | | | | | | | | | | | | 0 | 42 | 105 | 217 |
| -6 | | | | | | | | | | | | | | | | | 0 | 49 | 133 |
| -4 | | | | | | | | | | | | | | | | | | 7 | 56 |
| -2 | | | | | | | | | | | | | | | | | | | 7 |
| 0 | | | | | | | | | | | | | | | | | | | |
| 2 | | | | | | | | | | | | | | | | | | | |

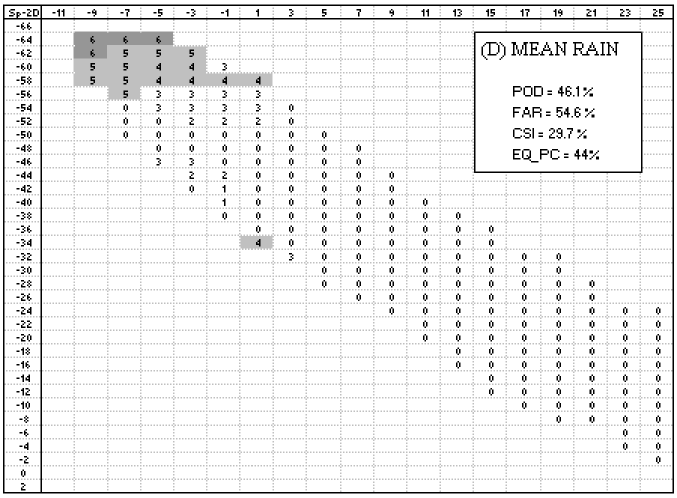

(D) MEAN RAIN

POD = 46.1 %
FAR = 54.6 %
CSI = 29.7 %
EQ_PC = 44%

| Sp-2D | -11 | -9 | -7 | -5 | -3 | -1 | 1 | 3 | 5 | 7 | 9 | 11 | 13 | 15 | 17 | 19 | 21 | 23 | 25 |
|---|---|---|---|---|---|---|---|---|---|---|---|---|---|---|---|---|---|---|---|
| -66 | | | | | | | | | | | | | | | | | | | |
| -64 | | 6 | 6 | 6 | | | | | | | | | | | | | | | |
| -62 | | 6 | 5 | 5 | 5 | | | | | | | | | | | | | | |
| -60 | | 5 | 5 | 4 | 4 | 3 | | | | | | | | | | | | | |
| -58 | | 5 | 5 | 4 | 4 | 4 | 4 | | | | | | | | | | | | |
| -56 | | | 5 | 3 | 3 | 3 | 3 | | | | | | | | | | | | |
| -54 | | | 0 | 3 | 3 | 3 | 3 | 0 | | | | | | | | | | | |
| -52 | | | 0 | 0 | 2 | 2 | 2 | 0 | | | | | | | | | | | |
| -50 | | | 0 | 0 | 0 | 0 | 0 | 0 | 0 | | | | | | | | | | |
| -48 | | | | 0 | 0 | 0 | 0 | 0 | 0 | 0 | | | | | | | | | |
| -46 | | | | 3 | 3 | 0 | 0 | 0 | 0 | 0 | | | | | | | | | |
| -44 | | | | | 2 | 2 | 0 | 0 | 0 | 0 | 0 | | | | | | | | |
| -42 | | | | | 0 | 1 | 0 | 0 | 0 | 0 | 0 | | | | | | | | |
| -40 | | | | | | 1 | 0 | 0 | 0 | 0 | 0 | 0 | | | | | | | |
| -38 | | | | | | 0 | 0 | 0 | 0 | 0 | 0 | 0 | 0 | | | | | | |
| -36 | | | | | | | 0 | 0 | 0 | 0 | 0 | 0 | 0 | 0 | | | | | |
| -34 | | | | | | | 4 | 0 | 0 | 0 | 0 | 0 | 0 | 0 | | | | | |
| -32 | | | | | | | | 3 | 0 | 0 | 0 | 0 | 0 | 0 | 0 | 0 | | | |
| -30 | | | | | | | | | 0 | 0 | 0 | 0 | 0 | 0 | 0 | 0 | | | |
| -28 | | | | | | | | | 0 | 0 | 0 | 0 | 0 | 0 | 0 | 0 | 0 | | |
| -26 | | | | | | | | | | 0 | 0 | 0 | 0 | 0 | 0 | 0 | 0 | | |
| -24 | | | | | | | | | | | 0 | 0 | 0 | 0 | 0 | 0 | 0 | 0 | 0 |
| -22 | | | | | | | | | | | | 0 | 0 | 0 | 0 | 0 | 0 | 0 | 0 |
| -20 | | | | | | | | | | | | 0 | 0 | 0 | 0 | 0 | 0 | 0 | 0 |
| -18 | | | | | | | | | | | | | 0 | 0 | 0 | 0 | 0 | 0 | 0 |
| -16 | | | | | | | | | | | | | 0 | 0 | 0 | 0 | 0 | 0 | 0 |
| -14 | | | | | | | | | | | | | | 0 | 0 | 0 | 0 | 0 | 0 |
| -12 | | | | | | | | | | | | | | 0 | 0 | 0 | 0 | 0 | 0 |
| -10 | | | | | | | | | | | | | | | 0 | 0 | 0 | 0 | 0 |
| -8 | | | | | | | | | | | | | | | | 0 | 0 | 0 | 0 |
| -6 | | | | | | | | | | | | | | | | | | 0 | 0 |
| -4 | | | | | | | | | | | | | | | | | | 0 | 0 |
| -2 | | | | | | | | | | | | | | | | | | | 0 |
| 0 | | | | | | | | | | | | | | | | | | | |
| 2 | | | | | | | | | | | | | | | | | | | |

Table 4.4. Baltic 2-D mean rain matrix, which has the same structure as table 4.3 (d) but performed by correlating satellite images with radar from the Baltic radars network. Here the EQ_PC parameter is lower than the one obtained for the Iberian Peninsula in the previous table and rain class distribution is smoother than other one.

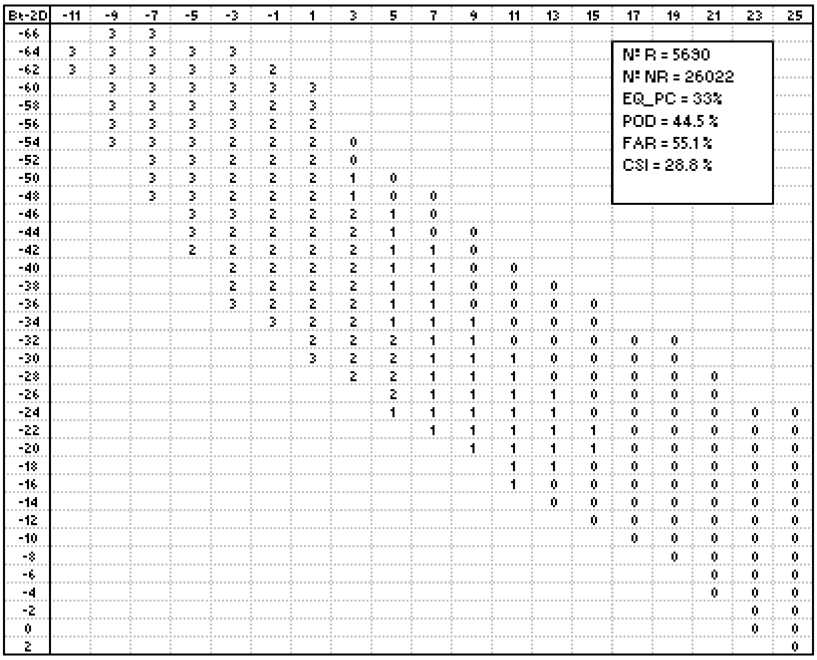

| Bt-2D | -11 | -9 | -7 | -5 | -3 | -1 | 1 | 3 | 5 | 7 | 9 | 11 | 13 | 15 | 17 | 19 | 21 | 23 | 25 |
|---|---|---|---|---|---|---|---|---|---|---|---|---|---|---|---|---|---|---|---|
| -66 |  | 3 | 3 |  |  |  |  |  |  |  |  |  |  |  |  |  |  |  |  |
| -64 | 3 | 3 | 3 | 3 | 3 |  |  |  |  |  |  |  |  |  |  |  |  |  |  |
| -62 | 3 | 3 | 3 | 3 | 3 | 2 |  |  |  |  |  |  |  |  |  |  |  |  |  |
| -60 |  | 3 | 3 | 3 | 3 | 3 | 3 |  |  |  |  |  |  |  |  |  |  |  |  |
| -58 |  | 3 | 3 | 3 | 3 | 2 | 3 |  |  |  |  |  |  |  |  |  |  |  |  |
| -56 |  | 3 | 3 | 3 | 3 | 2 | 2 |  |  |  |  |  |  |  |  |  |  |  |  |
| -54 |  | 3 | 3 | 3 | 2 | 2 | 2 | 0 |  |  |  |  |  |  |  |  |  |  |  |
| -52 |  |  | 3 | 3 | 2 | 2 | 2 | 0 |  |  |  |  |  |  |  |  |  |  |  |
| -50 |  |  | 3 | 3 | 2 | 2 | 2 | 1 | 0 |  |  |  |  |  |  |  |  |  |  |
| -48 |  |  | 3 | 3 | 2 | 2 | 2 | 1 | 0 | 0 |  |  |  |  |  |  |  |  |  |
| -46 |  |  |  | 3 | 3 | 2 | 2 | 2 | 1 | 0 |  |  |  |  |  |  |  |  |  |
| -44 |  |  |  | 3 | 2 | 2 | 2 | 2 | 1 | 0 | 0 |  |  |  |  |  |  |  |  |
| -42 |  |  |  | 2 | 2 | 2 | 2 | 2 | 1 | 1 | 0 |  |  |  |  |  |  |  |  |
| -40 |  |  |  |  | 2 | 2 | 2 | 2 | 1 | 1 | 0 | 0 |  |  |  |  |  |  |  |
| -38 |  |  |  |  | 2 | 2 | 2 | 2 | 1 | 1 | 0 | 0 | 0 |  |  |  |  |  |  |
| -36 |  |  |  |  | 3 | 2 | 2 | 2 | 1 | 1 | 0 | 0 | 0 | 0 |  |  |  |  |  |
| -34 |  |  |  |  |  | 3 | 2 | 2 | 1 | 1 | 1 | 0 | 0 | 0 |  |  |  |  |  |
| -32 |  |  |  |  |  |  | 2 | 2 | 2 | 1 | 1 | 0 | 0 | 0 | 0 | 0 |  |  |  |
| -30 |  |  |  |  |  |  | 3 | 2 | 2 | 1 | 1 | 1 | 0 | 0 | 0 | 0 |  |  |  |
| -28 |  |  |  |  |  |  |  | 2 | 2 | 1 | 1 | 1 | 0 | 0 | 0 | 0 | 0 |  |  |
| -26 |  |  |  |  |  |  |  |  | 2 | 1 | 1 | 1 | 1 | 0 | 0 | 0 | 0 |  |  |
| -24 |  |  |  |  |  |  |  |  | 1 | 1 | 1 | 1 | 1 | 0 | 0 | 0 | 0 | 0 | 0 |
| -22 |  |  |  |  |  |  |  |  |  | 1 | 1 | 1 | 1 | 1 | 0 | 0 | 0 | 0 | 0 |
| -20 |  |  |  |  |  |  |  |  |  |  | 1 | 1 | 1 | 1 | 0 | 0 | 0 | 0 | 0 |
| -18 |  |  |  |  |  |  |  |  |  |  |  | 1 | 1 | 0 | 0 | 0 | 0 | 0 | 0 |
| -16 |  |  |  |  |  |  |  |  |  |  |  | 1 | 0 | 0 | 0 | 0 | 0 | 0 | 0 |
| -14 |  |  |  |  |  |  |  |  |  |  |  |  | 0 | 0 | 0 | 0 | 0 | 0 | 0 |
| -12 |  |  |  |  |  |  |  |  |  |  |  |  |  | 0 | 0 | 0 | 0 | 0 | 0 |
| -10 |  |  |  |  |  |  |  |  |  |  |  |  |  |  | 0 | 0 | 0 | 0 | 0 |
| -8 |  |  |  |  |  |  |  |  |  |  |  |  |  |  |  | 0 | 0 | 0 | 0 |
| -6 |  |  |  |  |  |  |  |  |  |  |  |  |  |  |  |  | 0 | 0 | 0 |
| -4 |  |  |  |  |  |  |  |  |  |  |  |  |  |  |  |  | 0 | 0 | 0 |
| -2 |  |  |  |  |  |  |  |  |  |  |  |  |  |  |  |  |  | 0 | 0 |
| 0 |  |  |  |  |  |  |  |  |  |  |  |  |  |  |  |  |  | 0 | 0 |
| 2 |  |  |  |  |  |  |  |  |  |  |  |  |  |  |  |  |  |  | 0 |

Nº R = 5690
Nº NR = 26022
EQ_PC = 33%
POD = 44.5 %
FAR = 55.1 %
CSI = 28.8 %

Table 4.5. Operational structure 3-D matrix partially illustrated and statistical indices of the calibration process in percentages as in the previous tables. For each $T_{IR}$ value, the whole range of normalised visible counts is viewed from 148 to 240 each 4 counts as shown in the right column. This matrix continues until $T_{IR}$ = 2ºC, each 4 degrees. As well as the 2-D array, rows are represented by $\Delta T_{IR}$ from -11ºC to 25ºC every two degrees and elements of this matrix are classes which are transformed in rain rates or CRR 8-bit image according to table 4.2.

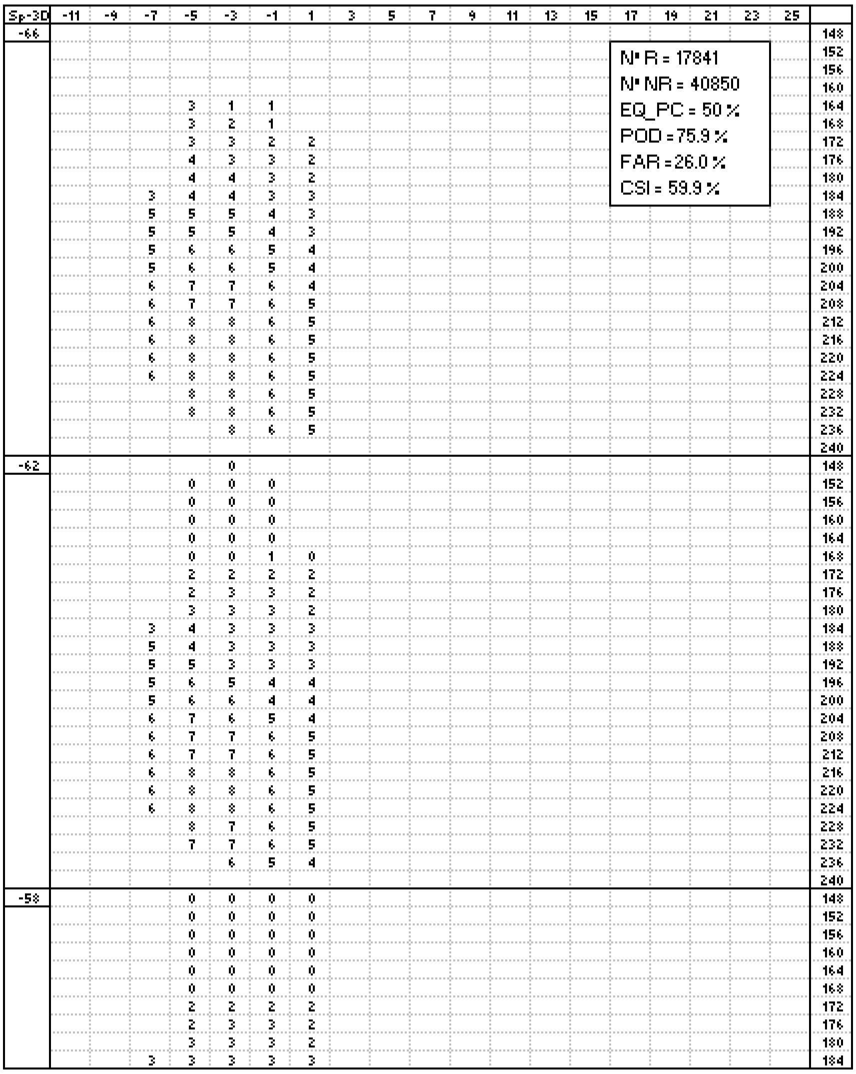

| Sp-3D | -11 | -9 | -7 | -5 | -3 | -1 | 1 | 3 | 5 | 7 | 9 | 11 | 13 | 15 | 17 | 19 | 21 | 23 | 25 | |
|---|---|---|---|---|---|---|---|---|---|---|---|---|---|---|---|---|---|---|---|---|
| -66 | | | | | | | | | | | | | | | | | | | | 148 |
| | | | | | | | | | | | | | | | | | | | | 152 |
| | | | | | | | | | | | | | | | | | | | | 156 |
| | | | | | | | | | | | | | | | | | | | | 160 |
| | | | | 3 | 1 | 1 | | | | | | | | | | | | | | 164 |
| | | | | 3 | 2 | 1 | | | | | | | | | | | | | | 168 |
| | | | | 3 | 3 | 2 | 2 | | | | | | | | | | | | | 172 |
| | | | | 4 | 3 | 3 | 2 | | | | | | | | | | | | | 176 |
| | | | | 4 | 4 | 3 | 2 | | | | | | | | | | | | | 180 |
| | | | 3 | 4 | 4 | 3 | 3 | | | | | | | | | | | | | 184 |
| | | | 5 | 5 | 5 | 4 | 3 | | | | | | | | | | | | | 188 |
| | | | 5 | 5 | 5 | 4 | 3 | | | | | | | | | | | | | 192 |
| | | | 5 | 6 | 6 | 5 | 4 | | | | | | | | | | | | | 196 |
| | | | 5 | 6 | 6 | 5 | 4 | | | | | | | | | | | | | 200 |
| | | | 6 | 7 | 7 | 6 | 4 | | | | | | | | | | | | | 204 |
| | | | 6 | 7 | 7 | 6 | 5 | | | | | | | | | | | | | 208 |
| | | | 6 | 8 | 8 | 6 | 5 | | | | | | | | | | | | | 212 |
| | | | 6 | 8 | 8 | 6 | 5 | | | | | | | | | | | | | 216 |
| | | | 6 | 8 | 8 | 6 | 5 | | | | | | | | | | | | | 220 |
| | | | 6 | 8 | 8 | 6 | 5 | | | | | | | | | | | | | 224 |
| | | | | 8 | 8 | 6 | 5 | | | | | | | | | | | | | 228 |
| | | | | 8 | 8 | 6 | 5 | | | | | | | | | | | | | 232 |
| | | | | | 8 | 6 | 5 | | | | | | | | | | | | | 236 |
| | | | | | | | | | | | | | | | | | | | | 240 |
| -62 | | | | | 0 | | | | | | | | | | | | | | | 148 |
| | | | | 0 | 0 | 0 | | | | | | | | | | | | | | 152 |
| | | | | 0 | 0 | 0 | | | | | | | | | | | | | | 156 |
| | | | | 0 | 0 | 0 | | | | | | | | | | | | | | 160 |
| | | | | 0 | 0 | 0 | | | | | | | | | | | | | | 164 |
| | | | | 0 | 0 | 1 | 0 | | | | | | | | | | | | | 168 |
| | | | | 2 | 2 | 2 | 2 | | | | | | | | | | | | | 172 |
| | | | | 2 | 3 | 3 | 2 | | | | | | | | | | | | | 176 |
| | | | | 3 | 3 | 3 | 2 | | | | | | | | | | | | | 180 |
| | | | 3 | 4 | 3 | 3 | 3 | | | | | | | | | | | | | 184 |
| | | | 5 | 4 | 3 | 3 | 3 | | | | | | | | | | | | | 188 |
| | | | 5 | 5 | 3 | 3 | 3 | | | | | | | | | | | | | 192 |
| | | | 5 | 6 | 5 | 4 | 4 | | | | | | | | | | | | | 196 |
| | | | 5 | 6 | 6 | 4 | 4 | | | | | | | | | | | | | 200 |
| | | | 6 | 7 | 6 | 5 | 4 | | | | | | | | | | | | | 204 |
| | | | 6 | 7 | 7 | 6 | 5 | | | | | | | | | | | | | 208 |
| | | | 6 | 7 | 7 | 6 | 5 | | | | | | | | | | | | | 212 |
| | | | 6 | 8 | 8 | 6 | 5 | | | | | | | | | | | | | 216 |
| | | | 6 | 8 | 8 | 6 | 5 | | | | | | | | | | | | | 220 |
| | | | 6 | 8 | 8 | 6 | 5 | | | | | | | | | | | | | 224 |
| | | | | 8 | 7 | 6 | 5 | | | | | | | | | | | | | 228 |
| | | | | 7 | 7 | 6 | 5 | | | | | | | | | | | | | 232 |
| | | | | | 6 | 5 | 4 | | | | | | | | | | | | | 236 |
| | | | | | | | | | | | | | | | | | | | | 240 |
| -58 | | | | 0 | 0 | 0 | 0 | | | | | | | | | | | | | 148 |
| | | | | 0 | 0 | 0 | 0 | | | | | | | | | | | | | 152 |
| | | | | 0 | 0 | 0 | 0 | | | | | | | | | | | | | 156 |
| | | | | 0 | 0 | 0 | 0 | | | | | | | | | | | | | 160 |
| | | | | 0 | 0 | 0 | 0 | | | | | | | | | | | | | 164 |
| | | | | 0 | 0 | 0 | 0 | | | | | | | | | | | | | 168 |
| | | | | 2 | 2 | 2 | 2 | | | | | | | | | | | | | 172 |
| | | | | 2 | 3 | 3 | 2 | | | | | | | | | | | | | 176 |
| | | | | 3 | 3 | 3 | 2 | | | | | | | | | | | | | 180 |
| | | | 3 | 3 | 3 | 3 | 3 | | | | | | | | | | | | | 184 |

Nº R = 17841
Nº NR = 40850
EQ_PC = 50 %
POD = 75.9 %
FAR = 26.0 %
CSI = 59.9 %

Table 4.6. 3-D Baltic matrix which has the same structure as the previous table 4.5 but calibrated by correlating Meteosat images with radar images from the Baltic radar network. In this case, another part of the array is shown since rainfall classes are larger.

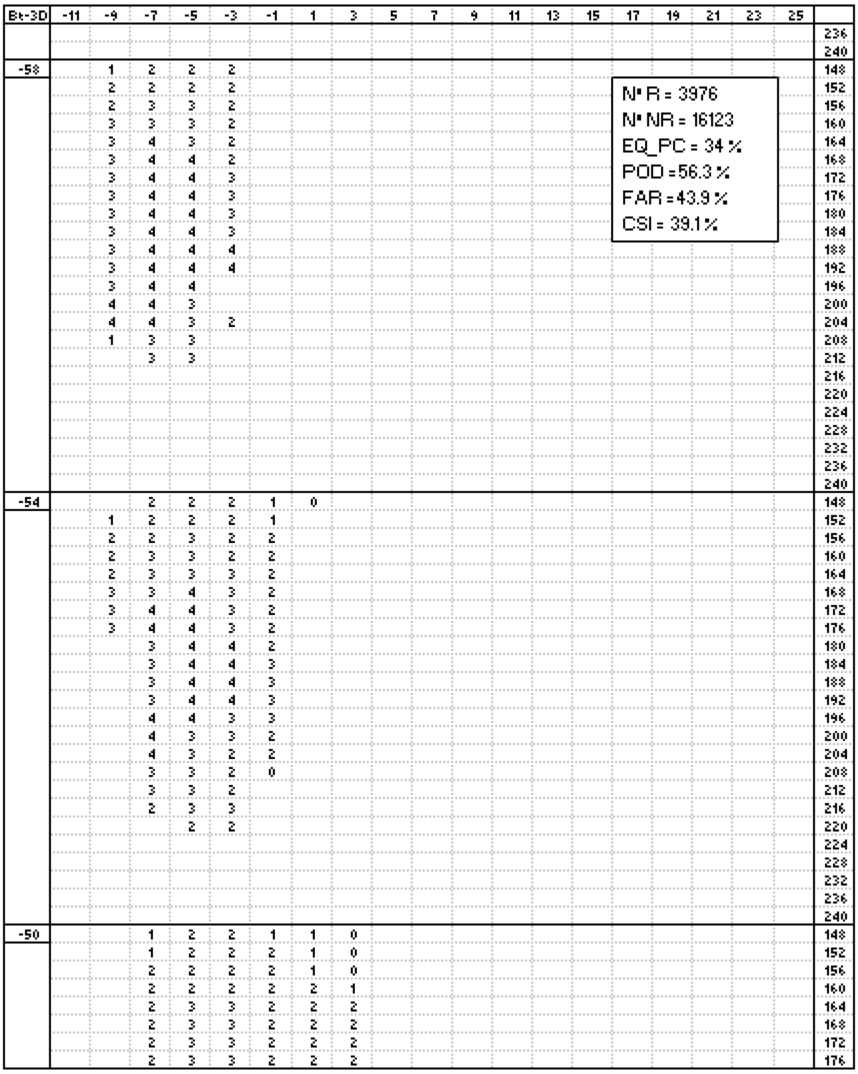

| Bt-3D | -11 | -9 | -7 | -5 | -3 | -1 | 1 | 3 | 5 | 7 | 9 | 11 | 13 | 15 | 17 | 19 | 21 | 23 | 25 | |
|---|---|---|---|---|---|---|---|---|---|---|---|---|---|---|---|---|---|---|---|---|
| | | | | | | | | | | | | | | | | | | | | 236 |
| | | | | | | | | | | | | | | | | | | | | 240 |
| -58 | | 1 | 2 | 2 | 2 | | | | | | | | | | | | | | | 148 |
| | | 2 | 2 | 2 | 2 | | | | | | | | | | | | | | | 152 |
| | | 2 | 3 | 3 | 2 | | | | | | | | | | | | | | | 156 |
| | | 3 | 3 | 3 | 2 | | | | | | | | | | | | | | | 160 |
| | | 3 | 4 | 3 | 2 | | | | | | | | | | | | | | | 164 |
| | | 3 | 4 | 4 | 2 | | | | | | | | | | | | | | | 168 |
| | | 3 | 4 | 4 | 3 | | | | | | | | | | | | | | | 172 |
| | | 3 | 4 | 4 | 3 | | | | | | | | | | | | | | | 176 |
| | | 3 | 4 | 4 | 3 | | | | | | | | | | | | | | | 180 |
| | | 3 | 4 | 4 | 3 | | | | | | | | | | | | | | | 184 |
| | | 3 | 4 | 4 | 4 | | | | | | | | | | | | | | | 188 |
| | | 3 | 4 | 4 | 4 | | | | | | | | | | | | | | | 192 |
| | | 3 | 4 | 4 | | | | | | | | | | | | | | | | 196 |
| | | 4 | 4 | 3 | | | | | | | | | | | | | | | | 200 |
| | | 4 | 4 | 3 | 2 | | | | | | | | | | | | | | | 204 |
| | | 1 | 3 | 3 | | | | | | | | | | | | | | | | 208 |
| | | | 3 | 3 | | | | | | | | | | | | | | | | 212 |
| | | | | | | | | | | | | | | | | | | | | 216 |
| | | | | | | | | | | | | | | | | | | | | 220 |
| | | | | | | | | | | | | | | | | | | | | 224 |
| | | | | | | | | | | | | | | | | | | | | 228 |
| | | | | | | | | | | | | | | | | | | | | 232 |
| | | | | | | | | | | | | | | | | | | | | 236 |
| | | | | | | | | | | | | | | | | | | | | 240 |
| -54 | | | 2 | 2 | 2 | 1 | 0 | | | | | | | | | | | | | 148 |
| | | 1 | 2 | 2 | 2 | 1 | | | | | | | | | | | | | | 152 |
| | | 2 | 2 | 3 | 2 | 2 | | | | | | | | | | | | | | 156 |
| | | 2 | 3 | 3 | 2 | 2 | | | | | | | | | | | | | | 160 |
| | | 2 | 3 | 3 | 3 | 2 | | | | | | | | | | | | | | 164 |
| | | 3 | 3 | 4 | 3 | 2 | | | | | | | | | | | | | | 168 |
| | | 3 | 4 | 4 | 3 | 2 | | | | | | | | | | | | | | 172 |
| | | 3 | 4 | 4 | 3 | 2 | | | | | | | | | | | | | | 176 |
| | | | 3 | 4 | 4 | 2 | | | | | | | | | | | | | | 180 |
| | | | 3 | 4 | 4 | 3 | | | | | | | | | | | | | | 184 |
| | | | 3 | 4 | 4 | 3 | | | | | | | | | | | | | | 188 |
| | | | 3 | 4 | 4 | 3 | | | | | | | | | | | | | | 192 |
| | | | 4 | 4 | 3 | 3 | | | | | | | | | | | | | | 196 |
| | | | 4 | 3 | 3 | 2 | | | | | | | | | | | | | | 200 |
| | | | 4 | 3 | 2 | 2 | | | | | | | | | | | | | | 204 |
| | | | 3 | 3 | 2 | 0 | | | | | | | | | | | | | | 208 |
| | | | 3 | 3 | 2 | | | | | | | | | | | | | | | 212 |
| | | | 2 | 3 | 3 | | | | | | | | | | | | | | | 216 |
| | | | | 2 | 2 | | | | | | | | | | | | | | | 220 |
| | | | | | | | | | | | | | | | | | | | | 224 |
| | | | | | | | | | | | | | | | | | | | | 228 |
| | | | | | | | | | | | | | | | | | | | | 232 |
| | | | | | | | | | | | | | | | | | | | | 236 |
| | | | | | | | | | | | | | | | | | | | | 240 |
| -50 | | | 1 | 2 | 2 | 1 | 1 | 0 | | | | | | | | | | | | 148 |
| | | | 1 | 2 | 2 | 2 | 1 | 0 | | | | | | | | | | | | 152 |
| | | | 2 | 2 | 2 | 2 | 1 | 0 | | | | | | | | | | | | 156 |
| | | | 2 | 2 | 2 | 2 | 2 | 1 | | | | | | | | | | | | 160 |
| | | | 2 | 3 | 3 | 2 | 2 | 2 | | | | | | | | | | | | 164 |
| | | | 2 | 3 | 3 | 2 | 2 | 2 | | | | | | | | | | | | 168 |
| | | | 2 | 3 | 3 | 2 | 2 | 2 | | | | | | | | | | | | 172 |
| | | | 2 | 3 | 3 | 2 | 2 | 2 | | | | | | | | | | | | 176 |

N° R = 3976
N° NR = 16123
EQ_PC = 34 %
POD = 56.3 %
FAR = 43.9 %
CSI = 39.1 %

*b) CRR images, qualitative observations*

Figures 4.3 and 4.5 are the CRR graphic output derived from satellite and matrices calibrated over the Iberian Peninsula and the Baltic Sea respectively. CRR was conceived principally to aid short-term weather prediction and timely production is of major importance. It was therefore decided to process all different CRR images and radar on a common spatial resolution and compare the different datasets in a qualitative way. Some convective cases in September and October of 2002 over the Iberian Peninsula and in June and July of 2000 over the Baltic Sea were analysed. It was observed that CRR images give a suitably clear idea of the position and intensity of cloudy convective systems with heavy rainfall and cold tops. However, rainfall areas detected via CRR method using only 2-D or nocturnal matrices, are spatially over-estimated in most cases and maximum rainfall areas are slightly displaced with respect to maximum radar rainfall zones. Les frequently it was observed that radar clusters are outside of the rain area defined by the CRR matrices. 2-D CRR have a general tendency to undervalue rainfall intensity with respect to radar precipitation. By analysing CRR images derived from 3-D matrices, the spatial correlation between radar and CRR rain areas are logically better than using 2-D matrices, although close to midday 3-D CRR tend to under-estimate precipitation.

A negative effect observed in 3-D CRR images during daytime with high solar zenith angles is noisy rainy spots with considerable rain intensity. Nevertheless, a significant spatial correspondence between the rainfall measured by radar (figures 4.2 and 4.4) to the corresponding approximation by the CRR algorithm (figures 4.3 and 4.5) has been observed in many cases. These figures are examples of mesoscale convective systems whose common feature is that they used to be difficult to be accurately forecasted by numerical models.

Figure 4.2 is a composite radar image for the Iberian Peninsula taken on the 9th October 2002, at 6.50 UTC. At that time, storms of varying intensity were located over northeast Spain and the maritime area to the north of the Balearic Islands, with maximum rainfall intensity greater than 13 mm $h^{-1}$ in some areas. At 0800 UTC, news about floods in various places of the metropolitan area of Barcelona city were reported. Figure 4.3 is a parallel CRR image remapped to radar to facilitate visual comparison between them, albeit ten minutes later. This estimated rainfall image is computed, from Meteosat and the 2-D matrix calibrated in the Iberian Peninsula (table 4.3d). Maximum values of 13 mm $h^{-1}$ are to be observed close to significant radar precipitating points however; CRR rain areas are clearly over-estimated.

Figure 4.4 is a composite radar image from the Baltex network over the Baltic area obtained on the 21st of June 2000 at 14.00 UTC. Here, clear signs of moderate rainfall over Sweden are observed due to yellow radar clusters, presumably, with significant rain. Figure 4.5 is the parallel CRR image remapped to radar spatial resolution as done for the Iberian Peninsula and processed at the same UTM time as radar. Now satellite measurements from the three Meteosat bands are associated with the 3-D array for the Baltic Sea (table 4.6) in order to estimate CRR rain rates. In spite of pixel deformation due to the high latitude of the scan from a geostationary satellite orbit and effects derived from the remap process, a big spatial correspondence to radar rainfall is easy to observe. However, as occurred in many other cases, CRR rain areas are over-estimated with respect to radar rain areas.

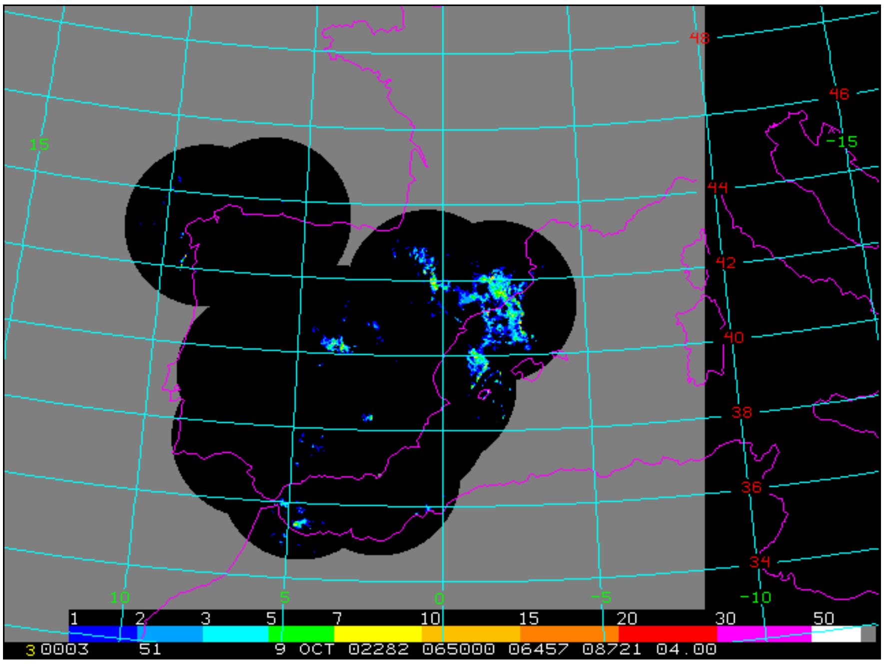

Figure 4.2. Composite radar image of the Iberian Peninsula for 0650 UTC 9 October 2002. Storms of various intensities are observed on the northeast Spain and the maritime area to the north of the Balearic Islands. Rain rates are around 15 mm $h^{-1}$ on some points of the image. At 0800 UTC floods were produced in some places of the metropolitan area of Barcelona city.

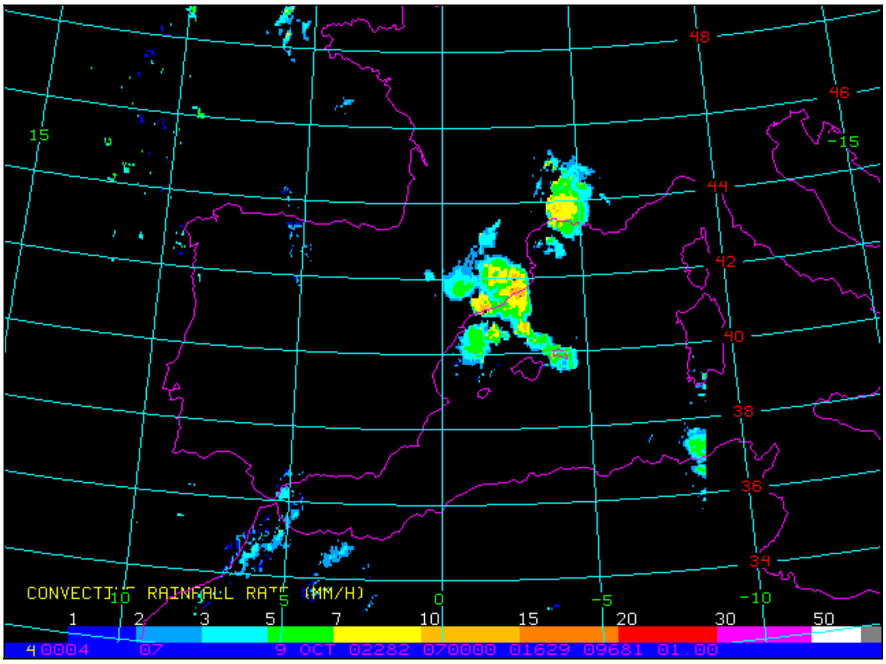

Figure 4.3. CRR image for 0700 UTC 9 October remapped to radar projection and resolution to make easy visual comparison with the previous figure. The only difference is that this image is generated ten minutes later. Rain rates as estimated from Meteosat-7 data and the 2-D matrix obtained for the Iberian Peninsula (table 4.3d) are shown. Values of 13 mm h$^{-1}$ can observed close to significant radar rain rates, although, CRR rain area is clearly over-estimated with respect to radar.

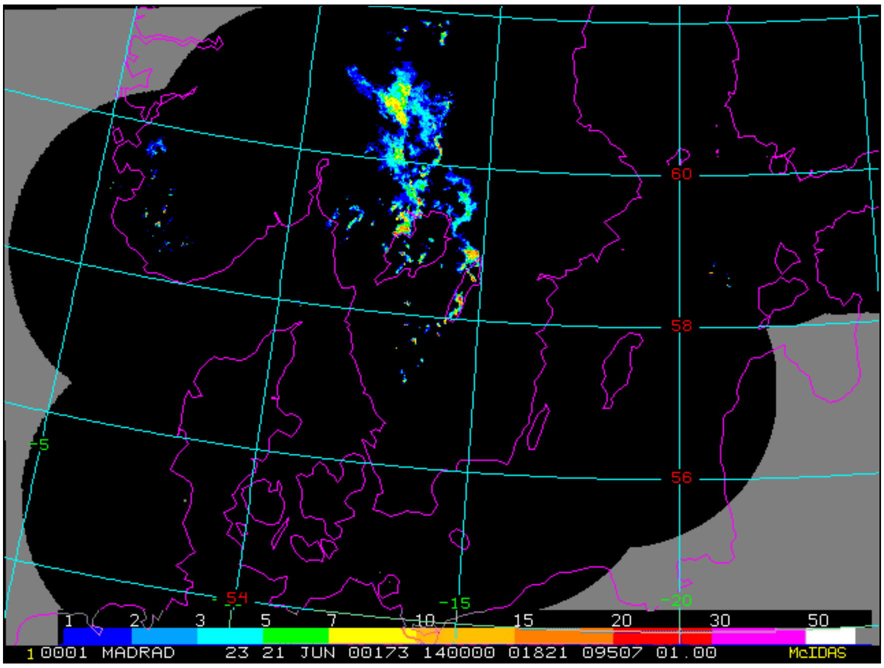

Figure 4.4. Radar image of the Baltex Project for the Baltic Sea to the South of Scandinavian Peninsula and Denmark. Obtained for 1400 UTC 21 June 2000. Here sings of active convection over Sweden are observed.

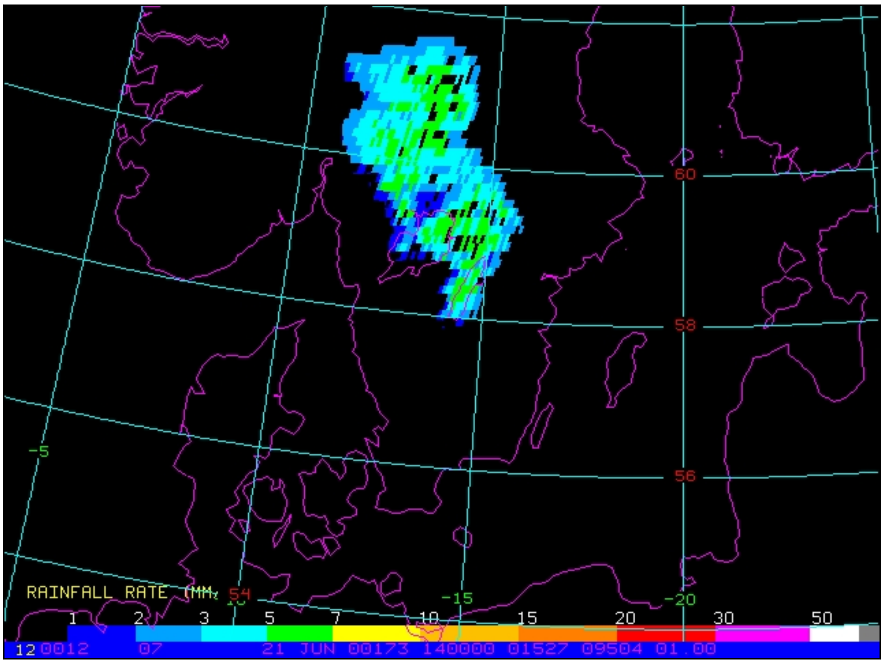

Figure 4.5. CRR image for the same area and time than the previous radar image. It was derived from Meteosat-7 data combined with the 3-D matrix for the Baltic Sea (table 4.6) and then remapped to radar. A good spatial correspondence with respect to the radar image can be observed.

*c) Two dimensional matrices differences*

Clear differences are observed after an analysis of the two 2-D matrices. Firstly, the main rainfall classes in the matrix obtained for the Iberian Peninsula (Table 4.3d) are found for values of $T_{IR}$ (columns) between -66ºC to -58ºC and for $T_{IR}$-$T_{WV}$ (rows) from -11ºC to -3ºC. Therefore a significant rain cluster with a mean rain rate around 10 mm $h^{-1}$ (by transforming classes in table 4.3d to rain rate according to table 4.2) is clearly localized in this spectral region of the table. For the 2-D rainfall array calibrated over the Baltic Sea (table 4.4) does not show a clear rain cluster, since the maximum rainfall intensity is not above 5 mm $h^{-1}$ in any point.

With respect to the rain elements distribution in both matrices, these are found mostly on the diagonal of matrices. A visual check of table 4.4 for the Baltic area confirms that the distribution of rain classes is much smoother than the table for the Iberian Peninsula. Table 4.7 is made to facilitate the observation of variations in the distribution of classes between the Baltic and Spanish arrays. In this table, cells in light grey showing ‘Bt’ statements are classes of the Baltic matrix, cells in black are classes from the two matrices and cells in dark grey with ‘Sp’ statements are classes corresponded only to the Spanish array. Here ‘Sp’ cells are not found, which implies that Spanish classes are all covered by the Baltic ones. In addition, since some ‘Bt’ cells are observed along the distribution diagonal edge, the Baltic matrix has a distribution of classes broader than the Spanish one.

Table 4.7. Same structure as Tables 4.3d and 4.4 but here the overlay of Baltic and Spanish matrices distribution of classes is shown. Cells in light grey with ‘Bt’ statements: types belonging only to the Baltic array, cells in black: types belonging to both matrices and cell in dark grey with ‘Sp’ statements are classes of the Spanish array.

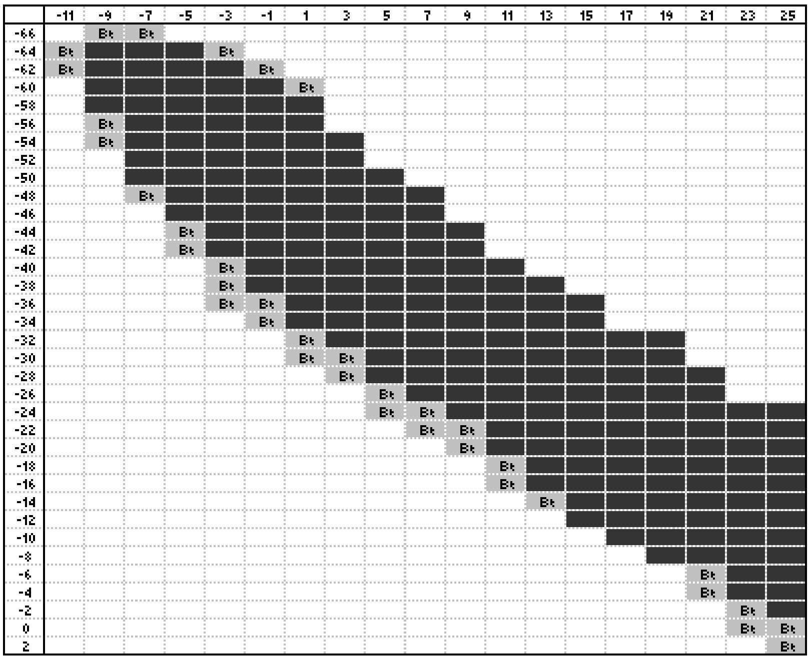

| | -11 | -9 | -7 | -5 | -3 | -1 | 1 | 3 | 5 | 7 | 9 | 11 | 13 | 15 | 17 | 19 | 21 | 23 | 25 |
|---|---|---|---|---|---|---|---|---|---|---|---|---|---|---|---|---|---|---|---|
| -66 | | Bt | Bt | | | | | | | | | | | | | | | | |
| -64 | Bt | ■ | ■ | ■ | Bt | | | | | | | | | | | | | | |
| -62 | Bt | ■ | ■ | ■ | ■ | Bt | | | | | | | | | | | | | |
| -60 | | ■ | ■ | ■ | ■ | ■ | Bt | | | | | | | | | | | | |
| -58 | | ■ | ■ | ■ | ■ | ■ | ■ | | | | | | | | | | | | |
| -56 | | Bt | ■ | ■ | ■ | ■ | ■ | | | | | | | | | | | | |
| -54 | | Bt | ■ | ■ | ■ | ■ | ■ | ■ | | | | | | | | | | | |
| -52 | | | ■ | ■ | ■ | ■ | ■ | ■ | | | | | | | | | | | |
| -50 | | | ■ | ■ | ■ | ■ | ■ | ■ | ■ | | | | | | | | | | |
| -48 | | | Bt | ■ | ■ | ■ | ■ | ■ | ■ | ■ | | | | | | | | | |
| -46 | | | | ■ | ■ | ■ | ■ | ■ | ■ | ■ | | | | | | | | | |
| -44 | | | | Bt | ■ | ■ | ■ | ■ | ■ | ■ | ■ | | | | | | | | |
| -42 | | | | Bt | ■ | ■ | ■ | ■ | ■ | ■ | ■ | | | | | | | | |
| -40 | | | | | Bt | ■ | ■ | ■ | ■ | ■ | ■ | ■ | | | | | | | |
| -38 | | | | | Bt | ■ | ■ | ■ | ■ | ■ | ■ | ■ | ■ | | | | | | |
| -36 | | | | | Bt | Bt | ■ | ■ | ■ | ■ | ■ | ■ | ■ | ■ | | | | | |
| -34 | | | | | | Bt | ■ | ■ | ■ | ■ | ■ | ■ | ■ | ■ | | | | | |
| -32 | | | | | | | Bt | ■ | ■ | ■ | ■ | ■ | ■ | ■ | ■ | ■ | | | |
| -30 | | | | | | | Bt | Bt | ■ | ■ | ■ | ■ | ■ | ■ | ■ | ■ | | | |
| -28 | | | | | | | | Bt | ■ | ■ | ■ | ■ | ■ | ■ | ■ | ■ | ■ | | |
| -26 | | | | | | | | | Bt | ■ | ■ | ■ | ■ | ■ | ■ | ■ | ■ | | |
| -24 | | | | | | | | | Bt | Bt | ■ | ■ | ■ | ■ | ■ | ■ | ■ | ■ | ■ |
| -22 | | | | | | | | | | Bt | Bt | ■ | ■ | ■ | ■ | ■ | ■ | ■ | ■ |
| -20 | | | | | | | | | | | Bt | ■ | ■ | ■ | ■ | ■ | ■ | ■ | ■ |
| -18 | | | | | | | | | | | | Bt | ■ | ■ | ■ | ■ | ■ | ■ | ■ |
| -16 | | | | | | | | | | | | Bt | ■ | ■ | ■ | ■ | ■ | ■ | ■ |
| -14 | | | | | | | | | | | | | Bt | ■ | ■ | ■ | ■ | ■ | ■ |
| -12 | | | | | | | | | | | | | | ■ | ■ | ■ | ■ | ■ | ■ |
| -10 | | | | | | | | | | | | | | | ■ | ■ | ■ | ■ | ■ |
| -8 | | | | | | | | | | | | | | | | ■ | ■ | ■ | ■ |
| -6 | | | | | | | | | | | | | | | | | Bt | ■ | ■ |
| -4 | | | | | | | | | | | | | | | | | Bt | ■ | ■ |
| -2 | | | | | | | | | | | | | | | | | | Bt | ■ |
| 0 | | | | | | | | | | | | | | | | | | Bt | Bt |
| 2 | | | | | | | | | | | | | | | | | | | Bt |

*d) Three dimensional matrices differences*

The structure of the 3-D matrices is modified with respect to those shown in Tables 4.5 and 4.6 in order to better illustrate the interaction of the visible band data over themselves. In the new column configuration, for each visible normalized count (*Vc*), the complete $T_{IR}$ range is shown every 4 degrees. Therefore, changes on mean rain class distribution can be observed in a matrix structure similar to the 2-D array by increasing *Vc*. Parts of the 3-D matrices obtained for the Iberian Peninsula and Baltic Sea are shown in Tables 4.8 and 4.9 respectively. The new scheme described in the beginning of this section is also illustrated in these tables and significantly different rain classes are highlighted by using two tones of grey. Classes of between 4 and 5 in light grey symbolize moderate rainfall from 3 to 7 mm $h^{-1}$ according to table 4.2 and classes between 6 and 8 in dark grey indicate heavier rain rates from 7 to 20 mm $h^{-1}$ according again, to table 4.2. An analysis of the two 3-D matrices highlights significant differences between the two arrays in respect of class values and their distribution.

The 3-D matrix for the Iberian Peninsula highlights a remarkable convective area with class values above 4 which evolves along the visible range. This area is gently increased with regard to the number of cells and the class values from $Vc$ = 188, to $Vc$ = 224 where an apparent peak is reached with maximum rain classes of around 8 (17 mm $h^{-1}$, according to table 4.2). Then this cluster decreases quickly in size and intensity until it almost disappears for $Vc$ = 240. Table 4.8 shows a section of this 3-D matrix where the highest rainfall clusters are situated.

In the Baltic 3-D matrix, a much less intense cluster of significant classes is illustrated, although none has a value above 4. This group grows slowly, mostly in sizes from $Vc$ = 168 to $Vc$ = 188 where a presumed maximum is reached. Then it decreases gradually until $Vc$ = 204 in which classes equal to 4 are observed for the last time. Table 4.9 shows the position in the Baltic 3-D array where maximum rainfall clusters are located.

Grey shaded tables highlight the distribution of classes, analogous to table 4.7, showing the overlap of 3-D matrices classes (see tables 4.10 and 4.11). As $Vc$ increases from 164 to 188, the diagonal distribution of classes in the 3-D matrix for the Iberian Peninsula begins to broaden on the left side of the distribution and to narrow on the right side (see table 4.10, shape of the group of ‘Sp’ cells plus black cells). This trend continues throughout until the end of the visible range although with a slight displacement of the whole distribution down (to warmer $T_{IR}$) and to the right (to bigger $T_{IR}$-$T_{WV}$). When $Vc$ = 232 is reached, the distribution of classes is found to be very compact (see table 4.11, ‘Sp’ plus black cells).

The distribution of classes of the 3-D matrix obtained over the Baltic area hold a diagonal shape along the whole range of the visible band from 148 to 208 (see table 4.10, ‘Bt’ plus black cells). Then it begins to narrow and shrink from left to right until the distribution of classes disappears completely for $Vc$ = 232 (see table 4.11, ‘Bt’ plus black cells).

Table 4.8. Section of the 3-D matrix obtained for the Iberian Peninsula where the highest rainfall classes are situated. This table shows the new scheme adequate for the analysis in which rows are $T_{IR}$-$T_{WV}$ , from -11ºC to 25ºC each 2 degrees and column axis show the whole range of $T_{IR}$ each 4 degrees for each visible brightness count ($Vc$). Cells shaded in light grey represent a group of moderate rainfall and cells in dark grey represent a cluster of heavy rainfall.

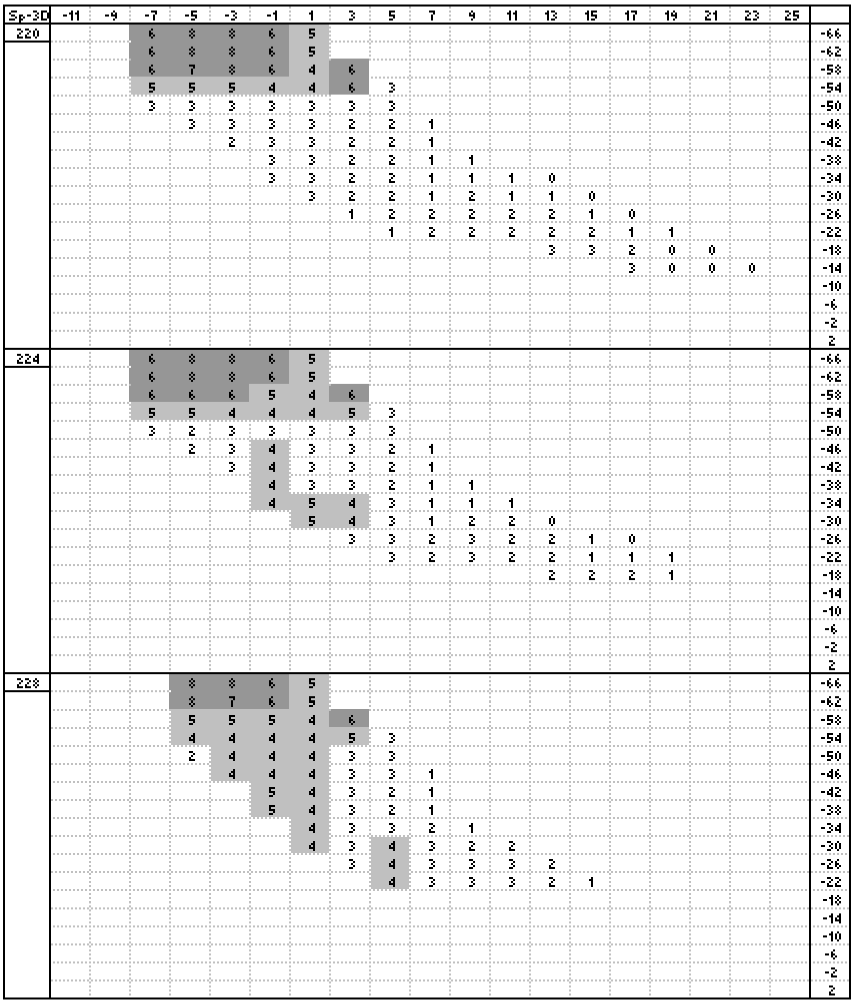

| Sp-3D | -11 | -9 | -7 | -5 | -3 | -1 | 1 | 3 | 5 | 7 | 9 | 11 | 13 | 15 | 17 | 19 | 21 | 23 | 25 | |
|---|---|---|---|---|---|---|---|---|---|---|---|---|---|---|---|---|---|---|---|---|
| 220 | | | 6 | 8 | 8 | 6 | 5 | | | | | | | | | | | | | -66 |
| | | | 6 | 8 | 8 | 6 | 5 | | | | | | | | | | | | | -62 |
| | | | 6 | 7 | 8 | 6 | 4 | 6 | | | | | | | | | | | | -58 |
| | | | 5 | 5 | 5 | 4 | 4 | 6 | 3 | | | | | | | | | | | -54 |
| | | | 3 | 3 | 3 | 3 | 3 | 3 | 3 | | | | | | | | | | | -50 |
| | | | | 3 | 3 | 3 | 3 | 2 | 2 | 1 | | | | | | | | | | -46 |
| | | | | | 2 | 3 | 3 | 2 | 2 | 1 | | | | | | | | | | -42 |
| | | | | | | 3 | 3 | 2 | 2 | 1 | 1 | | | | | | | | | -38 |
| | | | | | | 3 | 3 | 2 | 2 | 1 | 1 | 1 | 0 | | | | | | | -34 |
| | | | | | | | 3 | 2 | 2 | 1 | 2 | 1 | 1 | 0 | | | | | | -30 |
| | | | | | | | | 1 | 2 | 2 | 2 | 2 | 2 | 1 | 0 | | | | | -26 |
| | | | | | | | | | 1 | 2 | 2 | 2 | 2 | 2 | 1 | 1 | | | | -22 |
| | | | | | | | | | | | | | 3 | 3 | 2 | 0 | 0 | | | -18 |
| | | | | | | | | | | | | | | | 3 | 0 | 0 | 0 | | -14 |
| | | | | | | | | | | | | | | | | | | | | -10 |
| | | | | | | | | | | | | | | | | | | | | -6 |
| | | | | | | | | | | | | | | | | | | | | -2 |
| | | | | | | | | | | | | | | | | | | | | 2 |
| 224 | | | 6 | 8 | 8 | 6 | 5 | | | | | | | | | | | | | -66 |
| | | | 6 | 8 | 8 | 6 | 5 | | | | | | | | | | | | | -62 |
| | | | 6 | 6 | 6 | 5 | 4 | 6 | | | | | | | | | | | | -58 |
| | | | 5 | 5 | 4 | 4 | 4 | 5 | 3 | | | | | | | | | | | -54 |
| | | | 3 | 2 | 3 | 3 | 3 | 3 | 3 | | | | | | | | | | | -50 |
| | | | | 2 | 3 | 4 | 3 | 3 | 2 | 1 | | | | | | | | | | -46 |
| | | | | | 3 | 4 | 3 | 3 | 2 | 1 | | | | | | | | | | -42 |
| | | | | | | 4 | 3 | 3 | 2 | 1 | 1 | | | | | | | | | -38 |
| | | | | | | 4 | 5 | 4 | 3 | 1 | 1 | 1 | | | | | | | | -34 |
| | | | | | | | 5 | 4 | 3 | 1 | 2 | 2 | 0 | | | | | | | -30 |
| | | | | | | | | 3 | 3 | 2 | 3 | 2 | 2 | 1 | 0 | | | | | -26 |
| | | | | | | | | | 3 | 2 | 3 | 2 | 2 | 1 | 1 | 1 | | | | -22 |
| | | | | | | | | | | | | | 2 | 2 | 2 | 1 | | | | -18 |
| | | | | | | | | | | | | | | | | | | | | -14 |
| | | | | | | | | | | | | | | | | | | | | -10 |
| | | | | | | | | | | | | | | | | | | | | -6 |
| | | | | | | | | | | | | | | | | | | | | -2 |
| | | | | | | | | | | | | | | | | | | | | 2 |
| 228 | | | | 8 | 8 | 6 | 5 | | | | | | | | | | | | | -66 |
| | | | | 8 | 7 | 6 | 5 | | | | | | | | | | | | | -62 |
| | | | | 5 | 5 | 5 | 4 | 6 | | | | | | | | | | | | -58 |
| | | | | 4 | 4 | 4 | 4 | 5 | 3 | | | | | | | | | | | -54 |
| | | | | 2 | 4 | 4 | 4 | 3 | 3 | | | | | | | | | | | -50 |
| | | | | | 4 | 4 | 4 | 3 | 3 | 1 | | | | | | | | | | -46 |
| | | | | | | 5 | 4 | 3 | 2 | 1 | | | | | | | | | | -42 |
| | | | | | | 5 | 4 | 3 | 2 | 1 | | | | | | | | | | -38 |
| | | | | | | | 4 | 3 | 3 | 2 | 1 | | | | | | | | | -34 |
| | | | | | | | 4 | 3 | 4 | 3 | 2 | 2 | | | | | | | | -30 |
| | | | | | | | | 3 | 4 | 3 | 3 | 3 | 2 | | | | | | | -26 |
| | | | | | | | | | 4 | 3 | 3 | 3 | 2 | 1 | | | | | | -22 |
| | | | | | | | | | | | | | | | | | | | | -18 |
| | | | | | | | | | | | | | | | | | | | | -14 |
| | | | | | | | | | | | | | | | | | | | | -10 |
| | | | | | | | | | | | | | | | | | | | | -6 |
| | | | | | | | | | | | | | | | | | | | | -2 |
| | | | | | | | | | | | | | | | | | | | | 2 |

Table 4.9. Same as table 4.8 but shows the part of the Baltic matrix where the largest rainfall classes are to be found. The distribution of classes has a diagonal line shape and rainfall class values are not above 4 in any case.

| Bt-3D | -11 | -9 | -7 | -5 | -3 | -1 | 1 | 3 | 5 | 7 | 9 | 11 | 13 | 15 | 17 | 19 | 21 | 23 | 25 | |
|---|---|---|---|---|---|---|---|---|---|---|---|---|---|---|---|---|---|---|---|---|
| 184 | | | | | | | | | | | | | | | | | | | | -66 |
| | | 3 | 4 | 3 | | | | | | | | | | | | | | | | -62 |
| | | 3 | 4 | 4 | 3 | | | | | | | | | | | | | | | -58 |
| | | | 3 | 4 | 4 | 3 | | | | | | | | | | | | | | -54 |
| | | | 2 | 3 | 3 | 2 | 2 | | | | | | | | | | | | | -50 |
| | | | | 2 | 2 | 2 | 2 | 1 | 1 | | | | | | | | | | | -46 |
| | | | | | 1 | 1 | 2 | 1 | 1 | 1 | | | | | | | | | | -42 |
| | | | | | | 1 | 1 | 1 | 1 | 1 | 1 | 0 | | | | | | | | -38 |
| | | | | | | | 1 | 1 | 1 | 1 | 1 | 1 | 1 | | | | | | | -34 |
| | | | | | | | | | 1 | 1 | 1 | 1 | 1 | 1 | 0 | | | | | -30 |
| | | | | | | | | | | 1 | 1 | 1 | 1 | 1 | 1 | 1 | 0 | | | -26 |
| | | | | | | | | | | | | 1 | 1 | 1 | 1 | 1 | 1 | 1 | | -22 |
| | | | | | | | | | | | | | 0 | 1 | 1 | 1 | 1 | 0 | 0 | -18 |
| | | | | | | | | | | | | | | | 0 | 1 | 0 | 0 | 0 | -14 |
| | | | | | | | | | | | | | | | | 0 | 0 | 0 | 0 | -10 |
| | | | | | | | | | | | | | | | | | | 0 | 0 | -6 |
| | | | | | | | | | | | | | | | | | | | 0 | -2 |
| | | | | | | | | | | | | | | | | | | | | 2 |
| 188 | | | | | | | | | | | | | | | | | | | | -66 |
| | | 4 | 4 | 4 | | | | | | | | | | | | | | | | -62 |
| | | 3 | 4 | 4 | 4 | | | | | | | | | | | | | | | -58 |
| | | | 3 | 4 | 4 | 3 | | | | | | | | | | | | | | -54 |
| | | | 2 | 3 | 3 | 3 | 2 | | | | | | | | | | | | | -50 |
| | | | | 2 | 2 | 2 | 2 | 1 | | | | | | | | | | | | -46 |
| | | | | | 1 | 1 | 1 | 1 | 1 | 1 | | | | | | | | | | -42 |
| | | | | | | 1 | 1 | 1 | 1 | 1 | 1 | 0 | | | | | | | | -38 |
| | | | | | | | 1 | 1 | 1 | 1 | 1 | 1 | 1 | | | | | | | -34 |
| | | | | | | | | | 1 | 1 | 1 | 1 | 1 | 1 | 0 | | | | | -30 |
| | | | | | | | | | | 1 | 1 | 1 | 1 | 1 | 1 | 1 | 0 | | | -26 |
| | | | | | | | | | | | | 1 | 1 | 1 | 1 | 1 | 1 | 0 | | -22 |
| | | | | | | | | | | | | | 0 | 1 | 1 | 1 | 1 | 0 | 0 | -18 |
| | | | | | | | | | | | | | | | 0 | 0 | 0 | 0 | 0 | -14 |
| | | | | | | | | | | | | | | | | 0 | 0 | 0 | 0 | -10 |
| | | | | | | | | | | | | | | | | | | 0 | 0 | -6 |
| | | | | | | | | | | | | | | | | | | | | -2 |
| | | | | | | | | | | | | | | | | | | | | 2 |
| 192 | | | | | | | | | | | | | | | | | | | | -66 |
| | | 3 | 4 | | | | | | | | | | | | | | | | | -62 |
| | | 3 | 4 | 4 | 4 | | | | | | | | | | | | | | | -58 |
| | | | 3 | 4 | 4 | 3 | | | | | | | | | | | | | | -54 |
| | | | 2 | 3 | 3 | 3 | 2 | | | | | | | | | | | | | -50 |
| | | | | 2 | 2 | 2 | 2 | 1 | | | | | | | | | | | | -46 |
| | | | | | 1 | 2 | 2 | 1 | 1 | 1 | | | | | | | | | | -42 |
| | | | | | | 1 | 1 | 1 | 1 | 1 | 1 | | | | | | | | | -38 |
| | | | | | | | 1 | 1 | 1 | 1 | 1 | 1 | 1 | | | | | | | -34 |
| | | | | | | | | | 1 | 1 | 1 | 1 | 1 | 1 | 0 | | | | | -30 |
| | | | | | | | | | | 1 | 1 | 1 | 1 | 1 | 1 | 1 | | | | -26 |
| | | | | | | | | | | | | 1 | 1 | 1 | 1 | 1 | 1 | 0 | | -22 |
| | | | | | | | | | | | | | | 1 | 1 | 1 | 1 | 0 | 0 | -18 |
| | | | | | | | | | | | | | | | 1 | 0 | 0 | 0 | 0 | -14 |
| | | | | | | | | | | | | | | | | 0 | 0 | 0 | 0 | -10 |
| | | | | | | | | | | | | | | | | | | 0 | 0 | -6 |
| | | | | | | | | | | | | | | | | | | | | -2 |
| | | | | | | | | | | | | | | | | | | | | 2 |

Table 4.10. Same structure as the tables 4.8 and 4.9 but, in this case, shows the 3-D Baltic and Spanish matrices overlay. Light grey 'Bt' cells are classes corresponding only to the Baltic array, black cells are classes belonging to the two matrices and dark grey 'Sp' cells are classes corresponding only to the Spanish array.

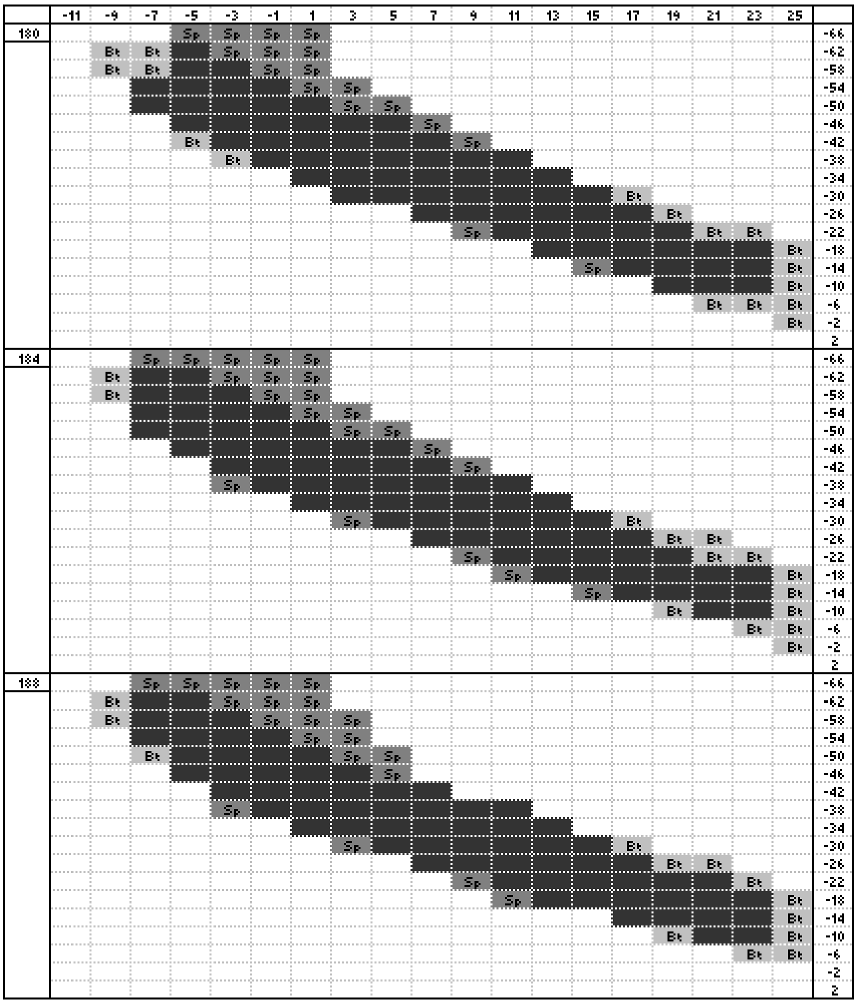

|  | -11 | -9 | -7 | -5 | -3 | -1 | 1 | 3 | 5 | 7 | 9 | 11 | 13 | 15 | 17 | 19 | 21 | 23 | 25 |  |
|---|---|---|---|---|---|---|---|---|---|---|---|---|---|---|---|---|---|---|---|---|
| 180 |  |  |  | Sp | Sp | Sp | Sp |  |  |  |  |  |  |  |  |  |  |  |  | -66 |
|  |  | Bt | Bt | ■ | Sp | Sp | Sp |  |  |  |  |  |  |  |  |  |  |  |  | -62 |
|  |  | Bt | Bt | ■ | ■ | Sp | Sp |  |  |  |  |  |  |  |  |  |  |  |  | -58 |
|  |  |  | ■ | ■ | ■ | ■ | Sp | Sp |  |  |  |  |  |  |  |  |  |  |  | -54 |
|  |  |  | ■ | ■ | ■ | ■ | ■ | Sp | Sp |  |  |  |  |  |  |  |  |  |  | -50 |
|  |  |  |  | ■ | ■ | ■ | ■ | ■ | ■ | Sp |  |  |  |  |  |  |  |  |  | -46 |
|  |  |  |  | Bt | ■ | ■ | ■ | ■ | ■ | ■ | Sp |  |  |  |  |  |  |  |  | -42 |
|  |  |  |  |  | Bt | ■ | ■ | ■ | ■ | ■ | ■ | ■ |  |  |  |  |  |  |  | -38 |
|  |  |  |  |  |  |  | ■ | ■ | ■ | ■ | ■ | ■ | ■ |  |  |  |  |  |  | -34 |
|  |  |  |  |  |  |  |  | ■ | ■ | ■ | ■ | ■ | ■ | ■ | Bt |  |  |  |  | -30 |
|  |  |  |  |  |  |  |  |  |  | ■ | ■ | ■ | ■ | ■ | ■ | Bt |  |  |  | -26 |
|  |  |  |  |  |  |  |  |  |  |  | Sp | ■ | ■ | ■ | ■ | ■ | Bt | Bt |  | -22 |
|  |  |  |  |  |  |  |  |  |  |  |  |  | ■ | ■ | ■ | ■ | ■ | ■ | Bt | -18 |
|  |  |  |  |  |  |  |  |  |  |  |  |  |  | Sp | ■ | ■ | ■ | ■ | Bt | -14 |
|  |  |  |  |  |  |  |  |  |  |  |  |  |  |  |  | ■ | ■ | ■ | Bt | -10 |
|  |  |  |  |  |  |  |  |  |  |  |  |  |  |  |  |  | Bt | Bt | Bt | -6 |
|  |  |  |  |  |  |  |  |  |  |  |  |  |  |  |  |  |  |  | Bt | -2 |
|  |  |  |  |  |  |  |  |  |  |  |  |  |  |  |  |  |  |  |  | 2 |
| 184 |  |  | Sp | Sp | Sp | Sp | Sp |  |  |  |  |  |  |  |  |  |  |  |  | -66 |
|  |  | Bt | ■ | ■ | Sp | Sp | Sp |  |  |  |  |  |  |  |  |  |  |  |  | -62 |
|  |  | Bt | ■ | ■ | ■ | Sp | Sp |  |  |  |  |  |  |  |  |  |  |  |  | -58 |
|  |  |  | ■ | ■ | ■ | ■ | Sp | Sp |  |  |  |  |  |  |  |  |  |  |  | -54 |
|  |  |  | ■ | ■ | ■ | ■ | ■ | Sp | Sp |  |  |  |  |  |  |  |  |  |  | -50 |
|  |  |  |  | ■ | ■ | ■ | ■ | ■ | ■ | Sp |  |  |  |  |  |  |  |  |  | -46 |
|  |  |  |  |  | ■ | ■ | ■ | ■ | ■ | ■ | Sp |  |  |  |  |  |  |  |  | -42 |
|  |  |  |  |  | Sp | ■ | ■ | ■ | ■ | ■ | ■ | ■ |  |  |  |  |  |  |  | -38 |
|  |  |  |  |  |  |  | ■ | ■ | ■ | ■ | ■ | ■ | ■ |  |  |  |  |  |  | -34 |
|  |  |  |  |  |  |  |  | Sp | ■ | ■ | ■ | ■ | ■ | ■ | Bt |  |  |  |  | -30 |
|  |  |  |  |  |  |  |  |  |  | ■ | ■ | ■ | ■ | ■ | ■ | Bt | Bt |  |  | -26 |
|  |  |  |  |  |  |  |  |  |  |  | Sp | ■ | ■ | ■ | ■ | ■ | Bt | Bt |  | -22 |
|  |  |  |  |  |  |  |  |  |  |  |  | Sp | ■ | ■ | ■ | ■ | ■ | ■ | Bt | -18 |
|  |  |  |  |  |  |  |  |  |  |  |  |  |  | Sp | ■ | ■ | ■ | ■ | Bt | -14 |
|  |  |  |  |  |  |  |  |  |  |  |  |  |  |  |  | Bt | ■ | ■ | Bt | -10 |
|  |  |  |  |  |  |  |  |  |  |  |  |  |  |  |  |  |  | Bt | Bt | -6 |
|  |  |  |  |  |  |  |  |  |  |  |  |  |  |  |  |  |  |  | Bt | -2 |
|  |  |  |  |  |  |  |  |  |  |  |  |  |  |  |  |  |  |  |  | 2 |
| 188 |  |  | Sp | Sp | Sp | Sp | Sp |  |  |  |  |  |  |  |  |  |  |  |  | -66 |
|  |  | Bt | ■ | ■ | Sp | Sp | Sp |  |  |  |  |  |  |  |  |  |  |  |  | -62 |
|  |  | Bt | ■ | ■ | ■ | Sp | Sp | Sp |  |  |  |  |  |  |  |  |  |  |  | -58 |
|  |  |  | ■ | ■ | ■ | ■ | Sp | Sp |  |  |  |  |  |  |  |  |  |  |  | -54 |
|  |  |  | Bt | ■ | ■ | ■ | ■ | Sp | Sp |  |  |  |  |  |  |  |  |  |  | -50 |
|  |  |  |  | ■ | ■ | ■ | ■ | ■ | Sp |  |  |  |  |  |  |  |  |  |  | -46 |
|  |  |  |  |  | ■ | ■ | ■ | ■ | ■ | ■ |  |  |  |  |  |  |  |  |  | -42 |
|  |  |  |  |  | Sp | ■ | ■ | ■ | ■ | ■ | ■ | ■ |  |  |  |  |  |  |  | -38 |
|  |  |  |  |  |  |  | ■ | ■ | ■ | ■ | ■ | ■ | ■ |  |  |  |  |  |  | -34 |
|  |  |  |  |  |  |  |  | Sp | ■ | ■ | ■ | ■ | ■ | ■ | Bt |  |  |  |  | -30 |
|  |  |  |  |  |  |  |  |  |  | ■ | ■ | ■ | ■ | ■ | ■ | Bt | Bt |  |  | -26 |
|  |  |  |  |  |  |  |  |  |  |  | Sp | ■ | ■ | ■ | ■ | ■ | ■ | Bt |  | -22 |
|  |  |  |  |  |  |  |  |  |  |  |  | Sp | ■ | ■ | ■ | ■ | ■ | ■ | Bt | -18 |
|  |  |  |  |  |  |  |  |  |  |  |  |  |  |  | ■ | ■ | ■ | ■ | Bt | -14 |
|  |  |  |  |  |  |  |  |  |  |  |  |  |  |  |  | Bt | ■ | ■ | Bt | -10 |
|  |  |  |  |  |  |  |  |  |  |  |  |  |  |  |  |  |  | Bt | Bt | -6 |
|  |  |  |  |  |  |  |  |  |  |  |  |  |  |  |  |  |  |  |  | -2 |
|  |  |  |  |  |  |  |  |  |  |  |  |  |  |  |  |  |  |  |  | 2 |

Table 4.11. Same as table 4.10 but for another part of the 3-D array very close to the end for *Vc* = 240. Spanish 'Sp' cells in dark grey plus black cells configure a very compact cluster while Baltic classes in light grey plus black cells are clearly declining with the increase of *Vc*.

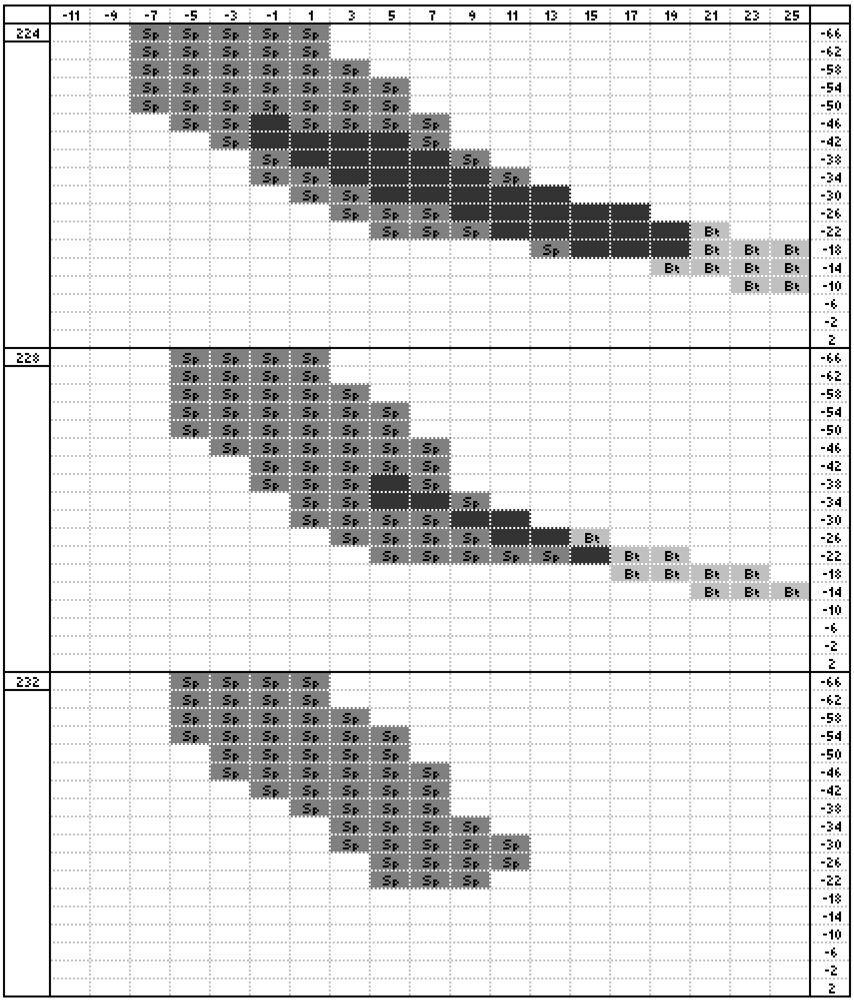

| | -11 | -9 | -7 | -5 | -3 | -1 | 1 | 3 | 5 | 7 | 9 | 11 | 13 | 15 | 17 | 19 | 21 | 23 | 25 | |
|---|---|---|---|---|---|---|---|---|---|---|---|---|---|---|---|---|---|---|---|---|
| 224 | | | Sp | Sp | Sp | Sp | Sp | | | | | | | | | | | | | -66 |
| | | | Sp | Sp | Sp | Sp | Sp | | | | | | | | | | | | | -62 |
| | | | Sp | Sp | Sp | Sp | Sp | Sp | | | | | | | | | | | | -58 |
| | | | Sp | Sp | Sp | Sp | Sp | Sp | Sp | | | | | | | | | | | -54 |
| | | | Sp | Sp | Sp | Sp | Sp | Sp | Sp | | | | | | | | | | | -50 |
| | | | | Sp | Sp | ■ | Sp | Sp | Sp | Sp | | | | | | | | | | -46 |
| | | | | | Sp | ■ | ■ | ■ | ■ | Sp | | | | | | | | | | -42 |
| | | | | | | Sp | ■ | ■ | ■ | ■ | Sp | | | | | | | | | -38 |
| | | | | | | Sp | Sp | ■ | ■ | ■ | ■ | Sp | | | | | | | | -34 |
| | | | | | | | Sp | Sp | ■ | ■ | ■ | ■ | ■ | | | | | | | -30 |
| | | | | | | | | Sp | Sp | Sp | ■ | ■ | ■ | ■ | ■ | | | | | -26 |
| | | | | | | | | | Sp | Sp | Sp | ■ | ■ | ■ | ■ | ■ | Bt | | | -22 |
| | | | | | | | | | | | | | Sp | ■ | ■ | ■ | Bt | Bt | Bt | -18 |
| | | | | | | | | | | | | | | | | Bt | Bt | Bt | Bt | -14 |
| | | | | | | | | | | | | | | | | | | Bt | Bt | -10 |
| | | | | | | | | | | | | | | | | | | | | -6 |
| | | | | | | | | | | | | | | | | | | | | -2 |
| | | | | | | | | | | | | | | | | | | | | 2 |
| 228 | | | | Sp | Sp | Sp | Sp | | | | | | | | | | | | | -66 |
| | | | | Sp | Sp | Sp | Sp | | | | | | | | | | | | | -62 |
| | | | | Sp | Sp | Sp | Sp | Sp | | | | | | | | | | | | -58 |
| | | | | Sp | Sp | Sp | Sp | Sp | Sp | | | | | | | | | | | -54 |
| | | | | Sp | Sp | Sp | Sp | Sp | Sp | | | | | | | | | | | -50 |
| | | | | | Sp | Sp | Sp | Sp | Sp | Sp | | | | | | | | | | -46 |
| | | | | | | Sp | Sp | Sp | Sp | Sp | | | | | | | | | | -42 |
| | | | | | | Sp | Sp | Sp | ■ | Sp | | | | | | | | | | -38 |
| | | | | | | | Sp | Sp | ■ | ■ | Sp | | | | | | | | | -34 |
| | | | | | | | Sp | Sp | Sp | Sp | ■ | ■ | | | | | | | | -30 |
| | | | | | | | | Sp | Sp | Sp | Sp | ■ | ■ | Bt | | | | | | -26 |
| | | | | | | | | | Sp | Sp | Sp | Sp | Sp | ■ | Bt | Bt | | | | -22 |
| | | | | | | | | | | | | | | | Bt | Bt | Bt | Bt | | -18 |
| | | | | | | | | | | | | | | | | | Bt | Bt | Bt | -14 |
| | | | | | | | | | | | | | | | | | | | | -10 |
| | | | | | | | | | | | | | | | | | | | | -6 |
| | | | | | | | | | | | | | | | | | | | | -2 |
| | | | | | | | | | | | | | | | | | | | | 2 |
| 232 | | | | Sp | Sp | Sp | Sp | | | | | | | | | | | | | -66 |
| | | | | Sp | Sp | Sp | Sp | | | | | | | | | | | | | -62 |
| | | | | Sp | Sp | Sp | Sp | Sp | | | | | | | | | | | | -58 |
| | | | | Sp | Sp | Sp | Sp | Sp | Sp | | | | | | | | | | | -54 |
| | | | | | Sp | Sp | Sp | Sp | Sp | | | | | | | | | | | -50 |
| | | | | | Sp | Sp | Sp | Sp | Sp | Sp | | | | | | | | | | -46 |
| | | | | | | Sp | Sp | Sp | Sp | Sp | | | | | | | | | | -42 |
| | | | | | | | Sp | Sp | Sp | Sp | | | | | | | | | | -38 |
| | | | | | | | | Sp | Sp | Sp | Sp | | | | | | | | | -34 |
| | | | | | | | | Sp | Sp | Sp | Sp | Sp | | | | | | | | -30 |
| | | | | | | | | | Sp | Sp | Sp | Sp | | | | | | | | -26 |
| | | | | | | | | | Sp | Sp | Sp | | | | | | | | | -22 |
| | | | | | | | | | | | | | | | | | | | | -18 |
| | | | | | | | | | | | | | | | | | | | | -14 |
| | | | | | | | | | | | | | | | | | | | | -10 |
| | | | | | | | | | | | | | | | | | | | | -6 |
| | | | | | | | | | | | | | | | | | | | | -2 |
| | | | | | | | | | | | | | | | | | | | | 2 |

### 4.4 CRR discussion

The resulting matrices can be evaluated from the statistical indices such as the *POD*, *FAR*, *CSI* and *EQ_PC*. A high *EQ_PC* parameter, greater than 40%, indicates that radar and satellite datasets are in accordance, the calibration process is equilibrated with respect to the number of radar and satellite points and resulting rainy cells in matrices have a significant rain probability. The best spatial correspondence is obtained for the Spanish 3-D array (table 4.5) due to the highest *POD*, *CSI*, *EQ_PC* and also the lowest *FAR*. In second place comes the Baltic 3-D matrix (table 4.6) by taking into account again the POD, FAR and CSI indices but with a low *EQ_PC*. This last factor may lend significance to the other three indices but unfortunately we are not able to quantify how much. Poor results are generated from the two 2-D arrays (table 4.3d and 4.4), where the Baltic Sea matrix should be considered with caution because it provides the worst statistical indices and the lowest *EQ_PC*. Correlation coefficients are around 0.4 for both 3-D matrices and around 0.3 for the 2-D arrays. These results suggest, as commented by Lovejoy and Austin (1979) and Cheng *et al.* (1993), that visible data in matrices can improve their accuracy for rain estimation purposes in regard to pure infrared methods. However, other negative factors may affect the rainfall estimation by taking into account visible radiances such as areas affected by shadows or extremely bright cloud zones due to direct reflections. Significant variations can be observed in the intensity of this visible radiation in the early mornings and in the late afternoons. These variations are produced in many cases by the effect of normalization of the visible pixels with cosine of the solar zenith angle in these hours of the day. In fact, noisy rainy spots with significant rain rate values during daytime are observed mostly when solar zenith angles are large. Under such conditions the normalisation process tends to over-measure visible cloudy brightness counts causing errors in the rain class extraction from the 3-D matrix. This effect can easily be avoided by limiting the use of the 3-D matrix to a smaller number of daytime hours; however this way increases the time for the employment of the 2-D matrix, which is less accurate.

One key question raised in this work was the selection of the calibration period to perform a long term calibration matrix. By selecting a considerable amount of radar and satellite data to develop the matrices over the Iberian Peninsula, statistical indices evolved into acceptable boundaries and rain classes have a tendency to converge to specific values and specific array positions. However, Baltic array classes have a tendency to drop to zero and to disperse to a broader distribution. That is presumably caused by different reasons: First, the geostationary satellite pixel is degraded due to remapping requirements in high latitudes. Second, the scarcity of convective rain cases in contrast to the stratiform over the Baltic area, even during the summer period, could be a negative factor in the calibration process. Stratiform precipitation is very difficult to be accurately detected from satellite and therefore radar and satellite rain rates do not match correctly causing a substantial drop in the probability of precipitation. A shorter calibration period seems to be important to develop the best Baltic arrays.

The present research confirms that $T_{WV}$ can exceed $T_{IR}$ in several degrees according to observations made by Schmetz *et al.* (1997). These special satellite measurements in which $T_{WV} > T_{IR}$ clearly corresponded to areas in our matrices where $T_{IR}$-$T_{WV} < 0$. Moreover, the highest rainfall classes are obtained in rainfall arrays for the coldest $T_{IR}$ and places in which $T_{IR}$-$T_{WV} < 0$ condition is satisfied (see tables 4.3d, 4.4, 4.8 and 4.9). This result is, also, in agreement with the work of Kurino (1997a) and shows the advantages in the use of brightness temperature differences between the 11 μm and 6.7 μm bands to detect deep convective clouds systems accompanied by heavy rainfalls.

Independent and qualitative studies not shown in this thesis report were performed for thin cirrus and stratiform clouds with precipitation over Spain. In the Baltic area the results of these studies were not definitive. The difference between $T_{IR}$ and $T_{WV}$ seems to be adequate to eliminate most of the cold thin cirrus clouds with no precipitation because we have observed that $T_{IR}$-$T_{WV}$ is greater than +3ºC for these kind of clouds and thus, they are outside the rain area in matrices. However, poor results for stratiform precipitation using CRR estimations are obtained. Stratiform rain cloud tops are not as cold as convective tops and stratiform radar rainfall signal are found, also, in the positive area in matrices where $T_{IR}$ and $T_{WV}$ difference are above or close to zero and rainfall probability is lower than the *EQ_PC* in most of cases (see table 4.3c). Other problems are related with radar rain pixels that are located outside the rain area as defined by the CRR matrices. In such cases the rain is probably produced by low clouds with warm cloud tops in the infrared band and/or with a $T_{IR}$-$T_{WV}$ great enough to be missed from the rain region of matrices.

The 3-D calibration table performed over Spain shows the greatest rainfall classes for high values of visible counts (*Vc* from 200 to 232 approximately). This can be explained taking into account that clouds with heavy convective cores and obviously, very thick, as studied by Vicente and Scofield (1996), are usually precipitating clouds in radar images and therefore they should be stored in the matrices as very bright clouds in the visible band. However, the 3-D matrix generated over the Baltic countries have smaller rain classes along lower visible brightness values (*Vc* from 168 to 204 approximately). This could be caused by two factors. Solar radiation impinges against the earth's surface and clouds with larger solar zenith angles in these high latitudes or the direct and reflected visible radiation has to pass through a longer atmospheric path, increasing energy absorption, before the satellite sensor is reached. The first factor should be corrected by the normalisation process of the visible pixel (Binder, 1988) but the second factor seems to be the most suitable for explaining any reduction of visible radiation over such high latitudes.

### *4.5 CRR conclusions*

In this chapter, a new convective version of the Rainsat Techniques is described. Long-duration probability and rainfall calibration tables were computed using a statistical method in which spatial correlations between radar and satellite images are performed. An analysis of the Meteosat information combined with radar is done to improve the rainfall area detection and rain rate estimations. Primarily, radar rainfall is ordered in rain, no rain and rain rate accumulation tables using satellite data as array coordinates. Secondly, after a statistical method, all the radar rainfall with a probability greater that the *EQ_PC* coefficient based on “stability criterion” methods is stored in 2-D and 3-D mean rain rate matrices.

Spectral calibration rainfall tables are generated for the north and south of Europe over the Baltic Sea and the Iberian Peninsula respectively. Statistical indices computed within each table help to determine that the best rain matrix was the 3-D one obtained over the Iberian Peninsula and the worst was the 2-D generated over the Baltic Sea.

Precipitation areas delimited via CRR are usually over-estimated with respect to radar rainfall. In addition, CRR points that correspond to maximum rain rates are slightly displaced with regard to radar maximum points. CRR images give a clear idea of the position and intensity of convective cores with heavy rainfall. Additionally, a significant spatial correspondence between radar rainfall and CRR estimates are observed in most cases. However, a numerical verification of CRR estimates including independent rain gauge measurements and radar over Spain and other places of Europe has been completed in sections 5.3 and 8.2 of the present document, and are important to evaluate errors in CRR rainfall estimates.

In general, matrices generated over the Iberian Peninsula have a mean convective rainfall value superior to those obtained for matrices over the Baltic Sea. Moreover, significant rainfall classes of the Spanish 2-D and 3-D arrays tend towards convergence in specific sectors of $T_{IR}$, $T_{IR}$-$T_{WV}$ and $Vc$ for a long calibration period. This feature was not observed in the Baltic Sea matrix. Rainfall classes tend to drop when the calibration period is too long. We have no explanation for this but it could be caused by the predominance of stratiform rain over convective.

Large temporal scale calibration tables as developed for CRR are useful in the operational context. These matrices are thought to have enough information to be employed in all kinds of convective meteorological events. Therefore, no further recalibration processes would be necessary, which is an advantage in computer processing. Satellite rainfall corrections, as described in the previous chapter of this work for A-E, could help to adapt CRR estimates to real conditions. However, an interesting experiment for scientific purposes, if radar data were available in real time, could be rapid updates of calibration tables for the coming hours. In chapter 8 a recalibration of matrices with radar seems to be necessary to improve the accuracy of CRR estimations for the Montserrat flood case.

New observations from satellite missions such as the Meteosat Second Generation (MSG), launched in August 2002, should improve the rain estimation algorithms situation, especially multi-spectral methods as CRR, through the use of observations from a 12-channel Spinning Enhanced Visible Infrared Imager (SEVIRI) sensor. In addition, the MSG provides 15-min image capture capability, enhancing the use of life history techniques with such data. At the present time the SAFNW project continues adapting the CRR method to the MSG satellite in the operational context. More information about this can be found in internet (http://nwcsaf.inm.es/) by searching CRR or PGE05 words.

## 5. Rainfall analysis of the Albanian case study

The Albanian event, which occurred from September the 20th to September the 26th 2002 with the heaviest precipitations happening on day 21, 22 and 23, is a clear example of a Mediterranean severe weather event with numerous small and steep river basins and highly populated areas affected by torrential precipitations. In addition, two important factors make this small country especially sensitive to such damaging episodes. The Albanian basin is opens to the west and, thus, to the Adriatic Sea where unstable weather systems pass regularly towards to the rest of the Balkan Peninsula. In addition, the east side of the country is surrounded by very high mountains of altitudes above 2000 m (figure 5.1), which increases the strength of such depressions. Secondly, at the time of writing this document, the lack of ground radars over the Albanian territory to monitor the precipitating systems approaching Albanian shores from the sea makes the use of remote sensing methods from satellite essential to the detection of heavy rainfall areas and to estimate the rain rates in real time with as much accuracy as possible.

This chapter presents results of daily rainfall estimates focused on the three days of heavy rainfalls from the 21st to the 23rd of September 2002. Estimated precipitations based on Meteosat-7 data and computed using various techniques developed for convective clouds are compared with ground observations. A single Infrared band technique known as Auto-estimator (chapter 3) and a three-channel Convective Rainfall Rate technique known as CRR (chapter 4) were considered. For both methods, a number of corrections, such as moisture, cloud growth rate, cloud top temperature gradient, parallax and orographic were performed and tested. Results show that the auto-estimator significantly over-estimates daily rainfall when compared with measurements taken on the ground whereas CRR gives more accurate estimates. The Auto-estimator power law curve was adjusted to the specific conditions using all the available measured rainfall intensities. A sensitivity test of correction factors for this flood case demonstrated that parallax, growth rate and orographic corrections can improve the delineation of satellite daily rainfall areas in the observed pattern, while the Auto-estimator curve calibration produces sensible changes on rainfall amounts.

The Numerical Mesoscale MM5 Model nestled within the grid analyses from the European Centre for Medium Range Weather Forecast (ECMWF), was employed to carry out a brief synoptic analysis of this case and to generate the precipitation water (PW) and relative humidity (RH) fields used to compute the moisture correction factor, as well as to provide the 850 hPa wind vector fields needed to calculate the orographic correction factor.

The Auto-estimator and CRR techniques are applied to this specific Albanian event to compute daily rainfall fields. In addition 6 satellite rainfall corrections are evaluated against surface observations for the 3 days with the largest accumulated precipitation of the period.

In contrast to CRR, the Auto-estimator algorithm in its original form has a strong tendency to over-estimate daily rainfall. This feature suggests that each convective episode has its own characteristics and the Auto-estimator cannot be considered as representative of the geo-climatic conditions of the study area. Consequently a straightforward procedure was performed to adjust the calibration coefficients of the infrared power-law curve using all available rain gauge measurements.

Any developed satellite rainfall method and later correction must be verified against appropriate in-situ measurements taken over the region of interest. Different verification methodologies have been applied by Marrocu *et al*. (1993) for Sardinia, Oh *et al*. (2002) for Korean peninsula, Menz (1997) for east Africa and Vicente et al. (1998) for areas in central US. The majority uses coarse grids of 0.25ºx0.25 or 0.50ºx0.50º or 1ºx1º resolution in order to minimize the strong spatial variability of rain rates and hourly precipitation. Some difficulties are compounded in this case with respect to verification. Firstly, as commented before, operative radars are still not installed and only 8 rain stations from 115 can provide rain rates. Secondly the verification could be completed using daily precipitation measurements from around 80 of the 115 available stations distributed over Albania. Fortunately daily measurements are much less sensitive to spatial and temporal variations of the precipitation and therefore the verification can be simplified as explained in the next subsection.

### *5.1 Datasets and study methodology*

#### *a) Dataset description*

The Meteosat-7 datasets used in this work are: infrared brightness temperature in Kelvin $T_{IR}$(K), infrared water vapour band in Kelvin $T_{WV}$(K) and the visible channel in brightness counts. The Meteosat datasets, provided by the INM, were produced by EUMETSAT in images every 30 minutes with a pixel spatial resolution over Albania around 7 by 7 km lat-lon. All satellite rainfall processing shown in the present chapter is performed on this spatial resolution. They were resized to 300 lines by 300 columns and centred in 40ºN 12.4ºE. The period of the satellite dataset used in this study was from 0000 UTC September 21 to 2330 UTC September 23.

Ground rainfall rates in mm $h^{-1}$ recorded every 30 minutes from 0100 to 2330 UTC by 8 stations during the three days of the flood case (see black boxes in figure 5.1). On September 21st only 6 stations of these have provided data, while the next day all the 8 stations were working properly but on September 23 the data of only 5 stations could be employed for this research. These rain rates were used for the infrared curve calibration process as described in section 5.4.

Rainfall accumulations in 24 hour period obtained between 0000 to 2400 UTC from September 21st to the 23rd by 115 stations in Albania. However only 81 were finally used after a supervised quality check (see white and black boxes in figure 5.1). These daily datasets were used for the verification of algorithms and the sensitivity test of rainfall corrections.

Grid analyses from the ECMWF are used to run the MM5 simulation. They have a 0.3º by 0.3º lat-lon resolution and are available every 6 hours from 0000 UTC September 21st to 0000 September 24th.

### *b) Study methodology*

In situ daily rainfall measurements from the 81 stations are interpolated by a "kriging" analysis method using the linear model for the variogram fit. This minimal error variance method is recommended for irregular grids with relatively low number of observations (<250) and has been widely used to compute rainfall fields from rain gauges (Krajewski 1987, Seo 1998, Bhagarva and Danard 1994). In the Albanian region as in many others, mountain areas are not well covered by the meteorological stations therefore daily precipitation may be under-estimated in these mountainous places. After careful supervision of the data analysis process, the resulting kriged daily rainfall fields obtained from the rain gauge measurements were, in our opinion, correctly delineated over these complex terrain areas. The interpolated rainfall fields are then remapped to a satellite projection and resolution for the three days of the flood case in order to facilitate visual and numerical comparisons with respect to the MM5 and satellite estimations.

In previous studies the verification has been performed using coarse grids of 0.25ºx0.25 or 0.50ºx0.50º or 1ºx1º resolution in an attempt to minimize the high spatial variability of rain rates and hourly precipitation measurements (Marrocu *et al*. 1993; Oh *et al.* 2002; Vicente *et al.* 1998). In the present research the “kriging” option has been selected because it allows a pixel by pixel comparison which is suitable for studies in small areas such as the Albanian territory. Other important reasons are: firstly, daily measurements are much less sensitive than rain rates and/or hourly fields to the spatial and temporal variations of the precipitation and, secondly, the Albanian rain gauge network (figure 5.1) is dense enough to capture the most important daily rainfall patterns in such a severe event.

The A-E computes rainfall rates based on a fixed, non-linear, power-law relationship as described in chapter 3. However before the algorithm was applied, cirrus cloud pixels with a low probability of rain, are filtered using the empirical slope test developed by Adler and Negri (1988). A qualitative study not shown in this report has illustrated to us that this simple process applied to infra-red images can detect cold pixels from homogeneous cloud top surfaces suspected of being non precipitating cirrus. These pixels are observed mostly in clouds that are moving but not growing and developing as occurred to convective. The method is simple, for each point *Po* an empirical slope *S* and a kind of temperature gradient *Gt* are computed in a window of 25 pixels centred in the point *Po*. The terms *Gt* and *S* are given by the following equations:

$$Gt = T_{avg} - T_{min} \tag{5.1}$$

$$S = 0.568(T_{min} - 217) \tag{5.2}$$

where $T_{min}$ is the local minimum and $T_{avg}$ is the average temperature in the grid of 5 by 5 pixels. A large *Gt* indicates convective clouds, a small *Gt* a weak gradient associated with cirrus clouds within the window. Pixels having *Gt* less than *S* are classified as cirrus clouds and therefore, considered as non-precipitating points with 0 mm $h^{-1}$.

Concerning the CRR algorithm; the 2-D and 3-D matrices developed over the Iberian Peninsula and shown as a table 4.3d and 4.5 respectively are used in the Albanian flood study. We are interested in a CRR algorithm evaluation in a place different from the one where matrices were tuned. However, both regions, the Iberian Peninsula and Albania, are located on similar latitudes in Europe. Visible counts from Meteosat images have to be normalized using the solar zenith angle (Binder, 1988) before the 3-D matrix is used to estimate the rain rate in a point. To avoid problems during the transition from night to day and from day to night, the use of the 3-D matrix has been limited from 0700 to 1500 UTC (daytime in Albania in September). The rest of the time has been employed by the 2-D matrix which only needs brightness temperatures from the two infrared bands.

Satellite rainfall images estimated from the different methods are rain rate fields in mm $h^{-1}$ units. Daily precipitation images are then computed using equation 5.3. It represents the numerical integration of rain rates each 30 minutes throughout a 24 hour period.

$$DP(x, y) = \sum_{t=1}^{48} IP_t(x, y) \cdot 0.5 \qquad (5.3)$$

where $DP(x,y)$ is the daily rainfall at image coordinates $(x, y)$ and $IP_t(x, y)$ is the rain rate every 30 minutes at that point.

MM5 accumulated rainfall in 24 hours is also remapped for each of the three days in order to test the accuracy of the numerical model simulation (see MM5 sets in the next subsection). Observed and estimated daily rainfall fields from satellite and MM5 are compared in a qualitative and quantitative manner. For the quantitative verification, common statistical indices such as the difference between the estimated and the observed spatial averaged daily precipitation (BIAS), root mean square errors (RMS) and Pearson correlation coefficient (CORR) are calculated in the area limited by kriging analysis derived from the rain gauges.

As illustrated in section 5.3, results show that A-E over-estimates strongly the daily precipitation and therefore the infrared power law curve was adjusted for the specific conditions by an experimental calibration process as described in section 5.4. Finally, A-E, CRR and calibrated A-E rainfall were corrected by moisture, cloud growth rate, cloud top temperature gradient, parallax and orographic and a sensitivity study was carried out.

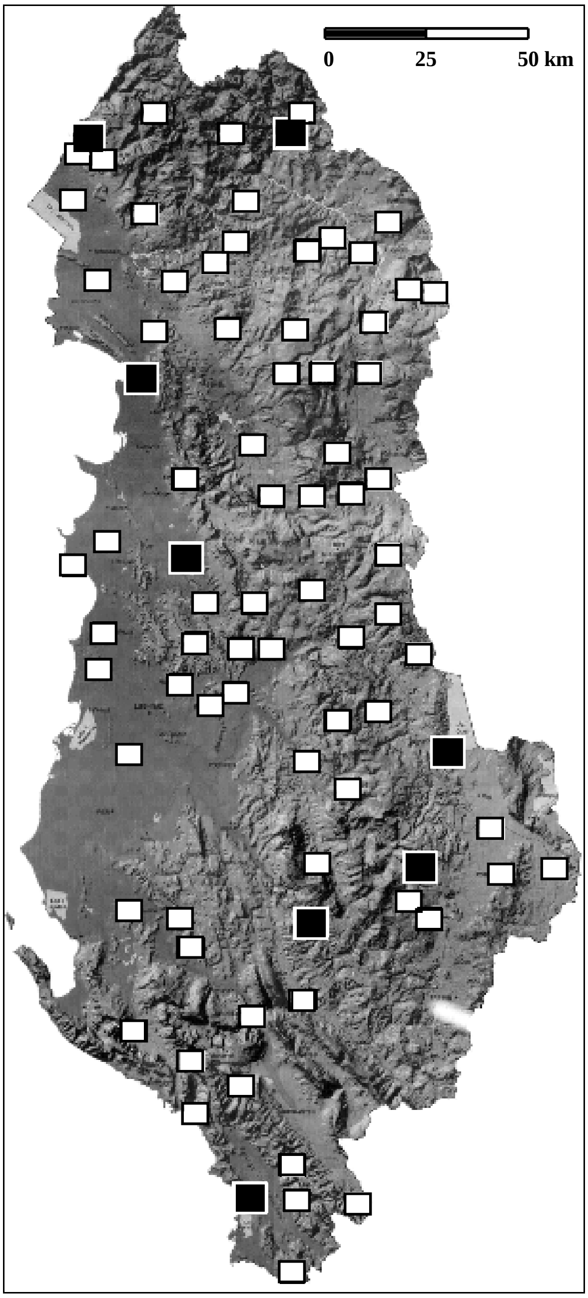

Figure 5.1. Albanian terrain and meteorological stations. White boxes represent daily rainfall measurements and black boxes daily measurements and rain rates. The territory is very irregular in general, but the highest mountains, above 2300 m, are found in the north and in the south of the country.

### *5.2 Case of study, MM5 settings and Synoptic description of the flood case*

*a) Case of study*

September 2002 was characterized by frequent stormy episodes with heavy rainfalls that have affected most of the Albanian territory. The present episode during the end of the month is atypical owing to three crucial aspects: the extreme rain rate, the intense precipitations extended period of 3 consecutive days with short interruptions and the high social impact caused by the resulting floods. The most intense precipitations were registered during late 22nd and first hours of 23rd, affecting northern and southern Albania, respectively. During the 22nd, the recorded 24h-accumulated rainfall amount exceeded 160 mm in many rain gauges of the region, which almost doubles the monthly average of the last 50 years. Cloud convection was prominent in the Meteosat 11µm infrared images during the 22. An intense semi-stationary convective system with extremely cold tops with minimums brightness temperatures below 205 K was observed over the north of the country during this day.

### *b) MM5 settings and Synoptic overview*

In order to capture the accumulated rainfall patterns and important mesoscale details of the episode, a 72 hours control simulation is set up using the MM5 model, beginning at 0000 UTC September 21st 2002. Three interacting domains under a Lambert Conformal map projection were used. The coarse one has 140 x 140 x 24 grid points and measures 5004 x 5004 km (grid length 36 km) and has numerical outputs every 6 hours; both the middle and fine domains have 151 x 151 x 24 grid points every 3 hours. The intermediate measures 1800 x 1800 km (grid length 12 km) and the fine domain measures 600 x 600 km (grid length 4 km) every 30 minutes. The three domains are centred at the region affected most by heavy rains over Albania. It was decided to use only the fine domain outputs to perform the moisture (PWRH) and orographic (OC) correction factors after a test not shown in this document. In this study the PWRH correction factor field was computed using MM5 numerical outputs from the coarse (6 hours, 36 km) and intermediate (3 hours, 12 km) domains. Corrected A-E daily rainfall using this PWRH factor from both domains was numerically verified using daily observations. The performance of the correction in both cases was sensibly lower than employing the numerical outputs corresponding to the higher resolution domain (30 min, 4 km).

The event developed under a synoptic pattern characterized by a large-scale ridge at mid-upper troposphere levels, which remained stationary during the event over the north Atlantic, west of the British Isles. This high pressure centre split the mid latitude westerly into two jet streams, one associated with a cold short-wave positively-tilted trough developing over Europe and a southern jet stream associated with a secondary trough identified over the western Mediterranean and south Iberian Peninsula (figure

5.2a). The second jet is extended towards the east coast lands of the Adriatic, reaching the area of study during the 22nd of September (figure 5.2b).

At low levels, a large area of anticyclone flow offshore of Libya favoured the eastward advection of warm and moist Mediterranean air towards Albania, reinforced by the cyclonic flow associated with an incipient Alpine lee cyclone (figures 5.2c and 5.2d).

In the hours that followed, the main mid-upper level cold trough progressed to the south-east bringing strong mid-level winds over the Adriatic (figures 5.3a and 5.3b). The secondary mid-upper level trough advanced eastward merging with the main system and reinforcing the strong south-westerly flow over the southern Adriatic and Ionian Seas. At low levels, the persistent westerly flow impinging Albania is reinforced by the confluence of flows associated with three different systems. First, the Alpine cyclone deepened and intensified the associated maritime westerly flow; next, the anticyclonic area centred over Libya remained almost stationary and finally, the Algeria mesocyclone progressed east, bringing southerly warm air to the confluence zone (figures 5.3c and 5.3d). This continuous supply of warm and moist air at low levels over Albania conduced to a convectively unstable environment that leaded to heavy rains over Albania during 22 and the second half of 23 September 2002.

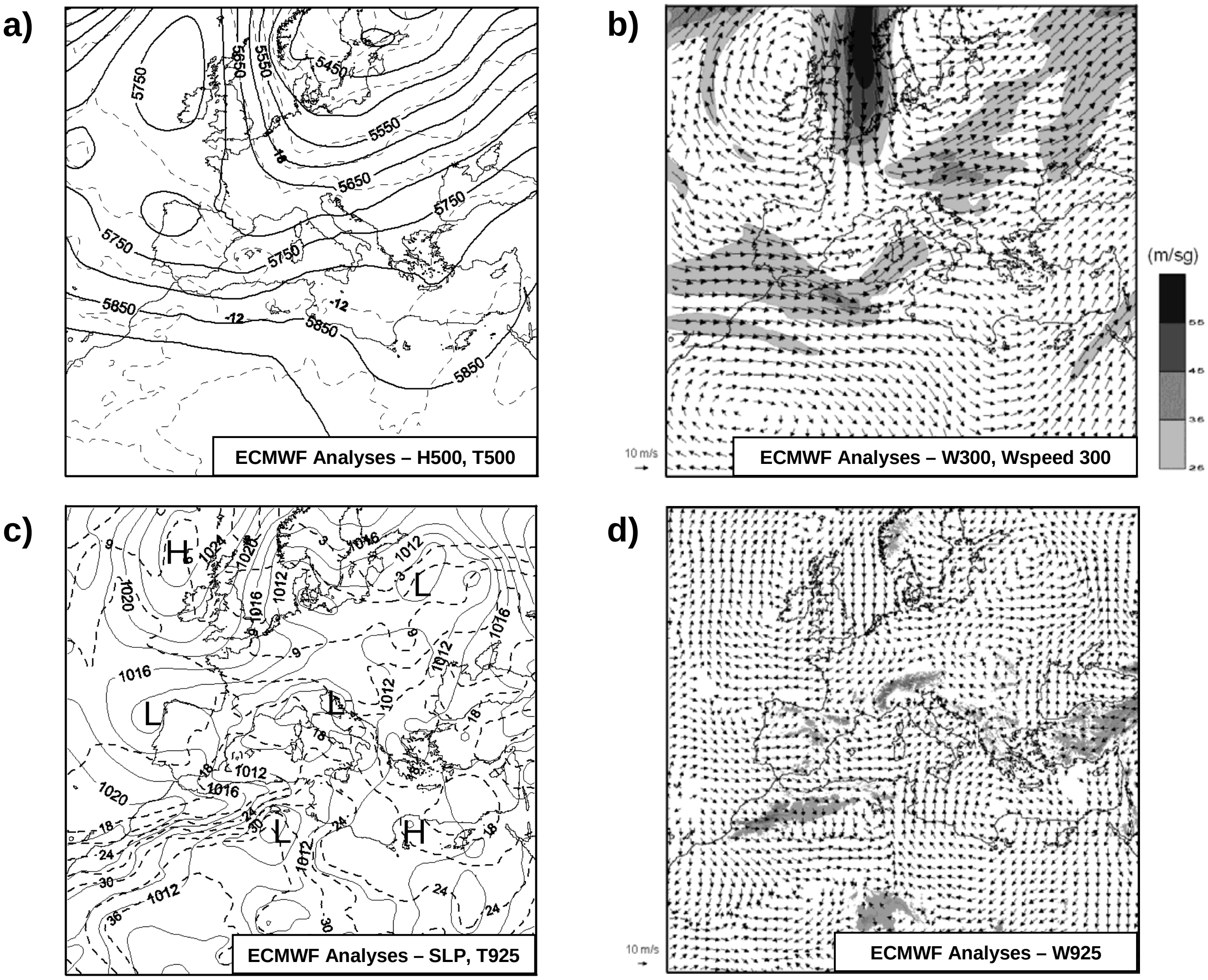

Figure 5.2. ECMWF map analysis at 0000 UTC 22 September 2002 showing: (a) Geopotential height at 500 hPa (continuous line, in gpm) and temperature at 500 hPa (dashed line, in ºC), (b) Horizontal wind (vectors) and wind speed (shaded according to scale, in $ms^{-1}$) at 300 hPa, (c) Sea level pressure (continuous line, in hPa) and temperature at 925 hPa (dashed line, in ºC) and (d) Horizontal wind (vectors) at 925 hPa.

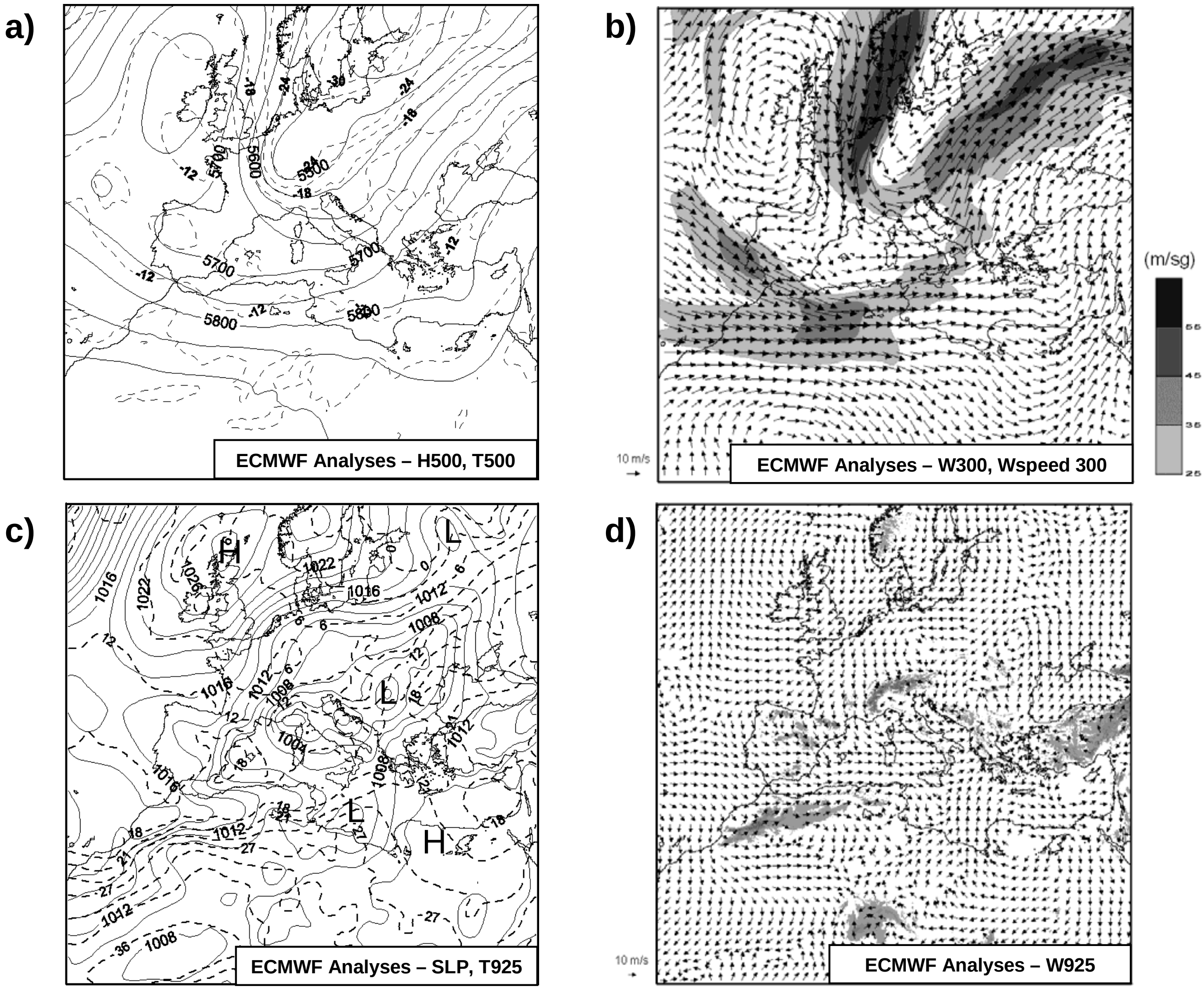

Figure 5.3 ECMWF map analysis at 0000 UTC 23 September 2002 showing: (a) Geopotential height at 500 hPa (continuous line, in gpm) and temperature at 500 hPa (dashed line, in ºC), (b) Horizontal wind (vectors) and wind speed (shaded according to scale, in m $s^{-1}$) at 300 hPa, (c) Sea level pressure (continuous line, in hPa) and temperature at 925 hPa (dashed line, in ºC) and (d) Horizontal wind (vectors) at 925 hPa.

### *5.3 Results of Auto-Estimator, CRR and MM5 daily rainfall*

A-E, CRR and MM5 daily rainfall are qualitatively and numerically verified against the observed interpolated daily precipitation. Gauge measured daily rainfall, original A-E, CRR and the MM5 model daily precipitation for the days 21, 22 and 23 September are displayed in figure 5.4, while statistical analysis taking in account zero pairs are shown in table 5.1. Both are illustrated at the end of this subsection.

On the first day most of the observed rainfall is confined to a small area on the north of Albania. Satellite and MM5 precipitation overlap, in general, areas of observed rainfall as shown in figure 5.4. In addition estimations provide relatively high correlation indices (CORR) compared to the other two days (Table 5.1). The maximum gauge measured rainfall is 130 mm (figure 5.4a) while A-E over measures this quantity with a maximum around 250 mm (figure 5.4d). Besides, CRR and MM5 estimate maximum daily amounts of 80 and 100 mm, respectively (figures 5.4g and 5.4j). Table 5.1 shows that A-E obtains the greatest CORR and the lowest BIAS while CRR has the lowest RMS (Root Mean Square Error).

The 22nd is the day of the heaviest precipitations, with two observed maxima over the territory (figure 5.4b). The strongest one located in the North of Albania with 200 mm and another one weaker in the south with 150 mm. Both values can not be directly observed in figure 5.4b because the plotting method using level curves produces a smoothed effect over the daily rainfall maps. In general, the three algorithms delineate the greatest accumulations a bit displaced to the north with respect the observed rain area. None of these methods detect the observed maximum located in the south of Albania. A-E is out of range with a maximum daily precipitation around 1000 mm as clearly illustrated in Figure 5.4e. CORR indices are significantly lower than one day before as shown in table 5.1, but here it can be observed that A-E has the largest CORR but also a huge BIAS error, and the worse RMS. The CRR has the lowest BIAS index and the MM5 obtain the lowest RMS but also the worse CORR.

The day of the 23rd is probably the most difficult one for satellite and MM5 rainfall estimation. Most of the observed rainfall occurs in the south of Albania with a main accumulation of 135 mm in 24 hours and a secondary daily maximum of 85 mm in the north coast (figure 5.4c). Satellite algorithms, in general, over-estimate the rainfall area but overlap the strongest observed accumulations in the south of the territory (figures 5.4f and 5.4i). The A-E is again out of range with an estimated main accumulation of 450 mm and the MM5 forecasts around 440 mm in 24 hours but mostly over the centre of the country (figure 5.4l). Low correlations for the three algorithms with respect to previous days are shown in Table 5.1 however, CRR gets the lowest BIAS and RMS.

Results vary significantly from one day to another after an analysis of the statistical indices in table 5.1. In order to gain a general view, global indices are computed and shown in the final 6 rows of the table. They are calculated taking in account estimated and observed points for the three days of the flood case. Now A-E provides, in general, the best CORR but also clearly over-estimates daily precipitation with the highest RMS and BIAS. The CRR and MM5 give much more adjusted daily precipitation amounts, according to the low BIAS, however the MM5 has a significant RMS and the lowest CORR.

Table 5.1 Results comparing A-E, CRR and MM5 with Observed daily rainfall. The Size box is the number of pixels over the region affected by the episode on each day. Mean, SD (standard deviation), BIAS and RMS (root mean square error) are in mm. Boldfaced numbers show best statistical results in every line. The last six rows are statistical results for the three days collected.

| | OBS | A-E | CRR | MM5 | Day |
|---|---|---|---|---|---|
| Size | | 2055 | | | 21 |
| Mean | 22.4 | 33.9 | 8.3 | 10.3 | |
| SD | 27.6 | 57.8 | 16.6 | 21.7 | |
| BIAS | | **11.6** | -14.0 | -12.1 | |
| RMS | | 47.9 | **26.8** | 30.7 | |
| CORR | | **0.61** | 0.57 | 0.36 | |
| Size | | 2777 | | | 22 |
| Mean | 44.2 | 268.6 | 53.7 | 24.9 | |
| SD | 36.5 | 274.4 | 56.7 | 36.5 | |
| BIAS | | 224.4 | **9.5** | -19.4 | |
| RMS | | 346.7 | 57.9 | **49.2** | |
| CORR | | **0.34** | 0.31 | 0.14 | |
| Size | | 1867 | | | 23 |
| Mean | 36.5 | 183.3 | 45.3 | 85.6 | |
| SD | 29.9 | 125.2 | 33.2 | 110.2 | |
| BIAS | | 146.8 | **8.7** | 49.0 | |
| RMS | | 191.5 | **41.5** | 136.7 | |
| CORR | | 0.19 | 0.17 | **-0.49** | |
| Total Size | | 6699 (2055+2777+1867) | | | 21, 22, 23 |
| Mean | 35.4 | 172.8 | 37.4 | 37.3 | |
| SD | 33.5 | 215.3 | 46.0 | 70.0 | |
| BIAS | | 137.5 | 2.1 | **1.9** | |
| RMS | | 246.5 | **45.7** | 80.6 | |
| CORR | | **0.39** | 0.37 | -0.10 | |

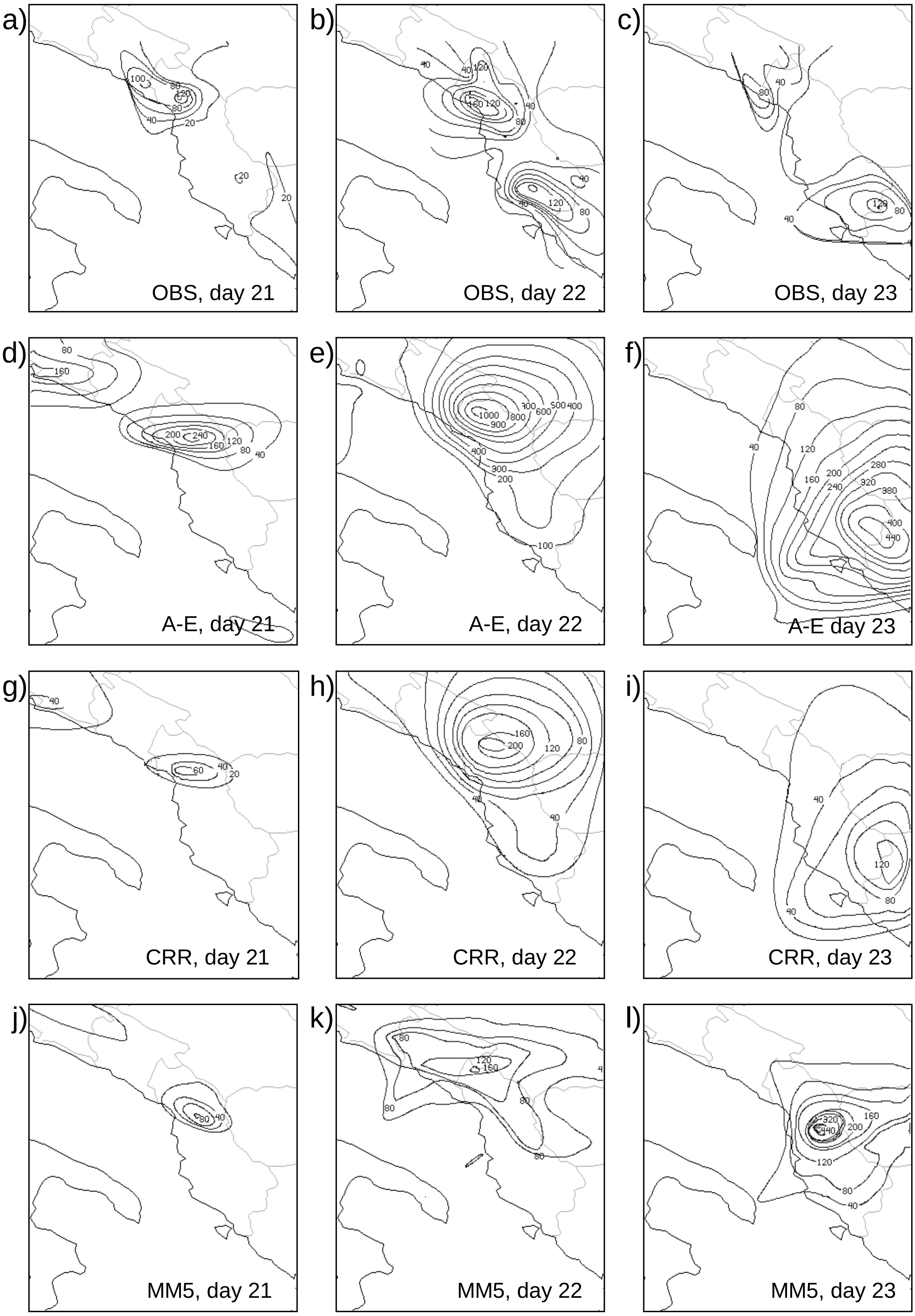

OBS, day 21
OBS, day 22
OBS, day 23
A-E, day 21
A-E, day 22
A-E day 23
CRR, day 21
CRR, day 22
CRR, day 23
MM5, day 21
MM5, day 22
MM5, day 23

Figure 5.4. Daily rainfall in mm for each day of the flood case. From (a) to (c): measured by the 81 stations, spatially interpolated and remapped to satellite projection and resolution, (d) to (f): estimated by A-E, (g) to (i) estimated by CRR and (j) to (l) simulated by the MM5 numerical model, remapped, also, to satellite projection and resolution.

### *5.4 Calibrating satellite measurements with rain gauges*

The A-E in its original form over-measures daily rainfall in the three days of the case of study. Additionally, as illustrated also in the next section 5.5, rainfall corrections applied over original A-E do not mend the high-bias problem between estimated and observed. The calibration procedure tries to adjust the A-E power law relation to the reality of the rainfall case by computing a new infrared-rain power law curve. In addition, it is interesting to explore new calibration possibilities of satellite measures directly from rain gauges. In many previous works meteorological radars were used as so-called “ground true” in order to complete this kind of experiments. Radars can provide accurate rain fields that would be very beneficial in our case but they produce other problems like ground echoes, beam overshoot or technical instabilities that makes it management complex in certain cases. The fact that the radar step could be skipped can simplify the calibration problem. As mentioned previously, radar images were not available for the Albanian territory at the time of writing.

The first calibration task is the association in time and space of every rain rate value in mm $h^{-1}$ from the Albanian rain gauge (figure 5.1) with the corresponding 11µm cloud temperature pixel measured from the satellite but corrected previously by parallax. In the three days of the flood with 8 stations providing rain rates in which 6, 8 and 5 of them were fully operative the days 21, 22 and 23 respectively, a total of 874 measurements were captured each 30 minutes. However, some anomalous ground rain measurements and satellite pixels are detected and skipped from the calibration process. These errors were mostly bad records of rain rates, small number of satellite images that were missed, few pixels affected by errors in the parallax correction and satellite points warmer than 290 K and therefore, not being considered. A total of 252 anomalous points were not used which remains 622 useful measurements including no rain points with 0 mm $h^{-1}$.

From this stage it was developed two different calibration methods called A-Ec1 and A-Ec2. Both compute mathematical power law relations like the A-E equation shown as 3.1 by using the calibration dataset (622 points) but applying different procedures as described in the following sections.

*a) A-Ec1*

Something approximating the Vicente *et al.* (1998) method is reproduced but using rain gauge measurements instead of radar pixels. The 622 rain rates are ordered depending on their satellite infrared temperature as shown in figure 5.5a. As observed, most of the rain points are related to cold temperatures $T_{IR}$ < 235 K meaning that the association process was correctly executed in our opinion. The next important step is the definition of an optimum interval of temperatures in order to calculate various magnitudes in each one such as: mean rain rate, standard deviation and number of points. This interval depends inversely on the size of the calibration dataset, therefore it would smaller if the number of points considered in calibration is larger. For example, Vicente *et al.* (1998), using radar images established 1 K size interval for a calibration dataset with 6800 points. In our case with only 622 points with a very irregular distribution as shown in the figure, we have set a criterion based on a minimum of 15 mandatory points in each interval. The result is an 8 K size interval from 200 K to 296 K (figure 5.5). Mean rain rate value shown as empty small box in figure 5.5a is calculated for every interval, these are connected with dashed lines forming a discontinuous curve. In addition to the minimum number of points criterion is important to configure a smooth discontinuous curve made with the mean rain rate values that should be diminishing with respect the increase of the satellite temperature. In each interval it is calculated the standard deviation to have an idea of the variability the mean point and they are shown in figure 5.5a as the black boxes connected by dashed lines.

The next step is to plot the mean points in the logarithm scale and select the best ones in order to compute a regression straight line. In first place the rain sector of the graph goes from 200 K to 260 K in view of the discontinuous mean curve in figure 5.5a with mean values greater than 0 mm $h^{-1}$ in each interval. This sector is plotted in the logarithmic scale in figure 5.5b where the points in the red circles are the ones used to perform the best fit regression line. These points are selected firstly because they are not in touch with the rain sector borders and secondly because they do not have an extremely high standard deviation with respect to the mean value. For example, the second point counting from the right side to the left in figure 5.5b has a mean value of 1 mm $h^{-1}$ as shown in the previous figure 5.5a but also a standard deviation of 4 mm $h^{-1}$ as illustrated in the same figure. This mean rain rate with a standard deviation 4 times greater is not substantial enough, in our opinion, to be included in the regression fit. The best line-fit in the logarithm scale derived from the five points inside the red circles is:

$$\log (R) = - 0.0929\, T_{IR} + 21.742 \qquad (5.4)$$

where the correlation coefficient for the fit is r = 0.94. This relation is transformed to rain rate in mm $h^{-1}$ in function of the satellite temperature in K by inverting the logarithm.

$$R = 2.7697\ 10^{9}\ exp(-0.0929\, T_{IR}) \qquad (5.5)$$

This curve from relation 5.5 is plotted by a solid line in figure 5.5a as the regression curve. Rain rates estimated from this relationship are called A-Ec1 in the following.

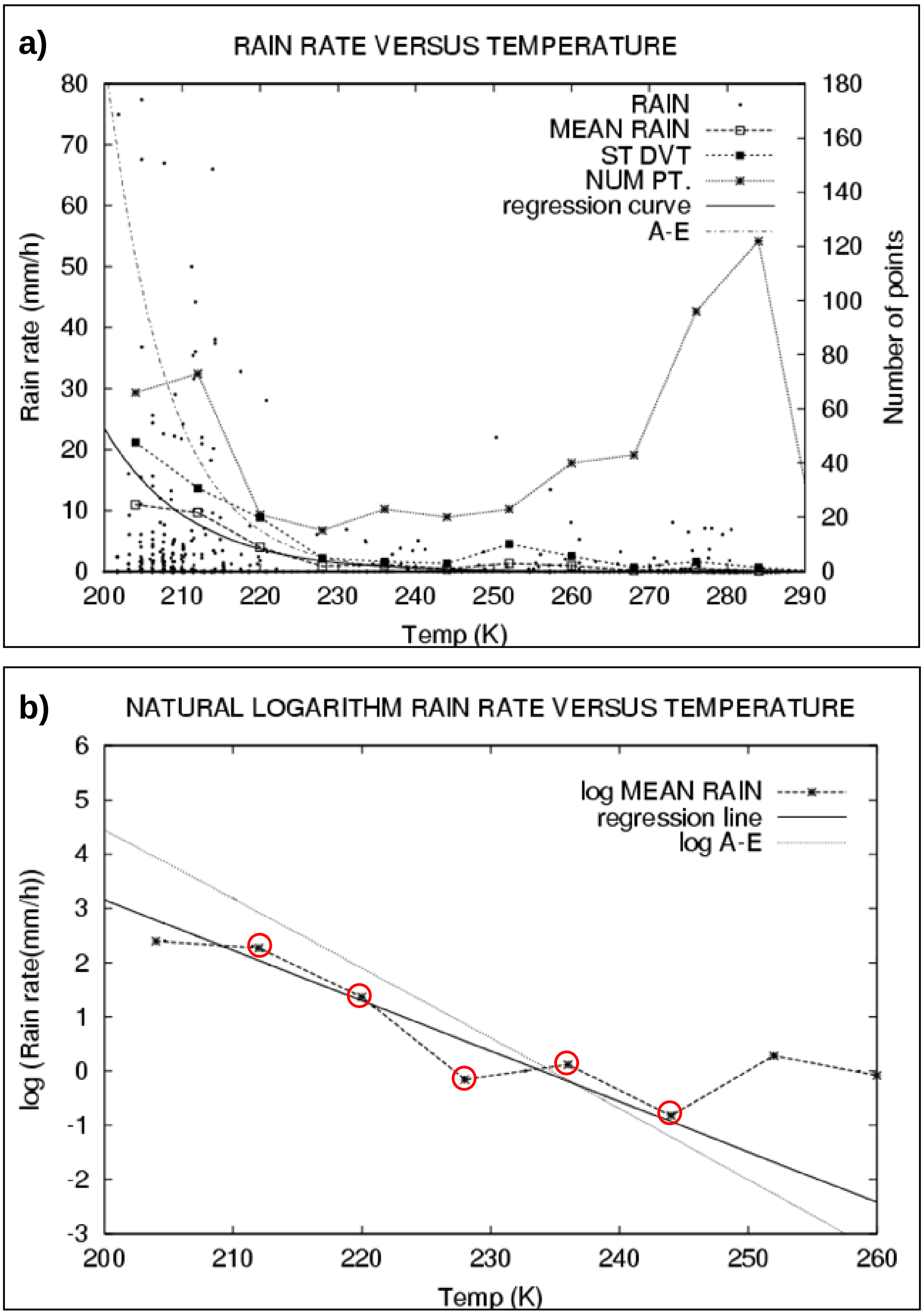

Figure 5.5. Rainfall curve calibration by the A-Ec1 method for the three days of the flood case. (a) Rain rates from Albanian rain gauges versus satellite temperatures. Mean rain rate, standard deviation and number of points for each 8 K interval. New rainfall curve derived from the A-Ec1 regression method plotted as a continuous curved line and shown as equation (5.5) in text. A-E original curve (dashed line) shown to facilitate visual comparison with the new regression curve. (b) Rain sector of the graph but in the logarithm scale. Mean rain rate points into the red circles used to calculate the regression line shown as equation (5.4) in the text.

*b) A-Ec2*

The second calibration method tries to select the most qualitative and convective rain rate points from the 622 that still remains. With the resulting ones it is performed a direct regression fit again in the logarithm scale. The process is done according to the following steps:

- Step 1. Rain Intensities associated to relatively warm satellite points ($T_{IR}$ greater than 240 K) are removed from calibration. As viewed in figure 5.5a, mean rain rates are almost zero for satellite temperatures greater than 240 K. A total of 326 points in which the 88% of them are 0 mm $h^{-1}$, are removed and 296 useful points remain.
- Step 2. Cold infrared points ($T_{IR}$ below 240 K) in which $T_{IR}$ is increasing with time are also removed. This process was made taking in account the cloud displacements in satellite images, as explained at the end of section 3.2 for the GR2 correction. A total of 108 points are warming with respect the previous satellite observation and therefore not considered in calibration.

A consequence from a straightforward association of data from very different origin and nature as satellite radiances against ground rain rates, are the generation of anomalous ($T_{IR}$ , R) points. In those, very low $T_{IR}$ pixels are linked to R with little or no rain and on the other hand, warm $T_{IR}$ pixels are associated to R with significant rainfall intensity. At this point many points are removed after the previous two steps (404) and the rest (218) are probably representative but also a scarce sample. Few anomalous pairs can affect negatively to the calibration and should be removed using the next simple criteria:

- Step 3. If $T_{IR}$ is smaller than 215 K and the observed rain intensity is smaller than 1 mm $h^{-1}$ the point data is not considered in calibration. 78 points are eliminated after this step.
- Step 4. If $T_{IR}$ is greater than 230 K and the observed rain intensity is greater than 1 mm $h^{-1}$ the point data is not considered in calibration. Only 6 points are removed.

Remained points are plotted against $T_{IR}$ in figure 5.6, where, the frame on the top corresponds to the natural logarithm of rain rates measured by the rain gauges versus $T_{IR}$ and, on the bottom, direct rain rates against $T_{IR}$ are represented. The distribution of points is nearly linear in the logarithm graphs and, even though some of the points are a bit spread out, a linear regression fit is performed. The logarithmic rainfall line is obtained using all the retrieved ($R$, $T_{IR}$) points ($N^oPt$ =104) from the three days of the flood as shown by the thick line in frame 5.6a corresponded to the fit equation with a correlation fit ($r$) equal to 0.31. The rain rate curve is then calculated by just inverting the logarithmic linear relation, which results equation (5.6) as follows and plotted, also, in figure 5.6b within the original A-E curve.

$$R = 6.171\ 10^{14} exp(-0.155\ T_{IR}) \qquad (5.6)$$

where $R$ is rain rate in mm $h^{-1}$. Precipitation computed using the power law relation (5.6) is called ‘A-Ec2’ in the present study.

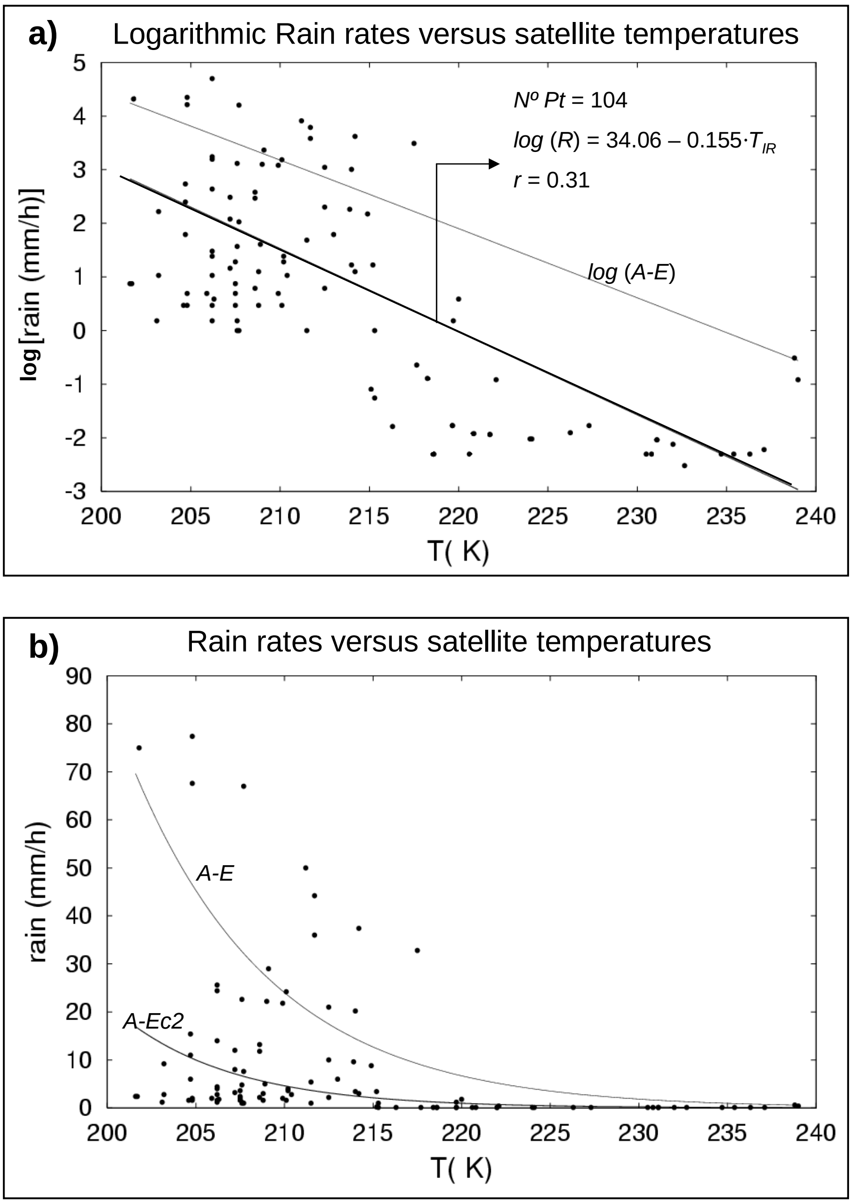

Figure 5.6. Rainfall curve calibration by the A-Ec2 method for the three days of the flood. (a) Natural logarithm of rain rates in mm $h^{-1}$ versus satellite 11 μm band brightness temperature in Kelvin for points not removed by the method. The solid black line is the best fit regression line while the other is the original A-E in the logarithmic scale shown as example. (b) Direct rain rates versus satellite temperatures (points) and rainfall curves from A-E (equation 3.1) and the new one A-Ec2 (equation 5.6).

### *5.5 Results of the new infrared rain curves*

The two new rainfall curves (A-Ec1 and A-Ec2) are compared with respect to the original A-E as shown in figure 5.7. It is clear that the A-E estimates higher rain rates than the other two curves while the A-Ec2 produces the lowest one. In fact, daily satellite estimates by the new curves for each day of the flood case, as illustrated in figure 5.8, show clearly that A-Ec1 produces bigger daily accumulations than A-Ec2. However compared to the original A-E in frames 5.4d, 5.4e and 5.4f the daily amounts from A-Ec1 and A-Ec2 are substantially lower as logical but the distribution of rainfall is quite similar. Therefore calibration tasks have an overall effect on the rainfall amounts and keep the rain areas unchanged with respect to the standard algorithm. Consequently, by comparing numerically the daily estimations from new curves with the rain gauge fields (frames 5.4a, 5.4b and 5.4c) CORR indices should be almost the same as the A-E ones that occur (see table 5.2), while BIAS and RMS indices should be reduced. Taking into account the results from these last two indices shown in table 5.2, the A-Ec2 is the infrared curve that generally produces the best daily rainfall estimates with respect the observations. However on the 21st, in spite of the best correlation coefficient (0.62), the A-Ec2 curve generates the strongest under-estimation of daily precipitation given by a clear negative BIAS (-16.4) in this table.

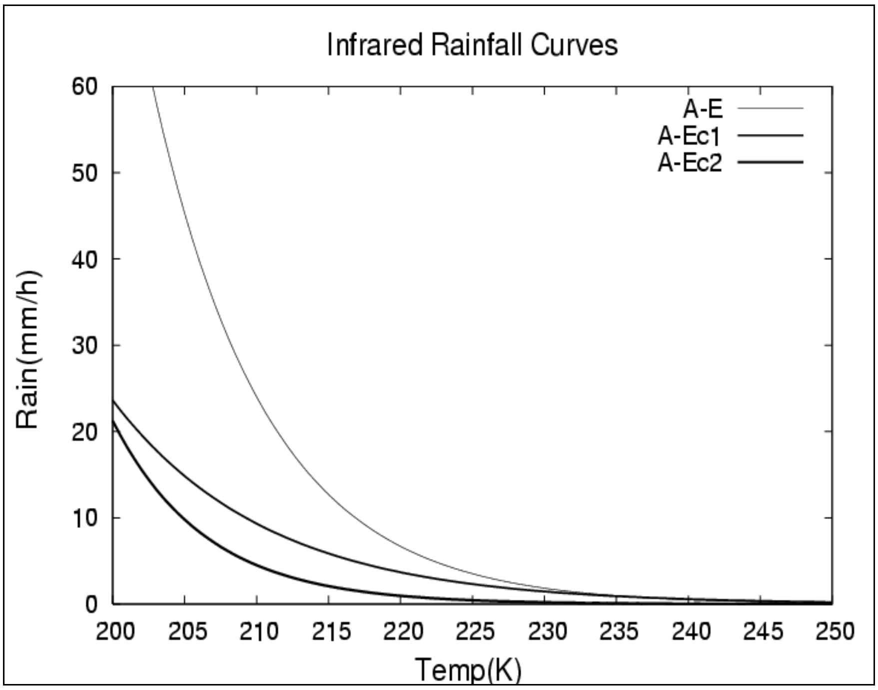

Figure 5.7. Infrared rainfall curves corresponded to the original Auto-Estimator (A-E equation 3.1) and the new methods developed in this work (A-Ec1, equation 5.5, and A-Ec2, equation 5.6).

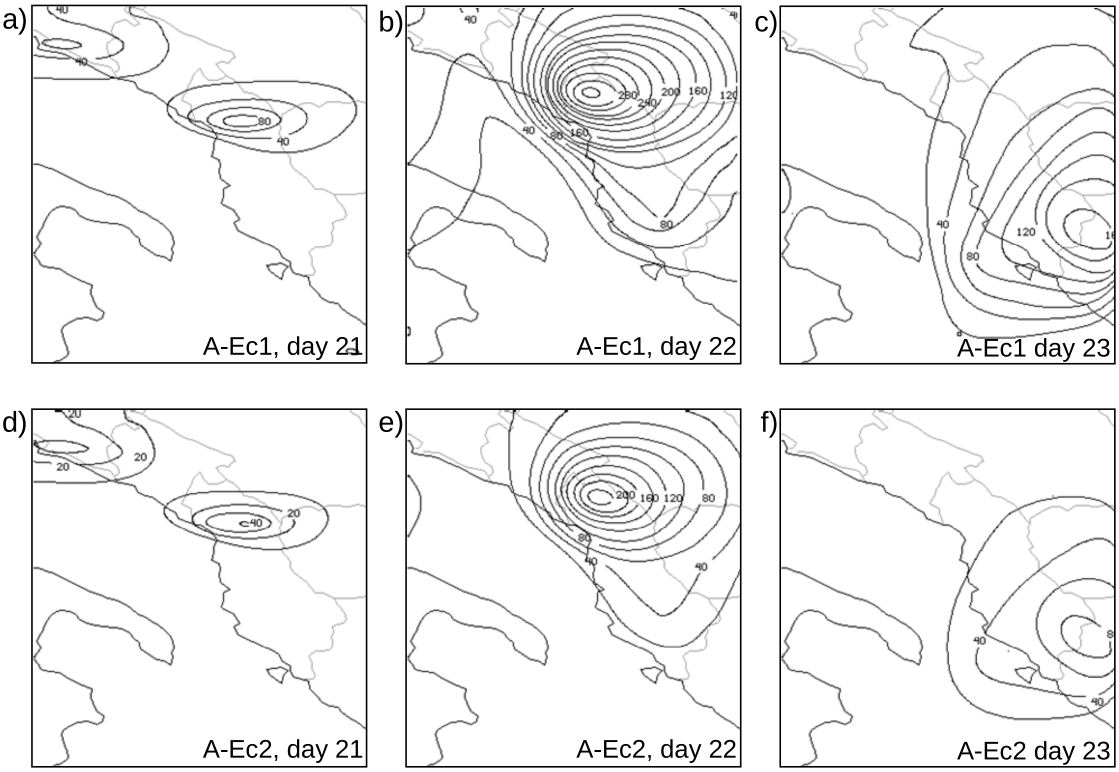

Figure 5.8. Daily accumulations derived from the two new rainfall curves A-Ec1 and A-Ec2 for each day of the flood case.

Table 5.2 Results comparing A-E, A-Ec1 and A-Ec2 with Observed daily rainfall. Boldfaced numbers show best statistical results in every line. (Same units of statistics indices as table 5.1)

| | OBS | A-E | A-Ec1 | A-Ec2 | Day |
|---|---|---|---|---|---|
| Size | 2055 | | | | 21 |
| Mean | 22.4 | 33.9 | 14.9 | 6.0 | |
| SD | 27.6 | 57.8 | 23.5 | 10.6 | |
| BIAS | | 11.6 | **-7.5** | -16.4 | |
| RMS | | 47.9 | **24.4** | 27.9 | |
| CORR | | 0.61 | **0.60** | 0.62 | |
| Size | 2777 | | | | 22 |
| Mean | 44.2 | 268.6 | 97.5 | 55.2 | |
| SD | 36.5 | 274.4 | 90.6 | 60.0 | |
| BIAS | | 224.4 | 53.3 | **11.0** | |
| RMS | | 346.7 | 101.1 | **59.5** | |
| CORR | | 0.34 | 0.33 | **0.35** | |
| Size | 1867 | | | | 23 |
| Mean | 36.5 | 183.3 | 74.4 | 34.1 | |
| SD | 29.9 | 125.2 | 45.7 | 24.7 | |
| BIAS | | 146.8 | 37.9 | **-2.4** | |
| RMS | | 191.5 | 63.4 | **34.2** | |
| CORR | | 0.19 | 0.15 | **0.23** | |
| Total Size | 6699 | | | | 21, 22, 23 |
| Mean | 35.4 | 172.8 | 65.7 | 34.2 | |
| SD | 33.5 | 215.3 | 73.4 | 46.1 | |
| BIAS | | 137.5 | 30.3 | **-1.1** | |
| RMS | | 246.5 | 74.4 | **45.1** | |
| CORR | | **0.39** | 0.38 | **0.39** | |

### *5.6 Sensitivity test of correction factors*

In order to assess the impact of each correction factor over the precipitation amounts, rainfall is estimated by using the A-E, A-Ec2 and CRR. Then, rain rates are modified by every correction factor and daily rainfall images are generated from them using equation (5.3). Finally the daily estimations affected by the correction factors are compared qualitatively (figure 5.9) and numerically (Tables 5.3a, 5.3b, 5.4, 5.5) with respect the observations (figures 5.4a, 5.4b and 5.4c). It is important to know that all the correction factors were applied to the two new curves, A-Ec1 and A-Ec2 however, we have preferred to show results of correction factors applied individually after A-Ec2 (Table 5.4) because it has obtained a slight better performance that A-Ec1 as illustrated in table 5.2.

The first important result is that none of the correction factors seems to solve substantially the high bias problem of the original A-E equation (3.1). Although, GR1, GR2 and TGR corrections have reduced significantly the BIAS error and RMS (Table 5.3a). The parallax correction (PC) provides the highest CORR values for the three satellite algorithms and for the three days of the flood case, but errors in BIAS and RMS are slightly changed (Tables 5.3a, 5.4 and 5.5). This indicates that the PC correction improves the results by just shifting precipitation in space as logical. In frames 5.9d to 5.9f for 'A-Ec2 + PC' compared to frames 5.9a to 5.9c for 'A-Ec2' it is observed a little movement of daily estimates to the south-west as expected. The PWRH, however, does not produce significant changes in any of the algorithms. Other corrections that have improved the daily precipitation correlation are the dynamic cloud growth rate correction (GR2) and the orographic correction (OC). Even though OC produces a very little improvement in the CORR, its RMS has growth appreciably. Moreover, a general observation for the OC and PWRH is that both corrections have increased the RMS index. These are the ones that have used data from the numerical model simulation therefore numerical outputs are probably causing these errors. Another problem with the OC that can cause other kind of inaccuracies is that since rain gauges in mountainous regions tend to be in the valleys, the rain gauge network may under-estimate the orographically enhanced rainfall that occurs in mountainous terrain.

The GR2 in general diminishes the daily rainfall because, as explained in section 3.2, this correction sets to zero rain rates in points where cloud top brightness temperatures are increasing with time. (Figure 5.9g to 5.9i compared with figures 5.9g to 5.9i for 'CRR + GR2'). The OC increases the daily rainfall on the windward side and tops of the highest mountains chains and diminishes it on the lee side of the ridges. This effect can be deduced from the Albanian terrain, shown in figure 5.1, comparing figures 5.9k and 5.9l for the 'CRR + OC' with 5.4h and 5.4i. The cloud-top temperature gradient correction (TGR) decreases, in general, the daily rainfall and improves slightly the correlation coefficients for all the algorithms.

The effect of GR1, GR2 and TGR is a general decrease in the RMS but they produce significant under-estimates of daily precipitation. This feature is deduced by considerable negative BIAS errors observed for the A-Ec2 and CRR in tables 5.4 for and 5.5. Therefore, the execution of these corrections after such algorithms adjusted to the geoclimatic conditions of the study area should remains under consideration. However, estimated daily rainfall amounts are closer to the observed when these last three corrections GR1, GR2 and TGR are applied separately after the A-Ec1 curve (results not shown in the tables).

The two versions proposed and studied by Vicente *et al*. (1998) "A-E+PWRH+GR1" and "A-E+PWRH+TGR" were tested and the results are shown in table 5.3b. Here it is observed in general a small improvement in the correlation coefficients and in rainfall amounts with respect the A-E infrared curve alone. The estimated daily rainfall in both cases are still suffering a sensible over-estimation unless for the first day of the flood where the performance of the two algorithm versions are going very well.

We have observed in general that the RMS is always lower when the satellite daily rainfall field is under-estimated, even when the under-estimation is important. On the other hand the RMS is much larger when satellite daily rainfall is over-estimated as natural, but paradoxically it happens also when over-estimation is small. In summary RMS are lower for cases in which strong negative errors in BIAS are also observed and, thus, we have to select which of the two statistical indices are more important. In order to evaluate the correction factors we have decided therefore to take into account in first place, the CORR parameter, in second place the BIAS and finally, the RMS.

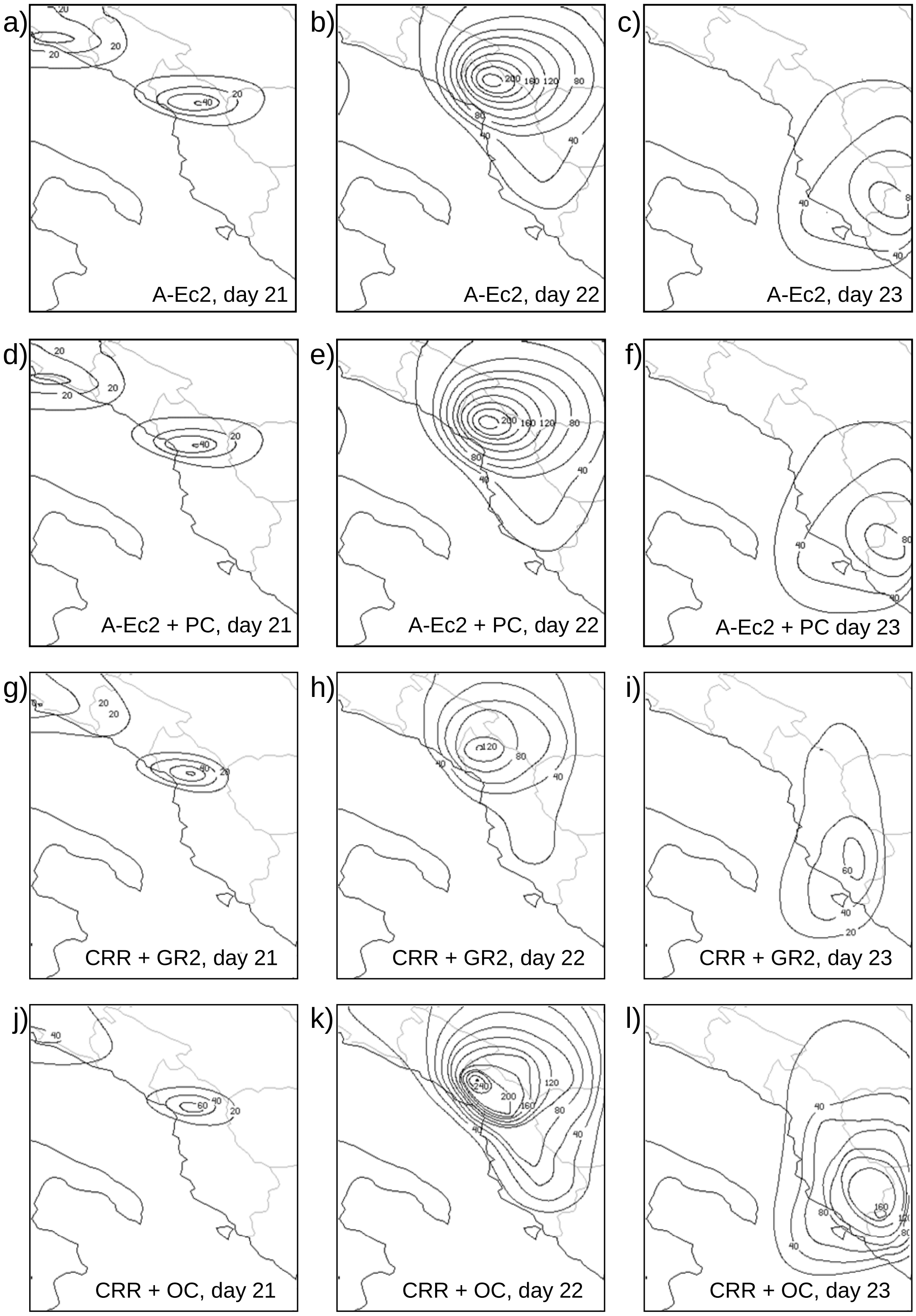

Figure 5.9. Daily A-Ec2 alone (a to c) and A-Ec2 and CRR modified by the corrections that have provided better correlation coefficients with respect to the observed rainfall.

Table 5.3. (a) Sensitivity analysis of correction factors over the A-E original equation (3.1). Where: PWRH is the moisture correction factor, GR1: cloud growth rate, GR2: dynamic cloud growth rate, TGR: Cloud-top temperature gradient, PC: Parallax correction and OC: Orographic correction. (b) Results comparing A-E, A-E+PWRH+GR1 and A-E+PWRH+TGR with Observed daily rainfall. The last two columns are the two versions proposed by Vicente *et al.* (1998) as the best. Boldfaced numbers show best statistical results in every line. (Same units of statistics indices as table 5.1).

| (a) | A-E | +PWRH | +GR1 | +GR2 | +TGR | +PC | +OC | Day |
|---|---|---|---|---|---|---|---|---|
| Size | | | | 2055 | | | | 21 |
| Mean | 33.9 | 30.8 | 24.5 | 18.9 | 22.3 | 34.1 | 35.0 | |
| SD | 57.8 | 52.8 | 413 | 37.1 | 37.8 | 57.3 | 60.0 | |
| BIAS | 11.6 | 8.5 | 2.1 | -3.4 | **-0.1** | 11.7 | 12.7 | |
| RMS | 47.9 | 41.5 | 32.5 | **27.8** | 30.6 | 50.5 | 49.9 | |
| CORR | 0.61 | 0.63 | 0.62 | **0.67** | 0.60 | 0.51 | 0.61 | |
| Size | | | | 2777 | | | | 22 |
| Mean | 268.6 | 267.6 | 173.9 | 168.0 | 157.6 | 285.3 | 307.7 | |
| SD | 274.4 | 277.9 | 177.2 | 192.0 | 158.8 | 270.0 | 316.3 | |
| BIAS | 224.4 | 223.4 | 129.7 | 123.8 | **113.4** | 241.1 | 263.5 | |
| RMS | 346.7 | 266.7 | 212.3 | 219.3 | **187.9** | 352.0 | 402.6 | |
| CORR | 0.34 | 0.37 | 0.35 | 0.39 | 0.35 | **0.43** | 0.38 | |
| Size | | | | 1867 | | | | 23 |
| Mean | 183.3 | 212.6 | 121.7 | 118.2 | 106.3 | 183.9 | 235.2 | |
| SD | 125.2 | 146.5 | 83.7 | 82.8 | 74.0 | 128.2 | 183.0 | |
| BIAS | 146.8 | 176.1 | 85.1 | 81.7 | **69.7** | 147.4 | 198.7 | |
| RMS | 191.5 | 145.7 | 119.2 | 115.8 | **102.0** | 192.8 | 267.3 | |
| CORR | 0.19 | 0.13 | 0.18 | 0.21 | 0.19 | **0.25** | 0.22 | |
| Total Size | | | | 6699 | | | | 21, 22, 23 |
| Mean | 172.8 | 179.7 | 113.5 | 108.4 | 101.8 | 180.0 | 203.9 | |
| SD | 215.3 | 221.3 | 139.5 | 146.8 | 125.1 | 216.7 | 255.7 | |
| BIAS | 137.5 | 144.3 | 78.1 | 73.0 | **66.4** | 144.6 | 168.5 | |
| RMS | 246.5 | 210.9 | 151.5 | 154.6 | **133.5** | 250.0 | 296.4 | |
| CORR | 0.39 | 0.39 | 0.40 | 0.42 | 0.40 | **0.45** | 0.41 | |

| (b) | A-E | +PWRH+GR1 | +PWRH+TGR | Day |
|---|---|---|---|---|
| Size | | 2055 | | 21 |
| Mean | 33.9 | 22.3 | 20.2 | |
| SD | 57.8 | 37.8 | 34.4 | |
| BIAS | 11.6 | **-0.1** | -2.2 | |
| RMS | 47.9 | 29.5 | 27.9 | |
| CORR | 0.61 | **0.63** | 0.62 | |
| Size | | 2777 | | 22 |
| Mean | 268.6 | 169.2 | 156.5 | |
| SD | 274.4 | 175.0 | 160.3 | |
| BIAS | 224.4 | 124.9 | **112.2** | |
| RMS | 346.7 | 206.7 | **187.5** | |
| CORR | 0.34 | **0.38** | **0.38** | |
| Size | | 1867 | | 23 |
| Mean | 183.3 | 141.5 | 120.9 | |
| SD | 125.2 | 97.9 | 84.4 | |
| BIAS | 146.8 | 105.0 | **84.3** | |
| RMS | 191.5 | 144.2 | **120.3** | |
| CORR | **0.19** | 0.12 | 0.13 | |
| Total Size | | 6699 | | 21, 22, 23 |
| Mean | 172.8 | 116.4 | 104.7 | |
| SD | 215.3 | 140.9 | 128.0 | |
| BIAS | 137.5 | 81.0 | **69.4** | |
| RMS | 246.5 | 154.2 | **137.3** | |
| CORR | 0.39 | **0.40** | **0.40** | |

Table 5.4 Statistical results of the A-Ec2 infrared curve and sensitivity analysis of correction factors. Boldfaced numbers show best statistical results in every line. (Same units of statistics indices as table 5.1).

| | A-Ec2 | +PWRH | +GR1 | +GR2 | +TGR | +PC | +OC | Day |
|---|---|---|---|---|---|---|---|---|
| Size | | | | 2055 | | | | 21 |
| Mean | 6.0 | 6.2 | 5.0 | 4.1 | 4.5 | 6.0 | 7.5 | |
| SD | 10.6 | 10.3 | 8.0 | 7.3 | 7.2 | 10.6 | 12.0 | |
| BIAS | -16.4 | -16.2 | -17.4 | -18.3 | -17.9 | -16.4 | **-14.9** | |
| RMS | **27.9** | 28.7 | 31.2 | 31.7 | 31.8 | 28.9 | 30.5 | |
| CORR | 0.62 | 0.63 | 0.62 | **0.67** | 0.61 | 0.53 | 0.61 | |
| Size | | | | 2777 | | | | 22 |
| Mean | 55.2 | 64.5 | 34.0 | 33.0 | 30.5 | 58.5 | 63.8 | |
| SD | 60.0 | 79.5 | 36.7 | 39.5 | 32.8 | 59.1 | 76.8 | |
| BIAS | 11.0 | 20.3 | **-10.0** | -11.2 | -13.7 | 14.3 | 19.6 | |
| RMS | 59.5 | 77.3 | **43.4** | 44.3 | 42.5 | 55.8 | 73.7 | |
| CORR | 0.35 | 0.36 | 0.36 | 0.39 | 0.36 | **0.45** | 0.39 | |
| Size | | | | 1867 | | | | 23 |
| Mean | 34.1 | 35.9 | 21.8 | 20.3 | 19.0 | 34.1 | 43.3 | |
| SD | 24.7 | 25.8 | 16.1 | 15.8 | 14.3 | 25.3 | 37.8 | |
| BIAS | **-2.4** | -0.58 | -14.7 | -16.2 | -18.5 | **-2.4** | 6.8 | |
| RMS | 34.2 | 36.2 | 35.2 | 36.1 | 36.2 | **33.4** | 42.4 | |
| CORR | 0.23 | 0.18 | 0.22 | 0.21 | 0.22 | **0.28** | 0.27 | |
| Total Size | | | | 6699 | | | | |
| Mean | 34.2 | 40.3 | 21.5 | 20.6 | 19.3 | 35.6 | 40.8 | |
| SD | 46.1 | 58.8 | 28.5 | 29.9 | 25.5 | 46.3 | 59.1 | |
| BIAS | -1.1 | 4.1 | -13.9 | -14.8 | -16.1 | **0.2** | 5.4 | 21, 22, 23 |
| RMS | 45.1 | 55.6 | **37.8** | 38.5 | 37.8 | 43.1 | 55.2 | |
| CORR | 0.39 | 0.37 | 0.40 | 0.41 | 0.40 | **0.46** | 0.41 | |

Table 5.5. Statistical results of the Sensitivity analysis of correction factors over the CRR. Boldfaced numbers show best statistical results in every line. (Same units of statistics indices as table 5.1)

| | CRR | +PWRH | +GR1 | +GR2 | +TGR | +PC | +OC | Day |
|---|---|---|---|---|---|---|---|---|
| Size | | | | 2055 | | | | 21 |
| Mean | 8.3 | 8.5 | 6.0 | 5.1 | 5.3 | 8.2 | 8.9 | |
| SD | 16.6 | 16.7 | 11.7 | 10.8 | 10.7 | 16.4 | 18.0 | |
| BIAS | -14.0 | -13.9 | -16.4 | -17.3 | -17.1 | -14.2 | **-13.5** | |
| RMS | **26.8** | 27.0 | 27.8 | 28.7 | 28.7 | 28.8 | 26.9 | |
| CORR | 0.57 | 0.55 | **0.61** | 0.60 | 0.59 | 0.45 | 0.55 | |
| Size | | | | 2777 | | | | 22 |
| Mean | 53.7 | 72.6 | 31.8 | 30.6 | 30.4 | 57.7 | 66.5 | |
| SD | 56.7 | 84.4 | 34.2 | 36.0 | 31.6 | 56.1 | 75.2 | |
| BIAS | **9.5** | 28.4 | -12.5 | -13.6 | -13.8 | 13.5 | 22.9 | |
| RMS | 57.9 | 85.8 | 44.5 | 42.8 | **42.1** | 55.4 | 74.3 | |
| CORR | 0.31 | 0.31 | 0.27 | 0.37 | 0.33 | **0.39** | 0.35 | |
| Size | | | | 1867 | | | | 23 |
| Mean | 45.3 | 62.1 | 30.0 | 27.0 | 24.9 | 46.1 | 59.7 | |
| SD | 33.2 | 50.5 | 22.6 | 19.9 | 18.0 | 34.2 | 49.6 | |
| BIAS | 8.7 | 25.6 | **-7.5** | -9.5 | -11.6 | 9.6 | 23.1 | |
| RMS | 41.5 | 59.8 | **34.4** | 35.1 | **34.4** | 41.0 | 57.1 | |
| CORR | 0.17 | 0.17 | 0.20 | 0.12 | 0.15 | **0.23** | 0.21 | |
| Total Size | | | | 6699 | | | | 21, 22, 23 |
| Mean | 37.4 | 50.0 | 23.1 | 21.8 | 21.2 | 39.3 | 46.9 | |
| SD | 46.0 | 67.3 | 28.3 | 28.4 | 25.6 | 46.5 | 61.4 | |
| BIAS | **2.1** | 14.6 | -12.3 | -13.6 | -14.2 | 3.9 | 11.6 | |
| RMS | 45.7 | 65.4 | 37.3 | 36.8 | **36.3** | 44.7 | 58.5 | |
| CORR | 0.37 | 0.35 | 0.36 | 0.40 | 0.39 | **0.42** | 0.39 | |

### *5.7 Combining CRR and new curves with rainfall corrections*

At the time of writing we have not found clear and specific information on the order of corrections applied operationally for the A-E in the US by NESDIS (National Environmental Satellite Data and Information Service). Therefore, different combinations of correction factors, not shown in this report, were tested by us for A-E, A-Ec1, A-Ec2 and CRR algorithms. The combination with the best resulting daily estimations is described in the next paragraphs, statistical indices are shown in table 5.6 and maps are illustrated in figure 5.10. The basic rain rates from the different algorithms are corrected firstly by GR2, then resulting rain rates are corrected by PC and finally by OC in that order. Then, corrected daily rainfall fields are computed using equation (5.3). In a second version, the PWRH factor is applied last in order to study the effects of moisture over the rainfall (see table 5.6). The idea is to apply all the corrections that have individually improved the correlation coefficient, as first index, and rainfall amounts (BIAS and RMS), as shown in the precedent section. Vicente *et al.* (1998) proposed the A-E+PWRH+GRT and A-E+PWRH+GR1 versions, obtaining varied results. In this research we have tested these versions as shown in table 5.3b and, have also integrated the PC and the OC, shown for the first time in a later publication (Vicente *et al.* 2002). It is important to mention that these corrections are operationally incorporated in the A-E and H-E (Hydro-Estimator) by NESDIS as described by Scofield and Kuligowski (2003), but, in this article it is not specified in which order.

The effect of GR1 or GR2 or TGR in decreasing daily precipitation is stronger than the effect of PWRH, OC and PC in increasing it. The GR2 factor, with the highest correlation coefficient than GR1 and TGR, can equilibrate alone the tendency to increase the daily rainfall derived from the PC plus OC plus PWRH. Apart from that, the optimum order of corrections that was found could be explained by the following hypothesis: GR2 is related to cloud dynamics computed from satellite temperatures, PC "matches" cloud points to ground points and OC and PWRH are corrections supported on the atmospheric properties of the event simulated by the MM5 model at different levels. The key point is that horizontal position of every model grid point at each height is centred on its horizontal position at ground level. Based on this obvious argument the PC should operate after GR2 (satellite) and before OC and PWRH (model), because the PC places satellite cloud points on different heights at their correct ground-reference position. However, other satellite rainfall algorithms PC used to be executed in first place. Therefore the option “Algorithm+PC+GR2+OC+PWRH” was tested without finding variations in the accuracy of the daily precipitation as opposed to the version proposed by us “Algorithm+GR2+PC+OC+PWRH”. In addition, the OC and PWRH are both multiplicative factors, therefore results do not logically change by ending the correction chain in any of the two following ways: “…+OC+PWRH” or “…+PWRH+OC”.

In order to show the results, the algorithms are separated between standards (A-E, CRR), table 5.6a and calibrated (A-Ec1, A-Ec2) table 5.6b. Correlation coefficients are increased in general after the application of a set of corrections for the three days of the flood case as shown in the final 6 rows of statistical results of each of the tables. An analysis of the corrected daily rainfall amounts with respect the basic algorithms shows that under or over-estimation tendencies are smoothed but not eliminated. For the version including the PWRH factor, correlations are slightly diminished or equal and RMS indices are increased in general, mostly for the corrected CRR. The exception in this case is the original A-E (Table 5.6a) where the PWRH correction applied as the last factor produces a clear improvement in the correlation coefficient.

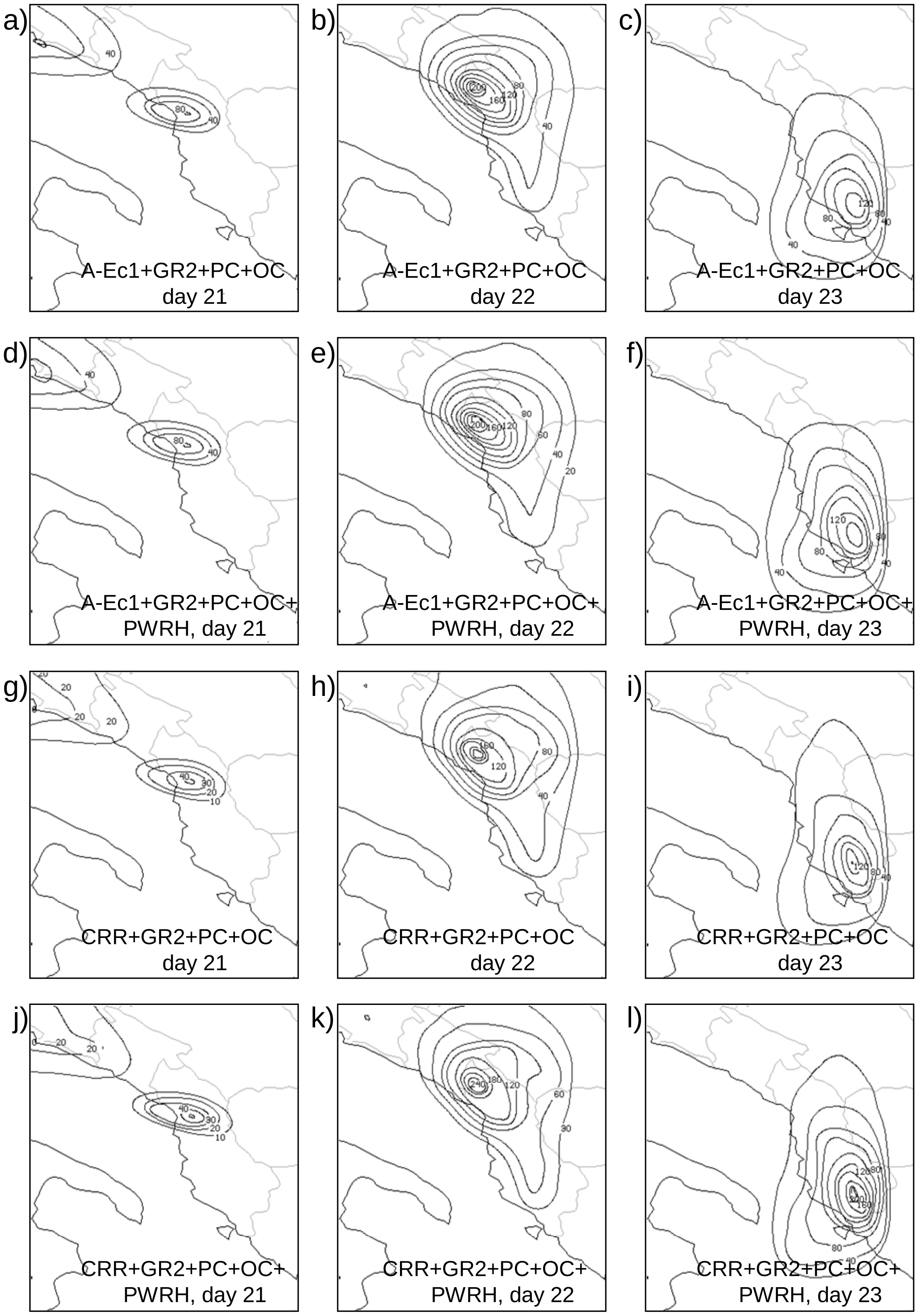

Figure 5.10. A-Ec1 and CRR corrected by GR2+PC+OC and by GR2+PC+OC+PWRH. Corrections are performed one after another using the rainfall rate images, then, daily precipitation fields are computed and shown. In the present figure the PWRH correction factor is applied last to show the effect of moisture in low levels over the daily rainfall.

Table 5.6. Statistical results of a chain combination of correction factors applied over old algoritms A-E and CRR (a) and new infrared curves A-Ec1 and A-Ec2 (b). The PWRH correction factor is applied apart to show the effect of moisture present in low levels over the daily rainfall. Boldfaced numbers show best statistical results in every line. (Same units of as table 5.1)

| (a) | A-E | A-E +GR2+PC +OC | A-E +GR2+PC +OC+PWRH | CRR | CRR+GR2+PC +OC | CRR+GR2+PC +OC+PWRH | Day |
|---|---|---|---|---|---|---|---|
| Size | 2055 | | | | | | 21 |
| Mean | 33.9 | 19.9 | 20.2 | 8.3 | 5.2 | 5.9 | |
| SD | 57.8 | 39.9 | 41.5 | 16.6 | 11.8 | 13.5 | |
| BIAS | 11.6 | -2.5 | **-2.1** | -14.0 | -17.1 | -16.5 | |
| RMS | 47.9 | 34.4 | 36.6 | **26.8** | 30.1 | 30.3 | |
| CORR | **0.61** | 0.53 | 0.50 | 0.57 | 0.44 | 0.40 | |
| Size | 2777 | | | | | | 22 |
| Mean | 268.6 | 203.8 | 206.9 | 53.7 | 40.6 | 55.2 | |
| SD | 274.4 | 224.3 | 232.3 | 56.7 | 48.2 | 72.1 | |
| BIAS | 224.4 | 159.6 | 162.7 | 9.5 | **-3.6** | 11.0 | |
| RMS | 346.7 | 262.5 | 269.8 | 57.9 | **44.7** | 64.9 | |
| CORR | 0.34 | 0.50 | **0.53** | 0.31 | 0.47 | 0.46 | |
| Size | 1867 | | | | | | 23 |
| Mean | 183.3 | 248.7 | 176.5 | 45.3 | 38.0 | 52.7 | |
| SD | 125.2 | 2085 | 150.2 | 33.2 | 34.8 | 52.2 | |
| BIAS | 146.8 | 212.2 | 139.9 | 8.7 | **1.5** | 16.2 | |
| RMS | 191.5 | 293.9 | 203.3 | 41.5 | **40.4** | 56.6 | |
| CORR | 0.19 | **0.24** | 0.19 | 0.17 | 0.23 | 0.22 | |
| Total Size | 6699 | | | | | | 21, 22, 23 |
| Mean | 172.8 | 159.9 | 141.2 | 37.4 | 29.0 | 39.4 | |
| SD | 215.3 | 206.1 | 189.3 | 46.0 | 39.9 | 58.9 | |
| BIAS | 137.5 | 124.5 | 105.8 | **2.1** | -6.3 | 4.0 | |
| RMS | 246.5 | 230.2 | 205.2 | 45.7 | **39.6** | 54.0 | |
| CORR | 0.39 | 0.44 | **0.48** | 0.37 | 0.44 | 0.43 | |

| (b) | A-Ec1 | A-Ec1 +GR2+PC +OC | A-Ec1 +GR2+PC +OC+PWRH | A-Ec2 | A-Ec2 +GR2+PC +OC | A-Ec2 +GR2+PC +OC+PWRH | Day |
|---|---|---|---|---|---|---|---|
| Size | 2055 | | | | | | 21 |
| Mean | 14.9 | 8.5 | 8.6 | 6.0 | 3.7 | 3.8 | |
| SD | 23.5 | 15.7 | 16.4 | 10.6 | 7.7 | 8.0 | |
| BIAS | **-7.5** | -13.9 | -13.8 | -16.4 | -18.7 | -18.6 | |
| RMS | **24.4** | 27.1 | 27.6 | 27.9 | 30.8 | 30.9 | |
| CORR | 0.60 | 0.54 | 0.51 | **0.62** | 0.53 | 0.50 | |
| Size | 2777 | | | | | | 22 |
| Mean | 97.5 | 74.8 | 76.7 | 55.2 | 45.9 | 46.1 | |
| SD | 90.6 | 79.9 | 83.1 | 60.0 | 56.6 | 58.0 | |
| BIAS | 53.3 | 30.6 | 32.5 | 11.0 | **1.6** | 1.9 | |
| RMS | 101.1 | 75.5 | 77.8 | 59.5 | **49.3** | 49.4 | |
| CORR | 0.33 | 0.51 | **0.54** | 0.35 | 0.51 | 0.53 | |
| Size | 1867 | | | | | | 23 |
| Mean | 74.4 | 60.1 | 71.5 | 34.1 | 28.6 | 33.7 | |
| SD | 45.7 | 46.6 | 57.4 | 24.7 | 25.4 | 29.9 | |
| BIAS | 37.9 | 23.6 | 34.9 | **-2.4** | -7.9 | -2.9 | |
| RMS | 63.4 | 55.1 | 69.8 | **34.2** | 34.5 | 37.5 | |
| CORR | 0.15 | 0.21 | 0.16 | 0.23 | **0.27** | 0.22 | |
| Total Size | 6699 | | | | | | 21, 22, 23 |
| Mean | 65.7 | 50.4 | 54.3 | 34.2 | 28.1 | 29.6 | |
| SD | 73.4 | 64.3 | 69.2 | 46.1 | 42.9 | 44.6 | |
| BIAS | 30.3 | 15.0 | 19.0 | **-1.1** | -7.3 | -5.7 | |
| RMS | 74.4 | 58.6 | 64.0 | 45.1 | **40.4** | 41.2 | |
| CORR | 0.38 | **0.48** | 0.47 | 0.39 | **0.48** | **0.48** | |

### *5.8 Discussion and conclusions*

*a) Discussion*

According to Vicente *et al.* (1998) article, the application of the A-E curve alone has a tendency to over-estimate daily precipitation compared to observed values. However, in this flood case the over-measurement is especially large. In contrast, the CRR algorithm gives adjusted daily rain amounts (see BIAS and RMS in Table 5.1 and figures 5.4d to 5.4i). This result suggests that the CRR is closer to the geo-climatic conditions of the Albanian region than the A-E algorithm. In fact the calibration of CRR matrices was performed over the Iberian Peninsula (see chapter 4.2) which is located at the same latitude as Albania and, in addition, part of this Peninsula is under strong influence of the Mediterranean Sea. However, correlations between CRR and observations are, in general, slightly lower than for A-E. A possible reason is that some Meteosat water vapour images were missed; producing bugs in the CRR data stream, these were then substituted with time averaged CRR images. A feature more difficult to explain is the strong CRR daily precipitation under-estimation for the day 21. With no available radar images our theory is that cloud microphysical properties were, on this particular day logically very different from that which could be deduced solely from satellite cloud top observations.

Two new infrared curves called A-Ec1 and A-Ec2 are generated with available rain rates from 8 rain gauges in Albania, applying two different methods. Both new curves have a general tendency to estimate lower rain rates than the original A-E curve as shown in figure 5.7. This experiment confirms that it is possible to transform satellite measurements to rain rates after a calibration by using only rain gauges. This supposes an advantage because it opens up a possibility to skip all the radar developments for calibration. However both curves are slightly different and the difficult question is, why? The first proposed method to configure the A-Ec1 curve is probably more straightforward and simple than the second method but still produces a clear over-estimation of daily precipitation (see results in table 5.2). The second curve (A-Ec2), is a more complex method but produces better daily estimations with lower BIAS and higher CORR (Table 5.2). Although this does not mean that A-Ec2 should be definitively better than A-Ec1, a verification of the estimated satellite rain rates and hourly precipitation with respect to radar is still very important. Unfortunately these kinds of experiments have to be performed in other regions with available radar images.

Other kinds of tests completed by us but not shown in this thesis report were the generation of one different curve for each day of the flood by applying the second calibration method (A-Ec2) as it has produced the best daily results. In this case, A-Ec2 infrared curves are, as expected, very different depending on the flood day they were computed. This result suggests that cloud top properties observed by the satellite and rainfall from their bases are changing relatively fast from one day to another. These substantial variations cannot be captured using a unique A-E relationship for all rainfall cases and for all days. In addition, correction factors do not seem to do the proper modifications, mostly, between days 21 and 22. One option to solve this problem is to perform operational calibrations every day between the satellite and the rain gauges. Unfortunately, this can cause other problems such as; definition of calibration-application optimal time periods, rain gauge and satellite data availability in real time and automatic quality checking to detect errors in the data stream. The second option is more elaborated and consists of the generation of rainfall curves at different seasons of the year and, in each season, one curve for every different type of synoptic system. For example, four categories as developed by Cheng and Brown (1995): cold fronts, warm fronts, and cold air convection and mesoscale convective systems.

### *b) Conclusions*

Calibrated curves (A-Ec1 and A-Ec2) for the three days over-estimate the daily precipitation area in general but under-estimate maximum rainfall quantities compared to observed daily rainfall (compare figures 5.4a to 5.4c for observations with figure 5.8 for A-Ec1 and A-Ec2). Two observed daily maxima, one of 150 mm in the south of the country on day 22 and the other of 85 mm in the north of Albania on day 23, are not captured by any of the satellite algorithms and MM5.

The parallax correction (PC), the dynamic cloud growth rate correction (GR2) and the orographic correction (OC) can improve correlations of the satellite daily precipitation while the results for the moisture correction (PWRH) are not clear. In general, calibration tasks have an overall effect on rainfall amounts, revealed by a substantial reduction of BIAS and RMS indices compared with the original A-E (Table 5.2).

GR1, GR2 and TGR diminished the RMS in general but they produce strong BIAS errors for the A-Ec2 and CRR. This suggests that the use of these corrections after algorithms adjusted to the geo-climatic conditions of the study area are not recommended unless they are combined with other correction factors that can compensate the strong under-estimation in the rainfall.

Daily satellite estimation results at this point appear to be encouraging; however, correlations are still lower than 0.5, BIAS greater than 5 mm and RMS greater than 40 mm in many cases. Qualitative analysis of the observed and estimated daily rainfall images by A-E and CRR also show that some significant maxima are not detected adequately. An option for the near future in a region with no available radar data is the employment of a passive microwave rainfall rate data derived from SSMI and AMRS sensors aboard polar satellites to improve the rainfall calibration of geosynchronous satellite infrared imagery. Alternatives in this direction were successfully explored by Kidd *et al.* (2003) and Turk *et al.* (2000).

The infrared curve calibration methods developed in the present work (A-Ec1 and A-Ec2) should be tested in other cases and other regions with the available rain gauge and radar measurements, in order to verify the accuracy of the methods. However, the analysis of the convective heavy rain event completed in this chapter has shown that any of the two calibration methods can be a feasible choice to adjust estimated rainfall rates to the reality of the case and with possible operational applications if data from satellite and rain gauges are available in real time.

Some corrections factors performed in this flood case, such as PC, GR2 and OC, have shown small improvements on the daily rainfall estimations. Additionally, the best ones can work one after another in a chain combination in order to gain any benefit. These can increase the flexibility of the rainfall estimation methods and are relatively easy to be implemented within an operational context with the help of a numerical model.

## 6. Rainfall analysis of the Montserrat case

During the 9th and 10th June 2000, the north-eastern part of the Iberian Peninsula was affected by heavy rains that produced severe floods over densely populated areas. The most affected zones were the provinces of Tarragona and Barcelona, located in the region of Catalonia (figure 6.1a and 6.1b). Five people were killed, five hundred were evacuated and property losses were estimated to exceed 65 M€. The episode was characterized by the entrance of an Atlantic low-level cold front and an upper-level trough that contributed to the generation of a mesolow (low-level mesoscale cyclone) offshore of eastern Spain. The circulation associated with this mesolow provided warm moist air to Catalonia from the Mediterranean Sea. The convergence zone between the easterly flow and the Atlantic front as well as the complex terrain of the region, are shown to be involved in the organization and triggering of the convective systems.

In this chapter a summary of the most important synoptic factors are briefly described, however the reader is referred to Martin *et al.* (2006) publication, where a much more detailed and accurate analysis about the case study within various numerical simulations are provided. In chapter 8 of this thesis a parallel study of rainfall estimates from the Meteosat-7 perspective is performed and explained. The difference between this and the Albanian case (chapter 5) is that now ground radar images from the INM covering the flood area are available. These images are used to verify the satellite estimated rain rates, added to the 24 hour rainfall accumulation evaluation as done in Albania. Unexpected troubles concerning radar are behind the radar calibration experiments by using rain gauges to transform radar measurements into rain rates as described in chapter 7. Here two methods, one from the bibliography and the second completely experimental, are performed and tested in order to select the optimum one to compute the best radar rain rates estimates. Calibrated radar rain rates are used later in section 8.

### *6.1 Case study and MM5 settings*

#### *a) Case of study*

The event of 9-10 June 2000 is atypical owing to the extreme rainfall intensities that were observed and the high social impact caused by the resulting flash flood. In fact, this is one of the cases that received the greatest amount of attention of the regional media in the XX century, with more than 75 references published in 5 local newspapers.

This is comparable only to few historical events such as the cases of September 1962, September 1981 or October 1982 (Llasat *et al*. 2003). On 10 June 2000, 5 people died and more than 500 were evacuated from the monastery of Montserrat (figure 6.1b). Total material loss, including the destruction of a bridge, was estimated to exceed 65 M€ by the media. In fact, this event is catalogued as catastrophic by Llasat *et al*. (2002), fitting their criteria of observed rainfall amounts, total affected area, death toll and economic losses (Llasat, 2001).

Three aspects contributed to this unique flood: the high rain rates, the stationary nature of the precipitating systems and the particular terrain configuration of the affected area. Some rain gauges in Catalonia recorded 5 min accumulations reaching 10 mm (120 mm $h^{-1}$), with a total 6 hours amount of over 200 mm. Radar in Barcelona captured the evolution of convective systems linked to an Atlantic front, as well as two mesoscale convective systems merging and becoming nearly stationary over Barcelona during the first hours of 10 June. As a consequence of such intense and persistent precipitation over the Montserrat basin, a prototype western Mediterranean hydrographical river basin with a complex mosaic of sub-basins defined by high and steep slopes, an exceptional flash flood occurred.

### *b) MM5 settings*

The MM5 numerical model is initialised with the global troposphere analyses from Global Data Assimilation system of the National Center for the Environmental Prediction (NCEP). They have a 2.5ºx2.5º lat-lon resolution and are available every 12 hours. These fields are remapped to the model grid by means of an objective analysis that incorporates surface and upper-air observations. With the aim of accurately simulating fine details of the precipitating systems for this event, three 82x82 grid points 2-way nested domains of 54, 18 and 6 km spatial resolution are defined, zooming-in over north-eastern Spain. In the vertical, 24 levels are used, with higher density near the surface to better resolve near-ground processes. The heavy rainfall that characterised this case was registered during the first hours of the 10th of June. Previous sections highlight the link between the intense convective activity and the cold front passage over Catalonia with strong rain rates. In order to capture the mesoscale details of the evolution of the front, as well as the mesolow offshore eastern Spain, a 36 hours control simulation, beginning at 0000 UTC 9 June, is set up. Meteorological fields are outputted every 6 hours for the coarse domain, every 3 hours for the intermediate and every 30 minutes for the fine domain. As done in the previous flood case over Albania (section 5.2), only the fine domain outputs are remapped to satellite projection and resolution and employed to compute the moisture (PWRH) and orographic (OC) correction factors evaluated in chapter 8 of this report.

### *6.2 Synoptic overview*

The event developed under a synoptic pattern characterized by an Atlantic cold upper-level trough over western Europe (Figures. 6.2a and 6.2b) and a low sea-level pressure area along the British Isles, western France and Spain, with an associated cold front extending south as far down as North Africa (Figures 6.2c). The front was deformed over the Iberian Peninsula by a warm mass associated with a secondary low. During the 9th of June, the upper-level short-wave trough became negatively tilted and was causing advection of cold and dry air over the Iberian Peninsula as the surface cold front advanced east (Figures 6.2b to 6.2d), producing snowfalls during the evening over parts of northern Spain. The eastern shift of the secondary low over Spain and the influence of cyclonic circulation off of Algeria favoured the entrance of warm advection during the 9th of June over Mediterranean Spain (Figures 6.2c and 6.2d). The cyclonic moisture flow established over the Western Mediterranean impinged the north-eastern Spanish littoral and provided a continuous supply of warm and moist air towards the Catalan coast, during the second half of the 9th of June. Thus, the NCEP analysis maps reveal several synoptic and sub-synoptic factors which presumably conduced to the intense rains over Catalonia during the first hours of 10th June: (i) a cold mid-troposphere trough, accompanied by a surface cold front passage, and (ii) warm moist south-easterly flow, reinforced by local circulations. The combined action of the low-level mesolow and the cold front at low-mid levels conduced to a convectively unstable environment with high CAPE. As a result, the frontal convergence zone was intensified and, together with the impinging maritime flow onto the Catalan coastal mountains triggered and sustained the highly efficient precipitation cells.

a) WESTERN MEDITERRANEAN REGION

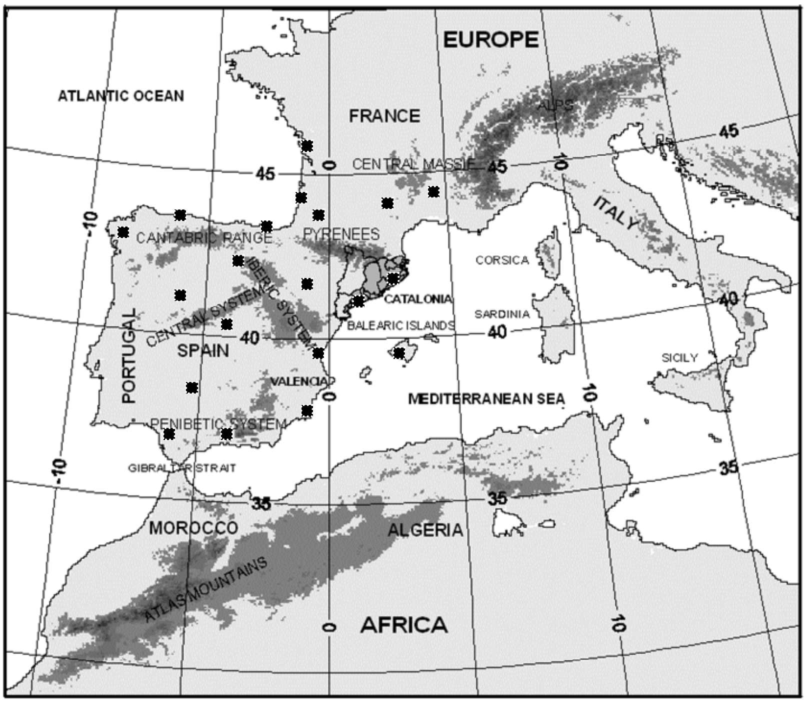

b) BASINS OF CATALONIA

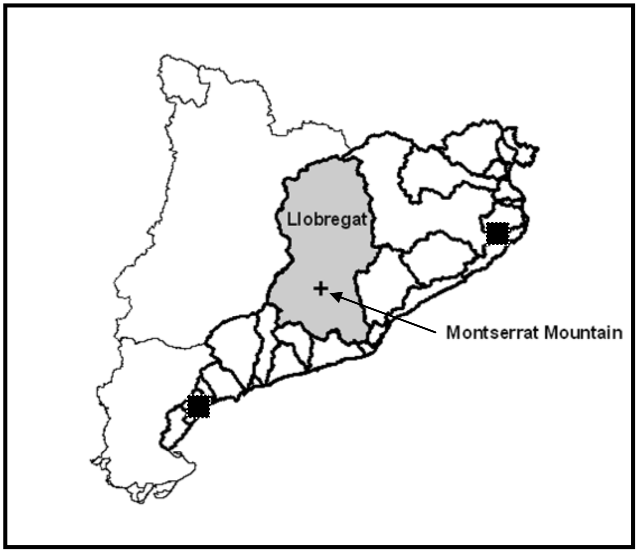

Figure 6.1. (a) Western Mediterranean region, showing major topographic features by means of terrain contours (shaded darker grey, intervals of 500 m, starting at 500 m). As thick continuous line, Catalonia and inside it, the Internal Basins of Catalonia (shaded dark grey) are shown: (b) Catalonia inset and the Internal Basins of Catalonia. The cross locates the Montserrat Mountain where the highest rainfall values were gathered. The Black boxes represent the position of stations from the INM lightning detection network used in chapter 8 of this thesis report.

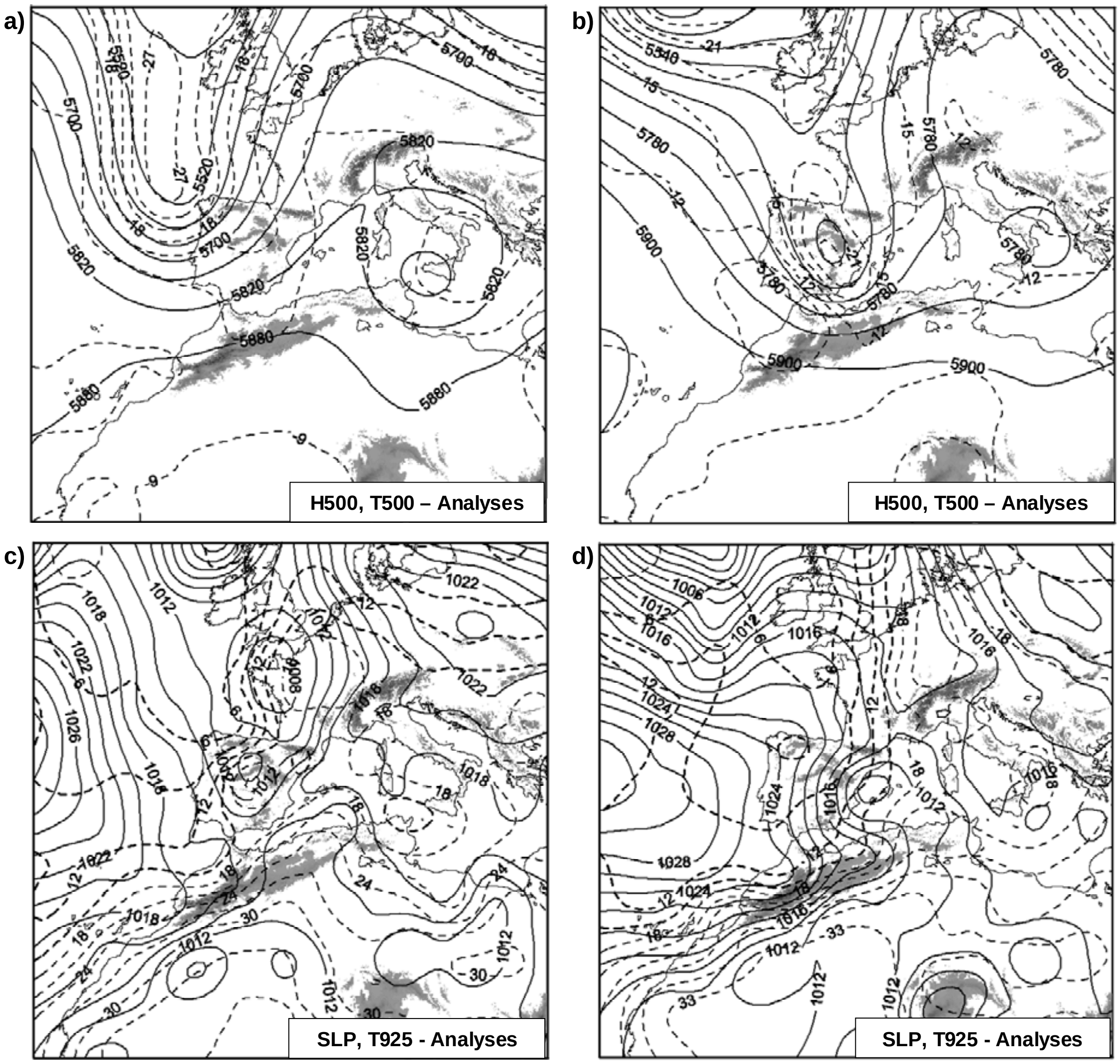

Figure 6.2.- Analyses maps: (Top) Geopotential height at 500 hPa (continuous line, in gpm) and temperature at 500 hPa (dashed line, in ºC) for the coarser domain: (a) at 0000 UTC 9 June 2000; and (b) at 0000 UTC 10 June 2000: (Bottom) Sea level pressure (continuous line, in hPa) and temperature at 925 hPa (dashed line, in ºC) for the coarser domain: (c) at 0000 UTC 9 June 2000; and (d) at 0000 UTC 10 June 2000. As thick dashed line, the cold front is shown. Main orographic systems are highlighted.

## 7. Assessment of radar measures

### *a) Abstract*

Precipitation estimates from radar systems are a crucial component of many hydro-meteorological applications, from flash flood forecasting to regional water budget studies or as ground observations for satellite calibration. This chapter assesses the accuracy of three methods which use single radar imagery to estimate precipitation in the convective environment of the Montserrat flood case in Catalonia, Spain, during the 9 th and 10th of June 2000. Results using $Z=a R^b$ (Marshall and Palmer Z-R relationship) with coefficients for stratiform rain ($a=200$, $b=1.6$) and convective rain ($a=800$, $b=1.6$) are compared with those obtained using the Histogram Matching Technique (HMT) and with another experimental procedure developed by us in the present study, called Direct Calibration Method (DCM). The HMT and the DCM were developed using the Barcelona radar and 126 automatic rain gauges well distributed over the affected area and, in a second stage, both methods were readjusted to fit with the calibration data. Rainfall derived from the Marshall and Palmer power law Z-R using stratiform and convective coefficients is found to highly under-estimate rain gauge measurements for a three hour accumulation period. Precipitation from the HMT is improved with respect to the other methods since correlation coefficients are higher while the DCM provides the lowest bias.

### *b) Introduction*

Meteorological radars have been used since 1940 to estimate rainfall. Efforts have focused on long time and/or big spatial scales due to data availability, range-height sampling considerations, and processing limitations. However, there are many hydrologic, surface modelling and satellite calibration applications that require accurate rain fields on shorter spatial and temporal scales.

There are two basic approaches to measure rainfall, which is usually highly variable spatially and temporally. First there are the rain gauges, which can generally measure accurate rainfall depths at a point scale. Ideally, a dense network would resolve the spatial distribution of rainfall, but this is not practical because of the prohibitive cost and poor accessibility to remote sites. Secondly, a remote sensor such as weather radar that gives an indirect measurement of the sizes of precipitation droplets and a quasi-continuous approach to the rainfall spatial distribution. However, a radar beam originates from the ground surface and within a few hundred kilometres will reach a height that is above the majority of the precipitation events. Other problems include uncertainties in converting radar echoes to rainfall, data processing problems, and radar range effects.

The aim of this research is to explore benefits after adjusting radar rainfall data using rain gauge data, to take advantage of radar’s ability to map the spatial variability of precipitation and of rain gauges to measure actual depths. In the last few years the combination of radars and rain gauges for short time scales is possible operationally due to improvements in computer processing and real time data availability.

For this case study it is interesting how different radar rainfall analyses using standard methods as a Marshall and Palmer Z-R relationship, $Z=a R^b$, with different coefficients (Marshall and Palmer, 1948), systematically under-estimate the precipitation amounts. This earlier work demonstrated the existence of a drop size distribution (DSD) which is a simple function of the rain rate, and therefore led to a corresponding direct relationship between radar reflectivity Z and rain rate R. After Marshall and Palmer many coefficients for the Z-R relationship were calculated for different rain regimes and places, obtaining various results. Several studies (Cairns, *et al*. 1998; Huggins and Kingsmill, 1998) have shown that the best Z-R relationship depends partly on geographic location. The direct calibration method (DCM) developed in this work is based on a linear regression fit between Z and R using the Marshall and Palmer Z-R relationship, in the logarithmic scale in order to resolve the two coefficients, a and b.

The Histogram Matching Technique or Probability Matching Method, as called in other publications, was introduced by Calheiros and Zawadzki (1987) and has been greatly elaborated by Rosenfeld *et al*. (1994, 1995). In essence the conditional probability distribution of the radar reflectivity and rainfall from collocated rain gauges are determined and later, the equality of the cumulative probabilities is obtained. Under this approach, Crosson *et al.* (1996) documented improvements in precipitation estimations over those obtained using a standard power law in which biases and root mean square errors are much lower.

Verification of the estimated results is performed by comparing qualitatively and numerically 3 hour radar rain accumulations estimated by the different methods with the corresponding interpolated rain gauge precipitation.

## *7.1 Data description and study methodology*

### *a) Datasets*

The observed rain dataset was provided by the Automatic System of Hydrological Information (SAIH) of the Catalan Water Agency (ACA). Records of precipitation in mm $h^{-1}$ at 126 automatic rain gauges (Figure 7.1), every 5 minutes from 1130 UTC 9 to 1230 UTC on the 10th of June, are available. The rain gauge network is located in the internal basins of Catalonia (closed polygonal line area in figure 7.1) and is considered dense enough to perform a kriging analysis method using a linear model for the variogram fit to create rain rate fields for the calibration process and 3 hours rain accumulation fields for the verification phase, both at 2 by 2 km resolution. This minimal error variance interpolation method is recommended for spatially irregular grids with a relatively low number of observations (<250) and has been widely used to compute rainfall fields from rain gauges (Krajewski 1987; Seo 1998; Bhagarva and Danard 1994). These fine grid fields were then remapped to radar projection in order to implement the different techniques.

The lower radar CAPPI (Constant Altitude Plan Position Indicator) images at 1.2 km altitude in dBZ units from the C-band radar of Barcelona are supplied by the INM. The radar is located 20 km to the southwest of Barcelona city at 654 m above sea level and the main radar characteristics are 0.9º 3-dB beam width, $\lambda$=5.4 cm and 20 elevation angles. The lowest CAPPI fields, used by various meteorological centres to estimate precipitation, were computed using software provided by the INM and called STArPcw (Riosalido, 1994). Under this approach, ground echoes were detected and substituted by suitable radar measurements derived from horizontal and vertical analyses (Martín and De Esteban, 1994). CAPPI fields were selected every 10 minutes from 2100 UTC 9 to 1230 UTC June 10th, with 2 by 2 km pixel resolution and covering a circular area of around 480 km diameter as shown in figure 7.1. Significant attenuation problems occurred in radar images from 0250 to 0430 UTC caused, presumably, by the high precipitation rate over the radar zone, and no valid images were available for that period.

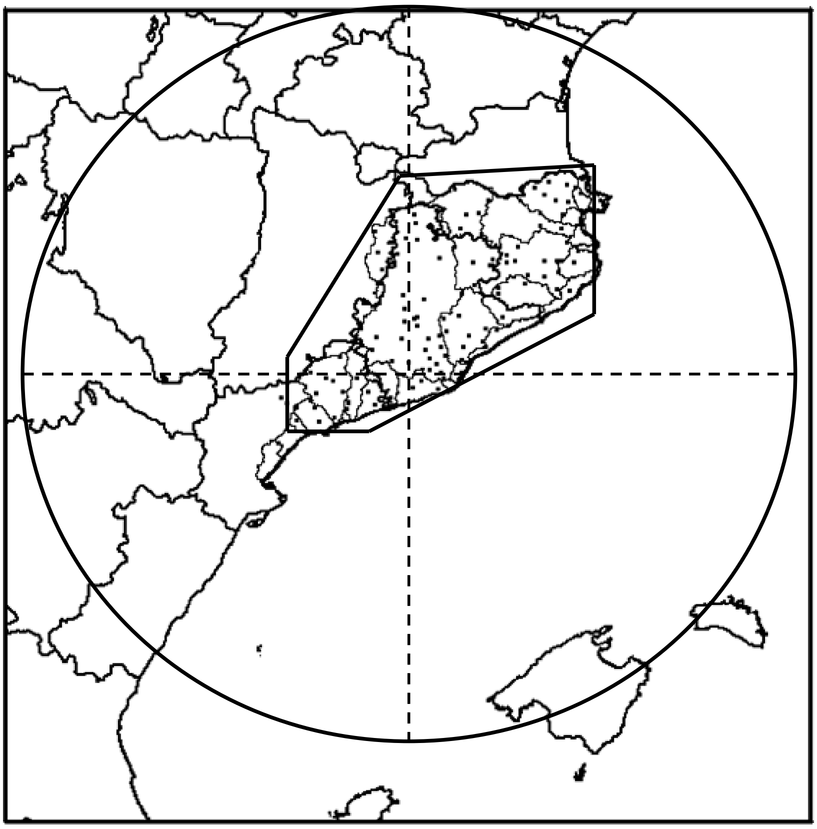

Figure 7.1 **A**rea inside the polygonal line in Catalonia well covered by the 126 ACA rain gauges (little black dots) and affected by the heavies' precipitations. The circle represents the radar area, which is located in Barcelona. The thick continuous line demarcates the Spanish and French provinces and the thin lines, the internal basins in the Catalonia region.

*b) Study methodology*

Radar reflectivies and interpolated rain rates from the ACA network were matched point to point during the hours of heaviest rainfalls in order to capture the main rainfall patterns of the Montserrat storm. The study domain is limited by the closed polygonal line shown in figure 7.1 and the radar-gauge association process was applied from 0020 to 0520 UTC on the 10th of June, every 30 minutes. The period between 0250 and 0430 UTC was avoided for calibration and verification because of the aforementioned radar problems. Table 7.1 shows the simultaneous radar-gauge fields and the number of matched radar-rain points taken into account in the calibration. A total of 38010 points (Table 7.1) were employed to delineate Z-R relationships by the HMT and the DCM and, also, used to test the Marshall and Palmer coefficients.

The verification is performed for rain rates comparing gauge and radar estimations from 2100 UTC on 9 June to 0830 UTC on the 10th of June every 30 minutes. In this case radar rain rates are tested in two ways: firstly, radar estimations are verified with respect to rain gauge data used in calibration in order to analyze the benefits of adjusted methods with respect the standards. Secondly, radar estimations are tested using independent gauge data outside the calibration period. On the other hand three hours of rainfall accumulations from 2100 to 0900 UTC of the next day divided into four periods, are also verified. To obtain the radar and gauge rainfall accumulation maps all available data at the highest temporal resolutions has been used (10 minutes for radar and 5 minutes for gauges).

The statistical indices employed in the quantitative verification in the area well covered by the rain gauges (polygonal area in figure 7.1) are: mean, standard deviation (SD), BIAS, standard deviations difference (SDD), root mean square error (RMS), and correlation coefficient (CORR). Special care has been taken in the present work about the BIAS and SDD parameters because they are used to execute adjustments after the main calibration processes. The first one, as in chapter 5, is the difference between the estimated and the observed spatial averaged precipitation while the second is the difference between both standard deviations, from the estimated and observed fields. Positive values of both parameters, BIAS and SDD, mean radar over-estimation, and negative values, radar under-estimation.

The spatial accuracy of the estimated radar rain rates can be calculated with the help of certain indices. The probability of detection (POD), false alarm ratio (FAR), and critical success index (CSI) indices are based on equations 4.5, 4.6 and 4.7 and computed from a contingency table as shown in section 4.2c of this thesis and described also by Marzban (1998). Another interesting index that can be easily calculated from the contingency table is the fraction correct (FRC) defined as follows.

$$FRC = \frac{hits\ +\ correct\ negatives}{hits\ + misses\ +\ false\ \ alarms\ +\ correct\ negatives} = \frac{A+D}{A+B+C+D} \qquad 7.1$$

where:

- *hits* (*A*), is the number of rain points from the rain gauges correctly estimated as rainy by the radar.
- *misses* (*B*), number of rain gauge points estimated as no rainy by the radar.
- *false alarms* (*C*), number of no rain gauge points estimated rainy by the radar.
- *correct negatives* (*D*), number of no rain gauge points correctly estimated as non rainy by the radar.

The FRC, besides to the CSI, takes into account the correct negatives points giving new information that can be complemented by the CSI. However, the results given by the FRC has to be interpreted with caution. Under certain circumstances of little or weak rainfall (which is not our case), the number of correct negatives (*D*) might be much larger than the rest of the parameters (D >> A, B, C) and therefore, FRC might show a high score, with a value close to one, while the CSI might give a much lower result.

Sometimes the interpretation of the results is not clear when using only the POD or the FAR indices; in these cases we can employ a derived index called the product coefficient POD (1-FAR). It was proposed by Marzban (1998) in order to obtain a unified result based on the two coefficients. This can be applied for the CSI and FRC indices with the direct product of both indices.

Table 7.1. Radar-rain images used for the calibration file generation.

| Day | Hour (UTC) | Number of collocated Z, R points[a] in the domain[b] | Comments |
|---|---|---|---|
| June-10-2000 | 0020 | 5430 | Radar-Rain images present |
| “ | 0050 | 5430 | “ |
| “ | 0120 | 5430 | “ |
| “ | 0150 | 5430 | “ |
| “ | 0220 | 5430 | “ |
| “ | 0250-0420 | 0 | Radar error |
| “ | 0450 | 5430 | Radar-Rain images present |
| “ | 0520 | 5430 | “ |
|  |  | 38010 | Total number of Z, R points in the calibration file |

[a] Every point correspond to a radar-rain image pixel where each one has a spatial resolution of 2 by 2 km.
[b] The domain is limited by the polygonal lines in figure 2 and correspond to the area well covered by the 126 ACA rain gauges.

### *7.2 The Histogram Matching Technique (HMT)*

The HMT was documented for the first time by Calheiros and Zawadzki (1987) as the probability matching method to derive Z-R relations. These relationships were determined to obtain "long-term" rainfall accumulations that can capture the "climatology" of the precipitation of a given space-time domain (Crosson *et al*. 1996). However we are interested in applying this method for the Montserrat flood, in a smaller space-time domain, in order to get a Z-R relation adjusted for this event.

The approach consists essentially of building a Z-R curve on (*Zi, Ri*) pairs in order to match their cumulative distribution functions (*CDFs*) as shown in equation (7.2)

$$CDF(Ri) = CDF(Zi) \tag{7.2}$$

where *CDF*s are defined using continuous functions and approximated later by discrete summations as shown in (7.3) and (7.4):

$$CDF(Ri) = \int_{Rt}^{Ri} F(R)dR \cong \sum_{Rt}^{Ri} F(Ri)\Delta R \tag{7.3}$$

$$CDF(Zi) = \int_{Zt}^{Zi} F(Z)dZ \cong \sum_{Zt}^{Zi} F(Zi)\Delta Z \tag{7.4}$$

*F*(*Ri*) and *F*(*Zi*) are frequency functions, *Rt* and *Zt* are threshold values and *ΔR* and *ΔZ* are constant intervals. To resolve (7.2) and to calculate (*Zi*, *Ri*) pairs we are following the modified procedure described by Atlas *et al*. (1990) according to (7.5) also in the form of discrete summations.

$$\frac{\sum_{Rt}^{Ri} RiF(Ri)\Delta R}{\sum_{Rt}^{\infty} RiF(Ri)\Delta R} = \frac{\sum_{Zt}^{Zi} ZiF(Zi)\Delta Z}{\sum_{Zt}^{\infty} ZiF(Zi)\Delta Z} \tag{7.5}$$

The use of this procedure with the correct threshold values *Rt* and *Zt* guarantees that the (*Zi*, *Ri*) pairs are distributed optimally over the high rain rates, which account for most of the accumulated precipitation. Therefore the threshold values *Rt* and *Zt* are defined so that the rest of (*Zi*, *Ri*) pairs are computed in the rain sector of the dataset. In the case of *Rt*, the minimum detectable rain rate measurable by the gauges is 0.2 mm $h^{-1}$. *Zt* is then chosen so that the percentage of the space-time domain over which $Z \geq Zt$ is equivalent to the percentage of the space-time domain for which $R \geq Rt$ (Rain areas limited by the frequency functions in figures 7.2a and 7.2c have the same size). In the present research all the points from the calibration dataset with a rainfall greater than 0.2 mm $h^{-1}$ is equalized with the number of radar points with a logarithmic reflectivity of 7.5 dBZ or greater. These values are very different from the ones obtained by other authors for diverse places, weather events, other radars and space-time scales. For example, Crosson *et al.* (1996) obtained $Rt = 1.27$ mm $h^{-1}$ and $Zt = 34$ dBZ from five discontinuous days in July and August 1991 in central Florida, with a temporal resolution of 12 minutes and 2x2 km spatial resolution. The present calibration process is focused on the 5 hours of heaviest precipitation that has produced a severe flood in a relatively small region (see Llasat *et al.* 2002). Due to the high variability of precipitation it is not strange to find unexpected results for shorter time periods. On the other hand, stability problems of the Barcelona radar transmitter have been detected, that combined with the strong rainfall over the radar place, resulted in a strong decrease of radar signal mostly between 0250 0430 UTC. This interval has been skipped from the calibration period however; a general small attenuation effect during the rest of the night was reported by Sempere *et al.* (2001). A logical consequence of a reduced radar signal by different causes is a decrease of the *Zt* with respect to normal values.

Based on the threshold values *Rt* and *Zt* the conditional *CDF*s of *R* and *Z* were calculated at 3-mm $h^{-1}$ and 3-dBZ intervals ($\Delta R$, $\Delta Z$) = (3, 3) and plotted in figure 7.2 (*CDF*(*Z*) in figure 7.2a, *CDF*(*R*) in figure 7.2c and *Ri*(*Zi*) in figure 7.2d as HMT curve). For example, in figure 7.2, 30 dBZ is corresponded to a *CDF(Z)* equal to 70% as shown by the red arrows in frame 7.2a. Following equation 7.3, for a *CDF(R)* equal to 70% we have a rain rate *R* around 28 mm $h^{-1}$ as shown in frame 7.2c, so that 30 dBZ is linked to 28 mm $h^{-1}$ and illustrated by the red circle in frame 7.2b (logarithm scale) and 7.2d (direct scale). Numerical results of the *Z*, *R* association and *CDFs* based on the HMT applied for this case are written in Table 7.2. Smooth curves can be drawn through (*Zi*, *Ri*) points, with the best-fit equation ($r^2 = 0.997$) found at

$$R = 0.0485\,Z^2 - 0.7099\,Z + 4.8289 \qquad (7.6)$$

with *R* in mm $h^{-1}$ and *Z* in dBZ as logical. However, in order to avoid errors produced by the employment of smooth curves, it has been decided to interpolate *R* linearly between the closest two values of *Zi*.

The calibration dataset is used also to validate the HMT method for this case by transforming *Z* from the radar to *R* using (7.6) or interpolate *R* linearly between the closest two values of *Zi* (table 7.2) and computing the statistics shown in the inset table on figure 7.2. An analysis of these numerical results demonstrates that relative over-estimation given by the BIAS is greater than 40 % and radar rainfall variability larger than 45 % as shown by the SDD. It seems that the new curve from the HMT has a tendency to produce biased estimations. Different methods were tried in an attempt to reduce these excesses. One of the most simple and effective was just a shift of the entire HMT logarithmic curve horizontally and/or vertically taking in account the evolution of the statistical indices derived from the calibration file. As a result of this last process it has been found, firstly, that CORR decrease is much lower after a horizontal translation of the HMT curve than by moving the curve in the vertical direction. On the second hand it has been observed that the BIAS can be reduced to almost null values and SDD can be decreased as much as 20% by shifting the curve 4 dBZ to the right as illustrated in figure 7.3. Therefore, each reflectivity measurement of the HMT curve was corrected by just adding 4 dBZ and the new Z-R associations are shown in table 7.3. Only the threshold values, Rt and Zt, stay the same as shown in this last table and in figure 7.3, in order to not change the size of the radar-gauge rain areas and to not decrease the accuracy of the rain detection (POD, FAR, CSI and FRC do not change in figure 7.3 after the bias adjustment). Numerical results of the adjusted HMT are shown in table 7.4.

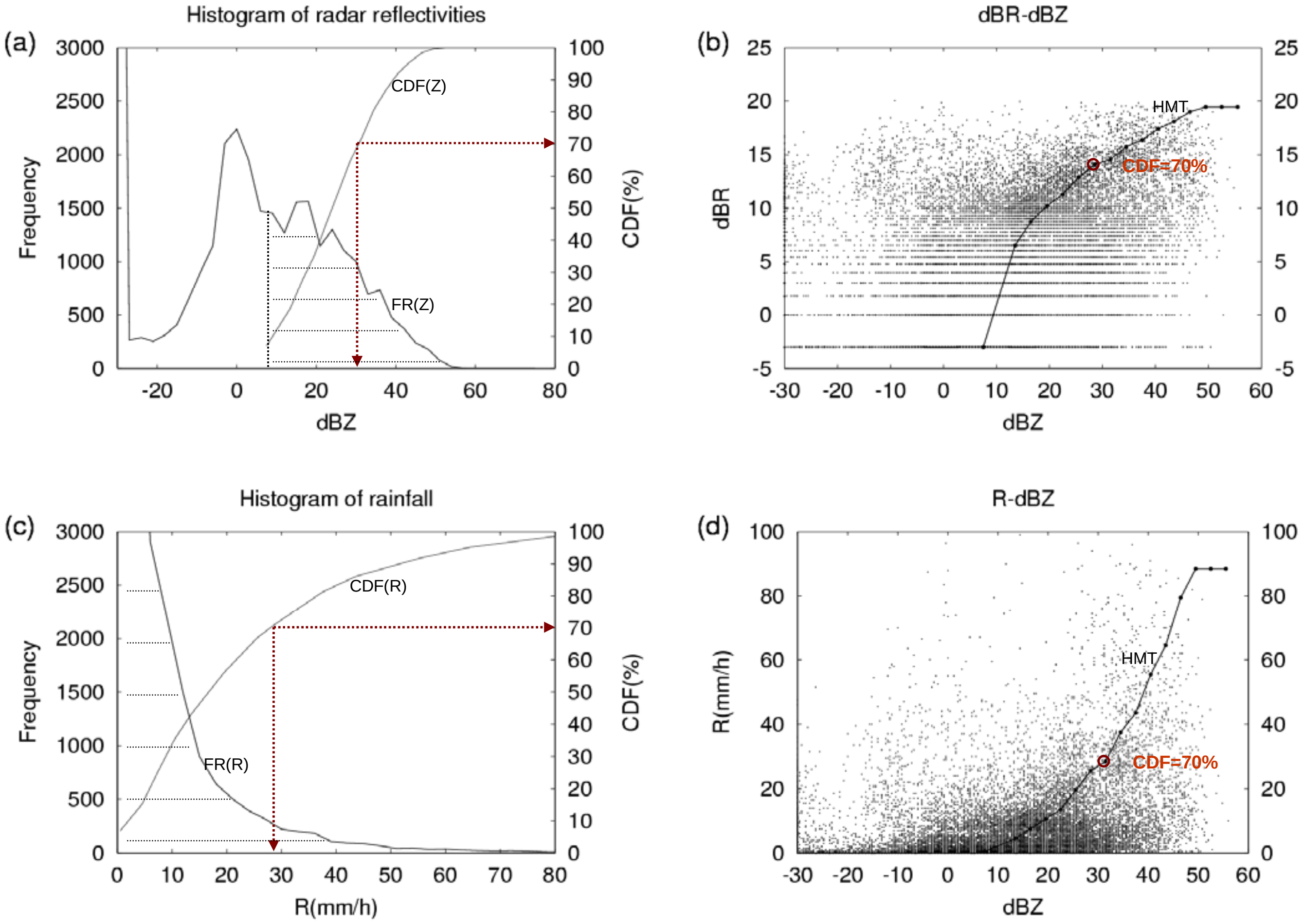

Figure 7.2 (a) Radar frequency, *FR*(*Z*) line and scale in the left axis and radar Cumulative distribution function or accumulated probability *CDF*(*Z*) curve and scale on the right axis. Rain area limited by the frequency function indicated with horizontal dashed lines. It should have the same size than the rain area shown in figure (c) if the threshold values (*Rt*, *Zt*) are correct. (b) Measured radar-rain points from the calibration file within the HMT curve in the logarithmic scale with dBZ and dBR as horizontal and vertical axis respectively. (c) The same than in figure (a) but for the ACA interpolated rainfall. (d) The same than figure (b) but illustrating dBZ versus *R* (rain rate in mm $h^{-1}$).

Table 7.2 cumulative distribution functions (*CDF*) and *Z*, *R* association for the HMT

| *CDF*(*Z*) | *CDF*(*R*) | *Zi*(dBZ) | *Ri*(mm $h^{-1}$) |
|---|---|---|---|
| 4.0 | 5.4 | **7.5** | **0.2** |
| 7.0 | 6.9 | 9.5 | 1.5 |
| 18.7 | 15.1 | 13.5 | 4.5 |
| 27.5 | 25.6 | 16.5 | 7.5 |
| 35.2 | 35.5 | 19.5 | 10.5 |
| 45.2 | 43.1 | 22.5 | 13.5 |
| 54.8 | 56.0 | 25.5 | 19.5 |
| 64.6 | 66.7 | 28.5 | 25.5 |
| 72.1 | 70.7 | 31.5 | 28.5 |
| 80.7 | 81.2 | 34.5 | 37.5 |
| 86.8 | 86.0 | 37.5 | 43.5 |
| 92.0 | 91.9 | 40.5 | 55.5 |
| 95.5 | 95.2 | 43.5 | 64.5 |
| 98.4 | 98.4 | 46.5 | 79.5 |
| 99.7 | 99.9 | 49.5 | 88.5 |
| 100.0 | 99.9 | 52.5 | 88.5 |
| 100.0 | 99.9 | 55.5 | 88.5 |

Table 7.3. *Z*, *R* association for the HMT after BIAS correction

| *Zi*(dBZ) | *Ri*(mm $h^{-1}$) |
|---|---|
| **7.5** | **0.2** |
| 13.5 | 1.5 |
| 17.5 | 4.5 |
| 20.5 | 7.5 |
| 23.5 | 10.5 |
| 26.5 | 13.5 |
| 29.5 | 19.5 |
| 32.5 | 25.5 |
| 35.5 | 28.5 |
| 39.5 | 37.5 |
| 41.5 | 43.5 |
| 44.5 | 55.5 |
| 47.5 | 64.5 |
| 50.5 | 79.5 |
| 54.5 | 88.5 |
| 56.5 | 88.5 |

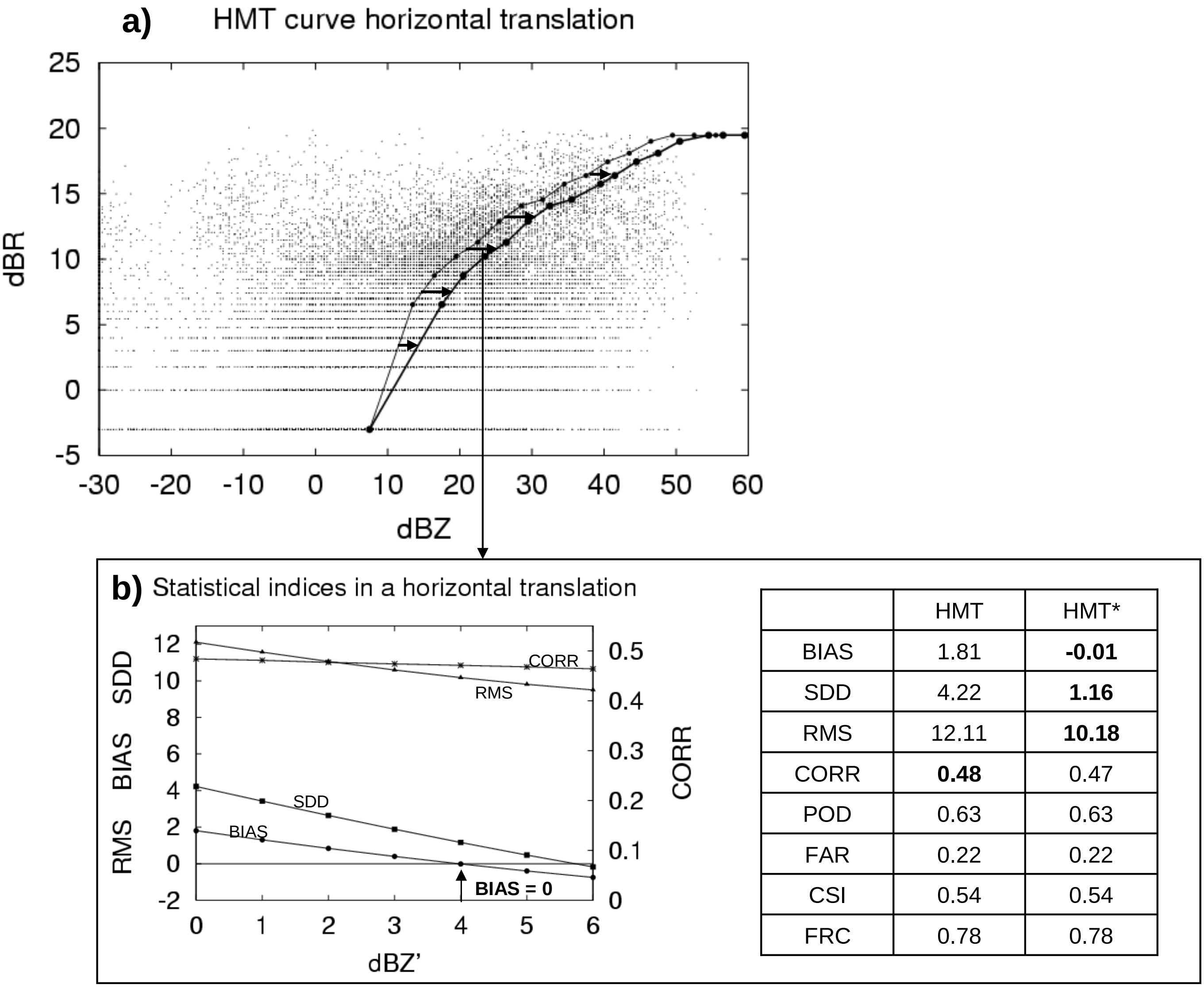

| | HMT | HMT* |
|---|---|---|
| BIAS | 1.81 | **-0.01** |
| SDD | 4.22 | **1.16** |
| RMS | 12.11 | **10.18** |
| CORR | **0.48** | 0.47 |
| POD | 0.63 | 0.63 |
| FAR | 0.22 | 0.22 |
| CSI | 0.54 | 0.54 |
| FRC | 0.78 | 0.78 |

Figure 7.3**.** (a) Measured radar-rain points from the calibration file and HMT curve in the logarithmic scale. The HMT curve is moved 4 dBZ to the right in order to approximate the BIAS to 0 as much as possible. (b) Behaviour of statistical indices with respect to dBZ'. This variable represent the horizontal translation of all the points to the right (dBZ'> 0). The left side of the graph shows the BIAS, RMS and SDD scale and the right the CORR scale. When the BIAS is closer to cero the translation is ended and statistical results are written in the contiguous table. The table show the Statistics before (HMT) and after the BIAS based translation (HMT*).

### *7.3 The Direct Calibration Method (DCM)*

The DCM is based on the $Z = a\ R^b$ relationship derived from the drop size distribution (Marshall and Palmer, 1948). This relation is linear in the logarithmic scale where Z and R are transformed to decibels as $dBR = 10 \log(R)$ and $dBZ = 10 \log(Z))$, so that:

$$dBZ = 10 \log(a) + b\ dBR \qquad (7.7)$$

The coefficients a and b are easily determined from the linear best fit using the Z-R point data from the calibration file. The best-fit equation was found to be

$$dBZ = -50.8131 + 9.4200\ dBR \qquad (7.8)$$

in which $a = 8.2925\ 10^{-6}$ and $b = 9.4200$. *dBR* was solved for *R* and left as a function of *dBZ* as shown in the next equation.

$$R(dBZ) = 10^{\left[\frac{dBZ - 10\log(a)}{10b}\right]} \qquad (7.9)$$

This last equation is very useful because INM radars provide *dBZ* and, with *a* and *b* coefficients, *R* can be easily computed in mm $h^{-1}$. A preliminary evaluation of these new *a* and *b* coefficients confirm that estimated rainfall leads to a bias due to the dominance of the zero and light rain observations. This feature is illustrated in the scatter plot in figure 7.4a in which interpolated gauge rain rates (observed) from the calibration file are compared to the correspondent radar rainfall estimates using the new *a* and *b* coefficients. In this figure a bi-dimensional distribution of frequencies on the densest area of the scatter plot from 0 to 40 mm $h^{-1}$ is shown in the upper right box. Based only on the statistical parameters shown in the first column of the table in figure 7.5, results using the new coefficients appear to be correct, only the SDD from the radar DCM rain distribution is significantly lower (SDD = -7.15 mm $h^{-1}$). The scatter plot in display 7.4a shows that low radar DCM estimates are over measured and estimated rain does not exceed 15 mm $h^{-1}$. The dominance of the zero and light rain observations derived from the best fit equation 7.8 has been corrected empirically case after two steps:

- A Rotation of the calibration regression line in order to increment the slope (figure 7.5a and 7.5b). This process, applied degree by degree, enhances the importance of higher rain rates and increases the dispersion of the estimated rainfall measured by its SD. The difference between estimated and observed SD defined in this work as SDD, changes with the slope angle as shown in figure 7.5a and has a logical tendency to be incremented with the angle of rotation. The centre of rotation was selected searching the point on the line surrounded by as many radar-rain points as possible. Mathematically, the distance (*D*) between the point on the line and each point of the plot from the calibration file ($D_1$, $D_2$ …$D_i$) is first calculated. Then, a weight factor (*W*) associated to each point of the line and defined as the sum of the inverse of the squared distances as shown in the equation 7.10 is computed.

$$W = \sum_{1}^{N} \frac{1}{D_i^2} \qquad (7.10)$$

where *N* is the total number of points used in the calibration (a total of 38010 radar-gauge points). *W* is greater for those line points surrounded by many data points at short distances, while it is lower for those points located far from the main cluster of data points. The centre of rotation is assigned to the point of the calibration line with the highest *W*.

Statistical indices and centre of rotation were calculated iteratively after each increment of the line slope as shown in figure 7.5b. The process continued until the SDD was closest to zero yielding an angle of 25º and the centre of rotation for this last iteration, located at 32 dBZ and 11 dBR (figure 7.5b). At this point the straight line equation is:

$$dBZ = 9.2921 + 2.1386\, dBR \qquad (7.11)$$

- Horizontal translation of the rotated calibration line (frames 7.5a and 7.5c). One way to adjust the BIAS while keeping the CORR unchanged is to move the line horizontally without changing the slope. A translation of 3 dBZ to the left (dBZ'= -3) led to a BIAS close to zero and to an increment of 30% of the SDD (figure 7.5c). This increment can be considered reasonable because radar rain distributions are more spread and irregular than the interpolated rain field from the rain gauges.

Finally, the resulting calibration line equation and $a$, $b$ coefficients after the two processes are:

$$dBZ = 4.8268 + 2.1386\, dBR \tag{7.12}$$

$a = 3.0386$, $b = 2.13869$. Estimated rain rates are higher as shown in the scatter plots in graph 7.4b. While the correlation coefficient is diminished from 0.49 to 0.41 through the two processes the spatial accuracy of radar rainfall is improved as shown by the CSI and FRC indices in figure 7.5. This can be quantified by just multiplying both coefficients, CSI and FRC, that gives 0.18 for DCM, 0.32 for DCM* and 0.34 for DCM** or by applying the product coefficient POD (1-FAR) that provides 0.42 for DCM, 0.36 for DCM* and 0.50 for DCM**. Numerical results of the adjusted DCM are shown in table 7.4, where DCM* refers to the results after rotation and DCM**, after rotation plus horizontal translation.

In another experiment (not shown) the rotation has been performed looking for the angle at which the RMS index begins to grow. This point corresponds to a rotating angle of 18º (display 7.5b) and centre of rotation at -7.2 dBZ, -3.0 dBR. Secondly the BIAS was adjusted to 0 mm $h^{-1}$ by shifting again the whole straight line 8 dBZ to the left. In this case the correlation coefficient was 0.45 but the derived calibration rainfall curve over-estimates rain rate for low reflectivities (a rain rate of 1.6 mm $h^{-1}$ is assigned for 0 dBZ) and the spatial accuracy is worse than the SDD-fit with 0.32 for CSI FRC and 0.46 for the POD (1-FAR) parameter.

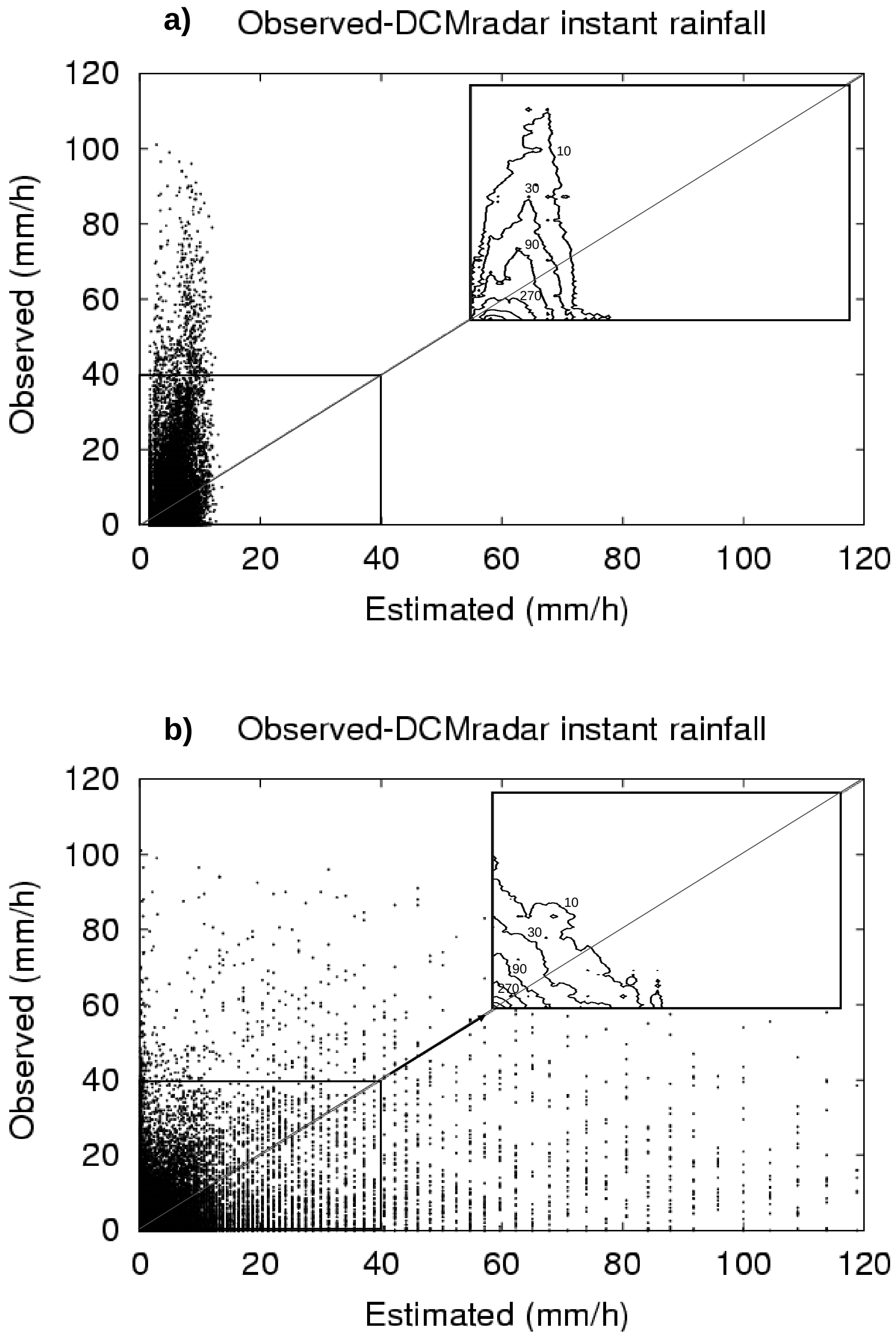

Figure 7.4. Scatter plots made from the calibration file comparing observed versus radar-DCM rain rates using equation (7.10) and a and b coefficients. The upper right box in both diagrams shows a bi-dimensional frequency distribution of the densest area of the scatter plot from 0 to 40 mm $h^{-1}$. (a) DCM dispersion plot results before the SDD based rotation and the BIAS based translation. (b) DCM dispersion plot results with the SDD and the BIAS corrected.

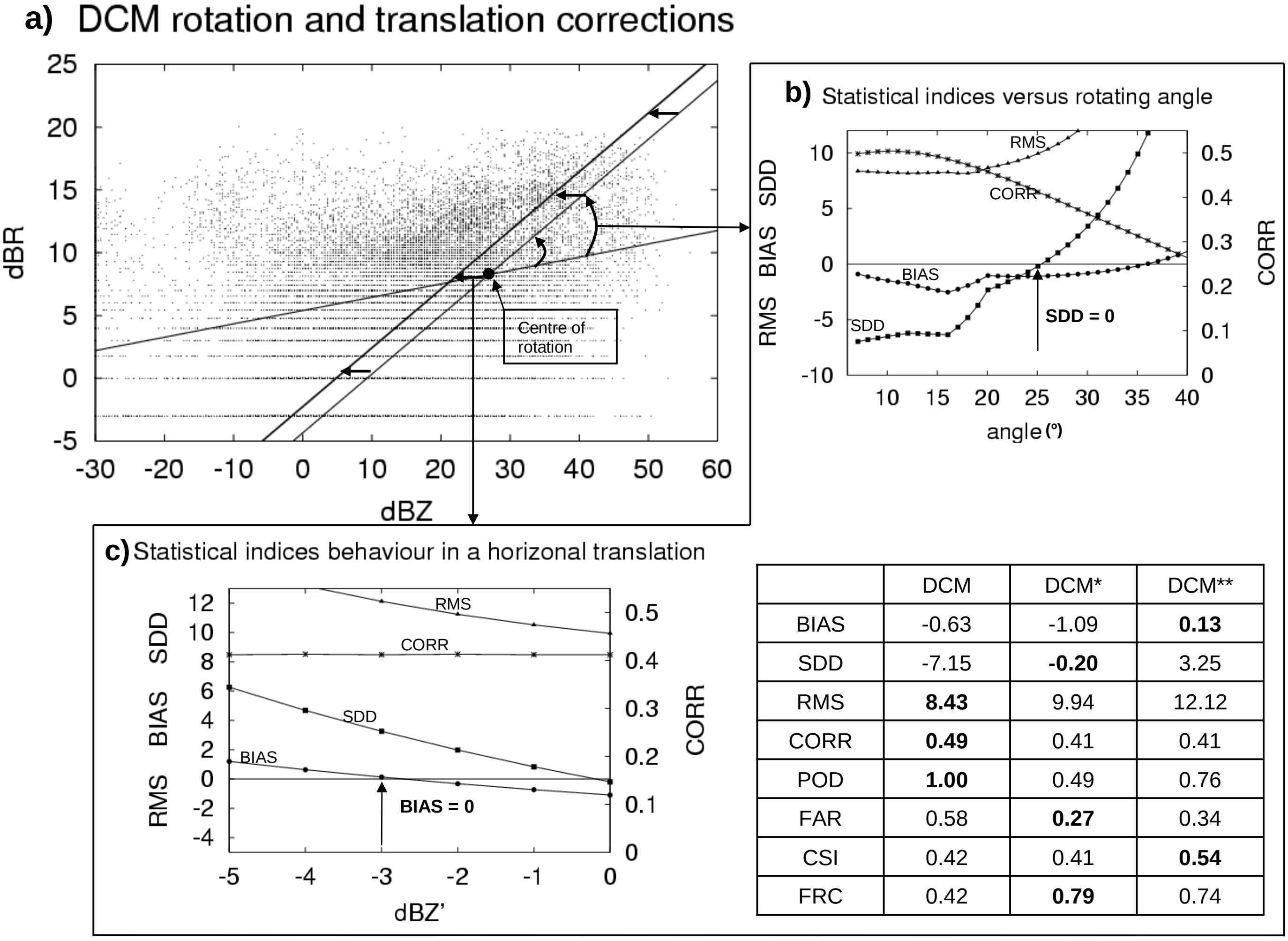

| | DCM | DCM* | DCM** |
|---|---|---|---|
| BIAS | -0.63 | -1.09 | **0.13** |
| SDD | -7.15 | **-0.20** | 3.25 |
| RMS | **8.43** | 9.94 | 12.12 |
| CORR | **0.49** | 0.41 | 0.41 |
| POD | **1.00** | 0.49 | 0.76 |
| FAR | 0.58 | **0.27** | 0.34 |
| CSI | 0.42 | 0.41 | **0.54** |
| FRC | 0.42 | **0.79** | 0.74 |

Figure 7.5. Illustration of the SDD and BIAS corrections for the DCM regression line. (a) DCM calibration straight line from equation 7.8 firstly rotated and secondly translated in the logarithmic scale. (b) Behaviour of statistical indices with respect to the angle of rotation. Statistical results are shown in the second column of the table (DCM*) for the angle in which the SDD is closer to 0. (c) Evolution of statistical indices for the DCM line shifting. This process is done until the BIAS is closer to 0 and at this point results are written in the last column of the table (DCM**).

### *7.4 Standards methods (MPS, MPC)*

These methods are based on the use of the Marshall and Palmer Z-R relationship taking into account coefficients for stratiform rain ($a$ = 200, $b$ = 1.6) and convective rain ($a$ = 800, $b$ = 1.6) according to the bibliography. In practice rain fields were computed transforming *dBZ* to *R* using equation 7.9 but changing the *a* and *b* coefficients in each case. In the present research, radar rain fields obtained by the Marshall and Palmer stratiform rain coefficients are called MPS and the ones obtained with the convective coefficients are called MPC. Both MPS and MPC curves have a clear tendency to under-estimate radar rain rates as revealed by the negative BIAS and very low SDD (table 7.4). The MPS and MPC rain curves in figure 7.6b require very high reflectivities to estimate substantial rain rates, but in the logarithmic scale, shown in figure 7.6b, the MPS and MPC linear relations have higher slopes than the adjusted DCM line. On the other hand is easy to observe that the adjusted HMT and the final DCM curves are nearly similar to one another in both figures (7.6a and 7.6b).

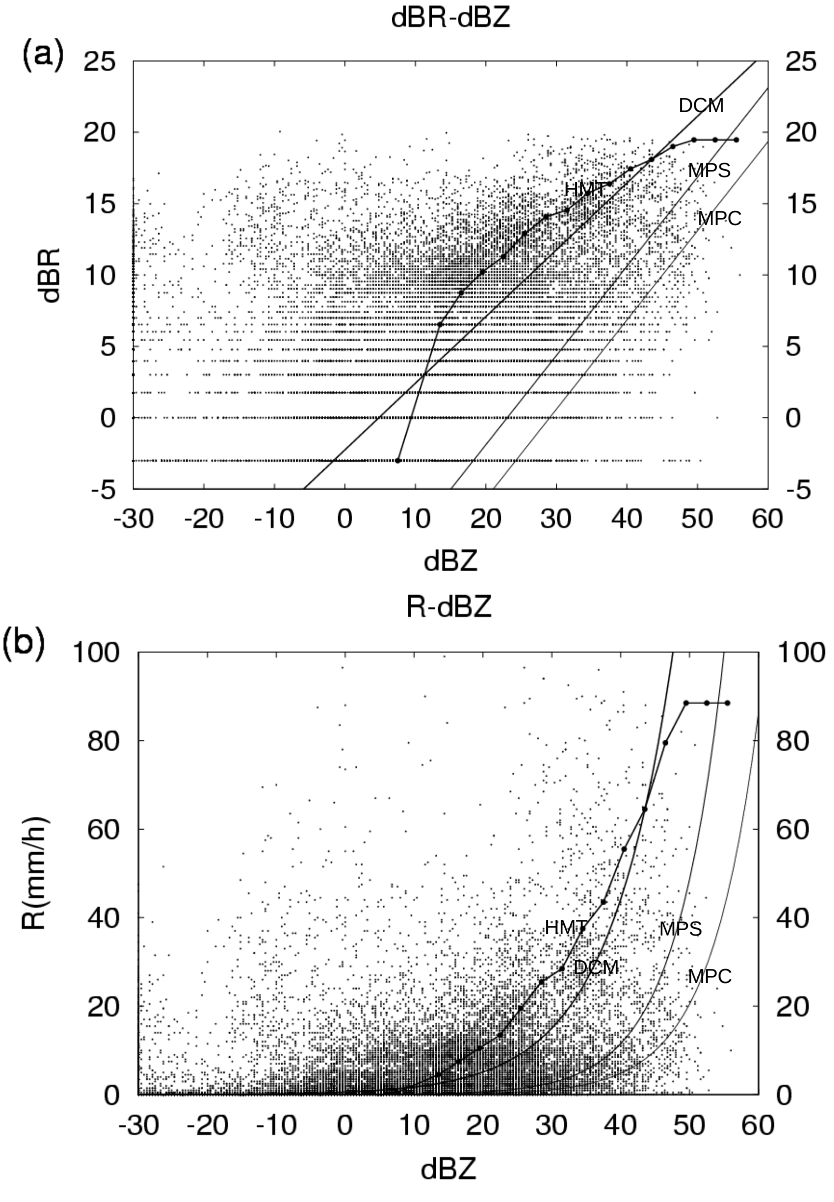

Figure 7.6 (a) Measured radar-rain points from the calibration file in the logarithmic scale with dBZ and dBR as horizontal and vertical axis respectively. HMT curve, DCM regression line, MPS and MPC lines. (b) The same than (a) but representing dBZ versus *R* (rain rates in mm h$^{-1}$).

### *7.5 Results of radar estimates*

Results are divided in two parts: First, validation of the calibration methods and rain rates by comparing instant ground interpolated rain rates with radar rainfall from the different methods and times is presented. Second, radar rain three hours accumulations versus ACA accumulations have been verified. In the rest of the chapter we are referring to the BIAS adjusted curve as HMT and BIAS plus SDD adjusted curve as DCM.

#### *a) Calibration methods and rain rates*

Qualitative comparisons between radar and ground rainfall fields show, in general, a good spatial correspondence. On the rain rates images, (not shown) big differences can be observed between the new methods (HMT and DCM) and the old ones (MPS and MPC). However, a quantitative analysis is important to determine the accuracy of the HMT and the DCM, since rain rate images in both cases look very similar. Radar rain rates and algorithms have been verified using interpolated gauge data as so-called “ground true” at different times than the ones used in calibration. In Table 7.4 it is shown numerical results employing data from calibration (half top) and independent (half bottom). It is easy to see how BIAS and SDD are smaller for the HMT and the DCM in the first case (half top of table 7.4), since both parameters have been minimized during the calibration process. The MPS and MPC obtained the lowest correlations and they under-estimate rain rates as indicated by the strong negative BIAS and SDD in both cases. Based only on the verification with independent data (half bottom of table 7.4), the HMT is the method that provides, in general, the best CORR, SDD and FRC. Then the DCM gets the best POD and CSI, the next best CORR and also a low BIAS but a higher SDD than the HMT (higher dispersion of the DCM estimates). The spatial distribution of rain rates cannot be evaluated easily only from the spatial statistics (POD, FAR, CSI and FRC) shown in table 7.4, but a special combination of these indices such as CSI FRC and POD(1-FAR) can help to clarify this aspect. For the HMT these relations provide 0.42 and 0.49, respectively; for the DCM, 0.40 and 0.50; for the MPS, 0.28 and 0.36; and finally, for the MPC, 0.19 and 0.24. Both methods, HMT and DCM, give similar spatial accuracy for rain rates and are significantly better than the other two.

Table 7.4. Statistical results for rain rates estimated by the different methods using data from the calibration dataset (half top) and independent (half bottom). The size is the number of radar-rain points considered in the verification. Mean, SD (Standard deviation), SDD (Standard deviation difference), BIAS and RMS (root mean square error) are in mm $h^{-1}$. The rest has no units. Boldfaced numbers show best statistical results in every line.

| | OBS | HMT | DCM | MPS | MPC |
|---|---|---|---|---|---|
| Size | | | 38010 | | |
| Mean | 4.3 | 4.4 | 4.4 | 1.0 | 0.4 |
| SD | 9.3 | 10.3 | 12.5 | 4.0 | 1.7 |
| BIAS | | **0.1** | **0.1** | -3.3 | -3.9 |
| SDD | | **1.0** | 3.3 | -5.3 | -7.6 |
| RMS | | 10.1 | 12.1 | **9.7** | 9.8 |
| CORR | | **0.47** | 0.41 | 0.34 | 0.34 |
| POD | | 0.63 | **0.76** | 0.41 | 0.28 |
| FAR | | 0.22 | 0.34 | 0.13 | **0.11** |
| CSI | | **0.54** | **0.54** | 0.39 | 0.27 |
| FRC | | **0.78** | 0.74 | 0.73 | 0.69 |
| Size | | | 114030 | | |
| Mean | 3.5 | 3.9 | 3.7 | 0.8 | 0.3 |
| SD | 7.1 | 8.8 | 10.3 | 3.3 | 1.4 |
| BIAS | | **0.2** | **0.2** | -2.7 | -3.1 |
| SDD | | **1.8** | 3.3 | -3.8 | -5.7 |
| RMS | | 8.7 | 10.1 | **7.3** | 7.4 |
| CORR | | **0.42** | 0.38 | 0.31 | 0.31 |
| POD | | 0.54 | **0.64** | 0.34 | 0.22 |
| FAR | | 0.16 | 0.27 | 0.13 | **0.11** |
| CSI | | 0.49 | **0.52** | 0.33 | 0.21 |
| FRC | | **0.71** | 0.69 | 0.63 | 0.58 |

### *b) Three hours accumulated radar rainfall*

The observed accumulated rainfall from the ACA network during 3 hours time spans in the period of heaviest precipitation of the Montserrat event is shown in figures 7.7a to 7.7c. Most of the rainfalls occurred over an area between the provinces of Tarragona (T), Lleida (L) and Barcelona (B) from 2100 UTC 9 June to 0600 UTC the next day.

Three hours radar rainfall derived from the 4 methods is shown in frames 7.7d to 7.7o, in which the period 0300 - 0600 UTC 10th June has been omitted owing to radar attenuation problems. In these figures the ability of radar to capture the fine details of the precipitation fields is worthy of note. The spatial distributions are very similar among the different calibration methods. On the other hand, rainfall amounts vary significantly from the HMT and DCM to the MPS and MPC (figure 7.7). The HMT and

DCM accumulations are very close to those measured by the ACA network. However, it is important to note that the maximum derived from the DCM between 00-03 hours (frame 7.7h) around 150 mm does not agree with the observed maximum of 115 mm (frame 7.7b). Second, the maximum estimated by the HMT between 06-09 hours (figure 7.7f) is around 80 mm, which disagrees with the observation of 45 mm from the ACA (figure 7.7c). The MPS and MPC accumulations are, in general, 20 mm and 40 mm below the observed amounts respectively.

Statistical indices are shown in table 7.5 for each method and for every time period. A brief analysis of this table illustrates that the correlation coefficient (CORR) decreases with the time period evolution for the four methods. The time lapse between 0000 to 0300 of day 10 was used also for the calibration of the algorithms, thus minimum BIAS errors are obtained for the HMT and DCM for 10/00-03 UTC accumulations as shown in table 7.5. Therefore this period was not taken into account in the global validation revealed in table 7.6. This last table, since it is more general, shows that the HMT provides the best spatial skill with a global CORR of 0.76 and also the best RMS. On the other hand the DCM gives the best precipitation amounts with a BIAS around 1.2 mm and a SDD of 5.3 mm while the CORR is a bit lower than the HMT. The MPS and MPC methods obtain both the lowest CORRs, they have a clear tendency to under-estimate accumulated precipitation as indicated by a strong negative BIAS and SDD.

Figure 7.8 displays observed versus estimated scatter plots for each method using all the 10860 grid points resulting from the two independent radar-gauge periods of accumulated precipitation. The scatter plot of the HMT and the DCM (figures 7.8a and 7.8b) are very similar but estimated amounts from the DCM are a bit more spread out with maximums values of 125 mm, while HMT estimated maximums are around 93 mm. It can be observed that the MPS and MPC (graphs 7.8c and 7.8d) under-estimate many observed rainfall amounts, since most of the points are closer to the vertical axis of the two plots.

Table 7.5. Results comparing 3 hours accumulated radar rainfall derived from the different methods and observed accumulations from the ACA network. The size is the number of radar-rain points. Mean, SD (Standard deviation), SDD (Standard deviation difference), BIAS and RMS (root mean square error) are in mm in 3 hours. The rest has no units. Boldfaced numbers show best statistical results in every line.

| | OBS | HMT | DCM | MPS | MPC | Day/period (hours) |
|---|---|---|---|---|---|---|
| Size | 5430 | | | | | 09/21-24 UTC |
| Mean | 5.8 | 8.2 | 9.4 | 2.2 | 1.0 | |
| SD | 10.4 | 15.3 | 18.0 | 5.3 | 2.2 | |
| BIAS | | **2.5** | 3.7 | -3.5 | -4.8 | |
| SDD | | **5.0** | 7.6 | -5.1 | -8.2 | |
| RMS | | 9.1 | 12.1 | **8.1** | 10.1 | |
| CORR | | **0.84** | 0.80 | 0.75 | 0.75 | |
| Size | 5430 | | | | | 10/00-03 UTC |
| Mean | 12.8 | 12.7 | 13.5 | 3.1 | 1.3 | |
| SD | 16.5 | 20.2 | 23.6 | 7.1 | 3.1 | |
| BIAS | | **-0.1** | 0.7 | -9.6 | -11.5 | |
| SDD | | **3.7** | 7.1 | -9.4 | -13.5 | |
| RMS | | **12.0** | 15.2 | 15.8 | 18.5 | |
| CORR | | **0.81** | 0.77 | 0.71 | 0.70 | |
| Size | 5430 | | | | | 10/06-09 UTC |
| Mean | 11.5 | 12.2 | 10.2 | 1.6 | 0.6 | |
| SD | 8.0 | 14.6 | 11.2 | 2.0 | 0.9 | |
| BIAS | | **0.6** | -1.4 | -10.0 | -10.9 | |
| SDD | | 6.6 | **3.1** | -6.0 | -7.2 | |
| RMS | | 11.0 | **8.1** | 12.1 | 13.3 | |
| CORR | | **0.70** | **0.70** | 0.64 | 0.61 | |

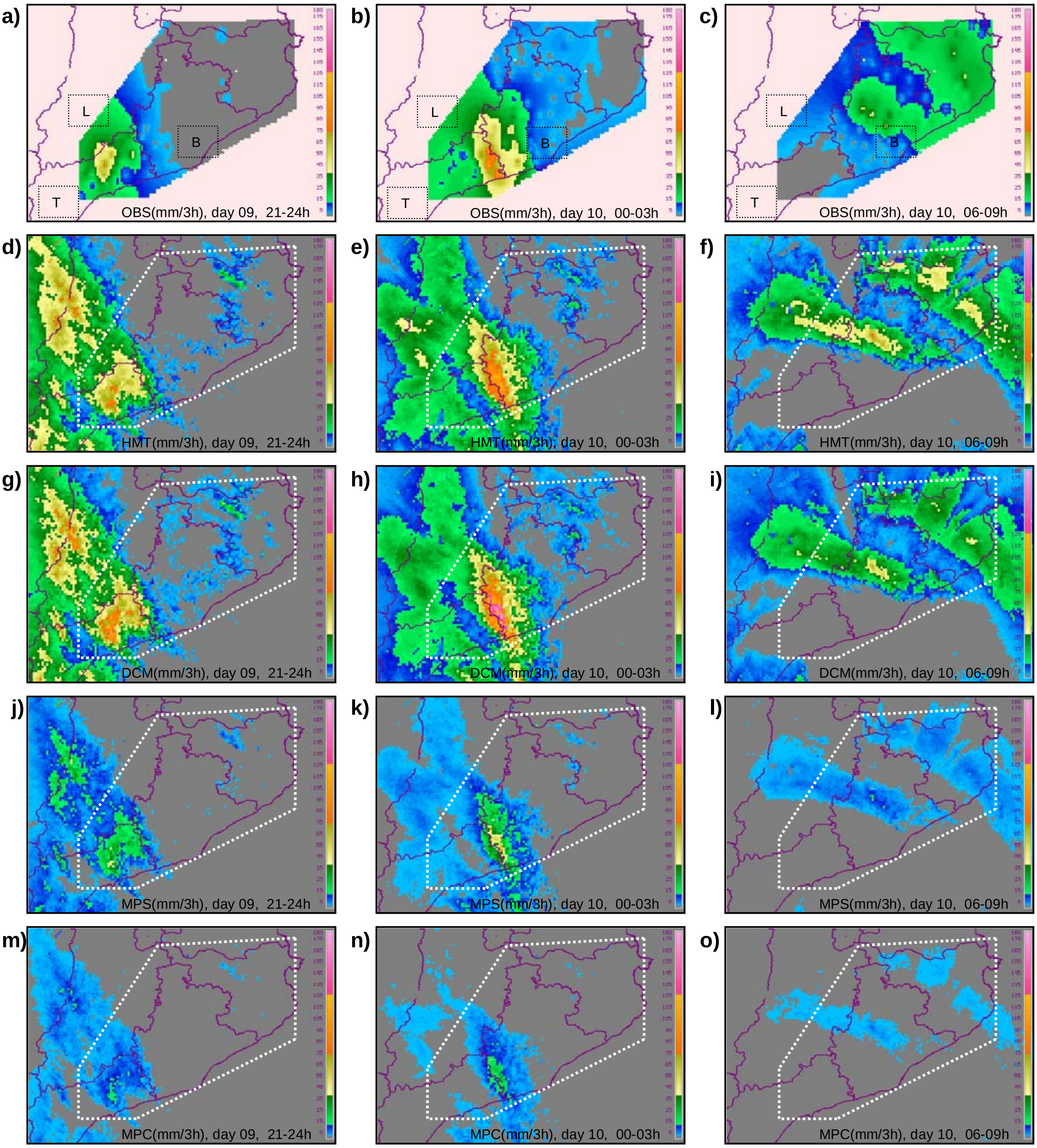

Figure 7.7. (a), (b) and (c) Observed 3 hours accumulated rainfall on the Catalonian provinces during the period of heaviest precipitations in the last hours of the day 9 and the first hours of the next day. The main precipitation occurred over Tarragona (T), Lleida (L) and Barcelona (B). Accumulations from the ACA rain gauges are spatially interpolated by a kriging analysis method and used as so called “ground true” for the verification of the radar accumulations. Rest of frames are radar rain accumulations for the same time periods (3 hours) derived by the different methods: HMT (d) to (f), DCM (g) to (i), MPS (j) to (l) and MPC (m) to (o). The period between 0300 to 0600 UTC day 10 has been omitted because of radar problems.

Table 7.6. Global statistical results with same units than table 7.5 but taking the two 3 hours accumulation periods different from the calibration period.

| | OBS | HMT | DCM | MPS | MPC | Day/period (hours) |
|---|---|---|---|---|---|---|
| Size | | | | 10860 | | |
| Mean | 8.6 | 10.2 | 9.8 | 1.9 | 0.8 | |
| SD | 9.7 | 15.1 | 15.0 | 4.0 | 1.7 | |
| BIAS | | 1.5 | **1.2** | -6.7 | -7.9 | 09/21-24 UTC +<br>10/06-09 UTC |
| SDD | | 5.4 | **5.3** | -7.3 | -8.0 | |
| RMS | | **10.1** | 10.3 | 10.3 | 11.8 | |
| CORR | | **0.76** | 0.74 | 0.63 | 0.62 | |

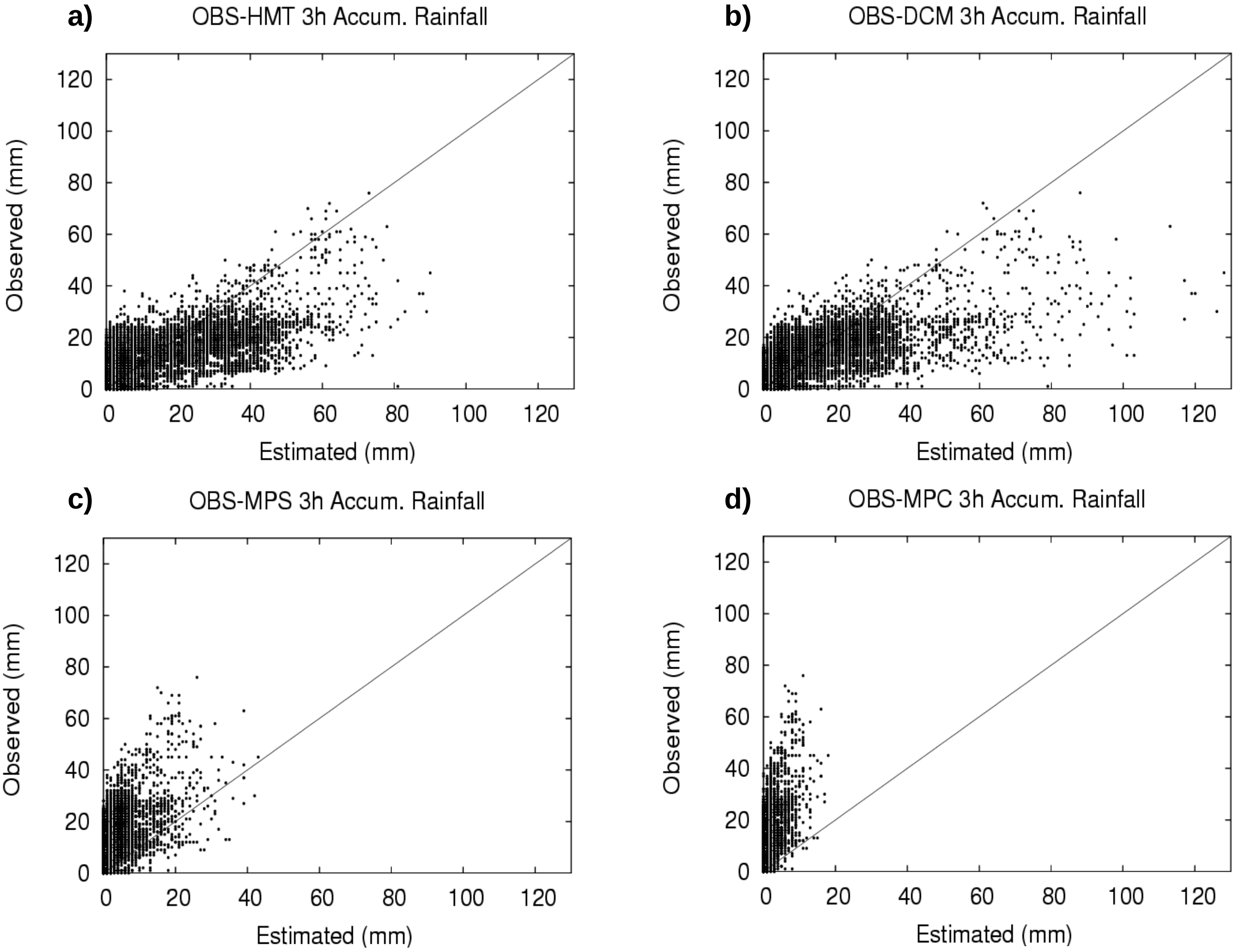
**a)** OBS-HMT 3h Accum. Rainfall

**b)** OBS-DCM 3h Accum. Rainfall

**c)** OBS-MPS 3h Accum. Rainfall

**d)** OBS-MPC 3h Accum. Rainfall

Figure 7.8. Observed by the ACA network versus radar estimated scatter plots for each method. It is plotted the 10860 points of accumulated precipitation collected during the two calibration independent periods (9/21-00 UTC + 10/06-09 UTC).

### *7.6 Discussion and conclusions*

#### *a) Discussion*

This chapter highlights the difficulties in estimating accurate radar rain rates by employing standard algorithms for severe events with heavy rainfalls. In fact, old coefficients such as those proposed by Marshall and Palmer have produced substantial errors, mostly in the areas where the maximum precipitation amounts were observed. Therefore, radar and rain gauges can be combined to improve the spatial distribution of the precipitation field and to accurately gain rainfall amounts within an operational context. However, as commented in previous chapters, calibration routines in real time produce other problems not explored here like: definition of calibration-application optimal time periods, rain gauge and radar data availability in real time and automatic quality checking to detect errors in the data stream.

The direct inter-comparison between instantaneous and simultaneous measurements such as radar reflectivity versus interpolated rain rates from the stations, produces a very widely spread distribution of the data as illustrated in figure 7.2d for the calibration file. Many reasons may be behind this increment of the dispersion. The kriging analysis method, employed for the spatial interpolation of the rain rates, probably produces errors mostly in mountainous regions because stations are often located in valleys. Also, there is a residual time lapse, not analysed by us, between radar detected targets at a height and the rain rate measured by a station on the ground. Radar signal may be attenuated in some areas, mainly places farther than 100 km from the radar site, such as part of the province of Girona located in the northeastern corner of the polygonal area (see any frame of figure 7.7).

An extended procedure in many meteorological centres is the separation of convective radar pixels from stratiform pixels by different techniques and later assignment of those pixels to the corresponding Marshall and Palmer convective or stratiform *a* and *b* coefficients. Choice of this option in the Montserrat case results in precipitation being somewhere between the MPS and the MPC developed in the present research, and therefore rain rates and accumulations would also be under-estimated. If calibration coefficients or tables are regularly updated in time (a few hours or few days) the main convective or stratiform character of the rainfall would be presumably captured within the new algorithm.

The synchronisation of radar points with interpolated rain gauge points on a limited area by searching the same *CDF* (Cumulative Distribution Function) value, such as performed initially by the HMT, has produced BIAS and SDD errors in the over-estimation of rainfall. Previous studies have documented radar over-estimation, in most cases applying probability matching curves (Crosson *et al.* 1996) and other authors (Krajewski and Smith, 1991) have also reported a tendency to produce biased estimates. In the present work a simple horizontal shift of the HMT curve seems to correct the BIAS error keeping the correlation coefficient almost unchanged.

The DCM was delineated directly assuming a fixed drop size distribution function (Marshall and Palmer, 1948) and computing, initially, the function coefficients by linear regression fit using the data from the calibration file in the logarithmic scale. These coefficients were readjusted in a second stage, applying a completely new methodology based on iterative slight rotations and conversions of the calibration line. This new method has demonstrated to be valid at least for the present flood case, however, many more cases should be tried in order to gain accurate assessment.

Radar fluctuations or small attenuations due to strong rainfall or caused by radar internal problems as reported by Sempere *et al.* (2001) for the same flood case, can not be avoided or easily corrected but radar rainfall estimations can be stabilised as much as possible performing calibration routines and testing results in short time periods.

### *b) Conclusions*

Old radar algorithms not adjusted or corrected for a specific area such as the MPS and MPC can produce significant errors in rainfall rates and accumulations. Secondly, for independent rain rate evaluation, both methods, HMT and DCM, have similar spatial accuracies and are sensibly better than the other two. Thirdly, for independent 3 hour accumulation verification, the HMT adjusted by the BIAS is the method that provides the best CORR and RMS while the DCM gives the best BIAS and SDD.

It is important to note that our results in radar calibration are derived under the circumstances of a flood case and should not be applied directly to events in other areas and situations. The authors have concentrated on providing the technical details necessary to develop similar methodologies in the operational context rather than to analyze the benefits for a large sample of events.

An open question is how long the calibration time lapse should be in order to get the highest radar rainfall accuracy. Table 7.5 shows that errors are higher for some periods than others. Experiments for the near future will explore the benefits of using shorter time periods (2-3 hours) to perform an optimal calibration process. This can be applied iteratively in order to capture rapid changes between radar reflectivity and rain rates. It is clear that the success of those techniques for operational purposes depends crucially on the radar and rain gauge data availability in real time.

## 8. Study of the Montserrat flood from the satellite perspective

### *a) Abstract*

This section assesses the accuracy with which geostationary satellite imagery can be used to estimate precipitation in Montserrat flash flood episode in Catalonia, Spain on days 9-10 June 2000. This well documented severe weather event was produced by a cold front perturbation combined with hot and moist air from the Mediterranean that favored a very unstable environment over the northeast of Spain. The main difficulty found in this case for the use of infrared Meteosat images to estimate precipitation was that convective cells were mostly covered by clouds with homogeneous and relatively warm tops, causing low accuracy when rain rates are estimated from satellite in preliminary attempts.

The Auto-estimator and CRR (Convective Rainfall Rate) algorithms were applied and a sensitivity test of rainfall correction factors like: parallax, orographic, moisture, cloud growth rate and cloud top temperature gradient for both methods was performed. Recalibration of the two algorithms using radar and rain gauges was done and evaluated. Finally, lightning data was implemented to facilitate the detection of convective zones. As shown in the following sections; the most outstanding result is an increment in the correlation coefficient of around 10% in satellite rain rates compared to radar and 19% in 24 hour rain accumulations after assimilating lightning data from the INM detector network.

### *b) Introduction*

Meteosat-7 infrared images show relatively warm and homogeneous cloud tops over the flood area (infrared temperatures were not below 218 K at any time)and from the numerical simulation it has been deduced that the perturbation has a cold frontal configuration (Martin *et al*. 2006) while radar images illustrated strong convective cells embedded in the system. This kind of cloud top produces rain rate under-estimation and significant errors in the accuracy of rain detection from satellite compared to radar, as occurred in preliminary attempts. Figure 8.1a illustrates the differences between infrared cloud top shape observed from Meteosat and radar reflectivity, taking into account that the microwave radar beam has the ability to travel through the cloud systems. Such frontal perturbations, very common in the western Mediterranean countries, have the most intense convective levels close to the base of the cloud system and thus, are difficult to be screened accurately from satellite. Valuable information about the cloud base is the location and intensity of rays between the cloud base and the ground provided by a lightning detector network. The hypothesis made is that lightning measurement that is associated with electrically charged ice particles in movement can provide better identification of the convective area, which could contribute to improving precipitation estimation (see figure 8.1).

The idea of combining lightning data with satellite data for rainfall estimation is not new. Among the latest approaches, Morales *et al.* (1997) have shown that lightning measurements associated with active convection in clouds can provide reliable delineation of the convective cores. Grecu *et al.* (2000) used a combination of lightning and infrared brightness temperature to retrieve rainfall. They showed that this combination could reduce the error variance by around 15% of rain volume estimation compared to an infrared only approach. Morales *et al.* (2003) proposed a real time precipitation estimation algorithm that had reduced bias errors by using lightning information and had produced sensible increments in correlation compared with a TRMM precipitation radar images.

The research is focussed on a study made for the Montserrat flood case in which rain rates were difficult to estimate by the satellite as a cause of a relatively warm and homogeneous cloud tops. Under these circumstances the two proposed algorithms, Auto-Estimator and CRR, are applied and later modified by different rainfall corrections. In a second stage both algorithms are recalibrated to study the differences in rain curves and matrices and finally, lightning information is assimilated as another correction factor in order to centre the main precipitation in the most convective zones.

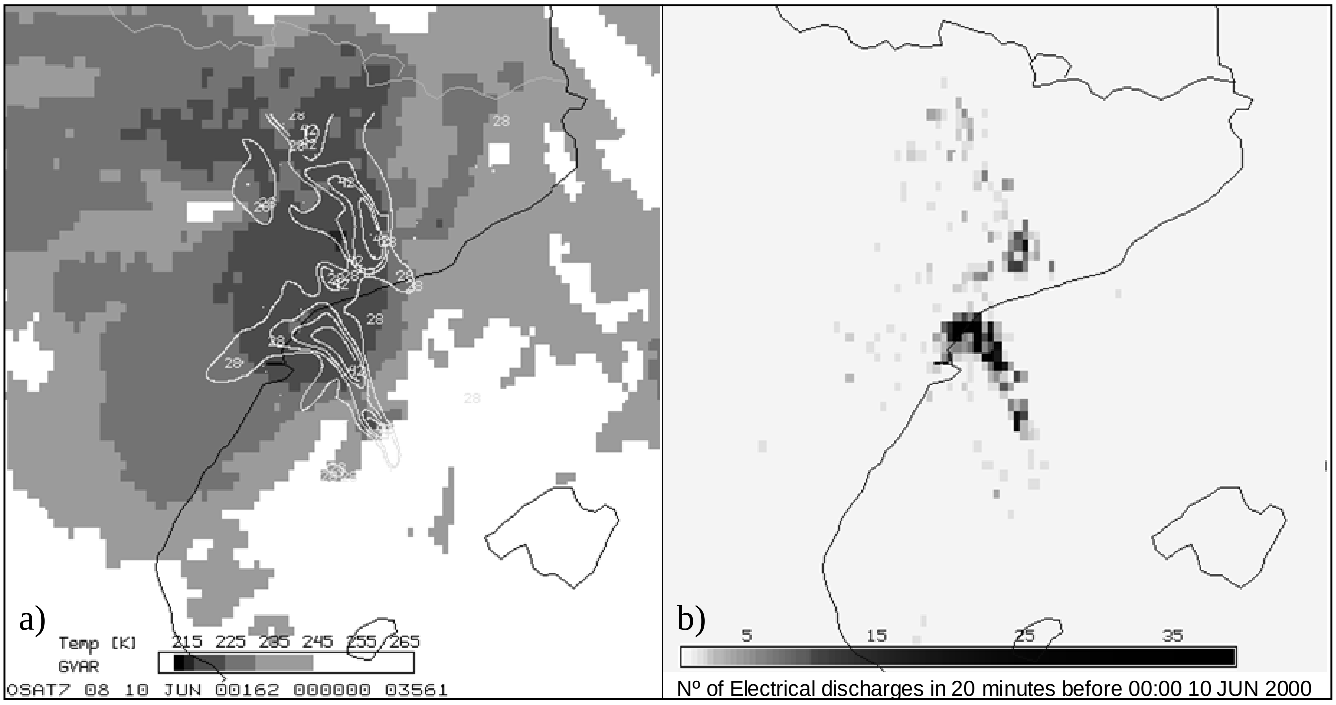

Figure 8.1 (a) Radar reflectivities (white continuous line, in dBZ) and satellite infrared brightness temperature (shaded according to scale, in K): at 0000 UTC 10 June 2000. (b) Electrical discharges on the satellite resolution in 20 minutes from 2340 UTC 9 June to 0000 UTC 10 June 2000. A total of 1520 discharges were detected and a total 201 satellite pixels were touched in this time lapse. Comparing both images, (a) and (b), is important to note the high spatial correspondence between the radar highest reflectivities and pixels touched by the electrical activity.

### *8.1 Data and study methodology description*

*a) Datasets*

Meteosat-7 images of the three spectral bands provided by EUMETSAT every 30 minutes with a pixel spatial resolution over Spain around 7 by 5.5 km lat-lon are used. The period of the satellite dataset used in this study was from 1130 UTC June 9th to 1230 June 10th of 2000.

Radar data from the INM radar of Barcelona and ACA network rain gauge measurements as detailed in section 7.1 of this thesis are used. The radar images, initially in reflectivity units (dBZ), are transformed into rain rate (mm $h^{-1}$) using table 7.3 derived from the HMT, as it was the method that has provided the best CORR as shown in the previous chapter. Then, radar rainfall images are remapped to the geostationary satellite images projection and resolution. As commented in chapter 7, attenuation problems have occurred in radar images from 0250 to 0430 UTC, presumably due to the high precipitation rate over the radar site and no valid images are available for that period. The ACA rain gauge measurements are employed to produce 24 hours of accumulated rainfall fields starting at 1200 UTC June 9 in the polygonal area covered by the stations (Figure 7.1). First, accumulations from the original rain rates, completed each 5 minutes, are calculated on every station point and secondly a kriging analysis method is applied to compute the precipitation fields that are later remapped to the Meteosat-7 images projection and resolution. This rain gauge network can be considered dense enough to perform the mentioned kriging method using a linear model for the variogram fit as made also in chapter 5 with the Albanian rain gauge network.

The detection network for electrical discharges of the INM has been working since 1992 with an initial deployment of 14 detection stations on the Spanish mainland and one in the Balearic Islands. Cooperation with France in 1999 raised this number to 20 IMPACT (Improved and Combined Technology) stations, 5 in the south of France and the rest in Spain. In June of 2000 the Catalonian region was well covered by the INM lightning network with a detection efficiency estimated over this area of around 90% (Pérez Puebla F., 2004). Figure 7.1 illustrates the position of the detector stations represented by black boxes. Every electrical discharge between the ground and the cloud base occurred over Spain and western Mediterranean Sea is detected (position, time and intensity) and stored by the INM. Data for June 9 and 10 of 2000 were kindly provided by this institution for the present research and it makes possible the generation of lightning images every 30 minutes as shown in Figure 8.1b.

### *b) Study methodology description*

The study can be structured into four parts. The first one is an assessment of the Auto-Estimator (A-E in the following) and CRR techniques within a sensitivity test of rainfall correction factors such as moisture, grow rate, gradient, parallax, orographic, etc, is performed. As in the Albanian flood case, 2-D and 3-D matrices calibrated over Spain (tables 4.3d and 4.5 respectively) are used by the CRR method and the required

MM5 outputs from the smaller domain focused over Montserrat and set as described in section 6.1 are employed for the moisture and orographic correction factors performance. Next, the A-E curve and CRR 2-D matrix are recalculated using the rainfall provided by the radar in order to study the deviation from average produced in the Montserrat flood. Thirdly, electrical discharges accumulated in a time lapse of 20 minutes are displayed in images each 30 minutes and compared to the radar ones to confirm the correct detection of the most convective cells. Then a new correction factor based on this lightning information is delineated to detect and enhance satellite estimated convective rain rates against the stratiform ones. Finally, the A-E curve and CRR 2-D matrix are recalibrated again but now using in situ rain gauge measurements instead of radar images. Here it is explored the possibility to skip the whole radar development and, thus, all the satellite calibration process could be simplified.

The verification of rain rates is made by comparing radar and satellite estimates from 2130 UTC on 9 June to 0900 UTC on the 10th June, every 30 minutes, avoiding the period used for calibration experiments (see table 8.1). Meteosat-7 satellite line scan starts from the south of the earth to the north, where, the time of the image is established. So that when Spain is scanned the time of the satellite image is at least 10 minutes delayed with respect the real UTC time as explained in chapter 2 of this thesis. This delay is compensated for in a practical way by comparing every satellite image with the corresponding radar image 10 minutes before. 24 hour satellite accumulation from 1200 UTC on 9 June to 1200 of the next day is verified in a qualitative and numerical manner against the ACA kriged accumulation fields. A numerical analysis is important to resolve the accuracy of the precipitation estimated methods and rainfall corrections. The statistical indices employed in the quantitative verification in the area covered by the radar and satellite are, as in previous chapters: mean, standard deviation (SD), BIAS, standard deviations difference (SDD), root mean square error (RMS), and correlation coefficient (CORR). Rain rates have been computed in addition to assess the spatial accuracy of points greater than zero mm $h^{-1}$: Probability of detection (POD), false alarm ratio (FAR), critical success index (CSI) and fraction correct (FRC).

Table 8.1. Radar-satellite rainfall images and points used in the calibration (bold) and rain rate verification.

| Day | Radar Hour (UTC) | Satellite Hour (UTC) | Number points | Comments |
|---|---|---|---|---|
| June-9-2000 | 2120 | 2130 | 2562 | Radar-Satellite images ok |
| “ | 2150 | 2200 | 2562 | “ |
| “ | 2220 | 2230 | 2562 | “ |
| “ | 2250 | 2300 | 2562 | “ |
| “ | 2320 | 2330 | 2562 | “ |
| “ | 2350 | 2400 | 2562 | “ |
| **June-10-2000** | **0020** | **0030** | **2562** | **“** |
| **“** | **0050** | **0100** | **2562** | **“** |
| **“** | **0120** | **0130** | **2562** | **“** |
| **“** | **0150** | **0200** | **2562** | **“** |
| **“** | **0220** | **0230** | **2562** | **“** |
| “ | 0250-0420 | 0300-0430 | 0 | Radar error |
| **“** | **0450** | **0500** | **2562** | **Radar-Satellite images ok** |
| **“** | **0520** | **0530** | **2562** | **“** |
| “ | 0550 | 0600 | 2562 | “ |
| “ | 0620 | 0630 | 2562 | “ |
| “ | 0650 | 0700 | 2562 | “ |
| “ | 0720 | 0730 | 2562 | “ |
| “ | 0750 | 0800 | 2562 | “ |
| “ | 0820 | 0830 | 2562 | “ |
| “ | 0850 | 0900 | 2562 | “ |
|  |  |  | **17934** | **Total number of points used in the calibration** |
|  |  |  | 33306 | Total number of points used in the verification |

### *8.2 Results of Auto-Estimator (A-E), CRR and correction factors*

A qualitative analysis of estimated precipitation from satellite by standard methods versus radar shows in general that maximum radar rain rates are under-estimated while radar rain areas are over-estimated by the satellite. Evidence of this is displayed in figure 8.2 in which the radar image at 0150 UTC 10 June is compared with the A-E and CRR rain rate images at 0200 UTC of the same day. The numerical analysis shown in table 8.2 for both satellite algorithms confirms a general under-estimation of rain rates with a negative BIAS. Higher CORR is obtained for the A-E, but, a slight improvement in the spatial accuracy of the rainfall is given by the CRR with greater FRC index. The under-estimation of both methods is much more evident for the 24 hours accumulated rainfall compared to the ACA rain gauge accumulation as observe in figure 8.3 and shown in table 8.3. In this last table BIAS error for A-E is around -24 mm and -42 mm for CRR, as opposed to rain rates, CORR index is higher for CRR (0.52) than for A-E (0.48).

A general result about the rainfall corrections proposed by Vicente *et al.* (1998, 2002) and applied to both standard satellite algorithms is that none of those produce significant improvements as shown in tables 8.4 and 8.5 for rain rates and in tables 8.6 and 8.7 for 24 hours accumulated rainfall. A brief analysis of tables 8.4 and 8.5 shows that only the parallax correction (PC) does not worsened the CORR index with respect to the original algorithms, and only the moisture correction (PWRH) and the orographic correction (OC) produce very little improvements in the BIAS, SDD and RMS statistical indices. With regard to the corrections for accumulated rainfall using the A-E method in table 8.6, only the PC and GR1 corrections seems to slightly increase the CORR index and vaguely improve the BIAS and RMS in the case of the PC. Rainfall accumulations using CRR algorithm in table 8.7, provide the best CORR obtained by the GR1 correction but also it provides the worst RMS and a very high BIAS error. In view of these unclear results, two options are explored in the next sub-sections:

- Recalibration of both algorithms using radar.
- Development of a method to correct the rainfall estimations by using the lightning information.

Table 8.2. Statistical results for the rain rates estimated by the different methods. The size is the number of radar-sat points. Mean, SD, SDD, BIAS and RMS are in mm $h^{-1}$. CORR, POD, FAR, CSI and FRC are magnitudes with no units. Boldfaced numbers show best statistical results in every line.

|  | RADAR | A-E | CRR |
|---|---|---|---|
| Size |  | 33306 |  |
| Mean | 2.3 | 1.6 | 0.9 |
| SD | 6.8 | 2.0 | 1.3 |
| BIAS |  | **-0.8** | -1.4 |
| SDD |  | **-4.8** | -5.5 |
| RMS |  | **6.2** | 6.6 |
| CORR |  | **0.45** | 0.37 |
| POD |  | **0.86** | 0.65 |
| FAR |  | 0.67 | **0.59** |
| CSI |  | 0.32 | **0.33** |
| FRC |  | 0.64 | **0.72** |

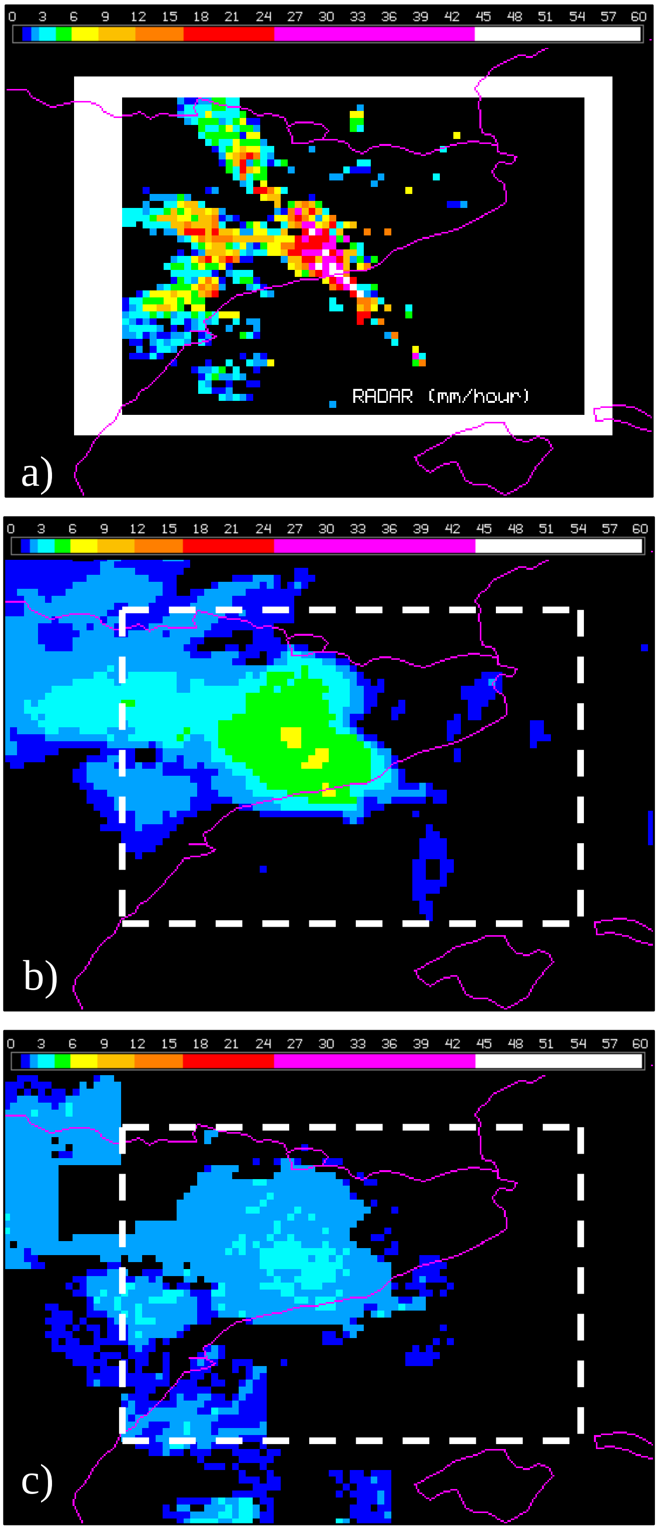

Figure 8.2. Rain Rates images with identical color table from (a) radar at 0150 UTC 10 Jun, (b) A-E method and (c) CRR method at 0200 UTC of the same day. The Radar area is indicated in the frames of this figure by the discontinuous white line.

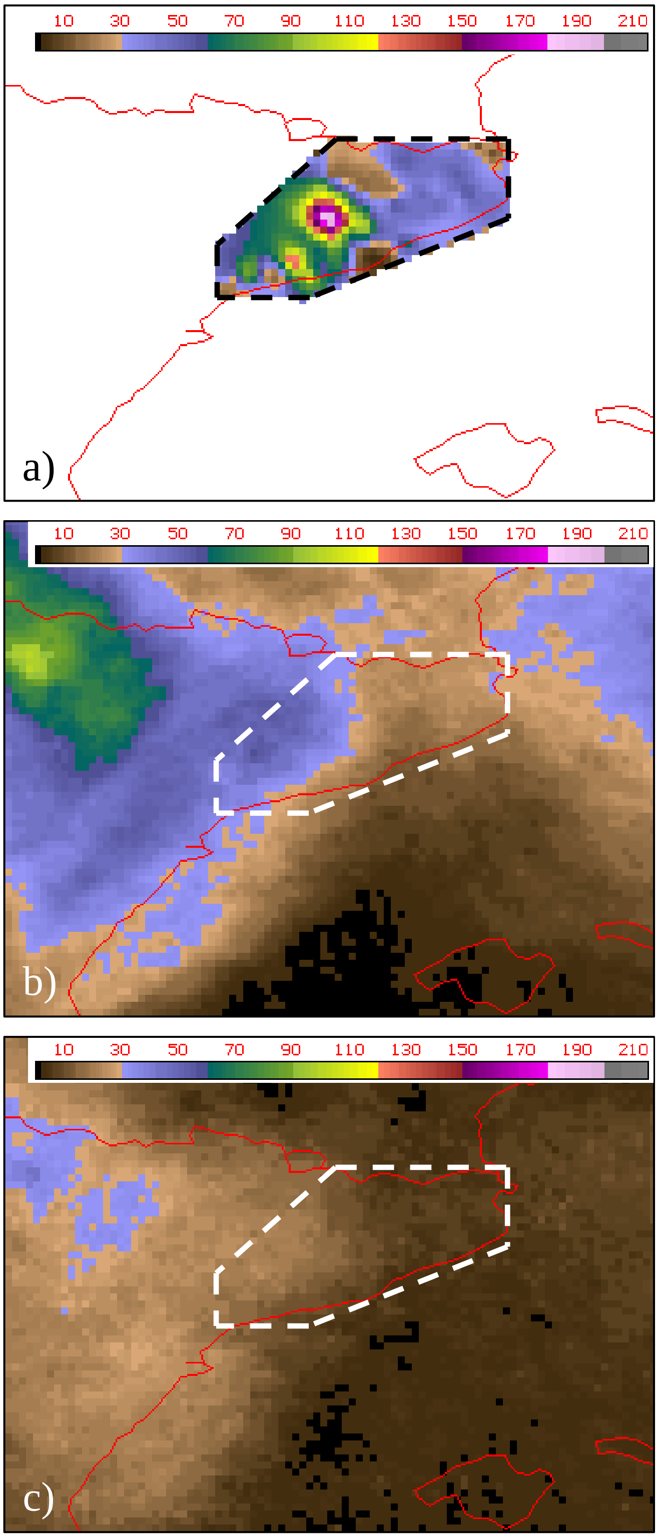

Figure 8.3. Rainfall accumulation maps in mm according to the colour scale for a period of 24 hours from 1200 UTC 9 June to 1200 UTC of the next day. Frame (a) from the ACA rain gauges, (b) from the A-E infrared curve and (d) from the CRR matrices.

Table 8.3. Statistics for 24 hours of rain accumulation estimated by the different methods from 1200 UTC of the first day to 1200 of the next day. The size is the number of radar-sat points. Mean, SD, SDD, BIAS and RMS are in mm. CORR has no units. Boldfaced numbers show best statistical results in every line.

| | ACA | A-E | CRR |
|---|---|---|---|
| Size | | 659 | |
| Mean | 52.1 | 28.3 | 10.5 |
| SD | 30.6 | 10.9 | 5.5 |
| BIAS | | **-23.8** | -41.7 |
| SDD | | **-19.6** | -25.0 |
| RMS | | **36.0** | 50.3 |
| CORR | | 0.48 | **0.51** |

Table 8.4. Statistical results of the sensitivity analysis of correction factors over the A-E.

| A-E | +PC | +GR1 | +GR2 | +GR | +PWRH | +OC |
|---|---|---|---|---|---|---|
| Mean | 1.6 | 0.9 | 0.9 | 0.9 | 1.4 | 1.4 |
| SD | 2.0 | 1.8 | 1.8 | 1.5 | 2.1 | 2.0 |
| BIAS | -0.7 | -1.2 | -1.5 | -1.4 | -0.7 | **-0.6** |
| SDD | -4.8 | -4.6 | -5.0 | -5.3 | **-4.3** | -4.4 |
| RMS | 6.2 | 6.2 | 6.5 | 6.6 | **5.9** | **5.9** |
| CORR | **0.45** | 0.33 | 0.36 | 0.35 | 0.41 | 0.43 |
| POD | **0.87** | 0.47 | 0.46 | 0.66 | 0.83 | 0.85 |
| FAR | 0.66 | 0.69 | 0.66 | 0.64 | 0.66 | 0.67 |
| CSI | **0.32** | 0.23 | 0.24 | 0.30 | **0.32** | **0.32** |
| FRC | 0.64 | **0.70** | 0.69 | 0.67 | 0.66 | 0.64 |

Table 8.5. Statistics results of the sensitivity analysis of correction factors over the CRR.

| CRR | +PC | +GR1 | +GR2 | +GR | +PWRH | +OC |
|---|---|---|---|---|---|---|
| Mean | 0.8 | 0.4 | 0.4 | 0.5 | 0.7 | 0.8 |
| SD | 1.3 | 1.0 | 1.0 | 0.9 | 1.4 | 1.3 |
| BIAS | -1.3 | -1.6 | -1.7 | -1.6 | -1.3 | **-1.2** |
| SDD | -5.2 | -5.4 | -5.4 | -5.5 | **-5.0** | -5.1 |
| RMS | **6.2** | 6.4 | 6.4 | 6.4 | **6.2** | **6.2** |
| CORR | **0.37** | 0.29 | 0.34 | 0.32 | 0.36 | 0.35 |
| POD | 0.63 | 0.35 | 0.35 | 0.48 | 0.60 | **0.65** |
| FAR | 0.59 | 0.59 | **0.51** | 0.57 | 0.56 | 0.59 |
| CSI | 0.33 | 0.23 | 0.26 | 0.29 | **0.34** | 0.33 |
| FRC | 0.75 | 0.78 | **0.80** | 0.77 | 0.78 | 0.75 |

Table 8.6. Statistics results of the sensitivity analysis of correction factors over the 24 hours A-E accumulations.

| A-E | +PC | +GR1 | +GR2 | +GR | +PWRH | +OC |
|---|---|---|---|---|---|---|
| Mean | 29.8 | 19.1 | 17.2 | 17.1 | 29.3 | 28.9 |
| SD | 10.7 | 7.0 | 7.5 | 7.0 | 10.3 | 11.0 |
| BIAS | **-22.3** | -33.0 | -34.9 | -35.1 | -22.8 | -23.3 |
| SDD | -19.8 | -23.5 | -23.0 | -23.5 | -20.3 | **-19.6** |
| RMS | **35.0** | 43.2 | 44.8 | 45.1 | 36.2 | 36.2 |
| CORR | **0.49** | **0.49** | 0.45 | 0.42 | 0.40 | 0.42 |

Table 8.7. Statistics results of the sensitivity analysis of correction factors over the 24 hours CRR accumulations.

| CRR | +PC | +GR1 | +GR2 | +GR | +PWRH | +OC |
|---|---|---|---|---|---|---|
| Mean | 10.8 | 6.2 | 6.0 | 6.0 | 10.8 | 10.8 |
| SD | 5.7 | 3.0 | 3.4 | 3.7 | 5.2 | 5.6 |
| BIAS | -41.5 | -45.9 | -46.1 | -46.1 | **-41.3** | -41.4 |
| SDD | **-24.9** | -27.6 | -27.1 | -26.8 | -25.3 | -25.0 |
| RMS | 50.2 | 54.4 | 54.5 | 54.5 | 50.3 | **50.1** |
| CORR | 0.47 | **0.52** | 0.50 | 0.47 | 0.44 | 0.48 |

### *8.3 Auto-Estimator and CRR recalibration with radar*

#### *a) Auto-Estimator*

The calibration method proposed by Vicente *et al.* (1998) and described in section 3 has been repeated for the Montserrat flood case taking 7 simultaneous radar satellite pairs of images during the time period of heaviest rainfalls. That is, from 0020 to 0520 on the 10th of June, as shown in bold in table 8.1. The mean radar rainfall was calculated for each 2.5 K instead of 1 K temperature interval from 215 to 260 K, looking for a smooth shape of the mean points. Another difference with respect to the calibration method documented by Vicente *et al.* (1998) is that now Meteosat infrared images from the 11.5 µm band are corrected by parallax. As shown in the previous subsection, this correction does not worsen the estimated precipitation accuracy. Figure 8.4 displays the scatter plot of radar-satellite points from the images used in calibration, the original A-E curve (3.1), the mean radar rain points each 2.5 K and the new best fit ($r^2 = 0.97$) curve (8.1) computed from the mean radar points distribution.

$$R = 1.677 \cdot 10^{11} \exp(-3.6382 \cdot 10^{-2} T_{IR}^{1.2}) \qquad (8.1)$$

where $R$ is the rainfall rate in mm $h^{-1}$ and $T_{IR}$ is the cloud top temperature in Kelvin. It is paradoxical that the two coefficients in the exponential index of this curve do not change with respect to the ones of the original A-E curve (3.1). However the first coefficient 1.677 $10^{11}$ is around 1.5 times greater than the one of the A-E equation (1.1183 $10^{11}$). Precipitation computed using the new power law relation (8.1) is called 'A-Ec' in the following.

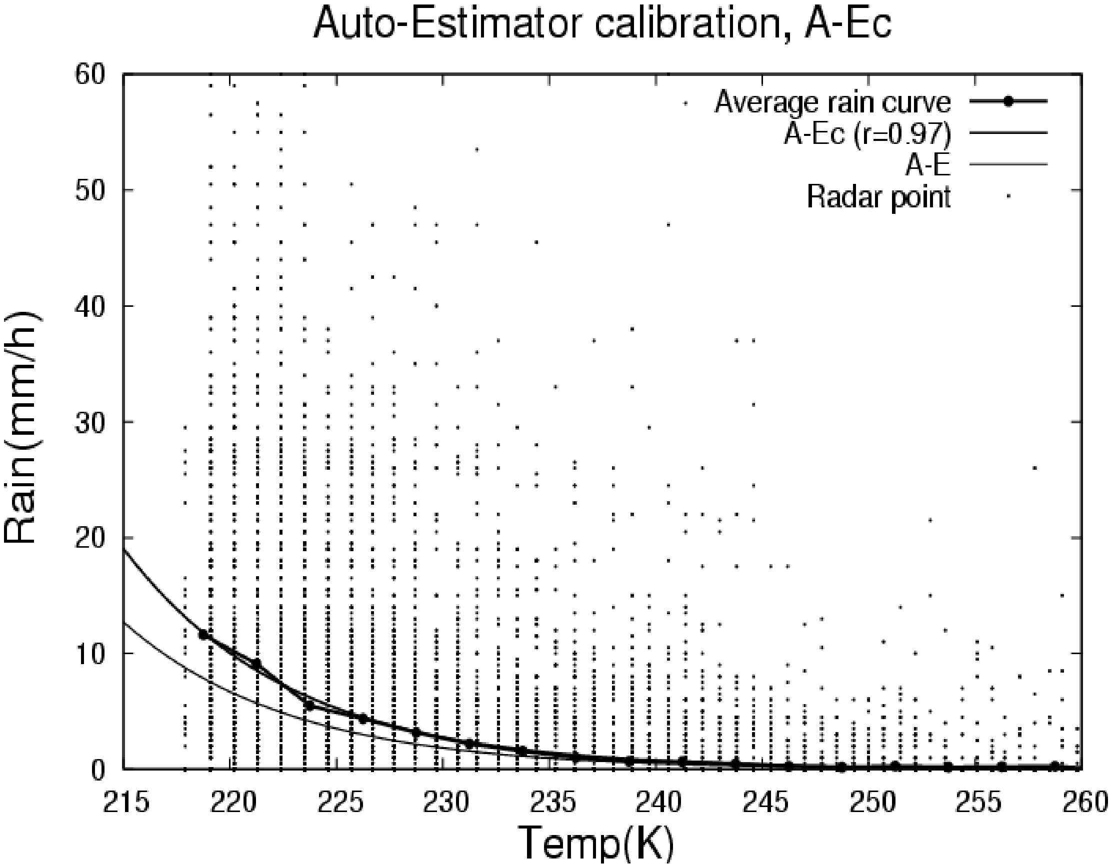

Figure 8.4. Radar rain rate in mm $h^{-1}$ versus satellite brightness temperature in K from the calibration file. Mean rain points each 2.5 K (big points connected by the thick line), the best fit A-Ec curve (equation 8.1) and original A-E curve (thinner line). It is important to note that the only difference between both power law curves is the first coefficient.

*b) CRR*

Most of the rainfall occurred over the Catalonian region close to the Barcelona radar between 0000 and 0500 of June 10, and no visible Meteosat-7 images were available in such night hours. A new two dimensional (2-D) rainfall matrix is generated from radar and satellite infrared bands corrected also by parallax, following the instructions given in section 4.2. The radar and satellite images employed in the calibration are shown in table 8.1. Elements of this 2-D matrix are classes that are transformed in rain rate in mm h$^{-1}$ using the same table, 4.2, as the one used for the original CRR matrices. This new rainfall matrix adjusted for the Monserrat flood case can be compared with the original (table 4.3D) performed in section 4 using a long set of radar and satellite data over the Iberian Peninsula. The most important differences are: the diagonal distribution of classes is displaced at least four degrees Kelvin to warmer infrared temperatures. Secondly, rainfall classes are significantly higher therefore producing much more rain than the older matrix. Precipitation computed using the new infrared matrix (table 8.8) is called ‘MCRR’ (Montserrat Convective Rainfall Rate) in the following.

Table 8.8. CRR 2-D new matrix adjusted for the Monserrat flood case. Vertical axis, temperature in Celsius of the Meteosat thermal band ($T_{IR}$). Horizontal axis, infrared and water vapour bands temperature difference ($T_{IR} - T_{WV}$). The numbers are rainfall classes that are transformed in rain rate using the table 4.2. Some of them are shaded to underline the highest rainfall classes from the rest. The solid line shows the position of the original matrix classes (see table 4.3D).

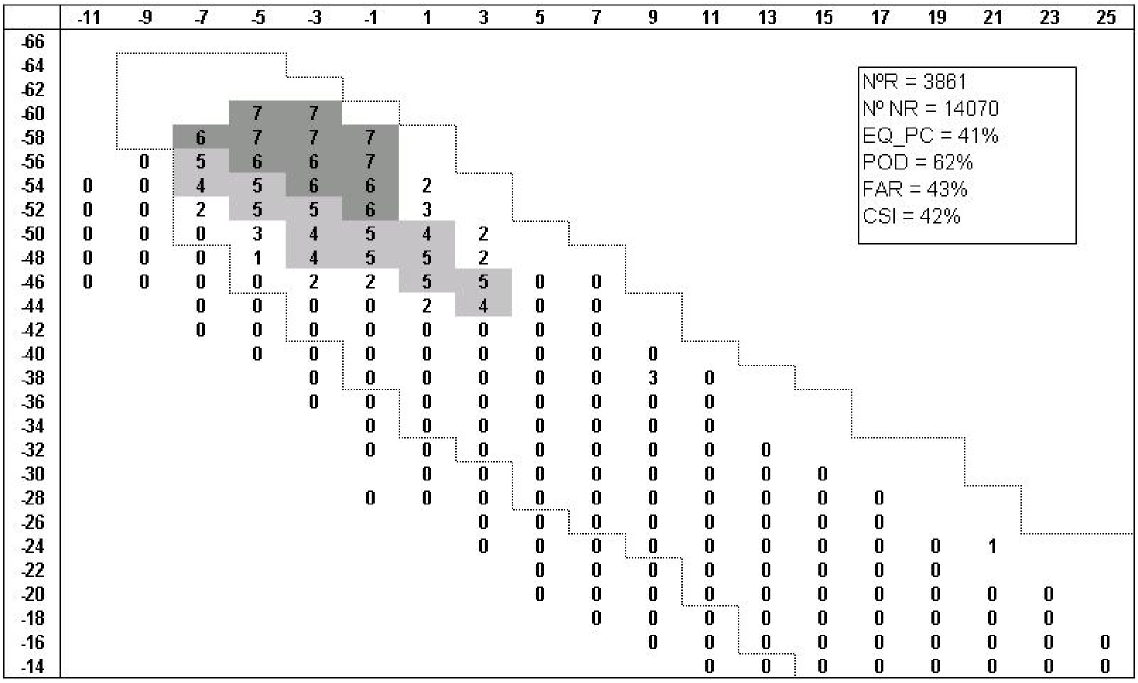

|  | -11 | -9 | -7 | -5 | -3 | -1 | 1 | 3 | 5 | 7 | 9 | 11 | 13 | 15 | 17 | 19 | 21 | 23 | 25 |
|---|---|---|---|---|---|---|---|---|---|---|---|---|---|---|---|---|---|---|---|
| -66 |  |  |  |  |  |  |  |  |  |  |  |  |  |  |  |  |  |  |  |
| -64 |  |  |  |  |  |  |  |  |  |  |  |  |  |  |  |  |  |  |  |
| -62 |  |  |  |  |  |  |  |  |  |  |  |  |  |  |  |  |  |  |  |
| -60 |  |  |  | 7 | 7 |  |  |  |  |  |  |  |  |  |  |  |  |  |  |
| -58 |  |  | 6 | 7 | 7 | 7 |  |  |  |  |  |  |  |  |  |  |  |  |  |
| -56 |  | 0 | 5 | 6 | 6 | 7 |  |  |  |  |  |  |  |  |  |  |  |  |  |
| -54 | 0 | 0 | 4 | 5 | 6 | 6 | 2 |  |  |  |  |  |  |  |  |  |  |  |  |
| -52 | 0 | 0 | 2 | 5 | 5 | 6 | 3 |  |  |  |  |  |  |  |  |  |  |  |  |
| -50 | 0 | 0 | 0 | 3 | 4 | 5 | 4 | 2 |  |  |  |  |  |  |  |  |  |  |  |
| -48 | 0 | 0 | 0 | 1 | 4 | 5 | 5 | 2 |  |  |  |  |  |  |  |  |  |  |  |
| -46 | 0 | 0 | 0 | 0 | 2 | 2 | 5 | 5 | 0 | 0 |  |  |  |  |  |  |  |  |  |
| -44 |  |  | 0 | 0 | 0 | 0 | 2 | 4 | 0 | 0 |  |  |  |  |  |  |  |  |  |
| -42 |  |  | 0 | 0 | 0 | 0 | 0 | 0 | 0 | 0 |  |  |  |  |  |  |  |  |  |
| -40 |  |  |  | 0 | 0 | 0 | 0 | 0 | 0 | 0 | 0 |  |  |  |  |  |  |  |  |
| -38 |  |  |  |  | 0 | 0 | 0 | 0 | 0 | 0 | 3 | 0 |  |  |  |  |  |  |  |
| -36 |  |  |  |  | 0 | 0 | 0 | 0 | 0 | 0 | 0 | 0 |  |  |  |  |  |  |  |
| -34 |  |  |  |  |  | 0 | 0 | 0 | 0 | 0 | 0 | 0 |  |  |  |  |  |  |  |
| -32 |  |  |  |  |  | 0 | 0 | 0 | 0 | 0 | 0 | 0 | 0 |  |  |  |  |  |  |
| -30 |  |  |  |  |  |  | 0 | 0 | 0 | 0 | 0 | 0 | 0 | 0 |  |  |  |  |  |
| -28 |  |  |  |  |  | 0 | 0 | 0 | 0 | 0 | 0 | 0 | 0 | 0 | 0 |  |  |  |  |
| -26 |  |  |  |  |  |  |  | 0 | 0 | 0 | 0 | 0 | 0 | 0 | 0 |  |  |  |  |
| -24 |  |  |  |  |  |  |  | 0 | 0 | 0 | 0 | 0 | 0 | 0 | 0 | 0 | 1 |  |  |
| -22 |  |  |  |  |  |  |  |  | 0 | 0 | 0 | 0 | 0 | 0 | 0 | 0 |  |  |  |
| -20 |  |  |  |  |  |  |  |  | 0 | 0 | 0 | 0 | 0 | 0 | 0 | 0 | 0 | 0 |  |
| -18 |  |  |  |  |  |  |  |  |  | 0 | 0 | 0 | 0 | 0 | 0 | 0 | 0 | 0 |  |
| -16 |  |  |  |  |  |  |  |  |  |  | 0 | 0 | 0 | 0 | 0 | 0 | 0 | 0 | 0 |
| -14 |  |  |  |  |  |  |  |  |  |  |  | 0 | 0 | 0 | 0 | 0 | 0 | 0 | 0 |

NºR = 3861
Nº NR = 14070
EQ_PC = 41%
POD = 62%
FAR = 43%
CSI = 42%

### *8.4 Lightning assimilation and correction factor*

As explained in the result section most of the applied rainfall corrections described by Vicente *et al.* (1998, 2002) do not show clear improvements in this study case when compared satellite estimations to radar and accumulations from ACA rain gauges. A new alternative using lightning data is explored in this research in order to make use of valuable electrical discharge information from the base of the clouds.

-The first step involves the localization in time and space of every positive and negative lightning strike and to score satellite pixels with the number of electrical discharges. As a result of a qualitative study (not shown), a time lapse of 20 minutes around the satellite image UTC time seems to be appropriate to situate and add rays to the image pixels. Taking in account that Meteosat-7 image has a real-time delay of 10 10 minutes from to the UTC time over Spain; lightning hits are located and represented in a period of 20 minutes before the UTC satellite time as illustrated in figure 8.6. In this display the radar image at 0150 UTC is associated to the Meteosat image at 0200 UTC but electrical discharges are retrieved from 0140 to 0200 UTC and the time assigned to this lightning image is 0150 UTC. So that, each satellite infrared image every 30 minutes also processes a parallel image showing lightning hits with identical geographical settings.

- The second step has to do with the separation of radar rain rates associated to lightning or no lightning and how they correspond to satellite thermal band temperature (11.5 µm) also corrected by parallax. Averaged lightning (*ALR*) and no lightning rain rates (*ANLR*) versus infrared brightness temperature ($T_{IR}$) are drawn in figure 8.5a by two different symbols (triangles and boxes respectively) connected by lines. The average rain rate line (*AR*) obtained by using data from the whole calibration dataset, and used to determine the A-Ec curve (8.1) as described in the previous section, is also plotted in this graph. While the *AR* and *ANLR* plots are very similar, the *ALR*, however, provide much more rain and it is more dispersed for warmer temperatures with a maximum of 23 mm $h^{-1}$ for 243 K.

-The third step is thought to increase the rain rate associated to lightning in function of the satellite temperature. Rainfall estimated from the A-Ec curve is first corrected by parallax and later should be multiplied by a correction coefficient, *KL*, on those points where electrical discharges are detected. The *KL* coefficient is calculated as illustrated in figure 8.5b. Firstly, the *ALR* points are divided by the *AR* ones each 2.5 K generating the Factor curve (*FC*). Secondly, a frequency curve of electrical discharges called, number of discharges (*ND*) in function of $T_{IR}$, also, each 2.5 K determines the sections of the *FC* best supported by the lightning data as shown in graph 8.5b. With 6079 strikes from the coldest cloud tops accumulated in the 217-222 K section and not shown in this figure, to as much as 30 hits in the warmest from 246 K to the end is the kind of information that can be obtained the *ND* plot. The *FC* curve represents the ideal correction factor but in practice we have averaged it in finite segments based on nearly constant sections of *ND* curve as follows:

$KL_1 = 1.5$ for $T_{IR} < 222.5$ K with a $\Sigma_1(ND_i) = 6079$
$KL_2 = 2.6$ for $222.5 \text{ K} \leq T_{IR} < 230$ K with a $\Sigma_2(ND_i) = 1699$
$KL_3 = 8.2$ for $230 \text{ K} \leq T_{IR} < 240$ K with a $\Sigma_3(ND_i) = 497$
$KL_4 = 14.1$ for $T_{IR} \geq 240$ K with a $\Sigma_4(ND_i) = 108$

where $KL_j$ is the correction factor derived from averaged sections of the *FC* curve and $\Sigma_j(ND_i)$ is the total number of electrical discharges in each temperature interval. The lengths of the Temperature interval have been selected from the coldest $T_{IR}$ in which most of the lightning hits have been detected and where *FC* is closer to 1, to warmer $T_{IR}$. We have find empirically that the $\Sigma_j(ND_i)$ can be divided by an value of 3.5 in order to select the approximate length of the next warmer interval of temperatures. This process continues until the number of discharges is nil.

-The fourth step diminishes the rain rate of those rain pixels not associated to lightning and therefore considered as stratiform rain pixels. This should be performed dynamically over the rain pixels that are surrounding the electrical ones as far as 15 pixels. The purpose of this process is to compensate the general tendency to increase the rain rate produced by the *KL* factor over the lightning pixels. The rain rate average in a stormy cloud area should stay unchanged after this stage. The mean rain rate decreases in stratiform rain pixels after this step, and for this case is around 10 %.

In summary, satellite rain pixels associated to lightning activity considered as convective are multiplied by the *KL* correction factor that depends on $T_{IR}$, the rest of rain pixels in the cloud considered as stratiform have a diminished rain rate in order to compensate for the increment produced by the *KL* factor. This process called ‘LG’ is applied as another correction factor to A-Ec and MCRR algorithms.

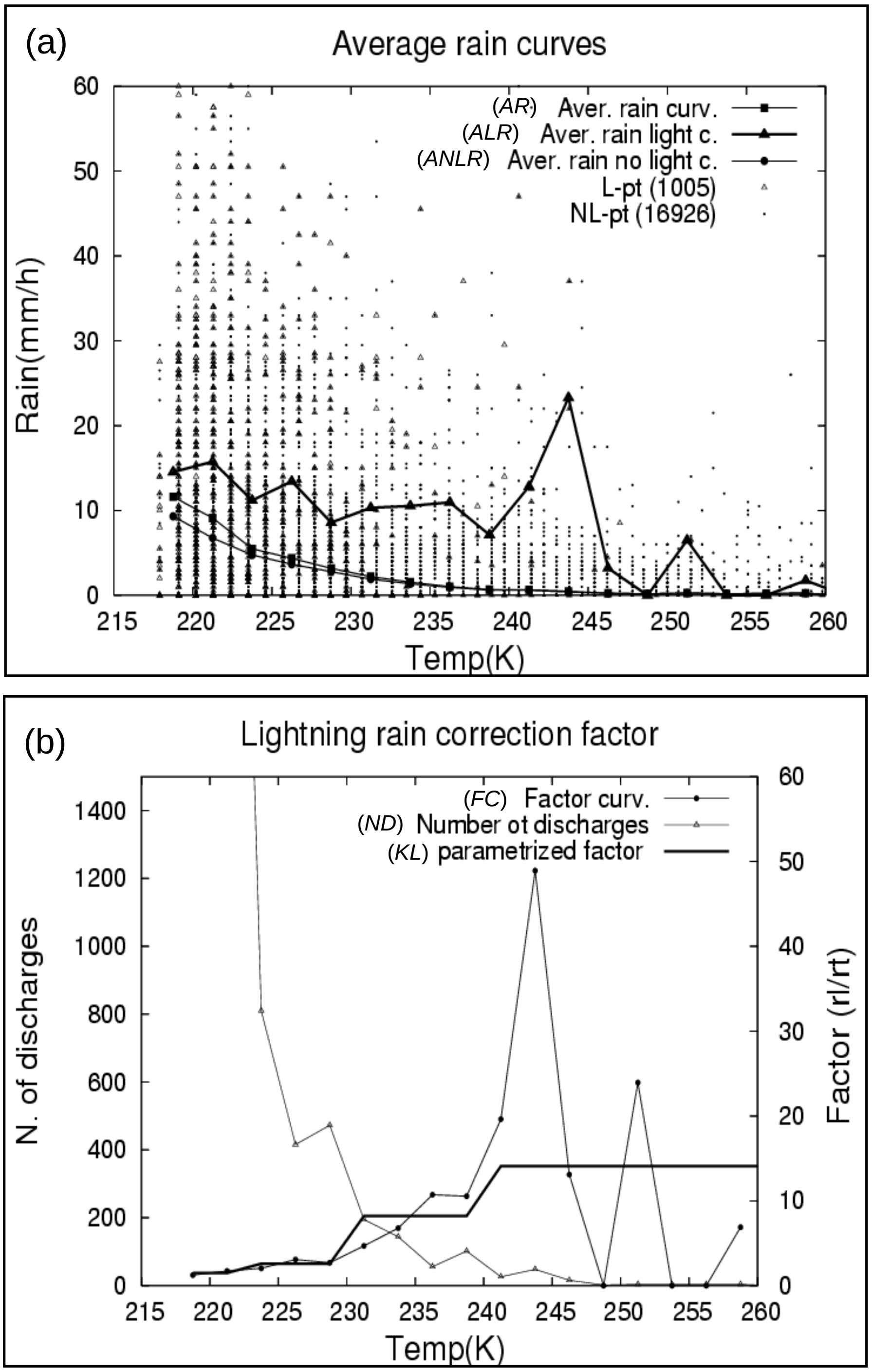

Figure 8.5. (a) Averaged lightning and no lightning rain rate points each 2.5 K. Plot using the boxes connected with lines: averaged rain (AR), as the previous figure. Triangles connected with lines: averaged lightning rain (ALR) from radar points associated to lightning pixels (1005 points). Circles connected with lines: averaged rain curve (ANLR) from radar points not associated to lightning pixels (16926 points). (b) Lightning correction factor figure. Total number of electrical discharges plotted by the line with triangles each 2.5 K (ND). The right axis represents the correction factor scale. It has no units because it is the averaged lightning rain points (ALR) divided by the averaged rain points (AR) each 2.5 K which generates the factor plot (FC) shown using black circles. The parameterized factor (KL) is the FC averages on limited sections taking in account a nearly constant number of accumulated discharges.

### *8.5 Results of calibrated algorithms and effect of lightning correction*

*a) Calibrated algorithms*

The new calibrated infrared rain curve performed as an equation (8.1) has been applied for the A-Ec and the new infrared CRR matrix shown as table 8.8 has been used for MCRR. Both have been verified against radar rainfall such as the standard algorithms (A-E, CRR) and the results for rain rates are illustrated in figure 8.6 and statistical indices in table 8.9. The results for the 24 hour rain accumulation of A-Ec and CCRR compared to the ACA rain gauge accumulation are shown in figure 8.7 and statistical indices in table 8.10. For both cases, rain rates (displays 8.6c and 8.6e) and accumulation (displays 8.7a and 8.7c) estimations have been increased with respect to the standard algorithms as expected. The growth in the estimated precipitation is clearly confirmed by the increase in the statistically estimated means and reduction of the BIAS as shown for rain rates in table 8.9 and accumulations in table 8.10. Maximum radar rain rates (around 55 mm $h^{-1}$ in figure 8.6a) are not reached by the satellite maximum estimations (around 10 mm $h^{-1}$ for A-Ec and MCRR in displays 8.6c and 8.6e respectively), while, as observed for the original algorithms, satellite over-estimates rain area compared to radar. This effect is also significant for the accumulations, while the ACA rain gauges have achieved a maximum accumulation of 190 mm in 24 hours in a small area as shown in figure 8.3a, both calibrated satellite algorithms have retrieved around 90 mm.

As expected, the calibration experiment has an overall effect on rainfall amounts and less rainfall accuracy as shown by the correlation coefficients. In most cases the CORR between original and calibrated algorithms stays unchanged apart from CRR and MCRR rain rates in which it increases from 0.37 (table 8.2) to 0.41 (table 8.9).

*b) Lightning correction.*

The effect of the lightning correction over the rainfall fields is clear. In places where cloud to ground electrical strikes are detected, rain rates are sensibly increased while the rest of the rainfall pixels are slightly decreased (see figure 8.6 from frame c to f). Qualitative comparisons were done between radar and the 20 minutes of lightning images and, as expected, a very good spatial correlation was observed between electrical points and the highest radar echoes (see figure 8.1 and displays 8.6a and 8.6b).

Improvements, independent from the rainfall amounts, can be quantified by checking the CORR index in tables 8.9 and 8.10 for rain rates and accumulation respectively. The first table corresponds to the estimated rain rate analysis compared with radar; the CORR index for A-Ec is increased from 0.45 to 0.49, which is a relative increment of 10%. For MCRR the CORR is increased a bit less, 8 %. However, increments are higher for the 24 hour accumulations with respect to the rain gauges as shown in table 8.10. Here the CORR index for A-Ec is increased 19% and for MCRR, 10%. Two reasons are behind the application of the parallax correction before lightning. The first one is because this correction is the only one that has not worsened in general the CORR index in the first analysis (Tables 8.4 to 8.7). The second reason is that this correction should perform a correct alignment between the cloud top observed by the satellite and the electrically convective cloud base detected by the INM lightning network.

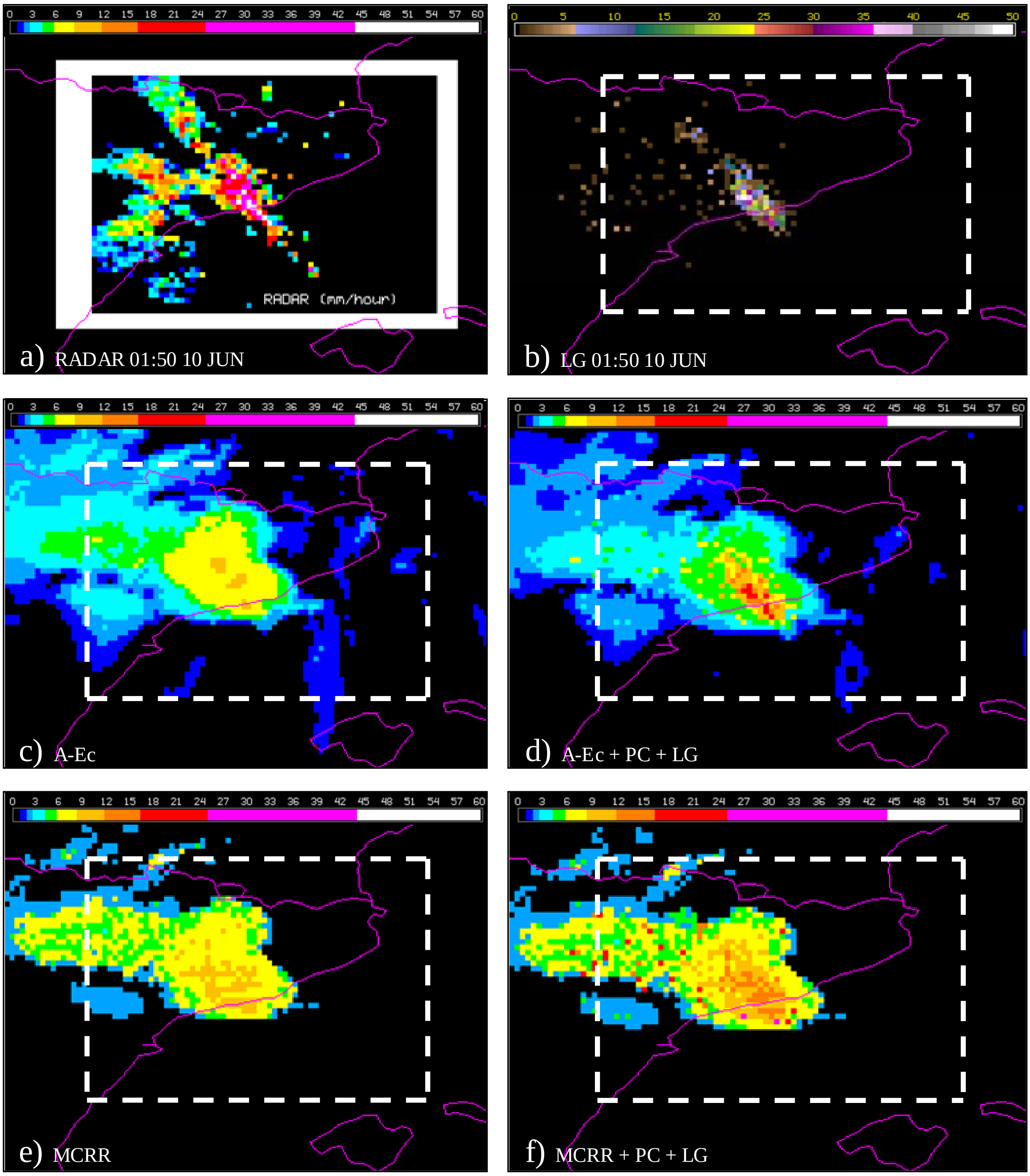

Figure 8.6. (a) Rainfall radar image in mm h$^{-1}$ at 0150 UTC. (b) Lightning image, in which position and number of electrical discharges detected in 20 minutes (from 0140 to 0200 UTC) are displayed. (c) A-Ec, Rain rate image in mm h$^{-1}$ from calibrated IR curve (8.1). (d) A-Ec image corrected first by parallax and then by the lightning correction factor *KL*. (e) MCRR, CRR image in mm h$^{-1}$ from the new 2-D matrix shown in table 8.8. (f) MCRR image corrected first by parallax and later by the lightning correction factor *KL*.

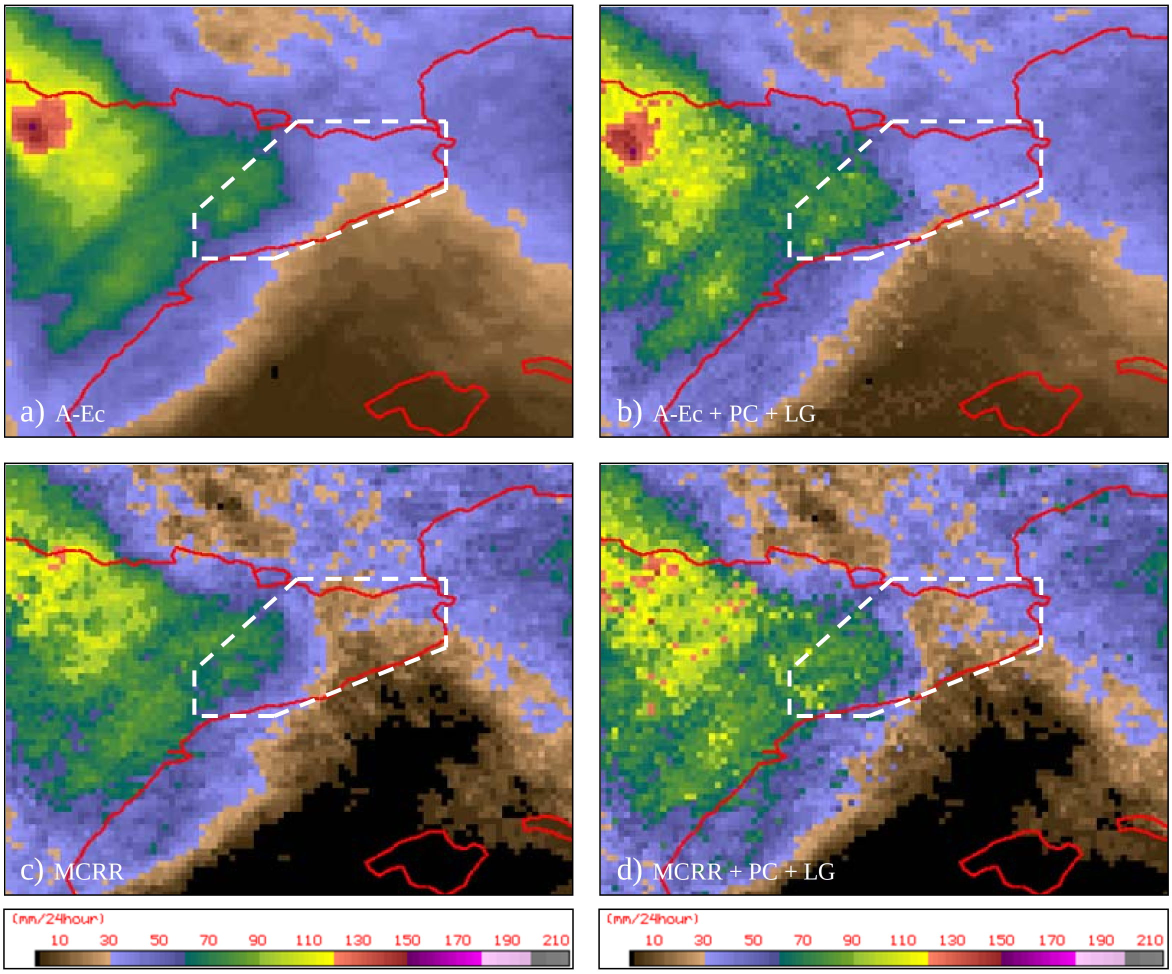

Figure 8.7. Rainfall accumulation maps in mm according to the colour scale for a period of 24 hours from 1200 UTC 9 June to 1200 UTC of the next day. (a) Calibrated Auto estimator, A-Ec. (b) A-Ec corrected firstly by parallax (PC) and secondly by lightning (LG). (c) Calibrated CRR for this flood case or MCRR. (d) MCRR corrected in first place by parallax (PC) and then by lightning (LG).

Table 8.9. Statistical results for the rain rates estimated by the calibrated Auto-Estimator (A-Ec) and calibrated CRR (MCRR) for this flood case. Then, both methods corrected firstly by parallax (PC) and, second, by the lightning correction factor (LG) are also evaluated. Boldfaced numbers show best statistical results in every line.

| | RADAR | A-Ec | MCRR | A-Ec+PC+LG | MCRR+PC+LG |
|---|---|---|---|---|---|
| Size | | | 33306 | | |
| Mean | 2.3 | 2.3 | 2.1 | 2.4 | 2.3 |
| SD | 6.8 | 3.0 | 3.8 | 3.5 | 4.5 |
| BIAS | | **0.0** | -0.2 | 0.1 | **0.0** |
| SDD | | -3.8 | -3.0 | -3.3 | **-2.2** |
| RMS | | 6.1 | 6.2 | **5.9** | 6.3 |
| CORR | | 0.45 | 0.41 | **0.49** | 0.44 |
| POD | | **0.89** | 0.64 | **0.89** | 0.65 |
| FAR | | 0.69 | **0.51** | 0.69 | 0.52 |
| CSI | | 0.30 | 0.38 | 0.30 | **0.39** |
| FRC | | 0.55 | **0.78** | 0.55 | 0.77 |

Table 8.10. Statistical results for 24 hours of rain accumulation estimated by the calibrated Auto-Estimator (A-Ec) and calibrated CRR matrix MCRR for the flood case. Then, both methods are corrected firstly by parallax (PC) and secondly by the lightning correction factor (LG). Boldfaced numbers show best statistical results in every line.

| | ACA | A-Ec | MCRR | A-Ec+PC+LG | MCRR+PC+LG |
|---|---|---|---|---|---|
| Size | | | 659 | | |
| Mean | 52.1 | 42.5 | 39.2 | 47.4 | 44.6 |
| SD | 30.6 | 15.5 | 19.2 | 17.4 | 22.7 |
| BIAS | | -9.6 | -12.9 | **-4.7** | -7.5 |
| SDD | | -15.1 | -11.4 | -13.2 | **-7.8** |
| RMS | | 27.9 | 29.7 | **25.1** | 27.0 |
| CORR | | 0.48 | 0.50 | **0.57** | 0.54 |

### *8.6 Calibrating satellite algorithms with rain gauges*

The Last experiment described this chapter investigates the possibility of calibrating the CRR and A-E algorithms directly with the data provided by the rain gauges. In the previous subsections, radar rain rates were indispensable for calibration routines in the Montserrat flood case. However, behind radar images are many problems that have to be solved in order to perform a correct estimation of the precipitation as discussed in chapter 7. Often these radar processes should be considered mainly when the final satellite rainfall accuracy is not as good as projected after being calibrated to radar. Other times radar data is simply not available for certain places or certain time periods. So for that and for other reasons, a method to calibrate satellite precipitation algorithms directly with rain gauges seems to us to be very useful. Secondly we are interested in testing the two calibration methods (A-Ec1 and A-Ec2) described in section 5.4 and to test new CRR matrices filled with data from rain gauges.

The Catalonian region, with 126 operative rain gauges in June 2000 well distributed over the study area as shown in figure 7.1, configures an extraordinary observational network for precipitation. In other places of the European continent it is normal to find 10 to 20 automatic rain gauges for a similar area size to Catalonia. The A-Ec1, A-Ec2 new curves and a new CRR rain matrix are performed firstly using all the rain gauges during the calibration period defined in table 8.1 (from 0030 to 0530 UTC for the 10 June). After analysis and evaluation of them we repeat the calibration process but in this case the number of rain gauges is diminished artificially in an attempt to find the minimum number than can be employed in five hours without reducing accuracy.

Over a five hour period, every 30 minutes, which effectively means 11 Meteosat-7 scans with the parallax effect corrected and 126 rain gauges, have produced a calibration dataset with a total of 1386 points that are used in calibration. In contrast to the Albanian case, there were not detected anomalous satellite pixels and rain gauge measurements during the process after a supervised quality check since the calibration period is shorter in this case. The next three subsections comment on the most important features from the application of the A-Ec1, A-Ec2 and CRR calibration methods, however for a full description of them the reader is referred to section 5.4 *a),* 5.4 *b)* and 4.2 respectively.

*a) A-Ec1*

The 1386 rain gauge observations are ordered depending on their satellite infrared temperature as shown in the figure 8.8a. As occurred in the previous occasion, (figure 5.5a) the highest rain rates are also logically related to the colder infrared temperatures. Here we have used the temperature interval of 2.5 K for two reasons: we believe that it is coherent to apply a similar interval size as for the A-E calibration exercise with radar (section 8.3). The mean points (empty boxes in figure 8.8a) have a smooth looking distribution. However we might have defined a smaller interval since the minimum number of 15 mandatory point condition would be satisfied and the distribution of mean points might gently diminish with respect to the growth of the temperature and could have a smooth looking shape. The second stage of the calibration process makes use of the standard deviation computed in each interval of 2.5 K to select the best mean points in order to perform a linear regression fit in the logarithmic scale. As in the previous occasion (section 5.4 *a)*), mean points closer to the borders are rejected within the mean points with larger standard deviation values compared to the mean. Those mean points in which the standard deviation exceeds more than three times the mean value were not considered in the calibration. So, as illustrated in figure 8.8b, seven mean points (red circles) remain and the best fit line in the logarithm scale is computed as follows.

$$\log(R) = -0.1469\, T_{IR} + 34.79 \qquad (8.2)$$

where the correlation coefficient for the fit is r = 0.97. This relation is transformed to rain rate in mm $h^{-1}$ in function of the satellite temperature in K by inverting the logarithm.

$$R = 1.2856\ 10^{15}\ exp(-0.1469\, T_{IR}) \qquad (8.3)$$

This curve is plotted as the solid line in figure 8.8a and it is called “regression curve” in this graph.

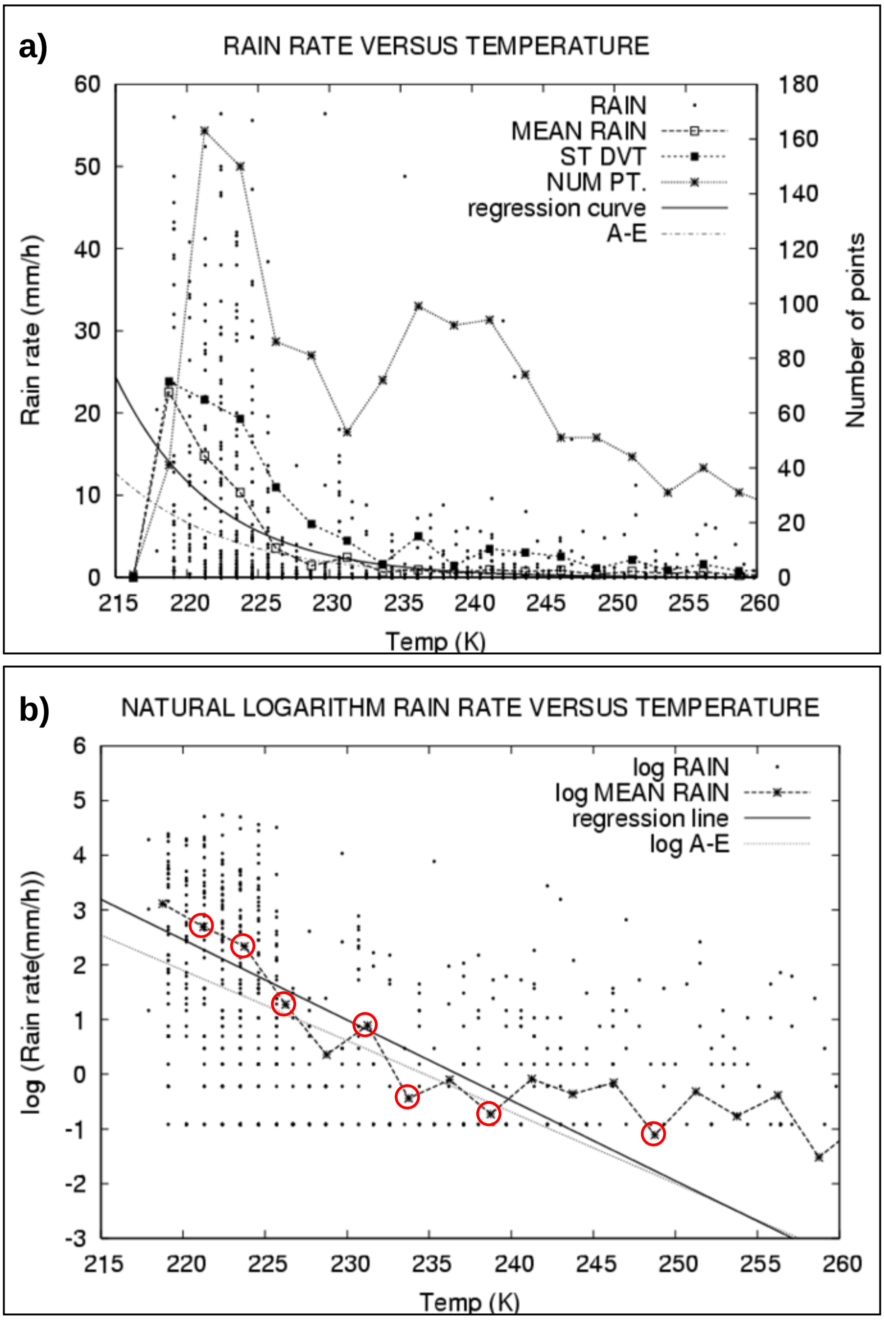

Figure 8.8. Rainfall curve calibration by the A-Ec1 method for the five hours of the calibration period (from 0030 to 0530 UTC for the 10 June) and all the 126 rain gauges. (a) Rain rates from ACA rain gauges versus satellite temperatures. Mean rain rate, standard deviation and number of points for each 2.5 K interval. New rainfall curve derived from the A-Ec1 regression method plotted as a continuous line curve and shown as equation (8.3). A-E original curve (dashed line) shown to make easy the visual comparison with respect the new regression curve. (b) Rain sector of the graph but in the logarithm scale. Mean rain rate points into the red circles used to calculate the regression line shown as equation (8.2).

*b) A-Ec2*

The second calibration method tries to select the most qualitative and convective rain rate points from the 1386 points. With the remaining ones it is performed a direct regression fit again in the logarithm scale. The process is done according to the following steps:

- Step 1. Rain Intensities associated to relatively warm satellite points ($T_{IR}$ greater than 250 K) are removed from calibration. As viewed in figure 8.8a, mean rain rates are almost zero for satellite temperatures greater than 250 K. A total of 268 points in which 79% of them are 0 mm $h^{-1}$, are removed and 1090 useful points remain.
- Step 2. Infrared points in which $T_{IR}$ is increasing with time are also removed. This process was made taking in account the cloud displacements in satellite images, as explained at the end of section 3.2 for the GR2 correction. A total of 584 points are warming compared to the previous satellite observation and therefore not considered in calibration. Therefore, after this second step there are still 506 points remaining.
- Step 3. If $T_{IR}$ is smaller than 215 K and the observed rain intensity is smaller than 1 mm $h^{-1}$ the point data is not considered in calibration. 0 points are eliminated after this step because in contrast to the Albanian case, cloud top temperatures are much warmer and no pixels are below 218 K (see figure 8.8a).
- Step 4. If $T_{IR}$ is greater than 230 K and the observed rain intensity is greater than 1 mm $h^{-1}$ the point data is not considered in calibration. Only 40 points are removed and thus, the rest, 466 points, are finally used in the A-Ec2 curve computation.

The logarithmic rainfall regression line is obtained using all the retrieved points ($N^oPt$ = 466) from the five hours of the flood and the 126 rain gauges. The thick line illustrated in frame 8.9a is the best fit equation obtained in the logarithmic scale with a correlation fit ($r$) equal to 0.42. The new rain rate curve (A-Ec2) is then calculated as in the Albanian case by just inverting the logarithmic linear relation, which results in the following equation, 8.4, plotted in figure 8.9b within the original A-E curve.

$$R = 4.566\ 10^{16}\ exp(-0.1642\ T_{IR}) \qquad (8.4)$$

where $R$ is rain rate in mm $h^{-1}$ and $T_{IR}$ is infrared temperature in Kelvin.

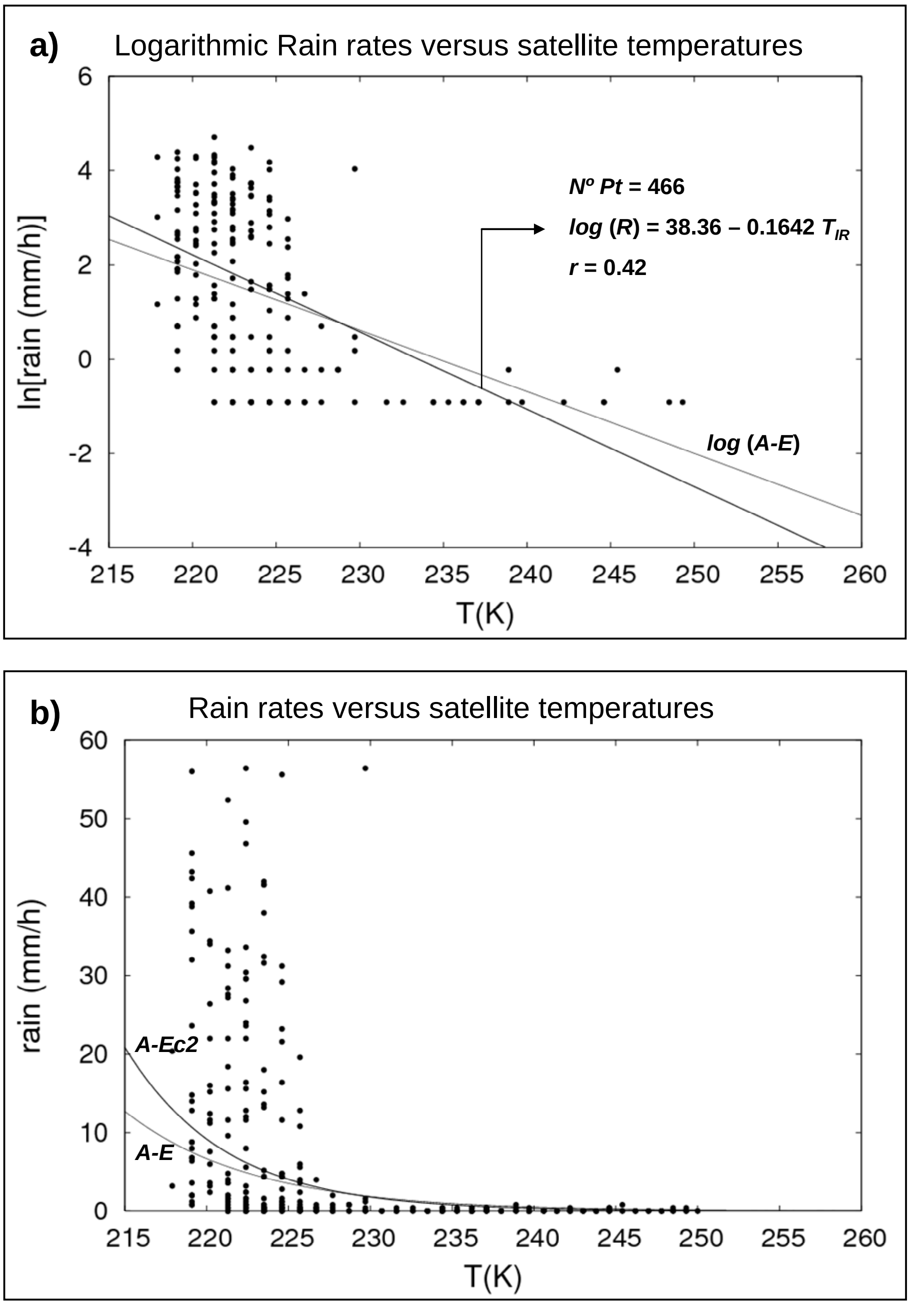

Figure 8.9. Rainfall curve calibration by the A-Ec2 method for the five hours of the calibration period (from 0030 to 0530 UTC for the 10 June) and the 126 rain gauges. (a) Natural logarithm of rain rates in mm $h^{-1}$ versus satellite 11 μm band brightness temperature in Kelvin for points not removed in the process. The solid black line is the best fit regression line while the other is the original A-E in the logarithmic scale shown as a reference. (b) Direct rain rates versus satellite temperatures (points) and rainfall curves from A-E (equation 3.1) and the new one A-Ec2 (equation 8.4).

*c) CRR*

Another two dimensional (2-D) rainfall matrix is generated from a direct association of the 126 rain gauge measurements and the satellite infrared bands previously corrected by parallax. The 1386 points are used to fill the rain, no rain and the accumulated rain matrices every two Kelvin and then the probability matrix and rain matrix within the EQ_PC parameter are generated following instructions given in section 4.2. Elements of this 2-D matrix are classes that are transformed into rain rates in mm $h^{-1}$ using the table 4.2 as the original CRR matrices. This new rainfall matrix is called MCRR2 and the following can be compared with the original (table 4.3D) performed in section 4 using a long set of radar and satellite data over the Iberian Peninsula and can also be compared with the last rain matrix computed for the same period but using radar rain rates (table 8.8).

Table 8.11. Same as table 8.8 but new 2-D CRR matrix (MCRR2) obtained from the combination of the 126 rain gauges and satellite two infrared bands for a calibration period of five hours. The numbers are rainfall classes that are transformed in rain rate using the table 4.2. Some of them are shaded to underline the highest rainfall classes from the rest. The solid line shows the position of the original matrix classes (table 4.3D). The arrow and the ellipse indicate the area in the matrix where anomalous non zero cells appeared in contrast to the other two matrices.

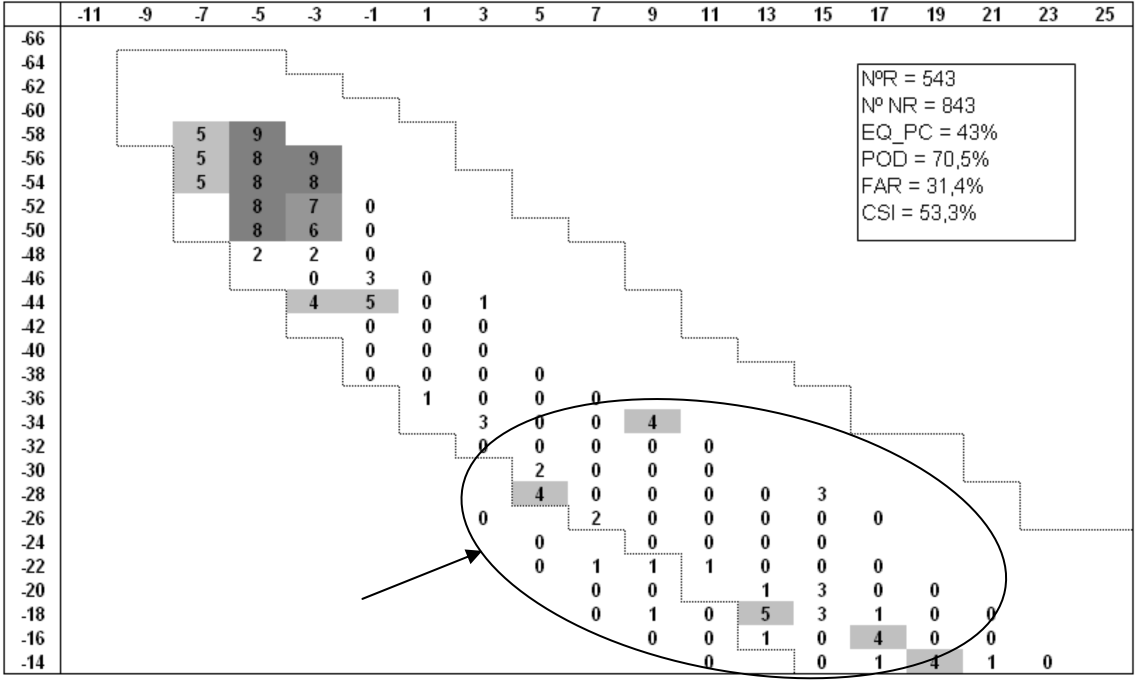

|  | -11 | -9 | -7 | -5 | -3 | -1 | 1 | 3 | 5 | 7 | 9 | 11 | 13 | 15 | 17 | 19 | 21 | 23 | 25 |
|---|---|---|---|---|---|---|---|---|---|---|---|---|---|---|---|---|---|---|---|
| -66 |  |  |  |  |  |  |  |  |  |  |  |  |  |  |  |  |  |  |  |
| -64 |  |  |  |  |  |  |  |  |  |  |  |  |  |  |  |  |  |  |  |
| -62 |  |  |  |  |  |  |  |  |  |  |  |  |  |  |  |  |  |  |  |
| -60 |  |  |  |  |  |  |  |  |  |  |  |  |  |  |  |  |  |  |  |
| -58 |  |  | 5 | 9 |  |  |  |  |  |  |  |  |  |  |  |  |  |  |  |
| -56 |  |  | 5 | 8 | 9 |  |  |  |  |  |  |  |  |  |  |  |  |  |  |
| -54 |  |  | 5 | 8 | 8 |  |  |  |  |  |  |  |  |  |  |  |  |  |  |
| -52 |  |  |  | 8 | 7 | 0 |  |  |  |  |  |  |  |  |  |  |  |  |  |
| -50 |  |  |  | 8 | 6 | 0 |  |  |  |  |  |  |  |  |  |  |  |  |  |
| -48 |  |  |  | 2 | 2 | 0 |  |  |  |  |  |  |  |  |  |  |  |  |  |
| -46 |  |  |  |  | 0 | 3 | 0 |  |  |  |  |  |  |  |  |  |  |  |  |
| -44 |  |  |  |  | 4 | 5 | 0 | 1 |  |  |  |  |  |  |  |  |  |  |  |
| -42 |  |  |  |  |  | 0 | 0 | 0 |  |  |  |  |  |  |  |  |  |  |  |
| -40 |  |  |  |  |  | 0 | 0 | 0 |  |  |  |  |  |  |  |  |  |  |  |
| -38 |  |  |  |  |  | 0 | 0 | 0 | 0 |  |  |  |  |  |  |  |  |  |  |
| -36 |  |  |  |  |  |  | 1 | 0 | 0 | 0 |  |  |  |  |  |  |  |  |  |
| -34 |  |  |  |  |  |  |  | 3 | 0 | 0 | 4 |  |  |  |  |  |  |  |  |
| -32 |  |  |  |  |  |  |  | 0 | 0 | 0 | 0 | 0 |  |  |  |  |  |  |  |
| -30 |  |  |  |  |  |  |  |  | 2 | 0 | 0 | 0 |  |  |  |  |  |  |  |
| -28 |  |  |  |  |  |  |  |  | 4 | 0 | 0 | 0 | 0 | 3 |  |  |  |  |  |
| -26 |  |  |  |  |  |  |  | 0 |  | 2 | 0 | 0 | 0 | 0 | 0 |  |  |  |  |
| -24 |  |  |  |  |  |  |  |  | 0 |  | 0 | 0 | 0 | 0 |  |  |  |  |  |
| -22 |  |  |  |  |  |  |  |  | 0 | 1 | 1 | 1 | 0 | 0 | 0 |  |  |  |  |
| -20 |  |  |  |  |  |  |  |  |  | 0 | 0 |  | 1 | 3 | 0 | 0 |  |  |  |
| -18 |  |  |  |  |  |  |  |  |  | 0 | 1 | 0 | 5 | 3 | 1 | 0 | 0 |  |  |
| -16 |  |  |  |  |  |  |  |  |  |  | 0 | 0 | 1 | 0 | 4 | 0 | 0 |  |  |
| -14 |  |  |  |  |  |  |  |  |  |  |  | 0 |  | 0 | 1 | 4 | 1 | 0 |  |

NºR = 543
Nº NR = 843
EQ_PC = 43%
POD = 70,5%
FAR = 31,4%
CSI = 53,3%

The main rain points are focused in a smaller spectral area (see shaded cells in table 8.11) and show larger rain classes than in the other two 2-D matrices (table 8.8 and table 4.3D). Many cells with relatively high rain classes can be identified in the area delimited by the ellipse that is not present in the other two matrices. Both features together produce irregular CRR images with areas of extremely high rain rates full of holes without rainfall as illustrated in the next figure 8.10.

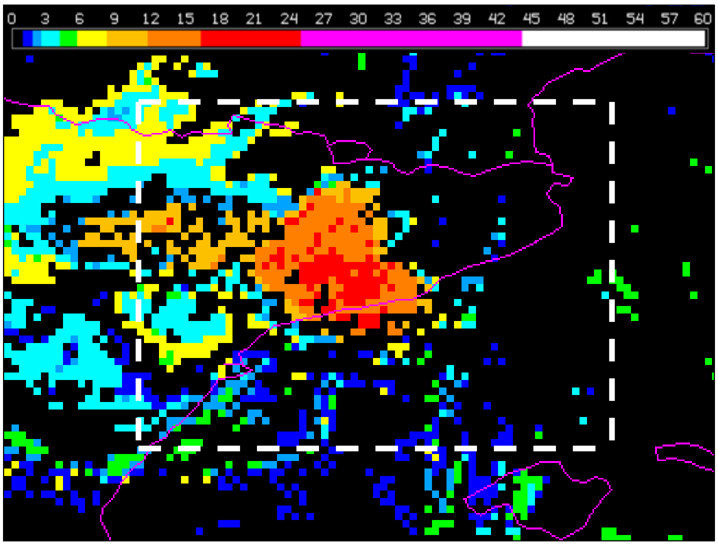

Figure 8.10. MCRR2 image at 0200 UTC.

*d) Results of algorithms calibrated using the 126 rain gauges*

Rain rate images and accumulated images from the two new curves, A-Ec1 and A-Ec2, are not very different than those shown in figures 8.6c and 8.7a, and correspond to A-Ec calibrated with radar, and therefore are not shown. However, with the help of statistical indices as applied in the previous experiments, it is possible to analyse the new algorithms. Satellite rain rates derived from the two new curves, A-Ec1 and A-Ec2 and the new CRR matrix (MCRR2) are verified to radar as shown in the next table 8.12. Satellite rain accumulation results in 24 hours from the new algorithms compared to kriged accumulations from rain gauges are shown in table 8.13. The first conclusion from the analysis of the statistical results illustrated in the next two tables is that the worse results correspond to the MCRR2 as expected in view of the rain rate images as the example shown in figure 8.10. It has produced the lowest CORR, the larger BIAS and RMS compared to the other algorithms. This suggests that the MCRR2 matrices derived from rain gauges are not as accurate as the other two, CRR and MCRR, generated with the help of the radar. Therefore the use of radar rainfall images instead of rain gauges to calibrate CRR matrices is recommended at least for short time calibration periods such as five hours. The other two algorithms A-Ec1 and A-Ec2 seem to work properly for rain rates in view of the numerical results in the tables. However the A-Ec2 has a stronger tendency to under-estimate accumulated precipitation with respect to A-Ec and A-Ec1 in view of the negative BIAS shown in table 8.13.

Table 8.12. Statistical results for the rain rates estimated by the satellite and the new curves and new matrix obtained from the 126 rain gauges. Boldfaced numbers show best statistical results in every line.

| | RADAR | A-Ec | A-Ec1 | A-Ec2 | MCRR2 |
|---|---|---|---|---|---|
| Size | | | 33306 | | |
| Mean | 2.3 | 2.3 | 2.5 | 1.8 | 3.3 |
| SD | 6.8 | 3.0 | 3.5 | 2.8 | 6.9 |
| BIAS | | **0.0** | 0.2 | -0.5 | 1.0 |
| SDD | | -3.8 | -3.3 | -4.0 | **0.1** |
| RMS | | **6.1** | **6.1** | **6.1** | 7.6 |
| CORR | | **0.45** | **0.45** | **0.45** | 0.39 |
| POD | | **0.89** | 0.88 | 0.84 | 0.60 |
| FAR | | 0.69 | 0.68 | 0.64 | **0.59** |
| CSI | | 0.30 | 0.31 | **0.34** | 0.32 |
| FRC | | 0.55 | 0.57 | 0.64 | **0.72** |

Table 8.13. Statistical results for 24 hours of rain accumulation estimated by the satellite and new curves, A-Ec1 and A-Ec2 and new matrix MCRR2. Boldfaced numbers show best statistical results in every line.

| | ACA | A-Ec | A-Ec1 | A-Ec2 | MCRR2 |
|---|---|---|---|---|---|
| Size | | | 659 | | |
| Mean | 52.1 | 42.5 | 47.4 | 34.0 | 59.2 |
| SD | 30.6 | 15.5 | 18.5 | 14.8 | 38.9 |
| BIAS | | -9.6 | **-4.7** | -18.1 | 7.1 |
| SDD | | -15.1 | -12.1 | -15.8 | **8.3** |
| RMS | | 27.9 | **27.3** | 31.4 | 38.0 |
| CORR | | **0.48** | 0.47 | 0.46 | 0.45 |

These results for the two new infrared curves A-Ec1 and A-Ec2 imply that infrared rainfall curves can be calibrated directly with rain gauges without decreasing substantially the accuracy. Satellite calibration tasks can be applied in this study case without the help of radar images but making use of a high number of rain gauges in a relatively small area. However in view of the accumulated results in table 8.13 a BIAS error for A-Ec2 of -18 mm $h^{-1}$ is significantly large. We believe, therefore, that the best calibration method is A-Ec1 for this case since it obtains the next higher CORR (0.47) after A-Ec, the lowest BIAS (-4.7 mm $h^{-1}$) and also lowest RMS (27.3 mm $h^{-1}$).

*e) Minimum number of rain gauges for the A-Ec1 method*

The next experiment studies the minimum number of rain gauges that are necessary for a correct performance of the A-Ec1 technique in a calibration time period of five hours. Another important reason is that 126 operative rain gauges in real time is a large number of automatic rain gauges for a region with a similar area size as the Catalonian internal basins, as commented in the beginning of section 8.6. It is very probable that part of the information acquired from this observational network is redundant for the calibration process. Therefore, we have an opportunity to assess the minimum number of rain gauges that could be employed for a correct adjustment of the A-Ec1 curve.

As shown in figure 8.11a each station is identified by a code number and they are distributed from station one in the north of the area to station 126 in the south. The experimental scheme is developed as follows. Firstly, from the 126 stations a small group was removed, each with an odd number scaled between 1 and 125. This procedure reduces the number of stations without producing significant uncovered zones in the study area. Then the A-Ec1 method is applied using the rest of the stations to compute a new infrared rain curve. The new curve is then compared with the older equation, 8.3, taken as a reference. Therefore a statistical coefficient that we have called Mean Rain Rate Error, MRRE, is used to quantify the mean anomaly in mm $h^{-1}$ of any curve compared to the reference curve. So, as shown in table 8.14 for 105 stations; MRRE is -0.99 mm $h^{-1}$ meaning that the new rainfall curve has a tendency to estimate 0.99 mm $h^{-1}$ less in average than the reference curve. We began initially to eliminate stations in groups of 10 but it was observed that the change in the MRRE index was not significant. So, we increased the number of removed stations in each time to 20 but by adding one more, 21, the process can be completed by removing exactly the 1/6 of the stations. In three iterations, 3/6, we can study the effect in calibration by removing exactly one half of the stations. Following the calibration process when one half of the stations (63) were removed, we decided to continue the process but decreasing the number of odd rain gauges at a rate of 10 in search of a more detailed MRRE index behaviour.

In each iteration other important indices in addition to the MRRE are calculated as shown in table 8.14; such as the correlation coefficient r of the best fit regression line, the temperature interval ΔT in Kelvin and the regression line A and B coefficients in the logarithm scale correspond to a linear equation structure as follows:

$$\log (R) = B\ T_{IR} + A \qquad (8.4)$$

where $R$ is rain rate in mm $h^{-1}$ that can be easily calculated from the satellite infrared temperature $T_{IR}$ in Kelvin by just inverting the logarithm.

Table 8.14. A and B are the linear coefficients derived from the best regression fit. ΔT (K) is the temperature interval between the mean points to perform the regression fit. r is best fit correlation coefficient. MRRE (mm $h^{-1}$) Mean Rain Rate Error of every new A-Ec1 curve obtained with the different number of rain gauge stations compared to the reference rain curve (equation 8.3). It is shaded the rows for which the MRRE grows appreciably.

| Nº of stations | A | B | ΔT (K) | r | MRRE (mm $h^{-1}$) |
|---|---|---|---|---|---|
| 126 | 34.7900 | -0.1469 | 2.5 | 0.97 | 0.00 |
| 105 | 31.2143 | -0.1309 | 4.0 | 0.98 | -0.99 |
| 84 | 34.6566 | -0.1465 | 4.0 | 0.98 | -0.61 |
| 63 | 33.3528 | -0.1405 | 3.0 | 0.94 | -0.47 |
| 53 | 32.7051 | -0.1371 | 4.5 | 0.98 | 0.34 |
| 43 | 32.2706 | -0.1348 | 4.5 | 0.98 | 0.97 |
| 33 | 35.8379 | -0.1512 | 5.0 | 0.98 | 1.15 |
| 23 | 28.8248 | -0.1213 | 10.0 | 0.99 | -3.11 |
| 13 | 21.7678 | -0.0902 | 11.0 | 0.98 | -4.51 |

The MRRE evolution with respect to the number of stations was largely unpredicted by us. Instead of an expected gradual growth of the MRRE while the available stations are eliminated, the results in table 8.14 show a decrease of MRRE with the lowest value of 0.34 mm $h^{-1}$ for 53 stations. It seems therefore that it exist a specific number of stations that produces a minimum MRRE. After this point, if the number of stations continues decreasing the MRRE grows appreciably (see shaded rows of table 8.14). Other observation from this table is that if a MRRE of 1.0 mm $h^{-1}$ is tolerable then 43 rain gauges working in five hours within satellite images time resolution of 30 minutes would give a suitable amount of data to perform an A-Ec1 curve. Therefore if the internal basins of Catalonia occupy an area of 16512 $km^2$ only 43 rain gauges in this area are needed for calibration, therefore, we have one station each 380 $km^2$ on average, which supposes, a minimum mean distance between stations of 19.6 km for an ideal network of rain gauges.

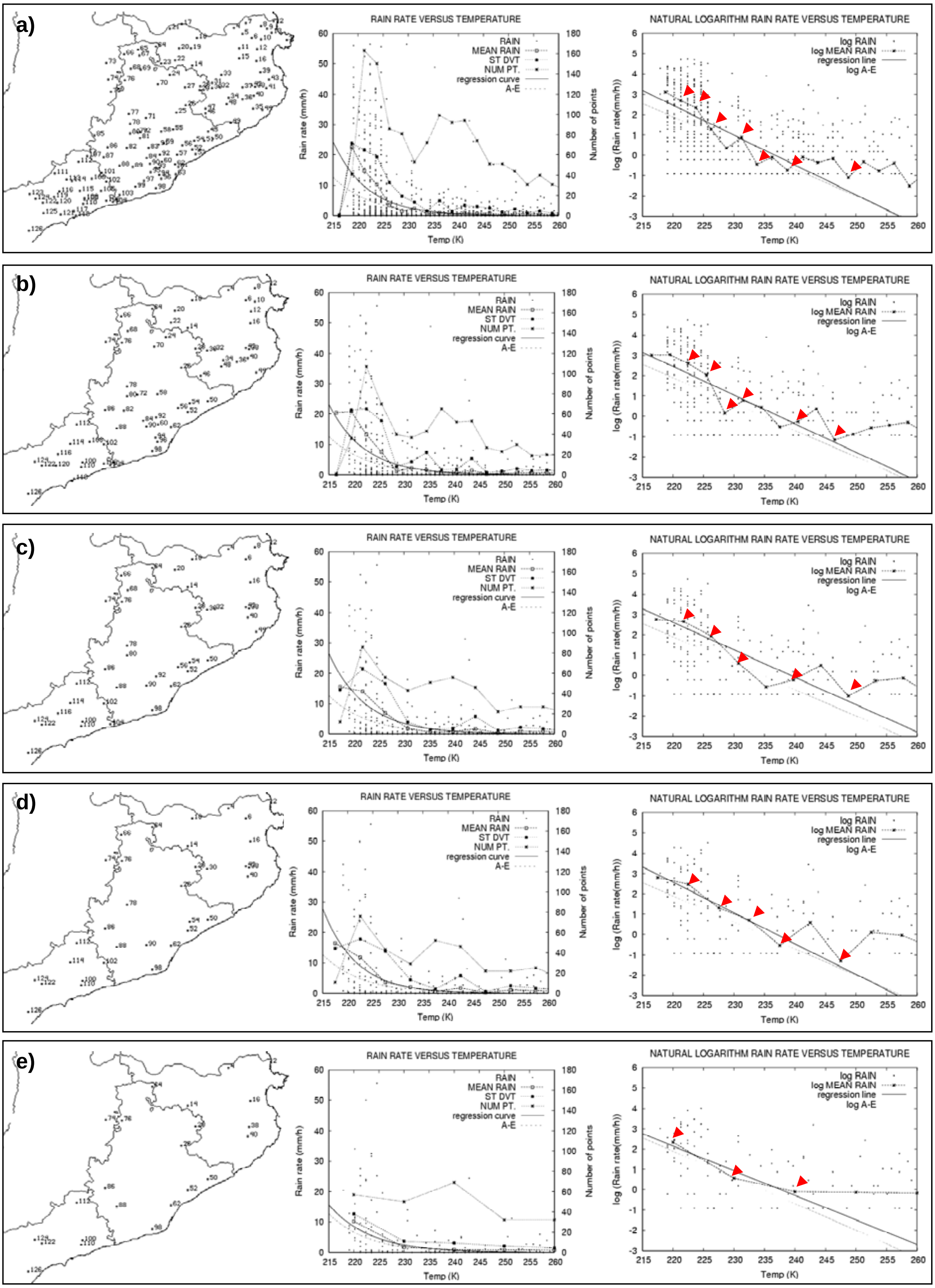

Figure 8.11. A-Ec1 calibration method applied using different number of rain gauges for the internal basins of Catalonia. (a) 126 stations, (b) 63 stations, (c) 43 stations, (d) 33 stations and (e) 23 stations. The red triangles indicate the mean points used in the line regression fit.

### *8.7 Discussion and conclusions*

#### *a) Discussion*

An important fact that makes this case of study difficult from the satellite point of view is that convective cells are covered by clouds with relatively homogeneous and relatively warm tops in this case study. This conclusion is based on a qualitative check of the infrared satellite images and radar images. The relatively warm cloud top produces a systematic under-estimation of the precipitation while the homogeneity of these cloud tops makes convection at medium and low levels almost invisible from Meteosat. Under these conditions and in view of the results, A-E and CRR standard satellite algorithms have a tendency to compute strongly under-estimated amounts of precipitation and to produce low accuracy compared to radar rain rates and 24 hour accumulations. These results are not very surprising when one considers that we are attempting to estimate precipitation on a very convective case using standard algorithms calibrated with a large amount of data. Therefore the use of these standard techniques in such severe events may still be under consideration and review.

The tested rainfall corrections do not solve, in general, the under-estimation and low accuracy problems. The causes of this are difficult to explain and need much more detailed sensitivity studies that should be performed on more precipitation cases. In the initial steps the application of the PWRH and OC correction factors was of great hope because they were the ones that could increase the rainfall amounts significantly. The reality, in view of the results in tables 8.2 to 8.7 for the two corrections, is that only mild and unclear improvements in the BIAS, SDD and, in some cases, on the RMS are observed but never in the CORR index. Only the parallax seems not to not worsen the rain rates and be slightly beneficial based on small improvements shown in the CORR index for the accumulated A-E. However, the GR1 correction appears to produce a little advance in the accumulated CRR precipitation but this result should be considered with caution because at the same time the BIAS and the RMS both suffer high deviations when compared to radar.

With the aim of resolving these problems two options were investigated. Firstly, both algorithms are recalibrated with the available radar data during the period of highest precipitation. In addition, the last section, 8.6, is focused towards the recalibration of satellite algorithms directly with data from the rain gauges. Secondly, we have developed a method to assimilate the lightning data in order to correct rain rates.

The calibration alternative can, obviously, correct the estimated rainfall amounts to others much closer to the real ones as shown by lower BIAS errors in Tables 8.9 and 8.10. However accuracy stays almost unchanged or a little bit improved as shown by the CORR index in the same tables. Calibration is easy to be performed once the case is over and the radar and satellite data are available. A much more difficult problem not explored in this work at the present time, is how could be apply the calibration in real time. Under our opinion a possible procedure could be as explained next:

The first step is the generation of a database of A-E rainfall curves and CRR matrices corresponded to flood cases occurred at different times of the year for the Catalonian region. Then, a method to select the most adequate curve and/or matrix from the database to each meteorological situation, based on the current weather forecast, should be developed. This best curve and/or matrix could be used for the initial stages of the storm. One time the meteorological event has began and a suitable amount radar and satellite images are available over the affected area (two or three hours) A-E and CRR calibration routines can start automatically in order to generate updated coefficients that can be used, maybe, for the next three hours. Then this calibration-application cycle can be repeated until the end of the storm.

From the *KL* factor generation during the calibration period is obvious that the radar rainfall is significantly greater in electrically charged points than the ones without electrical activity (see figure 8.5a). On the other hand, most of the cloud to ground lightning hits counted in the calibration period have occurred, as expected, for points corresponded to Meteosat infrared temperatures ($T_{IR}$) below 230 K as shown in figure 8.5b. These two factors imply that the three datasets; Meteosat, radar and lightning should be well correlated in time and space. However there exist some electrical discharges associated to $T_{IR}$ greater than 240 K and, in addition, correlated with high radar rain rates (see one small section of the *ALR* curve with rain rates greater than 20 mm $h^{-1}$ in figure 8.5a). This is the origin that the *KL* correction factor is inversely proportional to the Meteosat infrared temperature. Our hypothesis to explain the discrepancy between the *KL* and the $T_{IR}$ is that it is caused by strong convection occurred at low levels and, thus, in clouds with warm tops. Much more cases should be studied and the *KL* factor has to be computed and analyzed again to get more solid conclusions. But, if our supposition is true the use of the *KL* factor within lightning and satellite could be an adequate tool to highlight low level convective precipitating points. By employing only satellite images to detect them it would be a much more difficult task. The use of lightning to correct rain rates by the *KL* parameter has improved the results as explained at the end of section 8.5 and has also the big advantage that it is easily exportable to other cases. Such lightning detection systems can cover very high land and sea extensions and the information generated from them are perfectly combinable with geostationary satellite images or derived cloud products.

Comparing the two algorithms, A-E and CRR, calibrated or not and based on the CORR index in the tables, the first one has demonstrated in general a better performance for rain rates and the second one, better results for accumulations. The relatively CRR bad results for the rain rates could be motivated in part by few Meteosat-7 water vapor band images that were missed in the verification period causing bugs in the CRR data stream. In order to keep constant the number of points in the verification with respect to A-E these bugs were filled with time averaged CRR images. These could be in some measure behind the poor results for CRR rain rates evaluation.

Many times and in many places radar images are not available so that it was explored the possibility to do the recalibration of the satellite algorithms using rain rates from rain gauges as described in section 8.6. From the three tested methods, A-Ec1, A-Ec2 and CRR, the last produces the poorest results after a first verification with respect to radar precipitation images. In addition the new CRR images or MCRR2 images are full of noise as shown in figure 8.10 caused by several anomalous rain classes appeared in the new rain matrix (area indicated by the circle in table 8.11). This feature observed in the MCRR2 rain matrix and presumably behind the accuracy decrease, could be produced by the limited size of the calibration dataset with no more than 1386 points. This is probably not enough data to define correctly the no rain area in the rain matrix after applying the CRR statistical calibration method. A possible solution to this problem could be the enlargement of the calibration time to 12 or 24 hours, however in this case the calibration-application operability in short time periods would be almost impossible.

From the other two methods, A-Ec1 and A-Ec2, the second produce a sensible under-estimation of the 24 hours accumulated precipitation that unfortunately we cannot explain at the time of writing this thesis why the A-Ec1 method provides the best results. In the last experiment it was observed that assuming an error of 0.34 mm h$^{-1}$ in the estimated precipitation by the A-Ec1 method curve, the calibration can be performed with 53 rain gauges well distributed instead of 126, which is the total number of rain gauges. This result suggests that part of the information acquired by a dense network of stations for a A-Ec1 curve calibration is redundant and closer results can be obtained by using much less rain gauges. On the other hand assuming a greater error of 1 mm $h^{-1}$ (which corresponds to the use of 43 rain gauges as shown in table 8.14) and if the calibration is done using infrared images from the Meteosat-8 with a time resolution 15 minutes, then, we may have two possibilities that could be explored in the near future:

- The calibration period could be diminished to the half (two hours and a half) using 43 rain gauges.
- The number of stations could be diminished to the half (22) for a calibration period of five hours.

*b) Conclusions*

A-E and CRR standard algorithms applied to the Montserrat flood case has a strong tendency to under-estimate precipitation due to the relatively homogeneous and warm cloud tops found in this case of study.

From the different rainfall correction factors only the parallax one seems to not deteriorate the results after an analysis of the statistical indices.

In this flood case a recalibration experiment with radar of the A-E curve and CRR matrix can improve the estimated precipitation amounts as natural. The problem to solve in the near future is how to apply calibration routines in real time in such severe events.

The assimilation of lightning data by a new correction factor described in this work can give very valuable information about low level convection and can improve sensibly the estimation of the precipitation from satellite.

This study does not clarify which of the two algorithms A-E or CRR do better estimations in general. More cases in this sense should be still analyzed to get solid conclusions.

In the cases in which radar images are not available a direct calibration with rain gauges is possible using the 126 stations during 5 hours. From the three tested methods (A-Ec1, A-Ec2 and CRR), the A-Ec1 gives the best results after a verification with respect to radar rain rates and kriged 24 hours accumulations from the rain gauges. In addition, more than half of the rain gauges are not strictly necessary to calibrate a rainfall curve applying the A-Ec1 method by assuming an error of 0.34 mm $h^{-1}$ compared to the reference curve.

# 9. General conclusions and current studies

## 9.1 General conclusions

This thesis applies and verifies two satellite rainfall estimation methods, the Auto-Estimator and CRR, on two flood events occurring in two different places, Albania and the Catalonian region in Spain. Both zones have their coastlines along the Mediterranean Sea and therefore are subject to a strong influence of this sea. Both flood cases have very different origins. The first one was generated by a very moist and unstable air mass flowing from the west and southwest producing stationary severe convection over the Albanian basin. Thunderstorm clouds were highly developed with high cloud tops due to extraordinary cold pixels observed in the Meteosat infrared images. The principal consequence of this was the strong rainfall over-estimation produced by the Auto-Estimator. The second flood case was originated by an active cold front that crossed the Iberian Peninsula from the north to east. The violent interaction between the cold air mass coming from the north and the warm and moist Mediterranean environment was the principal cause of the heavy rainfalls that occurred over the Catalonian basin. However, here cloud top infrared temperatures from Meteosat were relatively warmer and the two satellite rainfall methods have experienced a strong tendency to under-estimate precipitation. These results are not very surprising when it is considered that we are attempting to estimate precipitation on flood cases using standard algorithms calibrated with a large amount of data. Therefore the use of these standard techniques in such severe events may remain under consideration.

Rainfall corrections proposed by Vicente in different publications (Vicente *et al*. 1998; 2002) should add flexibility to the standard algorithms in extreme flood cases. These have been performed and tested. The MM5 numerical model outputs were used for PWRH and OC correction factors. In general after a sensitivity study, any of these solved the over and under-estimation problems experienced in each case and has increased correlations significantly. While on the Catalonian flood case only PC and GR1 give mild and unclear improvements, over Albania the PC, GR2 and OC correction factors have produced encouraging results with respect to the spatial distribution of the daily precipitation. These have increased correlation coefficients of around 14% in average and a total of 20% by testing the three corrections together, one after another. It is evident that with only two studied flood cases it is difficult to get solid conclusions about these corrections. However we believe that PC, GR1, GR2 and

OC can contribute to improving the estimation and advances would be more significant for those cases with strong convective cloud tops as observed in the Albanian case. In any case, the research should continue with the analysis of more flood cases. Details concerning the development of new corrections are provided in this thesis. Firstly the GR2 is a dynamic version of the GR1 proposed by Vicente *et al.* (1998). It has the benefit of being able to calculate infrared temperature changes in time by following the movement of the cloud tops. Secondly, the lightning correction factor or KL factor can focus the main precipitation on those pixels where lightning activity is detected. It is especially recommended in cases in which convection is mostly developed on low levels in the troposphere or covered by a layer of clouds with homogeneous tops and therefore difficult to be identified from geostationary satellites. As mentioned, any of the standard corrections did not produce clear improvements in the Montserrat case, however, the use of electrical discharges through the KL factor had produced measurable advances. A mean increase around 9% over the correlation coefficients for rain rates and mean increase of 15% for 24 hours rain accumulations were observed.

Another important aspect studied in this research is that the recalibration performed directly over the flood cases can improve the results and show how far the new calibrated coefficients are from the standard. Logically, satellite rainfall estimates are in general well adjusted after a calibration but spatial skills in both flood cases were not substantially improved with respect to the original algorithms. Calibration has a significant impact on the rainfall curves for the Auto-Estimator and on CRR matrices compared to standard. These two facts make a short time calibration process necessary in order to improve the estimations on such severe events. However, calibration routines in real time are technically difficult and need a good synchronisation in time and space between the satellite, radar and/or rain gauge data streams. Other problems not explored in this work but planned for the near future, concern the time periods and optimal spatial domains necessary to perform correct calibration routines.

Albania is a region in which meteorological radars were not operative at the time of writing this thesis. We have tried a new calibration method combining Meteosat infrared images directly with eight rain gauges in three days of heavy rainfall. Results were encouraging as commented in chapter 5 but this experiment was only a small challenge, many studies have to be completed with other rainfall cases to assess these ideas before this method can be applied operationally. Over the Catalonian region, a c-band radar located near Barcelona city provides much more rainfall information over the study area. However, there are some disadvantages behind these sensors. For example; radar images can suffer from attenuation and calibration problems causing errors on the radar estimated precipitation. In this thesis chapter 7 was dedicated to the Barcelona radar and to study two different methodologies to get reliable radar rainfall estimations with the help of a rain gauge network. Once time radar attenuation periods are identified and radar rain rates are verified, they can be used for calibration and validation purposes for satellite rainfall methods. Advantages of radars in addition to the high volume of rainfall data that can be generated in one scan, is that spatial scope is greater than the one provided by a rain gauge network and the distribution of the precipitation is screened with a much higher space-time resolution. Therefore fast calibration routines between satellite and radar images could be started maybe a few hours before the dangerous part of the storm reaches highly populated areas around the area covered by radar. However in cases in which the radar is not available, a standard algorithm can be applied for the first hours while a direct calibration with rain gauges using the A-Ec1 or A-Ec2 method can be activated. The calibration time period using rain gauges depends on the number of operative stations. With only 8 rain gauges that can provide rain rates, as occurred in Albania, minimum periods of 24 hours are necessary (experiments done but not shown in this thesis) while using 126 rain gauges, as in Catalonia, five hours seems to be enough time. However, it probably could be reduced to a much smaller period assuming an error in the infrared curve estimations.

Other results about satellite rainfall direct calibration with rain gauges are that for CRR matrices generation need a big volume of rainfall data that only a radar can provide, at least for short calibration periods. The A-Ec2 method provide better results in the Albanian flood case while the A-Ec1 method is the best in the Montserrat case. In this situation is difficult to say which of the two methods is better, as more flood cases should be studied for clarification. The A-Ec1 calibration experiment for the second flood case, by assuming a minimum error of 0.34 mm $h^{-1}$ compared to the reference curve, the number of stations in five hours can be reduced from 126 to only 53. And, assuming a greater error the number of stations might be reduced significantly more.

Considering only the two studies over Albania and Catalonia, it is difficult to identify which of the two methods, A-E or CRR, can do better estimations. In the Albanian flood case the A-E has provided slightly higher CORR (0.39) indices for daily accumulations than CRR (0.37) but has also produced a strong over-estimation (A-E BIAS: +137 mm). CRR matrices have produced better estimated amounts (CRR BIAS:

+2.4 mm) and a recalibration was not necessary. Errors shown by RMS indices are very high A-E before calibration (246.5 mm) and much lower after calibration (45 mm) and have the same CRR value (45 mm). For the flood case in Catalonia CRR (0.51), accumulation in 24 hours was a bit better than A-E (0.48), taking into account again the CORR index. However, both algorithms have produced a strong under-estimation (CRR BIAS: -41.7 mm, A-E BIAS: -23.8 mm) justifying, the recalibration experiment with the radar rain rates. After this process, CRR correlation coefficient is still a bit higher that the one provided by the calibrated Auto-estimator. Errors given by the RMS index are around 27 mm for both algorithms before and after the calibration. Advantages of the CRR algorithm is that it can eliminate cold thin cirrus clouds with no precipitation as commented in section 4.4 and it has less rain rate classes (see table 4.2) which is more realistic due the high uncertainty of rainfall estimations. A possible error source, not taken into account for CRR, was that some Meteosat water vapour images are missed and bugs were filled with time averaged CRR images as explained in section 8.6. In general, more cases should be studied in order to know which method can perform better rainfall estimations.

It is clear that spectral interaction between cloud top radiation and the rainfall from their bases have a very dynamic and complex behaviour that can not be described with only one averaged calibration curve or matrix. In addition, discrepancies between cloud top radiation and averaged rainfall schemes seem to be increased in severe meteorological events just when these estimations in real time are really important. To improve the estimation of rain rates and accumulations from A-E and CRR, it is essential to study how calibration coefficients change with the season of the year or to each type of storm. To do that, a set of rainfall cases at different times of the year will be planned and a database of A-E rainfall curves and CRR matrices will be computed in the near future.

### *9.2 Current Studies*

The research and development work is still in progress in different ways: One important line, recently started, is focused on the application in real time of the Auto-Estimator and CRR algorithms within other updated methods. Here some post processing corrections are included that have shown some improvements such as parallax (PC), the dynamic cloud growth rate (GR2), orographic (OC) and lightning correction factor (LG). However, some of these applications are now operative at the time of writing and images are available at our web page http://eady.uib.es/web-grup/satellit/. At the same time and making use of the operational satellite data flow, a database of rainfall curves and CRR matrices generated every rainy day over the western Mediterranean area is archived for later analysis.

A second research line looks at very interesting meteorological features such as tropical-like hurricanes in the Mediterranean Sea (Emanuel, 2005; Fita *et al*. 2007) from a Meteosat perspective. Storms with a clear eye surrounded by an asymmetric cloud structure are quite unusual in the Mediterranean, one or two cases per year are identified in satellite images. Examples of these storms are shown in figure 9.1. At some point in time they are generated over the sea and can affect islands and continental coastal lands. Although documented tropical-like cyclones have not usually achieved hurricane intensity, their potential for damage is high due to the densely populated Mediterranean coastal regions. Different features of a set of these storms are analysed from a satellite point of view: storm trajectories, spatial lengths and speeds of displacement are analysed. Precipitation fields are estimated from Meteosat infrared images and convective cloud pixels are identified with the help of electrical discharge data. Low level winds are estimated from low cumulus clouds tracked in infrared images by applying a cross correlation method. Preliminary results at the time of writing were presented in the EUMETSACONF2007 which can be found at http://eady.uib.es/web-grup/satellit/ in the Medicanes section. This initiative was started for experiments based on sensitivity studies of these meteorological features applying the MM5 model within assimilation of satellite and lightning derived results. Here, remote sensing observations related to precipitation and convection is prepared to be assimilated by the model following a methodology similar to the one explored by Davolio and Buzzi (2002). Most of these works are developed into the framework of the Precioso project (MEC, CGL2005-03918/CLI). Results from assimilation experiments performed by Fita *et al*. (2007) can also be found at the same web page.

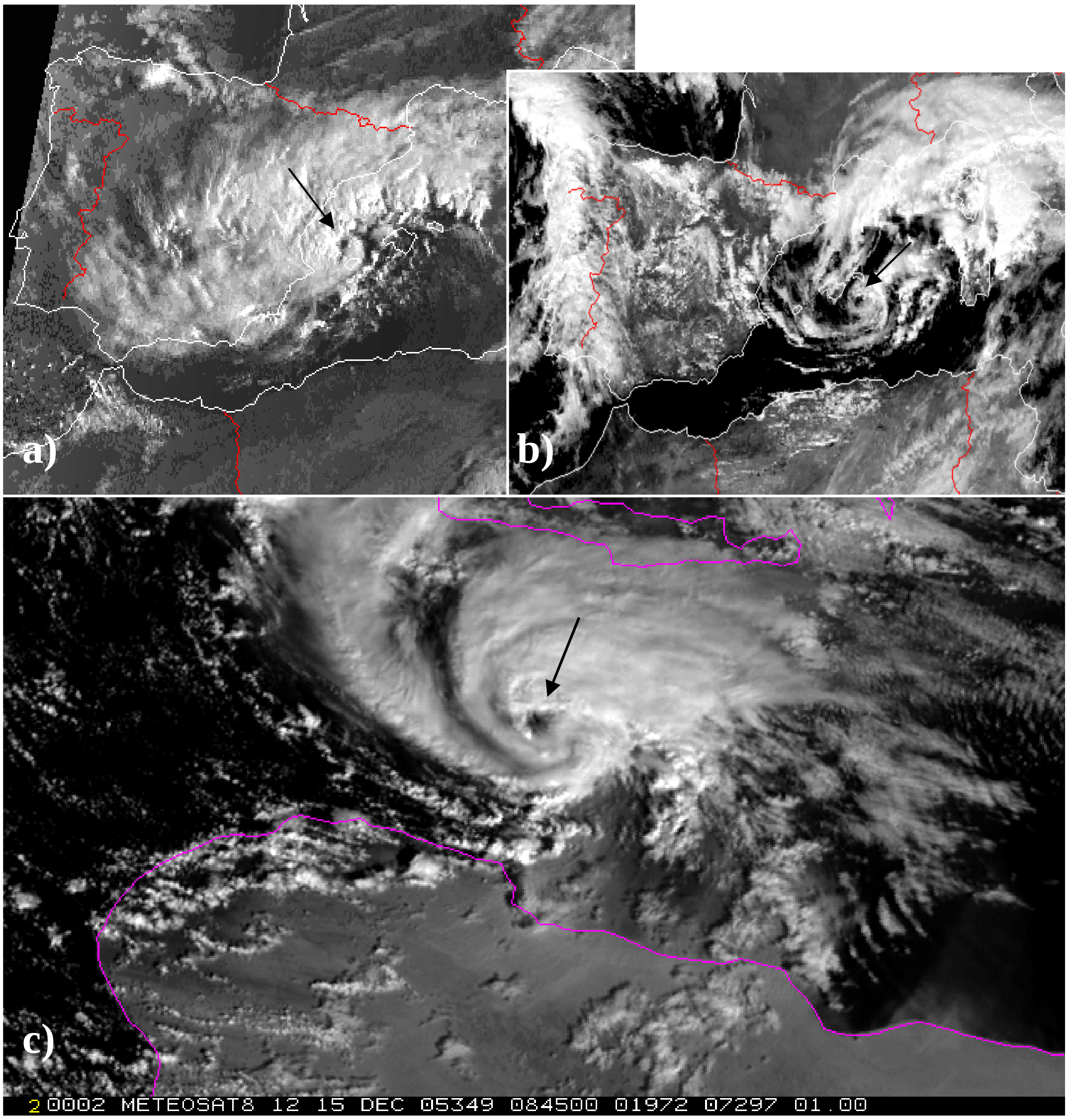

Figure 9.1: Examples of tropical-like Mediterranean storms in Meteosat visible images corresponded to three different cases: (a) 1996/09/12 at 0500 UTC, (b) 2003/10/18 at 1200 UTC and (c) 2005/12/15 at 0845 UTC. Black arrows are pointing to the storm's eye.

## Publications related to this work.

De Luque A., Porja T., Martín A., Guijarro J. A., Alonso S., 2006, A case of severe flood over Albania: a rainfall analysis from a satellite perspective, *Advances in Geosciences*, Vol. 7, pp 65-72 (Plinius 2005, proceeding, http://overview.sref.org/1680-7359/adgeo/2006-7-65)

Luque A., Gómez I., and Manso M., 2006, Convective Rainfall Rate multi-channel algorithm for Meteosat–7 and radar derived calibration matrices, *Atmósfera*, 19(3), 145-168. (http://www.ejournal.unam.mx/atmosfera/atmosfera_v19-3.html)

Luque A., T. Porja A. Martin, Romero R. and S. Alonso, 2006, Two satellite rainfall algorithms and corrections tested in a severe flood over Albania, Article submitted to *Annales Geophysicae*.

Luque A., Martin A., Romero R., Alonso S., 2006, Fine tuning of Radar Rainfall Estimates based on Bias and Standard Deviations Adjustments. *Fourth European Conference on Radar in Meteorology and Hydrology (ERAD 2006),* Barcelona (Spain), September 2006 (Book of proceedings, http://www.grahi.upc.edu/ERAD2006/proceedingsMask/00038.pdf)

Luque A., Martin A., Romero R., and Alonso S., Assessment of the Direct Calibration Method for radar rainfall estimation: a case study over a severe flood in Catalonia, Article under revision.

Luque A., Martin A., Romero R., Guijarro J. A. and Alonso S., A rainfall analysis of an active frontal perturbation over Catalonia using Meteosat, radar and lightning data, Article under revision.

Martín A., Romero R. Homar V., De Luque A., Alonso S., Rigo, T., and Llasat C. (2006), Sensitivities of a flash flood event over Catalonia: A numerical analysis, *Monthly Weather Review*. Vol. 135, No. 2, pages 651–669.

Mira A., Cuxart J., Jiménez M. A., Luque A., Alonso S. and J. A. Guijarro. Verification of a clear-sky mesosclale simulation using satellite-derived surface temperatures, Submitted in October 2007 to *Monthly Weather Review*.

## References

Adler R. F. and Mack R. A., 1984, Thunderstorm cloud height-rainfall rate relations for use with satellite rainfall estimation techniques, *Journal of Climatology and Applied Meteorology*, 23, 280-296.

Adler R. F. and Negri A. J., 1988, A Satellite Infrared Technique to Estimate Tropical Convective and Stratiform Rainfall, *Journal of Applied Meteorology*, 27, 30-51.

Anagnostou E. N., Negri A. J. and Adler R. F., 1999, A satellite infrared technique for diurnal rainfall variability studies, *Journal of Geophysical Research*, 104**,** 31477–31488.

Anthes R. A. and Warner T. T., 1978, Development of hydrodynamic models suitable for air pollution and other meso-meteorological studies, *Monthly Weather Review*, 106, 1045-1078.

Arkin P. A., 1979, The relationship between fractional coverage of high cloud and rainfall accumulations during GATE over the B-scale array, *Monthly Weather Review*, 106, 1153-1171.

Arkin P. A. and Janowiak J., 1991, Analysis of the global distribution of precipitation, *Dynamics of Atmospheres and Oceans*, 16, 5-16.

Arkin P. A. and Meisner B. N., 1987, The relationship between largescale convective rainfall and cold cloud over the Western Hemisphere during 1982-84, *Monthly Weather Review*, 115, 51-74.

Atlas D., Rosenfeld D. and Wolff D. B., 1990, Climatologically tuned rain rate relations and links to area-time integrals, *Journal of Applied Meteorology*, vol. 29, 1120-1125.

Barrett E. C. and Martin D. W., 1981, The Use of Satellite Data in Rainfall Monitoring, Academic Press, 340 pp.

Bellon A., Lovejoy S. and Austin G. L., 1980, Combining satellite and radar data for the short-range forecasting of precipitation, *Monthly Weather Review*, 108: 1554-1556.

Betts A. K. and Miller M. J., 1986, A new convective adjustment scheme. Part II: Single column test using GATE wave, BOMEX, ATEX and Artic air-mass data sets, *Quarterly Journal of the Royal Meteorological Society*, 112, 693-709.

Bhagarva M. and Danard M., 1994, Application of optimum interpolation to the analysis of precipitation in complex terrain, *Journal of Applied Meteorology*, 33, 508-518.

Binder P., 1988, A Normalization Procedure for Meteosat Visible Channel Data, *Journal of Atmospheric and Oceanic Technology*, Vol. 6, pp. 67-75.

Cairns M., Huggins A., and Vasiloff, S., 1998, Precipitation Algorithm improvements in the Eastern Sierra, NWS Western Region Technical Attachment No. 98-08, Salt Lake City, UT, 5 pp.

Calheiros R. V. and Zawadzki I., 1987, Reflectivity-rain rate relations for radar hydrology in Brazil, *Journal of Climate and Applied Meteorology*, vol. 26, 118-132.

Cheng M. and Brown R., 1995, Delineation of precipitation areas by correlation of Meteosat visible and infrared data with radar data, *Monthly Weather Review*,123: 2743-2757

Cheng M., Brown R. and Collier C. G., 1993, Delineation of precipitation areas using Meteosat infrared and visible data in the region of the United Kingdom, *Journal of Applied Meteorology*, 32: 884-898.

Crosson W. L., Duchon C. E., Raghavan R. and Goodman S. J., 1996, Assessment of Rainfall Estimated Using a Standard Z-R Relationship and the Probability Matching Method Applied to composite Radar Data in Central Florida, *Journal of Applied Meteorology*, **35**, 1203-1219.

Davolio S. and Buzzi A., 2002, Assimilation of precipitation into a regional model, Proceedings of the 4th EGS Plinius Conference, Mallorca, Spain.

De Luque A., Porja T., Martín A., Guijarro J. A. and Alonso S., 2006, A case of severe flood over Albania: a rainfall analysis from a satellite perspective. *Advances in Geosciences*, Vol. 7, pp 65-72 (Plinius 2005, proceeding, http://overview.sref.org/1680-7359/adgeo/2006-7-65)

Doswell III C. A., Ramis C., Romero R., and Alonso S., 1998, A diagnostic study of three heavy precipitation episodes in the western Mediterranean region, *Weather and Forecasting*, 13, 102-104.

Emanuel K. A., 2005, Genesis and maintenance of ”mediterranean hurricanes”, *Advances in Geoscience*, 2, 217–220.

Fita L., Romero R., Luque A., Emanuel K., and Ramis C. 2007, Analysis of the environments of seven Mediterranean tropical-like storms using an axisymmetric, nonhydrostatic, cloud resolving model, *Natural Hazards and Earth System Sciences*. MS-NR: nhess-2006-0063. Page(s) 41-56. (http://www.nat-hazards-earth-syst-sci.net/7/41/2007/nhess-7-41-2007.pdf)

Govaerts Y. M., 1999, Correction of the Meteosat-5 and -6 VIS band relative spectral response with Meteosat-7 characteristics, *International Journal of Remote Sensing*, 20, 3677-3677.

Govaerts Y.M., Pinty B., Verstraete M. M., and Schmetz J., 1998, Exploitation of angular signatures to calibrate geostationary satellite solar channels, IGARSS'98, Seattle, USA, 6-10 July 1998, 327-329.

Griffith C. G., Woodley W. L., Grube P. G., Martin D. W., Stout J., and Sikdar D. N., 1978, Rain estimation from geosynchronous satellite imagery - Visible and infrared studies, *Monthly Weather Review*, 106, 1153-1171.

Grecu M., Anagnostou E. N. and Adler R. F., 2000, Assessment of the use of lightning information in satellite infrared rainfall estimation, *Journal of Hydrometeorology*, 1, 211-221.

Gruber A., 1973, Estimating rainfall in regions of active convection, *Journal of Applied Meteorology*, 12, 110-118.

Gube M., Gärtner V., and Schmetz J., 1996, Analysis of the operational calibration of the Meteosat infrared-window channel, *Meteorological Applications*, 3, 307–316.

Homar V., Ramis C., Romero R., Alonso S., García-Moya J.A., and Alarcón M., 1999, A case of convection development over the western Mediterranean Sea: A study through numerical simulations, *Meteorology and Atmospheric Physics*, 71, 169-188.

Homar V., Romero R., Ramis C., and Alonso S., 2002, Numerical study of the October 2000 torrential precipitation event over eastern Spain: Analysis of the synoptic-scale stationarity, *Annales Geophysicae*, 20, 2047-2066.

Homar V., Romero R., Stensrud D. J., Ramis C., and Alonso S., 2003, Numerical diagnosis of a small, quasi-tropical cyclone over the Western Mediterranean: Dynamical vs. boundary factors, *Quarterly Journal of the Royal Meteorological Society*, 129, 1469-1490.

Hong S.-Y. and Pan H.-L., 1996, Non-local boundary layer vertical diffusion in a Medium-Range Forecast model, *Monthly Weather Review*, 124, 2322-2339.

Huggins A. and Kingsmill D., 1998, Improvements of WSR-88D Algorithms in the Intermountain West with Applications to Flash Flood Forecasts and Wintertime QPFs. CIASTA Annual Report on Progress under Task II: Weather Research. Desert Research Institute, Dandini Research Park, Reno, NV, 26 pp.

INM, 2000, Scientific Report for MTR on PGE05, Convective Rainfall Rate, EUMETSAT Technical & Scientific Documentation (SAF/NWC/INM/SCI/MTR/001).

INM, 2002, User Manual for the PGE05 of the SAFNWC/MSG, Scientific part, EUMETSAT Technical & Scientific Documentation (SAF/NWC/IOP/INM/SCI/SUM/05_v0.1)

Kain J. S. and Fritsch J. M., 1993, Convective parameterization for mesoscale models: The Kain-Fritsch scheme. The representation of cumulus in numerical models. K. A. Emanuel and D. J. Raymond, eds, Meteorological Monographs. *American Meteorological Society*, 165-170.

Kidd C., Kniveton D. R., Todd M. C., Bellerby T. J., 2003, Satellite Rainfall Estimation Using Combined Passive Microwave and Infrared Algorithms, *Journal of Hydrometeorology* **4**, 1088-1104.

King P. W. S., Hogg W. D. and Arkin P. A., 1995, The role of visible data in improving satellite rain-rate estimates, *Journal of Applied Meteorology*, 34, 1608-1621.

Krajewski W. F., 1987, Cokriging radar-rainfall and rain gauge data, *Journal of Geophysical Research*, 92(d8), 9571-9580.

Krajewski W. F. and Smith J. A., 1991, On the estimation of climatological *Z–R* relationships, *Journal of Applied Meteorology*, 30, 1436–1445.

Kurino T., 1997a, A Rainfall Estimation with the GMS-5 Infrared Splid Window and Water Vapor Measurements, Tech. Rep., Meteorological Satellite Centre, Japan Meteorological Agency.

Kurino T., 1997b, A Satellite Infrared Technique for Estimating ‘Deep/Shallow’ Precipitation. *Advances in Space Research*, 19(3), 511-514.

Llasat M. C., 2001, An objective classification of rainfall events on the basis of their convective features. Application to rainfall intensity in the North-East of Spain, *International Journal of Climatology*, 21, 1385-1400.

Llasat M. C., Martín F., Carretero O., Rigo T., and De Batlle J., 2002, Diagnosis of a strong convective event produced in Catalonia on June 10, 2000. Proceedings of the 3rd EGS Plinius Conference, held at Baja Sardinia, Italy, 1-3 October 2001, *GNDCI*, pub. n. 2560, 67-70.

Llasat M. C., Rigo T., and Barriendos M., 2003, The ‘Montserrat-2000’ flash-flood event: a comparison with the floods in the Northeastern Iberian Peninsula since the 14th century, *International Journal of Climatology*, 23, 453-469.

Levizzani V, Amorati R, and Meneguzzo F. 2002. A review of satellite-based rainfall estimation methods. MUSIC. http://www.isac.cnr.it/~meteosat/papers/MUSIC-Rep-Sat-Precip-6.1.pdf

Lovejoy S. and Austin G.L. ,1979, The delineation of rain areas from visible and IR satellite data from GATE and mid-latitudes, *Atmos.-Ocean*, 17, 77-92.

Luque A., Gómez I., and Manso M., 2006, Convective Rainfall Rate multi-channel algorithm for Meteosat–7 and radar derived calibration matrices, *Atmósfera*, 19(3), 145-168.

Luque A., Martin A., Romero R. and Alonso S., 2006, Fine tuning of Radar Rainfall Estimates based on Bias and Standard Deviations Adjustments. *Fourth European Conference on Radar in Meteorology and Hydrology (ERAD 2006)*, Barcelona (Spain), September 2006 (Book of proceedings, http://www.grahi.upc.edu/ERAD2006/proceedingsMask/00038.pdf)

Marrocu M., Pompei A., Dalu G., Liberti G.L. and Negri A., 1993, Precipitation estimation over Sardinia from satellite infrared data, *International Journal of Remote Sensing*, 14, 115-134.

Marshall J. S., and Palmer W. M. K., 1948, The distribution of raindrops with size, *Journal of Atmospheric Sciences*, 5, 165-166.

Martín F. y De Esteban L., 1994, Manual de interpretación Radar, Publicación interna, STAP, INM, Madrid.

Martín A., Romero R. Homar V., De Luque A., Alonso S., Rigo, T., and Llasat C., 2006, Sensitivities of a flash flood event over Catalonia: A numerical analysis, *Monthly Weather Review*, Vol. 135, No. 2, pages 651–669.

Marzban C., 1998, Scalar Measures of Performance in Rare-event Situations, *Weather and Forecasting*, 13, 753-763

Menz G., 1997, Regionalization of precipitation models in east Africa using Meteosat data, *International Journal Climatology*, 17, 1011-1027.

Mlawer E. J., Taubman S. J., Brown P. D., Iacono M. J. and Clough S. A., 1997, Radiative transfer for inhomogeneous atmospheres: RRTM, a validated correlated-k model for the longwave, *Journal of Geophysical Research*, 102, 16663-16682.

Morales C. A. and Anagnostou E. N., 2003, Extending the capabilities of high-frequency rainfall estimation from geostationary-based satellite infrared via a network of Long-Range lightning observations, *Journal of Hydrometeorology*, 4, 141-159.

Morales C. A., Weinman J. A., Kriz J. S. and Alexander G. D., 1997, Thunderstorm distributions from NASA/RDI sferics observing system. Abstracts, Fall Meeting, San Francisco, CA, American Geo-physic Union.

Negri A. J. and Adler R. F., 1981, Relationship of satellite based thunderstorm intensity to radar-estimated rainfall, *Journal of Applied Meteorology*, 20,288-300.

Negri A. J., Adler R. F. and Wetzel P. J., 1984, Rain estimation from satellite: An examination of the Griffith-Woodley technique, *Journal of Climate Applied Meteorology*, 23, 102-116.

Oh H. J., Sohn B. J., Smith E. A., Turk F. J., Ae-suk S., and Chung H. S., 2002, Validating infrared-based rainfall retrieval algorithms with 1-minute spatially dense raingauge measurements over Korean peninsula, *Meteorology and Atmospheric Physics*, 81, 273-287.

Pérez Puebla F., 2004, Cooperación entre las redes de rayos de España y Portugal. XXVIII Jornadas Científicas sobre La Meteorología y el Clima Atlánticos, en el marco del 5º Encuentro Hispano-Luso de Meteorología, Badajoz (Spain), February 11 – 13, 2004.

Reisner J., Rasmussen R. J., and Bruintjes R.T., 1998, Explicit forecasting of supercooled liquid water in winter storms using the MM5 mesoscale model, *Quarterly Journal of the Royal Meteorological Society*, 124B, 1071-1107.

Riosalido R., 1994, STArPc. Software para Tratamiento y Analisis de datos radar en Pc, Nota técnica STAP Nº18 INM.

Reudenbach C., Heinemann G., Heuel E., Bendix J., and Winiger M., 2001, Investigation of summertime convective rainfall in Western Europe based on a synergy of remote sensing data and numerical models, *Meteorology and Atmosferic Physics*, 76, 23-41.

Romero R., Doswell III, C. A., and Ramis C., 2000, Mesoscale numerical study of two cases of long-lived quasistationary convective systems over eastern Spain, *Monthly Weather Review*, 128, 3731-3751.

Romero R., Doswell III, C. A., and Riosalido R., 2001, Observations and fine-grid simulations of a convective outbreak in northeastern Spain: Importance of diurnal forcing and convective cold pools, *Monthly Weather Review*, 129, 2157-2182.

Romero R., Ramis C., and Guijarro J. A., 1999, Daily rainfall patterns in the Spanish Mediterranean area: An objective classification, *International Journal of Climatology*, 19, 95-112.

Rosenfeld D., Amitai E. and Wolff D. B., 1995, Classification of rain regimes by the three-dimensional properties of reflectivity fields, *Journal of Applied Meteorology*, 34, 198-211.

Rosenfeld D., Wolff D. B. and Amitai E., 1994, The window probability matching method for rainfall measurements with radar, *Journal of Applied Meteorology*, 33, 683-693.

Schmetz J.,1989, Operational calibration of the Meteosat water vapor channel by calculated radiances, *Applied Optics*, 28, 3030.

Schmetz, J., Tjemkes S. S., Gube M. and Van de Berg L., 1997, Monitoring deep convection and convective overshooting with Meteosat, *Advances in Space Research*, 19, No. 3, 433-441.

Scofield R. A., 1987, The NESDIS operational convective precipitation technique, *Monthly Weather Review*, 115, 1773-1792.

Scofield R. A. And Oliver V. J., 1977, A scheme for estimating convective rainfall from satellite imagery, NOAA Technical Memorandum NESS 86, U.S. Dept. Commerce, Washington, DC, 47 pp.

Scofield R. A., and Kuligowski R. J., 2003, Status and outlook of operational satellite precipitation algorithms for extreme precipitation events, *Weather and Forecasting*, 18, 1037-1051.

Sempere-Torres D., Sánchez-Diezma R, Córdoba M. A., Pascual R. and Zawadzki I., 2001, An operational methodology to control radar measurements stability from mountain returns. 30th International Conference on Radar Meteorology, Munich, Germany, 19-24 July 2001, 264-266.

Seo D. J., 1998, Real-time estimation of rainfall fields using radar rainfall and rain gage data, *Journal of Hydrology*, 208, 37-52.

Tjemkes S. A., König M., Lutz H.-J., van de Berg L. and Schmetz J., 2001, Calibration of Meteosat water vapour channel observations with independent satellite observations, *Journal of Geophysical Research*, Vol. 106, D6, 5199-5209.

Troen I., and Mahrt, L., 1986, A simple model of the atmospheric boundary layer: Sensitivity to surface evaporation, *Boundary Layer Meteorology*, 37, 129-148.

Turk F. J., Rohaly G., Hawkins J. D., Smith E. A., Grose A., Marzano F. S., Mugnai A. and Levizzani V., 2000, Analysis and assimilation of rainfall from blended SSMI, TRMM and geostationary satellite data. 10th AMS Conference on Satellite Meteorology and Oceanography, Long Beach CA, 15 Jan 2000. pp. 66-69.

Urbanski D. P., 1982, Use of geostationary satellite imagery to estimate convective precipitation over complex terrain in the western United States, Master Thesis, Department of Meteorology, University of Utah, USA.

Van de Berg L., Schmetz J. and Whitlock J., 1995, On the calibration of the Meteosat water vapor channel, *Journal of Geophysical Research*, lOO(DIO), 21069 - 21076

Vicente G. A., Davenport J. C. and Scofield R. A., 2002, The role of orographic and parallax corrections on real time high resolution satellite rainfall rate distribution, *International Journal of Remote Sensing* 23, 221-230.

Vicente G. A. and Scofield R. A., 1996, Experimental GOES-8/9 derived rainfall estimates for flash flood and hydrological applications, Proc. 1996 Meteorological Scientific User`s Conference, Vienna, Austria, EUM P19, 89-96.

Vicente G. A., Scofield R. A. and Menzel W. P., 1998, The operational GOES infrared rainfall estimation technique, *Bulletin of the American Meteorological Society*, 79, 1883-1898.

Woodley W. L., 1970, Precipitation results from pyrotechnic cumulus seeding experiment, *Journal of Applied Meteorology,* 9, 109-122.

Woodley W. L., Olsen A. R., Herndon A. and Wiggert V., 1975, Comparison of gauge and radar methods of convective rain measurements, *Journal of Applied Meteorology,* 14, 909-928.

Woodley W. L., Sancho B. and Miller A. H., 1972, Rainfall estimation from satellite cloud photographs, *NOAA Technical Memorandum,* ERL OD-11, 43 pp.

Wylie D. P., 1979, An application of a geostationary satellite rain estimation technique to an extra-tropical area, *Journal of Applied Meteorology*, 18, 1640-1648.